博士論文

Epitaxial Growth of Ge Layer with Low Threading Dislocation Density on Si Substrate for Light-Emitting Device Applications

（発光素子応用に向けたSi基板上低貫通転位密度Ge層のエピタキシャル成長）

八子　基樹

Epitaxial Growth of Ge Layer with Low Threading Dislocation Density on Si Substrate for Light-Emitting Device Applications

(発光素子応用に向けた **Si** 基板上 低貫通転位密度 **Ge** 層のエピタキシャル成長)

by

Motoki Yako

Submitted to the Department of Materials Engineering
in Partial Fulfillment of the Requirements for the Degree of
Doctor of Philosophy in Materials Engineering at
The University of Tokyo

ABSTRACT

The objective of this work is to establish a novel method to reduce threading dislocation densities (TDDs) in epitaxially grown germanium (Ge) layers on silicon (Si) for light-emitting device applications. This dissertation describes a proposal of novel TDD reduction model, numerical calculations of TDD reduction, experimental verifications for TDD reduction, direct observations of threading dislocations (TDs) by transmission electron microscopy (TEM), and a feasibility study for light-emitting device applications.

Silicon photonics has been considered as a promising technology to enable high-speed, large-capacity, and low-cost communication networks. For the practical applications of silicon photonics technology, the development of on-chip light sources has been one of the most important challenges fundamentally because of the indirect band structure of Si. As a candidate for on-chip light source material, tensile-strained n-type Ge was theoretically proposed in 2007, and first Ge laser diode (LD) was reported in 2012. Ge can emit (and detect) light around 1.55 μm, corresponding to optical communication wavelength, and is compatible with Si complementary metal oxide semiconductor processing. However, previously reported Ge LDs have shown substantially large threshold current densities J_{th}; almost two orders of magnitude larger than the theoretical prediction.

The major causes of the large J_{th} are considered as non-radiative recombination (NRR) at Ge surfaces and defect-assisted NRR in Ge layers. In the case for Ge epitaxial layers on Si, misfit dislocations are formed on Ge/Si hetero-interfaces, and threading dislocations (TDs) are formed in Ge epitaxial layers owing to lattice-mismatch between Ge and Si as large as 4.2 %. In the beginning of this dissertation, it is confirmed that NRR at Ge surfaces is suppressed by thermal oxidation, and then TDD reduction is required for Ge light-emitting device applications. Because of large lattice-mismatch between Ge and Si, the density of TDs in Ge on Si is as high as 10^9 cm^{-2}. Although many methods have been attempted to reduce TDD in Ge epitaxial layers on Si, the previous methods have drawbacks for light-emitting device applications in terms of dopant out-diffusion and/or optical confinement in Ge. Thus, a novel TDD reduction method is required for light-emitting device applications, i.e., to reduce J_{th} in Ge LDs.

A novel method for TDD reduction is proposed employing image force and selective epitaxial growth (SEG) technique. Image force is an attractive force between dislocations and free surfaces. Since epitaxial growth of Ge occurs on Si, but not on SiO_2, SiO_2 can be a mask material to form finite Ge epitaxial layers on Si, which is Ge SEG technique. The novel method is free from the drawbacks in previous attempts.

A theoretical model for the novel TD reduction method is proposed and numerical calculations are performed. The TDD reduction occurs as following steps:

(1) TDs are bent to be normal to growth surfaces owing to image force,

(2) bent TDs penetrate to bottom Ge/Si interfaces as Ge SEG proceeds, and

(3) some TDs are terminated to the bottom Ge/Si interfaces when SEG Ge layers coalesce each other, resulting in reduction of TDD observed on the top Ge surface.

The numerical calculations show that the rate of TDs terminated to the bottom Ge/Si interfaces is determined by aperture ratio of SEG mask, i.e., the rate of Ge growth area. The numerical calculations reveal that TDD reduction by a factor of 1/100 is achievable where aperture ratio is as small as 0.1.

Experimental verification of the theoretical model is carried out in 3 steps.

First, Ge growth in lateral direction over SiO_2 masks is investigated by cross-sectional scanning electron microscopy (SEM) observations. It is found the growth rate of Ge in lateral direction depends on the width of Ge growth area, which indicate that the Ge growth in lateral direction is dominated by the Ge facets of the slowest growth rate; {113} facets. As a result, it is found that SEG Ge layers coalesce when both the width of Ge growth area and the width of SiO_2 masks are narrow enough, finally forming flat-top films (coalesced Ge).

Then, experimental verification of TDD reduction is performed employing etch pit density (EPD) measurement method. It is revealed that TDD in coalesced Ge is reduced as theoretically predicted. In addition to the reduction of TDD, distribution of TDs penetrating to the top surface well reproduces the theoretical model. TDD as low as 4×10^7 cm^{-2} is obtained in coalesced Ge, where aperture ratio is 0.6. This TDD is two orders of magnitude lower than that in ordinary Ge epitaxial layers on Si.

Finally, TEM observations are performed to observe TDs in coalesced Ge. Cross-sectional TEM observations reveal that the termination of TDs at bottom surfaces actually occurs in coalesced Ge as predicted. Plan-view TEM observations directly show that TDD in coalesced Ge is lower than that in blanket Ge. Not only the behavior of TDs predicted by the theoretical model, cross-sectional TEM observations reveal that generation of TDs in coalesced Ge, and plan-view TEM observations reveal that there are TDs inclined to be parallel to SiO_2 masks in coalesced Ge. Both unpredicted behaviors of TDs are, however, understandable considering image force and slight misorientation among SEG Ge layers.

For a feasibility study to light-emitting device applications, tensile strain and n-type doping in coalesced Ge are investigated. Tensile strain is induced in coalesced Ge owing to thermal expansion mismatch between Ge and Si. N-type doping in coalesced Ge is performed by thermal diffusion of phosphorus (P). Both tensile strain and n-type doping level are enough for light-emitting device applications. In addition to that, simulation of optical propagation mode in coalesced Ge reveals that coalesced Ge has advantage over conventional structure in terms of less light intensity at defect-rich Ge/Si hetero-interfaces.

At the last part of this dissertation, light emission from coalesced Ge layers are observed by photo-

luminescence (PL) measurements and optical pumping measurements. PL measurements are carried out before and after the P thermal diffusion. PL measurements before the diffusion suggests that there are NRR centers in coalesced Ge, which is not TDs, and the NRR centers are removed during the P diffusion process.

Fabry-pérot (FP) resonators are fabricated using the coalesced Ge layers, and optical pumping measurements are carried out on the FP resonators. Threshold-like behaviors are observed with the threshold power density of 18 kW/cm^2. The observed threshold-like point is smaller than reported threshold in an optically pumped Ge laser, although it is still not due to laser operation because resonance-induced sharp peak is not observed. Since amplified spontaneous emission (ASE) also shows similar threshold behavior, the observed threshold-like behavior would be ascribed to ASE. Nevertheless, reduction of threshold-like point for ASE is observed in coalesced Ge, indicating that coalesced Ge layers are better than blanket Ge layers in terms of light-emitting device applications.

In summary, a novel method to reduce dislocations in Ge epitaxial layers on Si is theoretically proposed and experimentally verified. A feasibility study for light-emitting device applications show a promising result, i.e., enhancement of ASE compared to conventional Ge epitaxial layer on Si. Further reduction of TDD and laser operation is expecting employing the method proposed and verified in this dissertation.

Acknowledgement

I would like to appreciate many people who have supported and cooperated with me.

Since my doctoral course has partly been commissioned to Toyohashi University of Technology, I would like to thank to people both in the University of Tokyo and Toyohashi University of Technology.

The supervisor of this dissertation, Prof. Kazuki Morita, has been supported my Ph. D. research in every respects. His kind and generous supports are essential to my Ph. D. research.

In Toyohashi University of Technology, Prof. Yasuhiko Ishikawa has supervised me and given many advises on research direction, deep discussion on data analysis, writing skill on journal article, etc. I have learned many things from his accurate advises based on careful analysis.

I also like to appreciate Prof. Kazumi Wada in Massachusetts Institute of Technology in USA. He had been my supervisor when I was a master course student, but he has kept being co-researcher on the Ge-light-emitter project. Discussion with him has given me many ideas.

Professor Donghwan Ahn, in Kookmin University in Republic of Korea, has also been co-researcher on the Ge-light-emitter project. N-type doping by thermal diffusion has been performed by him and his students.

Professor Eiji Abe has helped me for TEM observations and discussions on dislocation analysis. His kind supports and deep knowledge on TEM are necessary for this dissertation.

During my doctoral course in the University of Tokyo, I would like to thank the staffs/students in Ishikawa lab., Morita lab., Abe lab, and Takeda clean room.

In Ishikawa lab., I would like to appriciate Dr. Naoyuki J. Kawai for his many advises on research direction and process design, Dr. Jiro Osaka for his supports on Ge epitaxial growth in the University of Tokyo, and Mrs. Hiroko Shimizu for her supports on my research in respect to paperwork. Students who had been in Ishikawa lab. had supported me and given me some ideas. Thank you for Mr. Naoki Higashitarumizu, Mr. Yuji Miyasaka, Mr. Michiharu Nishimura, Mr. Kazuki Ito, Mr. Daichi Iwahashi, and Ms. Miki Kawate.

In Morita lab., I would like to appreciate Mrs. Naomi Nakaya for her supports on many paperworks.

In Abe lab., I would like to appreciate Mr. Kenya Yamashita and Ms. Saho Hirata for their supports on TEM observations.

Many part of fabrication processes in the University of Tokyo had been performed in Takeda clean room. I would like to appreciate clean room manager, VDEC members and other users for their helps on experiments.

For my doctoral research in Toyohashi University of Technology, I would like to thank the students in Ishikawa lab. and the supporting staffs.

Students in Ishikawa lab., Mr. Ryota Oyamada, Mr. Kazuki Kawashita, Ms. Mayu Tachibana, Mr. Kyosuke Noguchi, Mr. Yuuki Ueno, Mr. Kyohei Sonoi, Mr. Asahi Degawa, and Mr. Kazuki Motomura, has been supported my research life in Toyohashi.

I would like to appreciate the supporting staffs in Toyohashi University of Technology for their help on machine setup and experiments. In particular, I would like to thank Dr. Takeshi Hizawa for his supports in many respects.

I also would like to appreciate Prof. Junya Matsui, Dr. Yoshiyuki Tsusaka, and Mr. Tetsuya Tsurumaru in University of Hyogo for their supports on measurements at SPring-8.

Photoluminescence dependence on temperature was supported by Dr. Naokatsu Yamamoto and Dr. Atsushi Matsumoto. I would like to appreciate for their kind help.

Finally, I really appreciate my family for their understanding and constant support for my doctoral course.

Motoki Yako

Contents

1 Introduction **1**
- 1.1 Silicon Photonics . . . 1
- 1.2 Status Quo of Light-Emitting Devices on Si . . . 3
- 1.3 Ge as a Gain Medium on Si . . . 4
  - 1.3.1 Strain-Induced Bandgap Engineering . . . 5
  - 1.3.2 N-Type Doping for Ge to be Pseudo-Direct Bandgap . . . 5
- 1.4 Outline of Thesis . . . 8

2 Ge Epitaxial Layers for Light Emitter **10**
- 2.1 Methods and Issues of Ge Epitaxial Growth on Si . . . 10
- 2.2 Carrier Recombination in Bulk Ge . . . 11
  - 2.2.1 Radiative Recombination . . . 12
  - 2.2.2 Dislocation-assisted NRR in Epitaxial Ge on Si . . . 12
  - 2.2.3 Auger Recombination and Free Carrier Absorption . . . 13
- 2.3 NRR at Surfaces/Interfaces on Epitaxial Ge on Si . . . 13
  - 2.3.1 Surface/Interface NRR Velocities: Background . . . 14
  - 2.3.2 Estimation of Surface/Interface NRR Velocities: Theory . . . 14
  - 2.3.3 Estimation of Surface/Interface NRR Velocities: Experimental Procedure . . . 16
  - 2.3.4 Estimation of Surface/Interface NRR Velocities: Results and Discussion 17
- 2.4 Requirements Toward Low-Threshold Ge LDs . . . 21

3 Theoretical Model and Calculation for the Reduction of TDs by Image Force **24**
- 3.1 Image Force: Driving Force for TD Bending . . . 24
- 3.2 Numerical Calculations of TD Reduction . . . 26
  - 3.2.1 TD Bending in SEG Ge Layers . . . 26
  - 3.2.2 Reduction of TDD Induced by TD Bending and Coalescence . . . 29
  - 3.2.3 Extensibility to other hetero-epitaxy . . . 34

4 Lateral Growth and Coalescence of SEG Ge Layers **35**
- 4.1 Experimental Procedure: Ge SEG on Si . . . 35
  - 4.1.1 Preparation of SEG Masks . . . 35
  - 4.1.2 Ge Epitaxial Growth on Si . . . 37
- 4.2 Ge Lateral Growth Over SiO_2 Masks . . . 38
  - 4.2.1 Experimental Observations of W_{window} . . . 38
  - 4.2.2 Ge Growth in Lateral Direction at 700 °C . . . 38
  - 4.2.3 Ge Growth in Lateral Direction at 650 °C . . . 42
  - 4.2.4 Ge Wetting Growth on SiO_2 . . . 42
- 4.3 Coalescence of SEG Ge Layers Over SiO_2 Masks . . . 44
- 4.4 Orientation Dependence for Lateral Growth and Coalescence of Ge . . . 48

5 Experimental Verification of Theoretical Model by Measurements of TDDs 52
5.1 Experimental Procedure: Measurements of TDDs by EPD Method 52
5.2 Comparison of TDDs Between Experimental Results and Theoretical Calculation 55
5.2.1 TDDs in Coalesced SEG Ge Layers 55
5.2.2 Correlation Between TDDs and Layer Thickness for Blanket Ge Layers 56
5.2.3 Normalized TDDs vs. Theoretical Model 56
5.3 Distribution of TDs in Coalesced Ge 59
5.4 Discussions 60
5.4.1 Absence of "TDD Re-Increase" in Coalesced Ge 60
5.4.2 Comparison with Other TDD Reduction Methods 61
5.4.3 Toward Further Reduction of TDD 62

6 TEM Observations of TDs in Coalesced Ge 67
6.1 Experimental Procedure: TEM Observations 67
6.2 Cross-Sectional TEM Observations 68
6.2.1 TDs in SEG Ge; before coalescence 68
6.2.2 TDs in coalesced SEG Ge 69
6.3 Plan-View TEM Observations 71
6.4 Discussions: Coalescence Induced Generation/Bending of TDs 74

7 Material Propaties of Coalesced Ge for Light-Emitting Device Applications 79
7.1 Tensile Strain in Coalesced Ge 79
7.1.1 Strain Simulation by Finite Element Method 79
7.1.2 Experimental Measurements of Strain in Coalesced Ge Layers 80
7.1.3 Characterization of Coalesced Ge Layers by Macro-XRD 82
7.1.4 Characterization of Local Strain in Coalesced Ge Layers by μ-XRD . 83
7.2 N-Type Doping by Thermal Diffusion 84
7.3 Optical Propagation Mode Push-Up in Coalesced Ge 87

8 Light Emission From Coalesced Ge Layers 91
8.1 PL from Coalesced Ge Layers at Room Temperature 91
8.1.1 Measurement Setup 91
8.1.2 Results and Discussions 92
8.2 Temperature Dependence of PL from Coalesced Ge Layers 96
8.2.1 Theoretical Background 96
8.2.2 Measurement setup 96
8.2.3 Results and Discussions 97
8.3 Optical Pumping Measurements 98
8.3.1 Fabrication of Fabry-Pérot Resonators 100
8.3.2 Measurement Setup 101
8.3.3 Light Emission Under Excitation by a CW Laser 103
8.3.4 Light Emission Under Excitation by a Micro-sec Pulsed Laser 105
8.3.5 Light Emission Under Excitation by Nano-sec Pulsed Laser 111

8.4 Discussions: Toward Low J_{th} Ge LDs 113
8.4.1 Optimization of the Measurement System 113
8.4.2 Optimization of the Active Ge Layers 114

9 Summary and Future Outlook **116**
9.1 Summary 116
9.2 Future Outlook 118
9.2.1 Controlling trajectories of TDs 118
9.2.2 Promising cross-sectional structure for Ge LDs 118

Appendix **121**
Appendix I. Enhancement of PL Induced by a Wet Chemical Treatment 121
Appendix II. TDD Dependence of PL from Ge Epitaxial Layers on Si 128

Bibliography **130**

Publication List **143**

List of Figures

1.1 Predictions for the market size of Si photonics-related products 2
1.2 A schematic illustration of EPIC on a Si substrate 3
1.3 Schematic illustrations of band engineering of Ge through tensile strain application and n-type doping 6
1.4 Calculated bandgap as a function of biaxial strain in <110> and <1$\bar{1}$0> direction 6
1.5 Calculated Fermi level ξ and Γ-lh bandgap (tensile strain of 0.1–0.3 %) as a function of active doping concentration 7
2.1 (a) A cross-sectional SEM image of Ge epitaxial layer and (b) a schematic illustration of cross-sectional structure. 16
2.2 PL spectra from a Si-capped Ge layer excited by a 457-nm laser (blue) and a 785-nm laser (red). 17
2.3 Calculated profiles of hole in Ge illuminated by (a) 785-nm laser and (b) 457-nm laser. (c) Calculated dependence of $\frac{I_{785}}{I_{457}}$ as a function of $S_{Ge/Si}$ and τ. 18
2.4 (a) A schematic illustration of cross-sectional structure, (b) measured PL spectra from a bare Ge layer, and (d) calculated dependence of $\frac{I_{785}}{I_{457}}$ as a function of $S_{Ge/air}$ and τ. 19
2.5 (a) A schematic illustration of cross-sectional structure, (b) measured PL spectra from a GeO_2-capped Ge layer, and (d) calculated dependence of $\frac{I_{785}}{I_{457}}$ as a function of S_{Ge/GeO_2} and τ. 20
2.6 Schematic illustrations of conventional TDD reduction methods: (a) thermal annealing, (b) SiGe graded buffer, (c) aspect ratio trapping, and (d) Ge growth on Si pillars. 22
3.1 Schematic illustrations of a σ_{xx} around an edge dislocation parallel to z axis where (a) far away from surface/interface and (b) near a free surface 25
3.2 Calculation results of shear stressed induced by image force as a function of a distance between a dislocation and a free surface 26
3.3 (a)–(c): Numerical calculation process to calculate a trajectory of a TD in a round-shaped SEG Ge. (d): Trajectories of TDs in a {113}-facetted SEG Ge . 28
3.4 TD reduction as the results of bending and coalescence 30
3.5 Calculated TDD reduction factor f as a function of APR. Dots indicate calculated values. 30
3.6 Trajectories of TDs in coalesced Ge when Ge does not grows on SiO_2 masks. 32
3.7 Trajectories of TDs in coalesced Ge originated from (a) round-shaped SEG Ge and (b) {113}-facetted SEG Ge, in the case for Ge grows on SiO_2 masks. . 33
3.8 Calculated TDD in coalesced Ge as a function of aperture ratio 33
4.1 Schematic illustrations of SEG mask, W_{window}, and W_{mask} 37
4.2 (a) A bird's eye view AFM image of SEG mask before Ge growth and (b) the relation between designed W_{window} and experimentally obtained W_{window} . . . 39
4.3 A cross-sectional SEM image of Ge grown in blanket area at 700 °C 40

4.4 (a) A typical cross-sectional SEM image of a SEG Ge layer grown at 700 °C (W_{window} = 0.8 μm in design) and (b) schematic illustration showing the relation among W_{window}, W_{Ge}, and $W_{overhang}$ 41
4.5 (a) $W_{overhang}$ as a function of W_{window} and (b) growth rates of Ge on (001) planes (GR_{001}) and {113} facets (GR_{113}). Growth rates are obtained from *Y. Mizuno, Master's thesis, The University of Tokyo, 2010*. 43
4.6 A cross-sectional SEM image of Ge grown in blanket area at 650 °C 44
4.7 (a) A cross-sectional SEM image of SEG Ge grown at 650 °C, (b) a schematic illustration of the SEM image, and (c) a schematic illustration of Ge wetting growth on SiO_2 masks. 45
4.8 A distribution maps of coalesced/non-coalesced Ge grown at (a) 700 °C and (b) 650 °C, (c) a cross-sectional SEM image and (d) plan-view OM image of coalesced Ge with flat-top surface, and (e) a cross-sectional SEM image and (f) plan-view OM image of coalesced Ge with non-flat-top surface. 46
4.9 Bird's eye view AFM images of (a) coalesced Ge (W_{window} = 0.5 μm, W_{mask} = 0.6 μm in design) and (b) blanket Ge grown on the same Si wafer 47
4.10 (a) A cross-sectional HAADF STEM image of SEG Ge grown at 700 °C with $Si_{0.3}Ge_{0.7}$ layers and (b) a schematic illustration of the STEM image 48
4.11 Plan-view SEM images of 0.7-μm-wide (in design) SEG Ge layers aligned to (a) 0°and (b) 30° deviated from [110] direction 49
4.12 OM images of (a) circle-shaped SEG mask (W_{window} = 0.9 μm, W_{mask} = 0.5 μm in design) and (b) coalesced Ge ring grown on the SEG mask, (c) a bird's eye view AFM image of the coalesced Ge ring, and (d) cross-sectional profile of convex part indicated by blue dashed line in (c). 50
5.1 Si etching rate by 2.38 % TMAH (NMD-3) at 80 °C 53
5.2 Schematic illustration of TDs visualization by $CH_3COOH/HNO_3/HF/I_2$ solution 54
5.3 Correlation between EPD measured by AFM and TDD obtained by plan-view TDD. The data indicated as black opened diamonds are obtained from *Y. Takada, Master's thesis, The University of Tokyko, 2010*. 54
5.4 Typical AFM images of (a) coalesced Ge grown at 700 °C, (b) coalesced Ge grown at 650 °C, and (c) blanket Ge grown at 700 °C after wet etching for TDs visualization 55
5.5 TDDs in blanket Ge layers as a function of the layer thickness 57
5.6 TDDs in coalesced Ge layers as a function of the layer thickness 59
5.7 A 10 μm × 10 μm bird's eye view AFM image on non-flat-top coalesced Ge (W_{window} = 1.0 μm and W_{mask} = 0.7 μm in design) after wet chemical etching for TD visualization 60
5.8 Comparison between ART work (J. G. Fiorenza, *et al.*, 2010) and this work in terms of TDD re-increase 61
5.9 The thickness of blanket Ge when SEG Ge layers coalesce as a function of W_{window} and W_{mask} at 700 °C 63
5.10 Schematic illustrations of (a) EB lithography system and (b) i-line stepper (photolithography with reduction projection lens) 64

5.11 Top-view SEM images of SiO_2 masks with (a) continuous lines and (b) intermittent lines. Exposure time was 470 msec for both of (a) and (b). 65

5.12 Schematic illustration showing conversion of W_{window} and W_{mask} employing (a)–(c) lift-off process and (d)–(f) LOCOS process 66

6.1 Schematic illustrations of TEM specimens for (a) cross-sectional and (b) plan-view TEM observations. 68

6.2 (a)–(c) Bright-field (110) cross-sectional TEM images of Ge selective epitaxial layers and (d)–(f) their schematic traces: (d), (e), and (f) correspond to (a), (b), and (c), respectively. 69

6.3 (a) A cross-sectional bright-field TEM image of coalesced Ge and (b) a cross-sectional bright-field STEM image of a TD terminated by a void. 70

6.4 Examples of bright-field (110) cross-sectional (a) STEM and (b) TEM images showing TDs around semicylindrical voids with incident electron beam slightly tilted from the [110] zone axis, and (c) an electron diffraction pattern obtained around TD seen at the center of (b). 72

6.5 Examples of bright-field (001) plan-view TEM images taken for (a) coalesced Ge layer and (b) blanket Ge layer. Top 200 nm of the Ge layers are observed as schematically shown by black dashed squares. The electron beam is slightly tilted from the [001] zone axis. 73

6.6 (001) dark-field plan-view TEM images of a coalesced Ge layer. A red-circled dislocation shown in (a) ($\mathbf{g}$ = [220]) is not shown in (b) ($\mathbf{g}$ = $[2\bar{2}0]$) indicating that the red-circled dislocation is a screw dislocation. On the other hand, white-circled dislocations do not disappear with any g vectors indicating that the green-circled dislocations are mixed dislocations. 75

6.7 (a) A plan-view SEM image showing the beginning of coalescence of SEG Ge layers and (b) a schematic illustration of $(1\bar{1}0)$ cross-section along the line A–A' in (a) showing the evolution of Ge coalescence. In (b), a TD inclined to [110] direction is also shown (red solid line), and the yellow area shows Ge layers already grown in Fig. 6.7 (a) whereas the light green area shows Ge layers to be grown. 76

6.8 Schematic illustrations showing defect generation at the coalesced interface of SEG Ge layers. (a) Rotation on the [110] direction, (b) rotation on the [001] direction, and (c) rotation on the $[1\bar{1}0]$ direction. 77

7.1 (a) A FEM simulation result showing strain profile in coalesced Ge, and (b) strain in coalesced Ge as a function of APR 81

7.2 (a) Raman spectra for a Ge wafer (black), blanket Ge (red), and coalesced Ge (blue), and (b) comparison between experimental results and simulation . . . 82

7.3 2θ-ω XRD results obtained from blanket Ge (black) and coalesced Ge of W_{mask} = 0.6 μm in design (blue; W_{window} = 0.6 μm in design, red; W_{window} = 0.8 μm in design). 83

7.4 A schematic illustration of scan direction Z during the μ-XRD measurements 84

7.5 ω-Z map obtained from (a) coalesced Ge (W_{window} = 0.6 μm, W_{mask} = 0.5 μm in design), (b) coalesced Ge (W_{window} = 0.8 μm, W_{mask} = 0.6 μm in design), (c) coalesced Ge (W_{window} = 0.6 μm, W_{mask} = 0.5 μm in design), and (d) blanket Ge. 85
7.6 Schematic illustrations of P diffusion process; (a) Ge epitaxial layer on Si, (b) PSG deposition, (c) P thermal diffusion into Ge, and (d) n-type Ge as the result of diffusion. 86
7.7 SIMS profiles of Si, Ge, and P in P-diffused Ge 87
7.8 Correlation between growth/anneal temperature and active doping concentration. Black opened circles are from J. Liu, *et al.*, *Thin Solid Films*, 520(8), 3354 (2012), showing decrease of doping concentration owing to out-diffusion. The yellow star indicates P concentration achieved by thermal diffusion in this work. 88
7.9 Optical propagation modes in (a) coalesced Ge, (b) optically pumped Ge laser reported by J. Liu, *et al.*, *Opt. Lett.*, 35(5), 679 (2010), and (c) electrically pumped Ge laser reported by R. E. Camacho-Aguilera *et al.*, *Opt. Exp.*, 20(10), 11316 (2012). 89
7.10 Optical propagation modes push-up in coalesced Ge layers 90
8.1 A schematic illustration of μ-PL measurement system used at room temperature. Red arrow indicates 785-nm excitation laser, and blue arrow indicates PL from Ge. 92
8.2 (a) Typical PL spectra from Ge wafer and as-grown blanket/coalesced Ge. (b) Integrated PL intensity (1500–1700 nm) as a function of APR. 93
8.3 (a) Typical PL spectra from Ge wafer and P diffused blanket/coalesced Ge. (b) Integrated PL intensity (1500–1700 nm) as a function of APR. 95
8.4 A (110) cross-sectional STEM image of a coalesced Ge layer with $Si_{0.3}Ge_{0.7}$ demarcation layers showing difference of growth rates. 96
8.5 Schematic illustrations of (a) indirect (bulk Ge) and (b) pseudo-direct (n-type doped) band structure for Ge. 97
8.6 A schematic illustration of μ-PL measurement system used at low temperature (4–200 K). Green arrow indicates 532-nm excitation laser, and blue arrow indicates PL from Ge. 98
8.7 PL spectra obtained at 4–200 K from (a) P diffused coalesced Ge and (b) bulk Ge, and (c) integrated PL intensity (1200–1700 nm) as a function of temperature. 99
8.8 Schematic illustrations of fabrication process flow for a FP resonator 101
8.9 Schematic illustrations of optical pumping measurement system for CW and micro-sec pulsed excitation 102
8.10 Schematic illustrations of optical pumping measurement system for nano-sec pulsed excitation 103
8.11 (a) Light emission spectra from the coalesced Ge and (b) light emission intensity as a function of input power density 104

8.12 A plan-view NIR microscope image of a coalesced Ge after optical pumping measurements by CW excitation 105
8.13 (a) Light emission spectra and (b) integrated emission intensity as a function of input power density 106
8.14 A bird's eye view SEM image of an as-cleaved edge of coalesced Ge 107
8.15 (a) An optical microscope image of melted Ge FP resonators after laser dicing and (b) a 3D laser microscope image of FIB polished edge of a Ge FP resonator 108
8.16 A cross-sectional SEM image of an FIB polished edge of Ge FP resonator . . 108
8.17 (a) Integrated intensities of light emission from a Ge FP resonator as a function of input power density, and (b) a typical spectra of light emission from the Ge FP resonators 109
8.18 Light emission spectrum obtained through measurements for 10 times. The peak indicated by black arrow reproduced during the 10 measurements. . . . 110
8.19 Integrated emission intensities from Ge FP resonators 110
8.20 Spectra of light emission from FP resonators excited by a nano-sec pulsed laser 112
8.21 Integrated emission intensity (in the range of 1550–1800 nm) as a function of input power density 112
8.22 A schematic illustration showing disalignment between an inverted-rib Ge FP resonator and the objective lens 113
9.1 Schematic illustrations showing an idea to control trajectories of TDs: (a) SiO_2 SEG masks, (b) SEG Ge before coalescence, and (c) Ge after coalescence. The red circles in (c) indicate where TDs accumulate (high TDD), and the blue circle in (c) indicates where low TDD area. 119
9.2 Schematic illustrations showing (a) n-type Ge completely surrounded by GeO_2, (b) n-type Ge surrounded by GeO_2 with small contact window, (c) an inverted-rib Ge structure with pn junction, and (d) simulated optical mode in inverted-rib Ge shown in (c). 119
10.1 Cross-sectional SEM images of an SEG Ge layer (a) before and (b) after the wet chemical treatment. The traces of the SEM images are shown and overlapped in (c). 122
10.2 Cross-sectional SEM images of an SEG Ge layer (a) before and (b) after the wet chemical treatment. The traces of the SEM images are shown and overlapped in (c). 123
10.3 PL spectra from SEG/blanket Ge layers before/after the wet chemical treatment 124
10.4 2D FDTD simulation results of magnetic field in (a) SEG Ge and (b) blanket Ge layers illuminated by x-polarized gaussian beam in 2-μm-diameter. 125
10.5 (a) PL spectra after the wet chemical treatment, and (b) integrated PL intensity (1300–1900 nm) as a function of SEG width. 126
10.6 (a) PL spectra observed on Ge epitaxial layers with various thicknesses, and (b) integrated PL intensity (1200–2000 nm) as a function of thickness. TDD is estimated from the TDD-thickness relation shown in Fig. 5.5. 129

List of Tables

1.1 Reported attempts for on-chip LDs 5
2.1 Reported methods for reduction of TDDs in Ge-on-Si 22
4.1 Process conditions for photoresist coating, EB lithography, and development. 36
5.1 Cross-sectional structures and EPDs of Ge layers shown in Fig. 5.4 55
5.2 Cross-sectional structures and TDDs in Ge layers shown in Fig. 5.6 58
5.3 Process conditions for photoresist coating, lithography, and development. . . 64

1 Introduction

Optical communication has played an essential role in information society since the birth of optical fiber in the 1960s. Optical communication has advantages over electrical communication in terms of data capacity, power consumption, RF interference, and safety, which have enabled today's wide spread long-haul communication via optical fiber, such as FTTH (Fiber-To-The-Home). In order to satisfy recent increasing demand for communication capacity, however, much shorter-distance optical communication is required, e.g., inside a data center, a mother board, and even a chip. The shorter-distance optical communication requires more mature technique for the integration of photonics and electronics, and silicon photonics is a promising candidate to realize integrated photonics. In this chapter, brief introductions of silicon photonics and on-chip light-emitting devices, one of the most important challenges for silicon photonics, are described.

1.1 Silicon Photonics

Silicon (Si) photonics has been developed as a technology to integrate photonic and electronic devices on a Si substrate employing Si CMOS (complementary metal oxide semiconductor) processing. Si photonics has an advantage in terms of fabrication cost because Si CMOS processing is much lower-cost than wafer bonding or off-chip integration, which have been required for the integration of III-V materials-based photonic devices with electronic circuits. Therefore, Si photonics enables low-cost fabrication of optical devices such as optical transceivers, active optical cables, multiplexers and attenuators on a Si substrate, which has been becoming more important in the shorter-distance optical communication. The advantage of Si photonics in terms of low-cost fabrication has brought expansion of the market size of Si photonics-related products since its emerging around 2010 (Fig. 1.1). As summarized in Fig. 1.1, it is predicted that the Si photonics market size will grow 20–30 % per annum, and reach several thousands of million dollars, by several companies [1–3]. These predictions shows

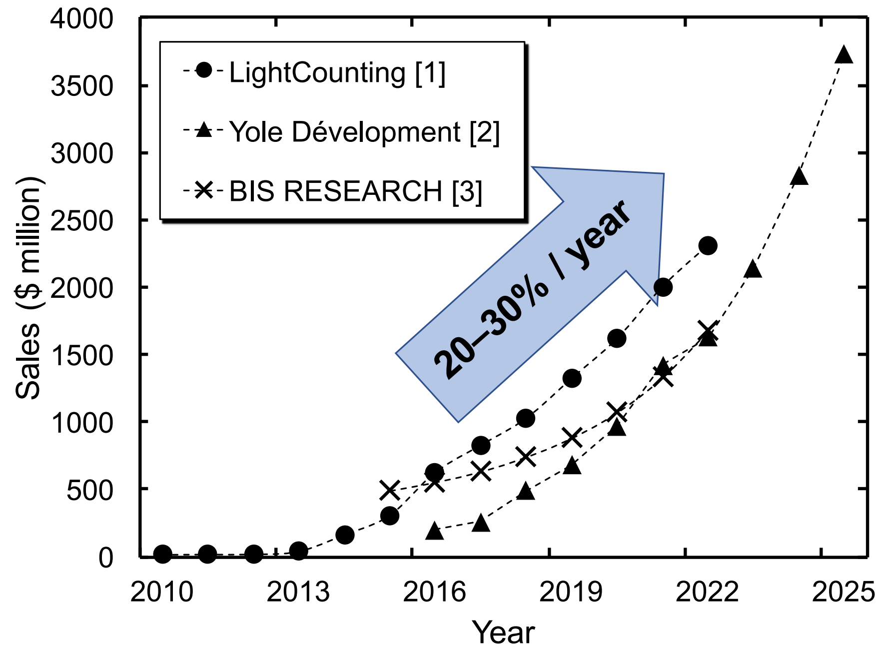

Figure 1.1: Predictions for the market size of Si photonics-related products

great expectation to Si photonics technology from market.

Another important application of Si photonics is the on-chip integration with electronic circuits for faster data processing. The performance of Si CMOS integrated circuit (IC) processors has been improved by increasing the number of transistors on an IC chip; so-called Moore's Law. The highly-dense integration of transistors results in, however, severe heat dissipation and RC delay, and thus the improvement of the performance of IC chips has been reaching its physical limit [4]. In order to solve these issues, the integration of photonic circuits with electronic circuits has been investigated; electronic-photonic IC (EPIC) [5]. Electronic circuits play a role in data processing part, and photonic circuits in data transmission part on EPIC (schematically shown in Fig. 1.2). Si photonics is a promising candidate for the photonics part of EPIC owing to its compatibility with Si CMOS process, which enables low-cost fabrication.

Photonic circuits require photonic devices such as waveguides (WGs), (de)multiplexer (MUX/DEMUX), photodetectors (PDs), modulators (MODs) and laser diodes (LDs). WGs and MUX/DEMUX have been reported on Si photonics platform employing Si and/or its compounds such as SiO_x, SiN_x, and SiO_xN_y, because they are transparent in optical communication wavelength (1.3–1.6 μm). Photodetectors, modulators and lasers have been important challenges for Si photonics because Si and its compounds cannot absorb/emit light of 1.3–1.6

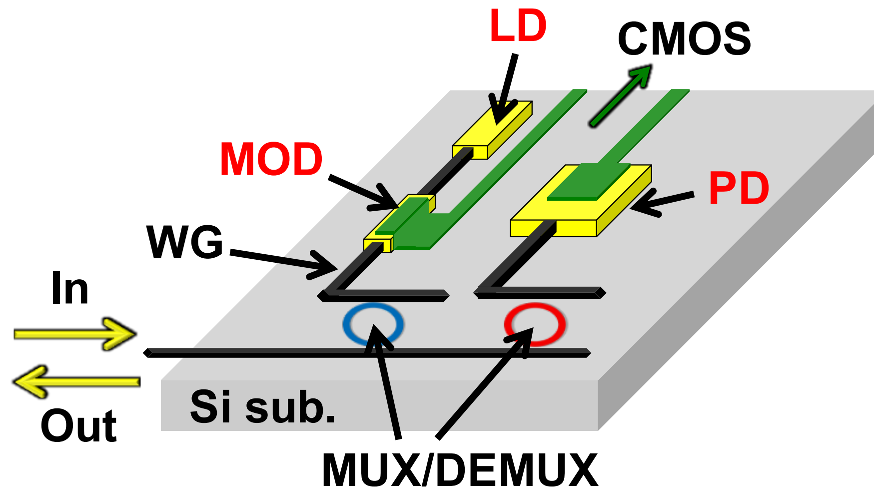

Figure 1.2: A schematic illustration of EPIC on a Si substrate

μm. Si-based MODs have been reported employing Mach-Zehnder interferometer, while their large footprint (typically as large as mm^2 [6]) is not preferable for on-chip integration. For on-chip PDs and MODs, Ge-based devices have been intensively studied because Ge has its direct bandgap at 0.8 eV, which is corresponding to wavelength of 1.55 μm, and absorbs light in optical communication band.

High performance PDs and MODs have been achieved employing Ge epitaxial layers on Si, in terms of high-responsivity, low-dark current and high-speed operation [7–25]. Although there is still rooms for improvement, PDs and MODs can be said that they are ready for practical application. On-chip LDs are, however, still far away from practical application. The fundamental problem is that Si and Ge are indirect bandgap materials, i.e., not suitable for laser material. Direct bandgap III-V materials are, however, not compatible with Si CMOS process. Therefore, the investigation for on-chip lasers is one of the biggest challenge for Si photonics.

1.2 Status Quo of Light-Emitting Devices on Si

Toward on-chip lasers, many attempts have been investigated such as Si and SiGe nanostructures, GeSn alloy, III-V on Si, and tensile-strained n-type Ge. Each method has pros and cons, as described following:

- Si and SiGe nanostructures had been intensively studied around 1990s–2000s [26–28]. Several-nm sized structure enables quantum confinement of excitons in Si or SiGe, resulting in improvement of light emission. Although the nanostructures have

successfully demonstrated an optical gain, they have had a difficulty in carrier injection because the nanostructures need to be buried in SiO_2.

- Erbium(Er)-doped Si has also been investigated as a gain medium [29–31]. Doped Er emits light of 1.54 μm, which has been employed in optical fiber amplifiers [32,33]. Er is doped in Si for on-chip application; in order to inject carrier electrically. Although light emitting diodes (LEDs) and optical gain have been demonstrated employing Er-doped Si, practicable laser have not been reported probably because Si is not a good host for Er or rare elements, as briefly mentioned in Ref. [34].

- Among Si CMOS compatible materials, i.e., group-IV materials, GeSn is a direct bandgap material. Electrically pumped lasers have been successfully demonstrated employing GeSn, but their emission wavelength are around 2–3 μm depending on the composition of Sn [35–37]. Such long wavelength emission is suitable for mid-IR application such as sensing, but not suitable for optical communication.

- The attempts above are to derive light from Si-based materials. Challenges from another direction has been attempted, i.e., to integrate direct bandgap III-V materials on Si. Electrically pumped InAs/InGaAs lasers on Si have been recently reported employing Si wafers patterned in V-groove [38, 39]. The InAs/InGaAs lasers show low threshold current density (J_{th}; ~1 kA/cm^2) and stable operation, while their emission wavelength is shorter than 1.3 μm and they require several-μm-thick buffer layers, which are not appropriate for on-chip application.

- Tensile-strained n-type Ge, main target of this study, is one of the most promising candidates for on-chip lasers. Ge is naturally indirect bandgap material as mentioned above, indicating that Ge cannot be a laser material. Nevertheless, it was predicted and demonstrated that Ge can be a laser material operating at 1.6 μm under heavily n-type doping and moderate tensile strain [40–44]. More details and issues will be described in the next section.

The drawbacks and typical J_{th} of the attempts are summarized in Table 1.1.

1.3 Ge as a Gain Medium on Si

Although Ge is naturally an indirect bandgap material, the energy difference between indirect bandgap (Γ–L; 0.66 eV) and direct bandgap (Γ–Γ; 0.80 eV) is small enough to be overcome by applicable band engineering, i.e., n-type doping and tensile strain as schematically shown in Fig. 1.3. Both Γ–Γ and Γ–L bandgaps shrink as tensile strain is induced, where shrinkage of Γ–Γ is more than Γ–L, resulting in reduction of energy gap between Γ-valley and L-valley.

Table 1.1: Reported attempts for on-chip LDs

Method	Drawback(s)	Typical J_{th}	References
Si and SiGe nanostructure	Difficulty in electrical injection	NA	[26–28]
Er-doped Si	Problem in host material?	NA	[29–31]
GeSn	Operation in mid-IR range	68–325 kA/cm^2	[35–37]
III-V on Si	Compatibility with CMOS processing	~1 kA/cm^2	[38, 39]
Tensile-strained n-type Ge	Large J_{th}	280–510 kA/cm^2	[40–44]

L-valley in conduction band is filled as the result of n-type doping. Brief literature survey and fundamental calculations are described following in this section.

1.3.1 Strain-Induced Bandgap Engineering

Tensile strain of 0.1–0.2 % is naturally induced in Ge-on-Si when Ge-on-Si is cooled down from growth temperature (normally 500–700 °C) to room temperature. The tensile strain is ascribed to the difference of thermal expansion coefficients between Ge and Si, and results in shrinkage of Ge bandgap [45]. The effect of strain on band structure is calculated by k·p perturbation method. Calculated bandgap (Γ–L and Γ–Γ) is shown in Fig. 1.4 as a function of biaxial strain in <110> and <1$\bar{1}$0> direction.

Grown-in tensile strain (0.1–0.2 %) induce shrinkage for both Γ–L and Γ–Γ, but the shrinkage is more effective to Γ–L than Γ–Γ. Under 0.2 % tensile strain, for instance, Γ–L shrinks for 0.017 eV, while Γ–Γ shrinks for 0.032 eV. Thus, tensile-strained Ge is more direct-like than unstrained Ge. Figure 1.4 also shows that Ge will be direct bandgap when tensile strain of ~1.8 % is induced. Under such strong tensile strain, however, direct bandgap becomes as small as 0.5 eV, resulting in emission wavelength longer than 2 μm [46]. In order to derive light emission around 1.6 μm, no intentional strain is induced except for grown-in tensile strain.

1.3.2 N-Type Doping for Ge to be Pseudo-Direct Bandgap

N-type doping in Ge provides carriers to the conduction band filling the gap between L-valley and Γ-valley, i.e., resulting in elevation of Fermi energy E_f. Ge, naturally indirect bandgap material, can be a pseudo-direct bandgap material when E_f reaches the Γ valley. The Fermi energy level ξ can be calculated using following equation,

$$\xi = E_i + kTln\frac{n}{n_i} \tag{1.1}$$

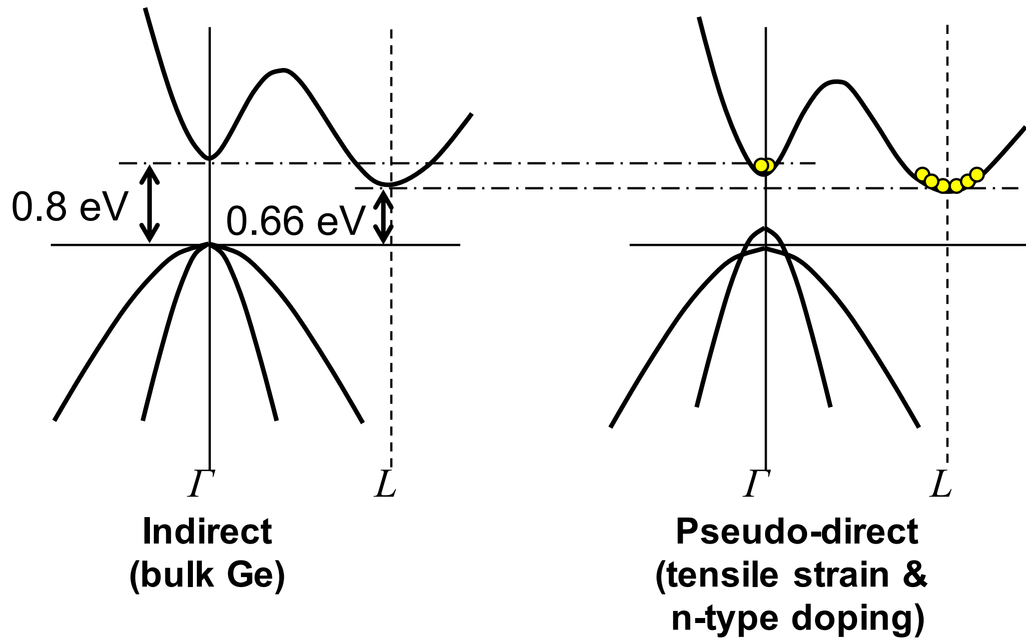

Figure 1.3: Schematic illustrations of band engineering of Ge through tensile strain application and n-type doping

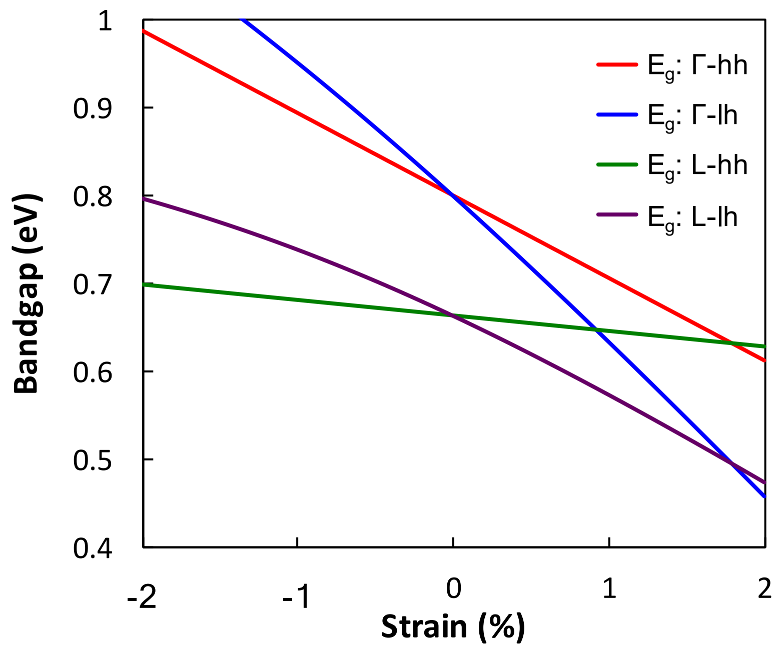

Figure 1.4: Calculated bandgap as a function of biaxial strain in <110> and <1$\bar{1}$0> direction

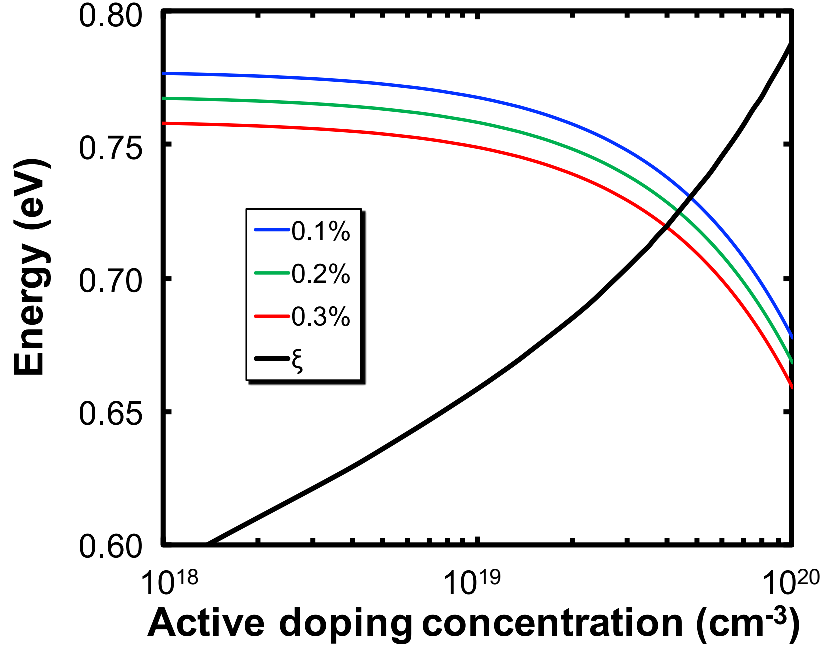

Figure 1.5: Calculated Fermi level ξ and Γ-lh bandgap (tensile strain of 0.1–0.3 %) as a function of active doping concentration

where E_i is the Fermi energy for intrinsic Ge, k is the Boltzmann's constant, T is the temperature, n_i is the intrinsic carrier concentration, and n is the carrier concentration calculated as $n = \int_{-\infty}^{\infty} \varrho(E) f(E) dE$. Here, $\varrho(E)$ is the total electron density, and $f(E)$ is the Fermi-Dirac probability function.

In addition to the elevation of Fermi energy, bandgap narrowing (BGN) occurs when Ge is heavily doped for n-type [47]. According to Ref. [47], correlation between n-type doping concentration (N_D) and BGN (ΔE) for Γ-Γ bandgap is approximately expressed as Eq. (1.2) from experimental results where N_D is on the order of 10^{19} cm^{-3}.

$$\Delta E[\text{eV}] = 0.013[\text{eV}] + 10^{-21}[\text{eV/cm}^{-3}] \times N_{\text{D}}[\text{cm}^{-3}]. \tag{1.2}$$

Taking into account the elevation of Fermi energy and BGN, pseudo-direct bandgap is achieved where n-type doping concentration is mid-10^{19} cm^{-3}, as shown in Fig. 1.5.

Under excitation, carriers are excited to Γ-valley even active doping concentration is not enough for Ge to be pseudo-direct bandgap. Therefore, Ge laser with doping concentration of 1×10^{19} cm^{-3} has already been reported [41], which is not enough to fill L-valley.

1.4 Outline of Thesis

The goal of this dissertation is to propose a new method for TDD reduction toward Ge lasers. This dissertation describes theoretical calculation, verification of the method by experimental measurements and observations, and feasibility study for light-emitting devices employing the method.

In **Chapter 2**, requirements for Ge epitaxial layers on Si toward on-chip laser is investigated through a literature survey and fundamental experiments. Theoretical analyses are given on a quantitative basis in terms of non-radiative recombination (NRR) in bulk/surface of Ge epitaxial layers on Si.

In **Chapter 3**, a theoretical model of image-force-induced TDD reduction is described with numerical calculations. Quantitative investigation is described in terms of image force applied to TDs in Ge epitaxial layer on Si. The TDD reduction occurs when selective epitaxial growth (SEG) Ge layers coalesce with adjacent ones leaving voids near Ge/Si interfaces. It is numerically shown that the combination of image-force-induced TD bending and coalescence of SEG Ge layers contribute to the reduction of TDD in Ge.

In **Chapter 4**, Ge growth in lateral direction (in [110] orientation) over SiO_2 masks is investigated. It is shown that Ge epitaxial layers with voids are formed as a result of coalescence of SEG Ge layers. Conditions for the coalescence of SEG Ge layers are described via quantitative analysis for lateral growth of Ge over SiO_2 masks.

In **Chapter 5**, the verification of the theoretical model shown in chapter 3 is shown via measurements of TDDs using etch pit density (EPD) counting method. Observed TDDs well reproduces the calculated ones, and the distribution of TDs in coalesced Ge is consistent with the theoretical model.

In **Chapter 6**, TDs in coalesced Ge layers are directly observed by transmission electron microscope (TEM). Cross-sectional TEM observations show the bending of TDs in separated SEG Ge layers and the termination of a TD by a bottom surface in a coalesced Ge layer, both are predicted by the theoretical model in chapter 3. In addition to that, cross-sectional TEM observations show TD generation when SEG Ge layers coalesce. Plan-view TEM observations show a unique behavior of TDs in coalesced Ge; TDs inclined to be parallel to substrate. The mechanisms of the TD generation and the inclined TDs are discussed.

In **Chapter 7**, characterization and design of coalesced Ge are described in view of a light emitting material. Characterization of tensile strain in coalesced Ge is described via Raman spectroscopy. N-type doping of the coalesced Ge layers is described employing thermal diffusion method. It is also described that coalesced Ge layers with voids at Ge/Si interfaces have advantages in terms of NRR at interfaces. I.e., optical mode in coalesced Ge is pushed-up owing to voids at Ge/Si interfaces, and thus negative effects from Ge/Si interfaces are reduced.

In **Chapter 8**, light emission characteristics are described via micro-photoluminescence (μ-PL) and optical pumping measurements, as a feasibility study for light-emitting device applications. In optical pumping measurements, CW, micro-sec pulsed, and nano-sec pulsed lasers are used as excitation lasers.

Finally, a summary and future outlook are given in **Chapter 9**.

2 Ge Epitaxial Layers for Light Emitter

Epitaxial Ge on Si has been intensively investigated as a material for on-chip light-emitting devices. The advantages of Ge in terms of applications for on-chip light-emitting devices are its direct bandgap (0.8 eV) corresponding to optical communication wavelength (1.55 μm) and compatibility with Si-CMOS processing. Although Ge LDs have been experimentally achieved [42, 43], the reported J_{th} were two orders of magnitude higher than theoretical prediction [40, 48]. The difference between theoretical J_{th} and experimental one is ascribed to NRR in Ge active layers and/or NRR at Ge surfaces. In order to clarify the requirements for Ge epitaxial layers toward low-threshold LDs, fundamental of Ge epitaxial growth on Si, radiative/non-radiative recombination in Ge epitaxial layers on Si, and surface/interface NRR velocities for Ge epitaxial layers on Si are investigated and summarized.

2.1 Methods and Issues of Ge Epitaxial Growth on Si

In order to fabricate high performance active photonic devices, single crystal Ge layers are required to be grown on Si substrates. Considering crystal quality and application for industrial production, a chemical vapor deposition (CVD) method has been widely employed, and considered to be suitable for Ge growth on Si. Under appropriate conditions, Ge layers grown on Si take over the crystal orientation from substrate Si. The Ge growth taking over the crystal orientation from the substrate is called as "epitaxial growth," and the grown Ge layer is called as "Ge epitaxial layer." In this work, an ultra-high vacuum CVD (UHV-CVD) method is employed to grow Ge in order to reduce impurities in Ge: base pressure was mid-10^{-7} Pa before Ge growths, which guarantees substantially low partial pressure of impurities such as O_2, N_2, and so on.

However, there is a fundamental problem on Ge epitaxial layers on Si; lattice mismatch between Ge and Si as large as 4.2 %. Such a large lattice mismatch leads the critical thickness

(the maximum thickness for pseudomophic heteroepitaxial growth) as thin as atomic layers. As the thickness of a Ge layer exceed the critical thickness, misfit dislocations (MDs) and their threading segments (threading dislocations, TDs) are formed in order to release the lattice-mismatch-induced strain in epitaxial Ge on Si. In highly mismatched system such as GaAs on Si (4 % mismatch), it has been reported that 60° mixed TDs are formed as the threading segments of misfit dislocations to release strain [49, 50]. The critical thickness increases through the optimization of growth temperature and the introduction of Si_xGe_{1-x} graded buffer layers. Although dislocation-free heteroepitaxial growths have been reported employing the optimization of growth temperature [51] and the introduction of Si_xGe_{1-x} graded buffer layers [52], both are not suitable for Ge epitaxial growth on Si in terms of application for integrated photonic devices. The optimization of growth temperature is not able to increase the critical thickness as thick as several hundred nm, normally required for active photonic devices, and the introduction of Si_xGe_{1-x} graded buffer layers requires several μm thick buffer layers, which is not favorable for the integration on Si substrates.

Instead of the increase of the critical thickness, a two-step growth method is widely employed to obtain (relatively) high quality Ge epitaxial layers on Si. During the two-step growth, the layer-by-layer plus island growth mode (Stranski–Krastanove mode) appears instead of layer-by-layer growth mode (Frank–van der Merwe growth mode) [53]. By controlling the growth temperature, pseudomophic layer-by-layer growth occurs at the initial stage of Ge growth, and with the elevation of growth temperature, the epitaxial layer release strain energy by forming MDs and TDs. As the results of the two-step growth with optimized conditions, Ge epitaxial layers with TDs at a density of $\sim 10^9$ cm^2 were formed on Si [54]. Although the TD density (TDD) of $\sim 10^9$ cm^2 is considerably low taking into account the lattice mismatch between Ge and Si (4.2 %), TDD should be reduced in order to reduce non-radiative recombination (NRR) in Ge epitaxial layers on Si.

2.2 Carrier Recombination in Bulk Ge

In a bulk intrinsic semiconductor material, the carrier recombination rate R is expressed as a function of the electron concentration n:

$$R(n) = An + Bn^2 + Cn^3 = \frac{n}{\tau} \tag{2.1a}$$

$$\tau(n) = (A + Bn + Cn^2)^{-1}. \tag{2.1b}$$

Here, An indicates the dislocation-assisted NRR, Bn^2 indicates the spontaneous radiative recombination, and Cn^3 indicates Auger NRR. The bulk lifetime is expressed as τ in Eq. (2.1b). The carrier recombination processes are overviewed in this section.

2.2.1 Radiative Recombination

Radiative band-to-band recombination spontaneously occurs and the recombination rate R_{sp} is in proportion to the electron and hole concentrations, i.e.,

$$R_{sp} = Bnp \tag{2.2}$$

where B is the recombination coefficient, n is the electron concentration, and p is the hole concentration. In the case for n-type Ge, on the other hand, the electron concentration is assumed to be constant since it is much higher than injected minority carrier, hole, concentration, i.e.,

$$R_{sp} = Bnp \approx B'p \tag{2.3}$$

where B' is the modified recombination coefficient taking into account the electron concentration. In the case for tensile-strained n-type Ge, direct transition rate R_Γ and indirect transition rate R_L are 1.3×10^{-10} (cm^3/s) [40] and 5.1×10^{-15} (cm^3/s) [55], respectively.

In laser diodes (LDs), however, stimulated radiative recombination occurs under population inversion. I.e., injected light stimulates the carrier recombination, resulting in light emission which is coherent with the injected light. The stimulated radiative recombination rate R_{st} is expressed as

$$R_{st} = (1 - \exp(\frac{\hbar\omega - (F_2 - F_1)}{kT}))R_{sp}. \tag{2.4}$$

$F_2 - F_1$ is refered to as "inversion factor," where F_2 and F_1 are quasi-Fermi levels under injection. Note that $R_{sp} + R_{st} + R_{NRR} = R_{ab}$ under equilibrium, where R_{NRR} and R_{ab} are the total NRR rate and the absorption rate.

2.2.2 Dislocation-assisted NRR in Epitaxial Ge on Si

Dislocations in Ge epitaxial layers create defect states at the middle of the bandgap of Ge, and the carrier recombination through the defect states, Shockley-Read-Hall (SRH) recombination, is a non-radiative process [56]. In SRH recombination process, recombination rates for electrons (R_n) and holes (R_p) are described as following equations:

$$R_n = c_n n N_d (1 - f_t) \tag{2.5a}$$

$$R_p = c_p p N_d f_t \tag{2.5b}$$

where c_n is the capture coefficient for electrons, c_p is the capture coefficient for holes, N_d is the defect density, n is the electron concentration, p is the hole concentration, and f_t is the occupation probability of the defect. Equations (2.5) indicate that the recombination rate is in proportion to TDD. The recombination rate is experimentally observed as the minority carrier lifetime τ. Under low doping level, the minority carrier lifetime in Ge epitaxial layer

(TDD $\approx 10^8$–10^9 cm^{-3}) is dominated by SRH recombination process, as reported in Ref. [57]. The minority carrier lifetime in intrinsic Ge epitaxial layers are reported as 2.0–3.0 ns, as in Refs. [58–60]. The τ dependence on TDD is also seen in Ge photodetector research, such as reported in Ref. [9].

2.2.3 Auger Recombination and Free Carrier Absorption

The impact of Auger generation-recombination process, the term Cn^3 in Eq. (2.1a), on the minority carrier lifetime τ become larger as doping density increase, as reported in Ref. [61, 62]. Under the doping level of $\sim 10^{19}$ cm^{-3}, the minority carrier lifetime in bulk Ge is determined by Auger NRR process. However, the minority carrier lifetime dominated by Auger recombination τ_A is 0.1 μs where doping level is $\sim 10^{19}$ cm^{-3} and Auger recombination coefficient $C = 10^{-31}$ cm^{6}s^{-1}. Thus, if doping level is $\sim 10^{19}$ cm^{-3}, τ_A is two orders of magnitude longer than SRH-dominated carrier lifetime in Ge epitaxial layers (2.0–3.0 ns).

It has been widely known that free carrier absorption α_{FCA} follows Drude's model (Eq. 2.6) under low doping level.

$$\alpha_{FCA} = \frac{q^2 \lambda^2 n_c}{4\pi^2 c^3 \varepsilon_0 n_r m_c \tau_c} \tag{2.6}$$

where q is the elementary charge, λ is the wavelength of photon, n_c is the doping concentration, ε_0 is the permittivity of free space, n_r is the refractive index, m_c is the effective mass of carriers, and τ_c is the scattering time owing to free carriers. In heavily n-type doped Ge, however, α_{FCA} does not follow the Drude's model, and α_{FCA} has been experimentally obtained as in Ref. [63]. According to Ref. [63], in the case for 0.25 % tensile strained n-type Ge ($n_c = 1 \times 10^{19}$ cm^{-3}), α_{FCA} is effective in the range $\lambda \geq 6$ μm, but the absorption in the range $\lambda \leq 2$ μm is dominated by direct gap absorption. Thus, in the case for optical communication wavelength (1.3–1.6 μm), α_{FCA} is not a dominant factor.

Summarizing above, in bulk n-type Ge ($n_c = 1 \times 10^{19}$ cm^{-3}), TDD would be a dominant factor on the minority carrier lifetime τ.

2.3 NRR at Surfaces/Interfaces on Epitaxial Ge on Si

Recently, it was found that interface NRR velocity for Ge is one of the critical factors to realize Ge lasers on Si [64]. I.e., with large surface/interface NRR velocity, J_{th} is dominated not by τ but by surface/interface NRR velocity. In this section, an estimation of NRR velocities at Ge/Si, Ge/air, and Ge/GeO_2 interfaces in Ge epitaxial layers on Si is performed using a method employed in Refs. [64, 65], where the surface/interface NRR velocity was determined by a comparison of PL intensities obtained under two different wavelengths of excitation lasers.

2.3.1 Surface/Interface NRR Velocities: Background

It has recently been reported that large J_{th} values in the previous Ge LDs [42, 43] are ascribed to the NRR of carriers at the hetero-interfaces of Ge/Si with a large lattice mismatch of 4 %, rather than NRR in the Ge layer with a TDD [64, 66]. In order to achieve J_{th} as low as 10 kA/cm^2, the interface NRR velocity is required to be less than 10^4 cm/s [64], while the surface/interface NRR velocities were reported on the order of 10^5 cm/s at the Ge/air surfaces [58] and Ge/Si interfaces [60, 64]. A suitable surface/interface passivation for Ge is required, as in the case for Ge-channel metal-oxide-semiconductor field effect transistors [67–69]. So far, an enhanced photoluminescence (PL) intensity has been reported by surface oxidation of Ge microdisks [70] and Ge nanowires [71], although no quantitative analysis on the NRR velocity at the Ge/GeO_2 interfaces has been reported yet. In order to estimate NRR velocities at Ge/GeO_2 interfaces as well as Ge/Si interfaces and Ge/air surfaces, PL measurements with two different excitation lasers were performed for Ge epitaxial layers on Si referring the method employed in Refs. [64, 65]. The surface/interface NRR velocities are determined by comparing PL intensities obtained under two different wavelengths of excitation lasers.

2.3.2 Estimation of Surface/Interface NRR Velocities: Theory

The PL intensity under a shorter wavelength of excitation is more sensitively degraded by the surface/interface NRRs than that with a longer wavelength, since the shorter wavelength of light usually shows a shorter depth of penetration, i.e., a significant decrease occurs in the excess carrier concentration near the surface. The carrier profiles under the laser excitation with a photon flux per unit area Φ are calculated as a function of the depth x by solving the continuity equation

$$\frac{Dd^2(\Delta n)}{dx^2} - \frac{\Delta n}{\tau} + \Phi(1-R)\alpha \exp(-\alpha x) = 0 \tag{2.7}$$

applying the boundary conditions

$$x = 0 \Rightarrow \frac{Dd\Delta n}{dx} = S_{top}\Delta n(x=0) \tag{2.8a}$$

$$x = d \Rightarrow \frac{Dd\Delta n}{dx} = S_{btm}\Delta n(x=d). \tag{2.8b}$$

Here, D is the carrier diffusion constant, Δn is the concentration of excess carriers, τ is the carrier lifetime, R is the reflectivity for the excitation light, α_{ex} is the absorption coefficient at the excitation wavelength λ_{ex} , d is the Ge layer thickness, S_{top} is the NRR velocity at a top surface/interface, and S_{btm} is the NRR velocity at a bottom Ge/Si interface.

From Eqs. (2.7) and (2.8), the carrier profile is expressed as

$$\Delta n = K_1 \left[\frac{K_2 \sinh(\frac{A-x}{L}) + K_3 \cosh(\frac{A-x}{L}) + \exp(-\alpha A)\{K_4 \sinh(\frac{x}{L})\} + K_5 \cosh(\frac{x}{L})}{K_6 \sinh(\frac{A}{L}) + K_7 \cosh(\frac{A}{L})} \right], \quad (2.9)$$

where

$$K_1 = \frac{(1-R)\Phi\alpha\tau}{\alpha^2 L^2 - 1} \quad (2.10a)$$

$$K_2 = \frac{S_{top} S_{btm} L}{D} + S_{btm}\alpha L \quad (2.10b)$$

$$K_3 = S_{top} + \alpha\frac{L^2}{\tau} \quad (2.10c)$$

$$K_4 = \frac{S_{top} S_{btm}\tau}{L} - S_{top}\alpha L \quad (2.10d)$$

$$K_5 = S_{btm} - \alpha\frac{L^2}{\tau} \quad (2.10e)$$

$$K_6 = \frac{S_{top} S_{btm}\tau}{L} + \frac{L}{\tau} \quad (2.10f)$$

$$K_7 = S_{top} + S_{btm}. \quad (2.10g)$$

The PL intensity I_{PL} is then calculated using

$$I_{PL} = \int_0^d \{B_\Gamma n(x) p(x) - n_i^2 \exp(-\alpha x)\} dx \quad (2.11)$$

where B_Γ is the radiative recombination coefficient for the direct transition in Ge [40], $n_\Gamma(x)$ the electron concentration in the Γ valley of conduction band, $p(x)$ the hole concentration, n_i the intrinsic carrier concentration, and α_{PL} is the absorption coefficient at the wavelength of PL emission.

The ratio of PL intensities between the two different excitation wavelengths was calculated as a function of surface/interface recombination velocities using Eqs. (2.7) and (2.11). As described below, two excitation lasers were used with the wavelengths of λ_{ex} = 457 nm and λ_{ex} = 785 nm in the experiments as well as in the calculations. The $1/e$ penetration depths in Ge are approximately 20 nm (α_{ex} = 500000 cm^{-1}) and 100 nm (α_{ex} = 100000 cm^{-1}) for λ_{ex} = 457 nm and λ_{ex} = 785 nm, respectively. The reflectivity R was calculated by the Fresnel equation for each wavelength. By comparing the experimental ratio of PL intensity with the calculated ones, the interface recombination velocity was estimated. The carrier lifetime τ is one of the most important parameters in the calculations. For undoped Ge epitaxial layers on Si, τ has been reported mostly around 2.0 ns, i.e., 2.0 ns in Ref. [58], 2.0–2.7 ns in Ref. [59], and 3.0

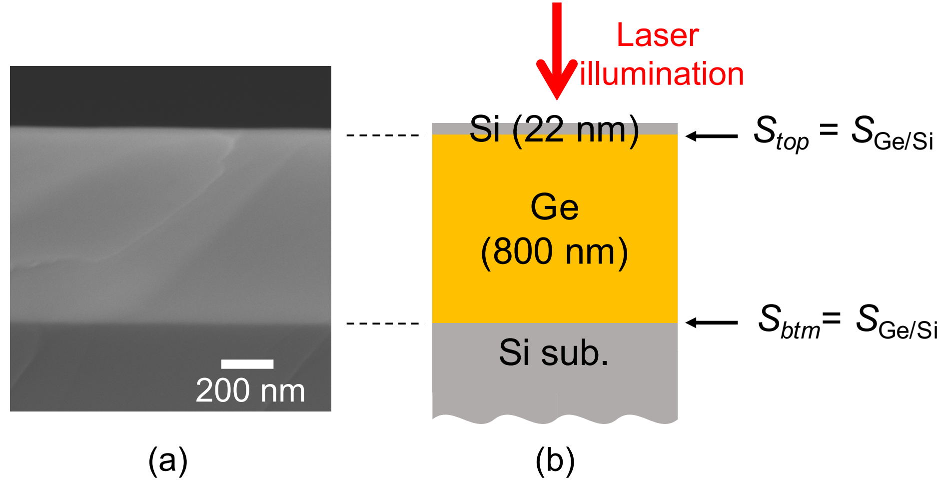

Figure 2.1: (a) A cross-sectional SEM image of Ge epitaxial layer and (b) a schematic illustration of cross-sectional structure.

ns in Ref. [60]. The shortest τ would be 0.6 ns obtained for a 1-μm-wide Ge waveguide as thin as 0.2 μm citeSrinivasanAPL2016, and the longest τ would be 5.3 ns obtained for Ge grown on a Ge-on-insulator (GOI) substrate [58]. Thus, the typical value of τ should be 2.0 ns, although the calculations were performed for τ in the range of 0.5–5.0 ns. The diffusion constant D for holes and electrons were estimated from the Einstein equation $D = \frac{kT}{q\mu}$, where μ is the hole/electron mobility in Ge [72].

2.3.3 Estimation of Surface/Interface NRR Velocities: Experimental Procedure

An undoped Ge epitaxial layer (800 nm) with a Si capping layer (22 nm, measured by an ellipsometry at $\lambda = 633$ nm) were grown on a 4-inch B-doped p-Si(001) wafer (1–100 Ω cm) byUHV-CVD. GeH_4 gas diluted at 9 % in Ar and Si_2H_6 gas diluted at 10 % in Ar were used as the source gases. Two-step growth (370/700 °C) method was employed in order to obtain a high-quality Ge epitaxial layer [54]. Subsequently after the Ge growth, a Si capping layer was grown at 600 °C in the same UHV-CVD chamber. Such a Si capping layer is often used as a passivation layer to protect the chemically unstable Ge surface. No post-growth annealing at higher temperatures was performed. The TDD in Ge grown in the same condition was approximately 2×10^8 cm^{-2}, and according to the Hall-effect measurements, the Ge layers showed slightly p-type with the hole concentration around 10^{16} cm^{-3}. A typical cross-sectional scanning electron microscope (SEM) image is shown in Fig. 2.1 (a), indicating the formation of uniform layers of Ge and Si.

After the epitaxial growth, the wafer was divided into small chips. Several different surface structures of Ge/Si, Ge/air, and Ge/GeO_2 were prepared for the estimation of NRR velocity. For the Ge/air interface, the Si capping layer was removed in an alkaline solution of 2.38 %

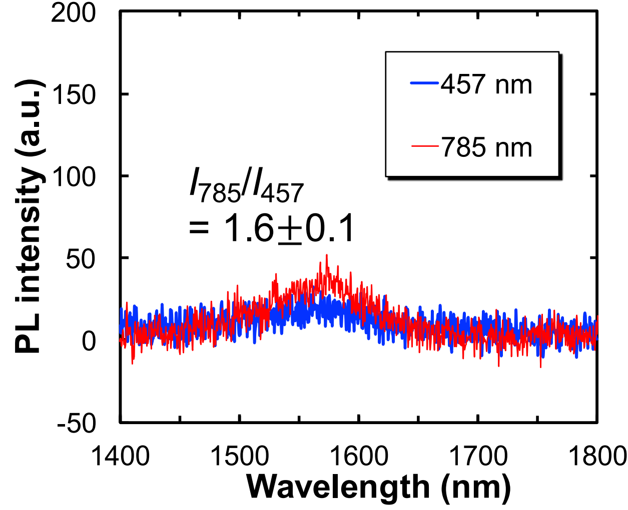

Figure 2.2: PL spectra from a Si-capped Ge layer excited by a 457-nm laser (blue) and a 785-nm laser (red).

Tetramethylammonium hydroxide (TMAH) at 65 °C for 3 min. The removal was confirmed by the Raman spectroscopy with λ_{ex} = 457 nm. Before the PL measurement, the sample was dipped in deionized water in order to remove native oxide formed on Ge surface at room temperature, which is usually removed by deionized water [73]. For the Ge/GeO_2 interface, Ge surfaces were thermally oxidized in a tube furnace of a dry O_2 ambient at 550 °C for 30 min or 120 min after the removal of Si capping layer. According to the ellipsometry (λ = 633 nm), a 24-nm-thick GeO_2 layer was formed after the 30-min oxidation, and a 42-nm-thick GeO_2 layer was formed after the 120-min oxidation.

PL measurements were carried out at room temperature employing two different wavelengths of excitation lasers, λ_{ex} = 457 nm and 785 nm. As illustrated in Fig. 2.1 (b), the sample surface was illuminated from the top through an objective lens. The diameter of $1/e^2$ intensity was approximately 2 μm. The values of excitation laser power were 3.3 mW for λ_{ex} = 457 nm and 1.9 mW for λ_{ex} = 785 nm, corresponding to the photon flux density of 2.4×10^{23} $cm^{-2}s^{-1}$ in both cases. The PL emission was collected from the top with the same lens as that used in the excitation, and the intensity was detected through a monochrometer with an extended InGaAs detector in the wavelength range of 1400–1800 nm.

2.3.4 Estimation of Surface/Interface NRR Velocities: Results and Discussion

Figure 2.2 shows typical PL spectra from the Ge layer having the Si capping layer. The PL intensity using λ_{ex} = 785 nm is higher than that using λ_{ex} = 457 nm. After the integration of intensity in the wavelength range of 1500–1650 nm, where the direct transitions occur, the ratio of integrated PL intensity between the excitations of λ_{ex} = 785 nm and λ_{ex} = 457 nm, $\frac{I_{785}}{I_{457}}$, was obtained to be 1.6±0.1.

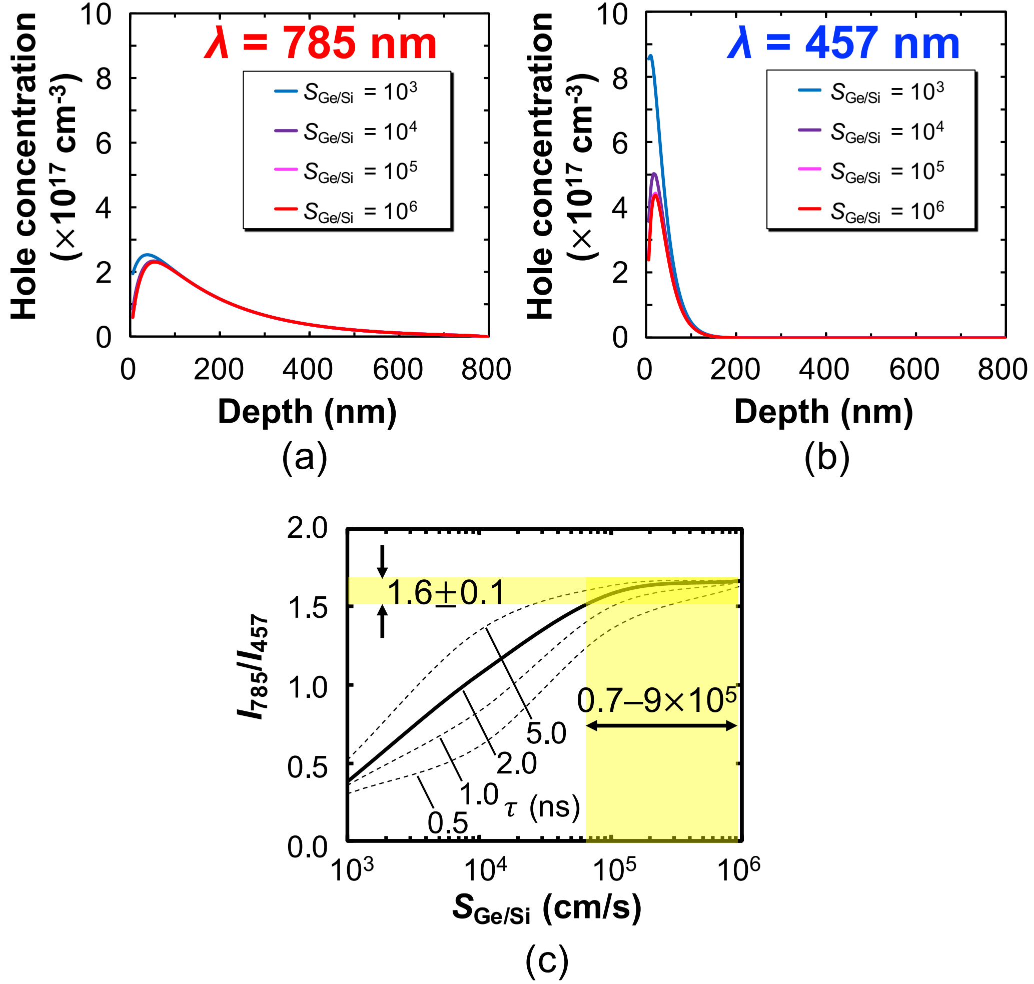

Figure 2.3: Calculated profiles of hole in Ge illuminated by (a) 785-nm laser and (b) 457-nm laser. (c) Calculated dependence of $\frac{I_{785}}{I_{457}}$ as a function of $S_{Ge/Si}$ and τ.

Based on the calculated excess hole (electron) concentrations for λ_{ex} = 785 nm and λ_{ex} = 457 nm shown in Figs. 2.3 (a) and 2.3 (b) as well as the excess electron concentrations in the Γ valley n_Γ, $\frac{I_{785}}{I_{457}}$ was calculated as a function of the NRR velocity at the Ge/Si interface $S_{Ge/Si}$, as shown in Fig. 2.3 (c). Here, the interface NRR velocity at the top Ge/Si interface S_{top} was assumed to be equal to that at the bottom Ge/Si interface S_{btm}, although there is almost no effect of S_{btm} because the excess carrier concentration is negligible at the bottom interface.

The carrier lifetime τ in Ge were changed as a parameter to be 0.5, 1.0, 2.0, and 5.0 ns, as indicated in Fig. 2.3 (c). The yellow areas indicate the observed $\frac{I_{785}}{I_{457}}$ and the corresponding range of $S_{Ge/Si}$. As a result, $S_{Ge/Si}$ in the range of 10^5 cm/s was obtained for τ = 2.0 ns. $\frac{I_{785}}{I_{457}}$ increases with increasing τ, corresponding to the decrease in $S_{Ge/Si}$. Assuming τ = 1.0 ns,

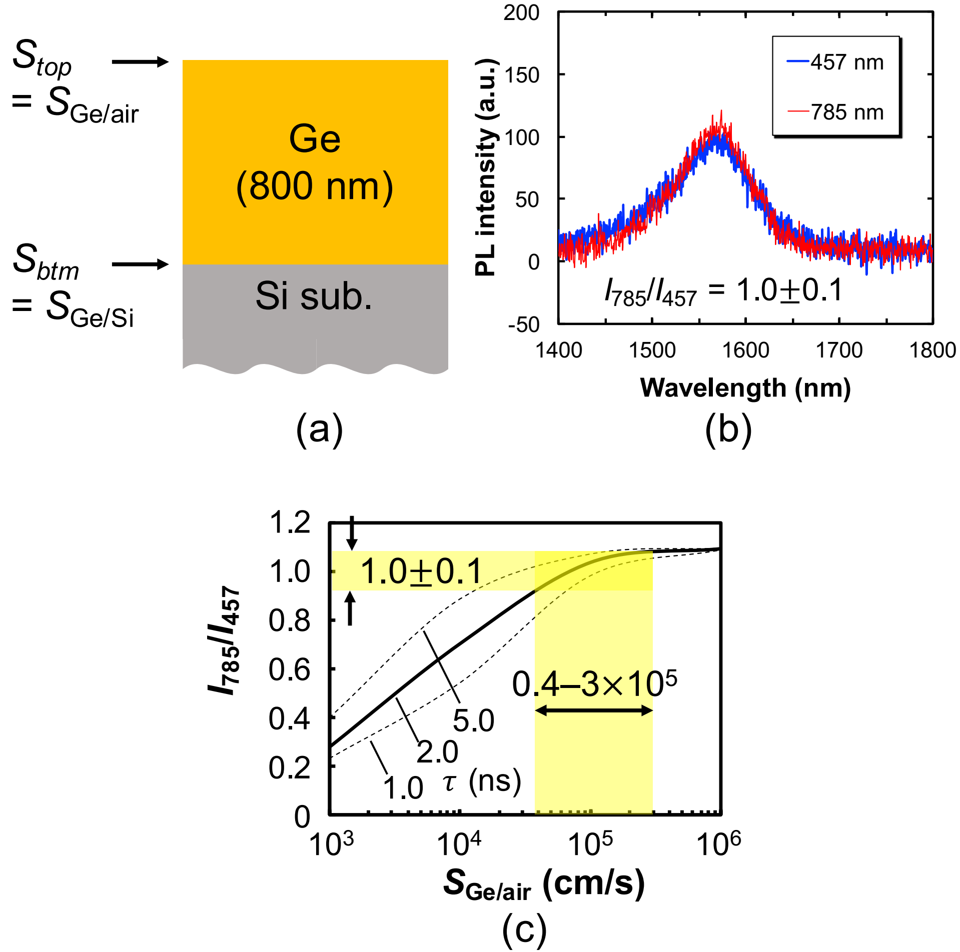

Figure 2.4: (a) A schematic illustration of cross-sectional structure, (b) measured PL spectra from a bare Ge layer, and (d) calculated dependence of $\frac{I_{785}}{I_{457}}$ as a function of $S_{Ge/air}$ and τ.

$S_{Ge/Si}$ was estimated to be in the range of 10^5 cm/s, being similar to the case of τ = 2.0 ns as well as to the previous reports [60, 64]. Even assuming the longer lifetime τ = 5.0 ns, $S_{Ge/Si}$ was estimated to be larger than the middle of 10^4 cm/s. It should be mentioned that $S_{Ge/Si}$ was not estimated for the shorter lifetime of τ = 0.5 ns, because the experimental $\frac{I_{785}}{I_{457}}$ of 1.6±0.1 is larger than the calculated ones even for the infinite $S_{Ge/Si}$. This suggests that τ in Ge is longer than 1.0 ns, as in the previous reports showing τ around 2.0 ns for intrinsic Ge epitaxial layers on Si [58–60].

The NRR velocities at the Ge/air interface, $S_{Ge/air}$, and at the Ge/GeO$_2$ interface, S_{Ge/GeO_2}, were obtained in the same way as in the case of $S_{Ge/Si}$. For the Ge/air interface, Figs. 2.4 (a), 2.4 (b), and 2.4 (c) show schematic illustrations of cross-sectional structure, PL spectra, and $\frac{I_{785}}{I_{457}}$ as a function of $S_{Ge/air}$ for τ of 1.0, 2.0, and 5.0 ns, respectively.

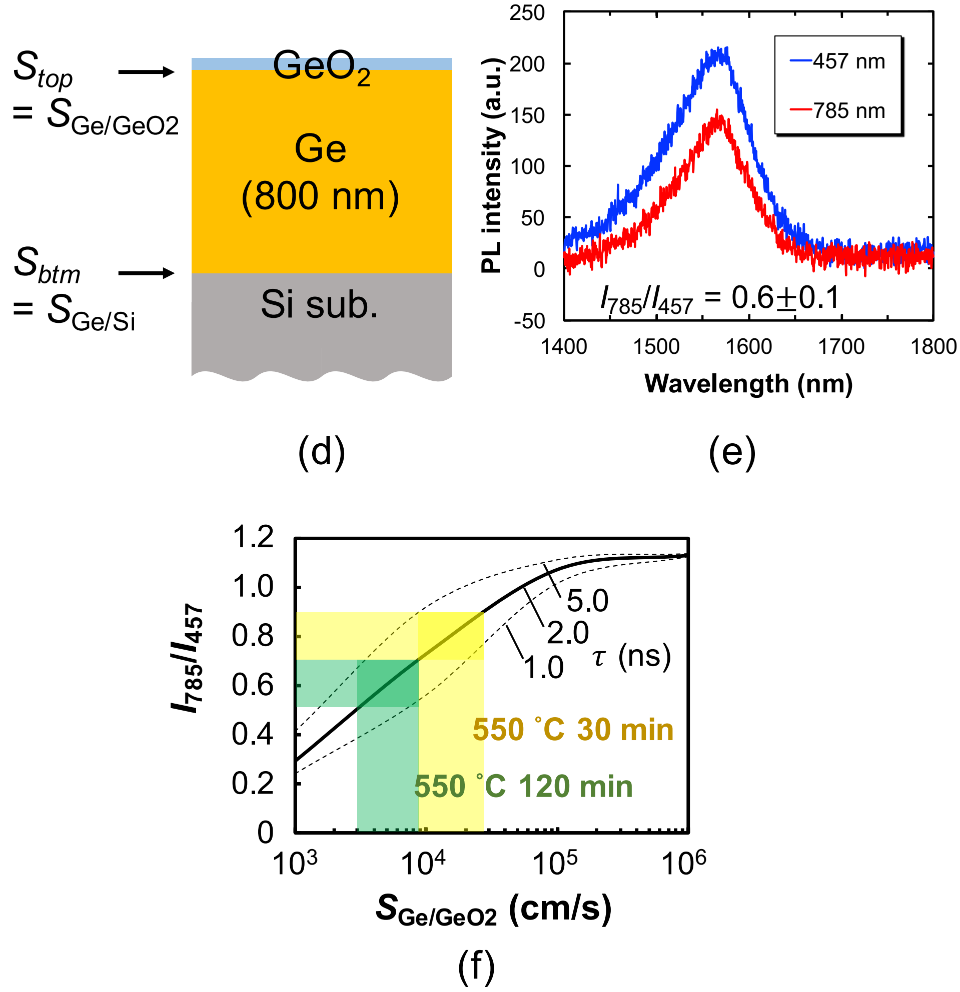

Figure 2.5: (a) A schematic illustration of cross-sectional structure, (b) measured PL spectra from a GeO_2-capped Ge layer, and (d) calculated dependence of $\frac{I_{785}}{I_{457}}$ as a function of S_{Ge/GeO_2} and τ.

Figures 2.5 (a), 2.5 (b) and 2.5 (c) show the schematic illustrations of cross-sectional structure, PL spectra, and $\frac{I_{785}}{I_{457}}$ as a function of $S_{Ge/air}$ for the Ge/GeO_2 interface. From Figs. 2.4 and 2.5, surface/interface NRR velocities were obtained for τ = 2.0 ns, as $S_{Ge/air}$ = 0.4–3×10^5 cm/s, S_{Ge/GeO_2} (550 °C, 30 min) = 0.9–3×10^4 cm/s, and S_{Ge/GeO_2} (550 °C, 120 min) = 3–9×10^3 cm/s.

The obtained $S_{Ge/air}$ is consistent with the previously reported one as large as 1×10^5 cm/s [58]. On the other hand, it is noted that the obtained S_{Ge/GeO_2} values are one or two orders of magnitude smaller in comparison with $S_{Ge/Si}$ and $S_{Ge/air}$. In the case of 120-min oxidation, S_{Ge/GeO_2} was on the order of 10^3 cm/s. Such a small NRR velocity should have a significant impact to reduce J_{th} in Ge lasers [64]. The observed difference in S_{Ge/GeO_2}

between the 30-min and 120-min oxidations may be ascribed to the transition from non-stoichiometric GeO_x to stoichiometric GeO_2. According to Ref. [71], the oxidized Ge surface initially possesses GeO_x, while GeO_2 is gradually formed with an elongated oxidation time. S_{Ge/GeO_2} obtained for the shorter oxidation time of 30 min would be referred to as S_{Ge/GeO_x}.

2.4 Requirements Toward Low-Threshold Ge LDs

As mentioned above, TDD is a dominant factor for τ in bulk n-type Ge ($n_c = 1 \times 10^{19}$ cm^{-3}). Although it has not been reported the correlation between τ and TDD, considering typical size of photonic devices such as $\sim$100 μm cm^2, TDD as low as 10^6 cm^{-2} can achieve TD-free Ge photonic devices on Si. Thus, in the present status, 10^6 cm^{-2} is a sufficient goal for TDD in Ge epitaxial layers on Si.

Figure 2.6 shows schematic illustrations of 4 typical conventional methods for TDD reduction, which have been attempted in Ge epitaxial layers on Si. These methods have successfully been shown TDD reduction in Ge epitaxial layers on Si, but there are drawbacks when the methods are employed to light emitting devices. Note that the optical confinement in Ge is an essential factor as well as tensile strain and n-type doping, in terms of light-emitting device applications of Ge on Si.

- (a) Thermal annealing [54, 74, 75]. This stimulates movement of TDs leading reduction of TDD, typically to 2×10^7 cm^{-2}. The drawback is possible intermixing of Si and Ge and out-diffusion of dopants in Ge such as phosphorus.

- (b) SiGe graded buffer layer [52, 76, 77]. This increases the critical thicknesses and suppresses the generation of TDs leading reduction of TDD, typically to 2×10^6 cm^{-2}. The drawback is the thick buffer reduces light coupling efficiency between Ge devices and Si waveguides underneath.

- (c) Aspect ratio trapping (ART) [78–80]. This is one of selective epitaxial growth (SEG) methods and reduces TDs by trapping TDs at sidewalls of thick SiO_2 trenches, typically to $< 1 \times 10^6$ cm^{-2}. The ART method uses a thick SiO_2 mask to reduce TDD in Ge over the SiO_2 masks, which locates far above Si, ended up with the same drawback in (b).

- (d) Ge growth on Si pillar seeds and annealing [81–83]. This method is similar to the ART method enabling TD trapping by high aspect ratio Ge growth, to $< 1 \times 10^5$ cm^{-2}. The drawback is a high temperature annealing for Ge coalescence ended up with the same drawbacks in (a), (b) and (c).

The reported TDDs, drawbacks, and typical references are summarized in Table 2.1. All 4 methods have drawback(s) in terms of application to light-emitting devices.

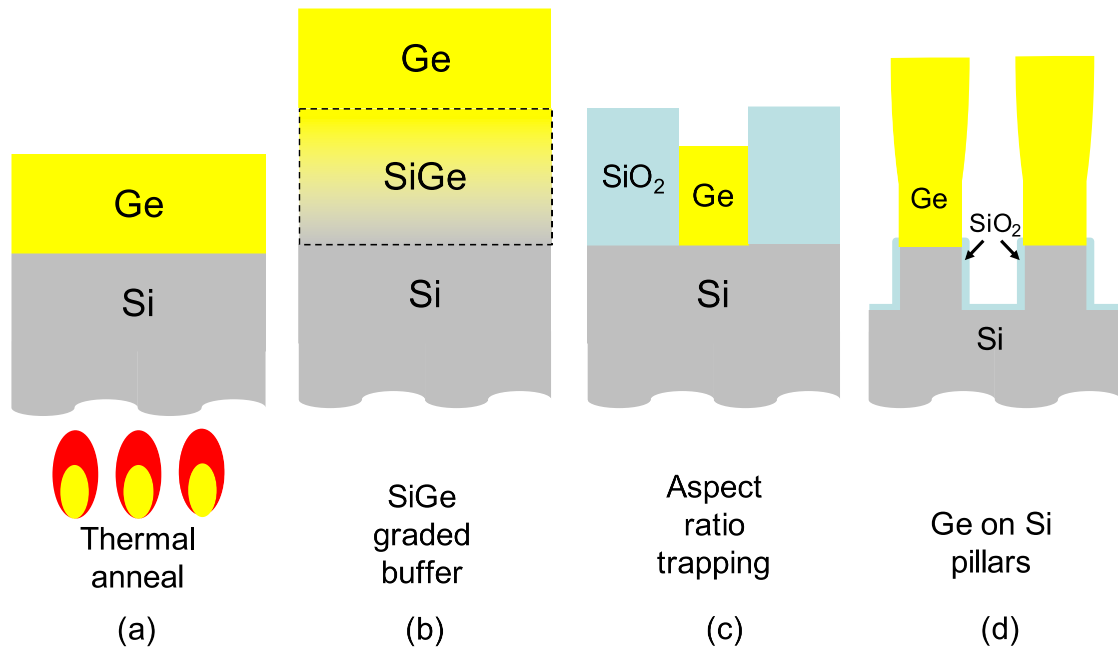

Figure 2.6: Schematic illustrations of conventional TDD reduction methods: (a) thermal annealing, (b) SiGe graded buffer, (c) aspect ratio trapping, and (d) Ge growth on Si pillars.

Table 2.1: Reported methods for reduction of TDDs in Ge-on-Si

Method	Achieved TDD (cm^{-2})	Drawback(s)	Typical References
Thermal annealing	2×10^7	Si-Ge intermixing dopant out-diffusion	[54, 74, 75]
SiGe graded buffer	2×10^6	bad light coupling weak optical confinement in Ge	[52, 76, 77]
ART	1×10^6	bad light coupling	[78–80]
Si pillar seeds	1×10^5	Si-Ge intermixing bad light coupling weak optical confinement in Ge	[81–83]

As for surface/interface NRR velocity S, S as small as 10^4 cm/s is required to achieve Ge laser with J_{th} as low as 10 kA/cm^2 [64]. As shown in Fig. 2.5, S as small as 10^4 cm/s can be achieved by thermal oxidation. Thus, Ge active layer is preferable to be surrounded by thermal oxidation layer as much as possible.

Based on these requirements, a novel TDD reduction method is proposed and theoretically shown in Chapter 3, and experimentally verified in Chapters 4–6 in order to achieve low-TDD Ge epitaxial layers on Si, which is free from the drawbacks above. Then, the low-TDD Ge epitaxial layers on Si were oxidized to reduce surface NRR velocity, and application to light emitting device will be investigated in Chapters 7 and 8.

3 Theoretical Model and Calculation for the Reduction of TDs by Image Force

It has already been known that dislocations near free surfaces are attracted from the free surfaces. There are many reports on image force observed in Si [84], SiC [85], and in theory [86–88]. Although many reports on image force have been published, there is no attempt to reduce TDD in Ge epitaxial layers on Si. Therefore, this work is the first attempt to reduce TDD in Ge epitaxial layers on Si utilizing image force. In this chapter, a model to reduce TDD is proposed in the case for Ge epietaxial layers on Si. It has been observed that TDs in Ge epitaxial layers on Si are bent to be normal to growth surfaces [89–91]. Although cross-sectional transmission electron microscopy (TEM) observations have revealed the TD bending in previous works, there has been no investigation nor discussion about them. In this study, I focus on the TD bending to be normal to the growth surfaces for the first time, and investigate their application to reduce TDD in Ge on Si. At the last part of this chapter, extensibility to other material system is considered.

3.1 Image Force: Driving Force for TD Bending

In a bulk material, a dislocation generate a symmetric strain field as schematically shown in Fig. 3.1 (a). In Fig. 3.1(a), calculated distribution of σ_{xx} is shown around an edge dislocation parallel to z axis. Red color indicates the positive displacement of atoms, blue color indicates the negative displacement, and green color indicates no displacement. Such a symmetric strain field is, however, not maintained when the dislocation locates near a surface/interface, as shown in Fig. 3.1(b). In Fig. 3.1(b), it is assumed that there is a free surface near the dislocation as indicated by the black dashed line, and the strain is released at a free surface. Then, the strain field is modified and become asymmetric (left half of Fig. 3.1 (b)).

The modified strain field corresponds to the strain field under the situation that there is a dislocation at a mirror position with the opposite Burgers vector (right half of Fig. 3.1 (b)).

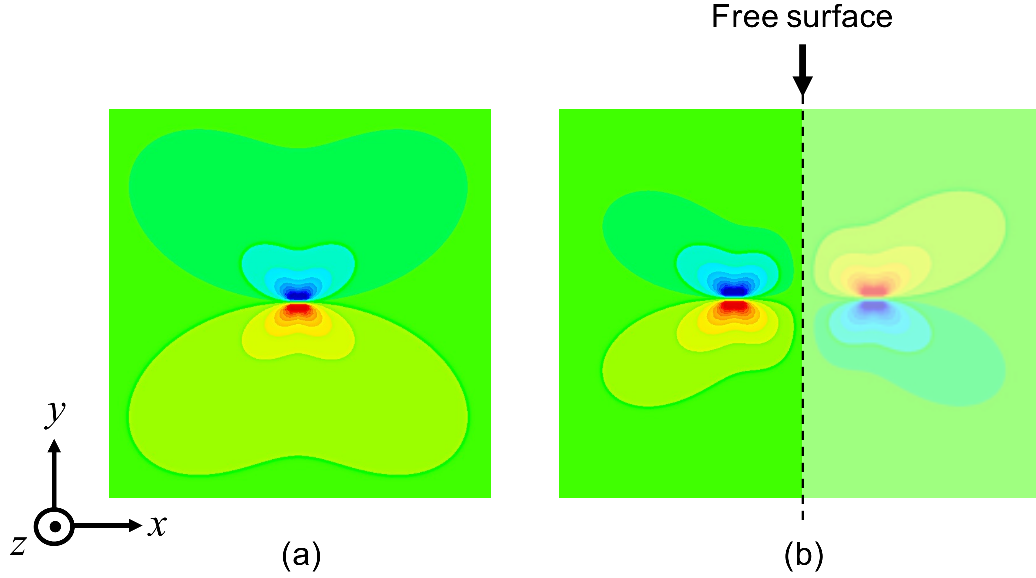

Figure 3.1: Schematic illustrations of a σ_{xx} around an edge dislocation parallel to z axis where (a) far away from surface/interface and (b) near a free surface

The "real" dislocation and the "image" dislocation attract each other, resulting in bending of "real" dislocation to be normal to the free surface. Therefore, the magnitude of image force is calculated as:

$$F_{screw} = \frac{\mu b^2}{4\pi V l} \cos\theta \tag{3.1a}$$

$$F_{edge} = \frac{\mu b^2}{4\pi V l(1-\nu)} \cos\theta \tag{3.1b}$$

where F_{screw} and F_{edge} are image forces for a screw dislocation and an edge dislocation, respectively, ν is Poisson's ratio, μ is the modulus of rigidity, b is the absolute value of the Burgers vector, V is the volume of a dislocation, l is the distance between a dislocation and a free surface, and θ is the angle between a dislocation and a free surface. In the case of Ge, μ = 75 GPa, b = 0.4 nm, and ν = 0.26. Assuming that the volume V is equal to the product of the TD length of 100 nm and the radius of strained layer 0.4 nm, the shear stresses due to the image force close to the growth surfaces are estimated from Eqs. (3.1a) and (3.1b), as shown in Fig. 3.2.

In the case for the distance l as small as 20–30 nm, the shear stress originated from image force becomes even larger than the Peierls stress of 0.5 GPa reported for 60° dislocations in Ge [92]. In addition to that, TD bending can occur under smaller shear stress than the Peierls stress since the TD bending occurs during crystal growth at high temperature (600–700 °C).

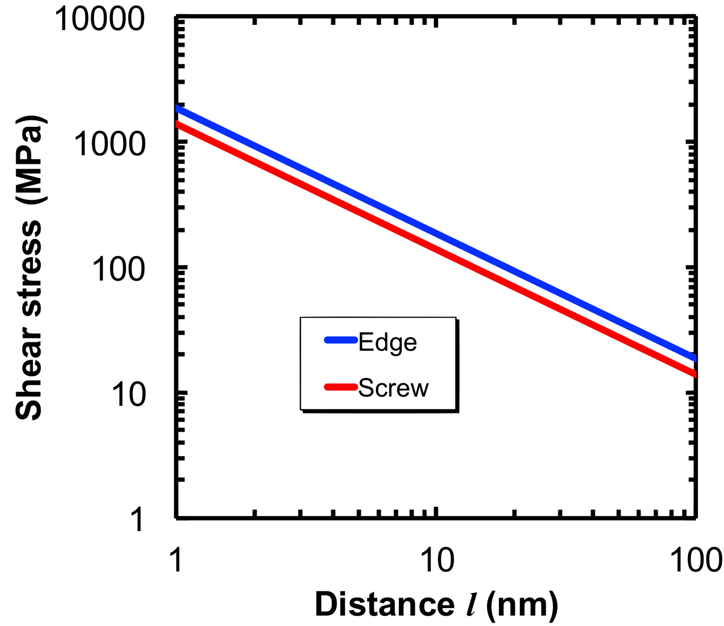

Figure 3.2: Calculation results of shear stressed induced by image force as a function of a distance between a dislocation and a free surface

According to reported dislocation mobility in bulk Ge, the mobility of dislocations in Ge reaches more than 10 μm/sec under 10 MPa shear stress at 900 K [93]. Thus, it is reasonable to consider that the image force is strong enough for TDs to be bent normal to the growth surfaces.

Note that the image force does not depend on crystal orientation. This suggests that image-force-induced TD bending should occur in SEG Ge of any structure and any orientation, as long as TDs are close to free surface. It is also notable that there are many reports on the interaction between dislocations and interface due to image force [84–88].

3.2 Numerical Calculations of TD Reduction

The magnitude of image force in Ge was calculated in the previous section, showing that the image force should be strong enough to bend TDs in Ge to be normal to free surfaces. In this section, the methods and results will be shown for the numerical calculation of TD trajectories in SEG Ge and TDD reduction as a function of aperture ratio, which is defined as $\frac{W_{window}}{W_{window}+W_{mask}}$. It will also be shown that Ge growth on SiO_2 masks has negative effects on the reduction of TDD as the result of coalescence.

3.2.1 TD Bending in SEG Ge Layers

In SEG Ge layers, trajectories of TDs can be calculated assuming that the TDs are bent to

be normal to growth surfaces. Specific method of the numerical calculation is described as follows.

(I) Definition of growth surfaces: In order to calculate trajectories of TDs in a SEG Ge layer, growth surfaces of the SEG Ge layer is required to be defined, i.e., the cross-sectional shape of the SEG Ge layer should be defined. For instance, consider a simple case, a line-shaped SEG Ge layer with a round-shaped growth surfaces. The growth surfaces are expressed by following equation:

$$x^2 + (y - (r_i - h_i))^2 = r_i^2 \tag{3.2}$$

where i is the parameter showing the development of the growth ($n = 1, 2, 3, ..., i-1, i, i+1, ...$), and r_i and h_i are the radius and height of the growth surface when $n = i$. Figure 3.3 (a) shows a schematic illustration showing the situation expressed by Eq. (3.2). In Fig. 3.3 (a), the growth surfaces satisfy both (i) center points of the all circles are on y-axis, and (ii) the all circles passes $(\frac{W_{window}}{2}, 0)$ and $(-\frac{W_{window}}{2}, 0)$, where W_{window} is the width of the window area opened for Ge epitaxial growth. In the calculation, the thickness of the SiO_2 masks is assumed to be thin enough to ignore ART effect on TD reduction.

(II) Calculation of normal directions for arbitrary location: As the growth surfaces are defined, normal lines at arbitrary points can be calculated. A TD passing a point (x_3, y_3) heads a next point (x_4, y_4), which is obtained by solving following simultaneous equations:

$$\begin{cases} y = \dfrac{y_3 - (h_3 - r_3)}{x_3} x + h_3 - r_3 & \text{(3.3a)} \\ x^2 + (y - (r_4 - h_4))^2 = r_4^2. & \text{(3.3b)} \end{cases}$$

Equation (3.3a) indicates the normal line at (x_3, y_3), and Eq. 3.3b indicates the growth surface when $n = 4$. Figure 3.3 (b) shows the situation expressed by Eq. 3.3. Here, the red line between (x_3, y_3) and (x_4, y_4) indicates a part of a TD trajectory passing the point (x_3, y_3). Expanding the calculation steps above, (x_{i+1}, y_{i+1}) can be calculated from (x_i, y_i). Therefore, a trajectory of one TD due to the image force can be calculated when the location of TD generation $(x_0, 0)$ is given, as shown in Fig. 3.3 (c). In other words, trajectories for arbitrary TDs can be calculated by the method described above. In addition to that, note that the cross-section of SEG Ge is not need to be round-shaped. I.e., facetted crosse-section cases are also able to be calculated expressing the cross-section by another equation. Figure 3.3 (d) shows the trajectories of TDs with various generation point x_0 in {113}-facetted SEG Ge, for instance. In Fig. 3.3 (d), it is assumed that SEG Ge does not grow on SiO_2. Thus, the sidewalls of the {113}-facetted SEG Ge are assumed to be round-shaped in order not to touch SiO_2 masked area.

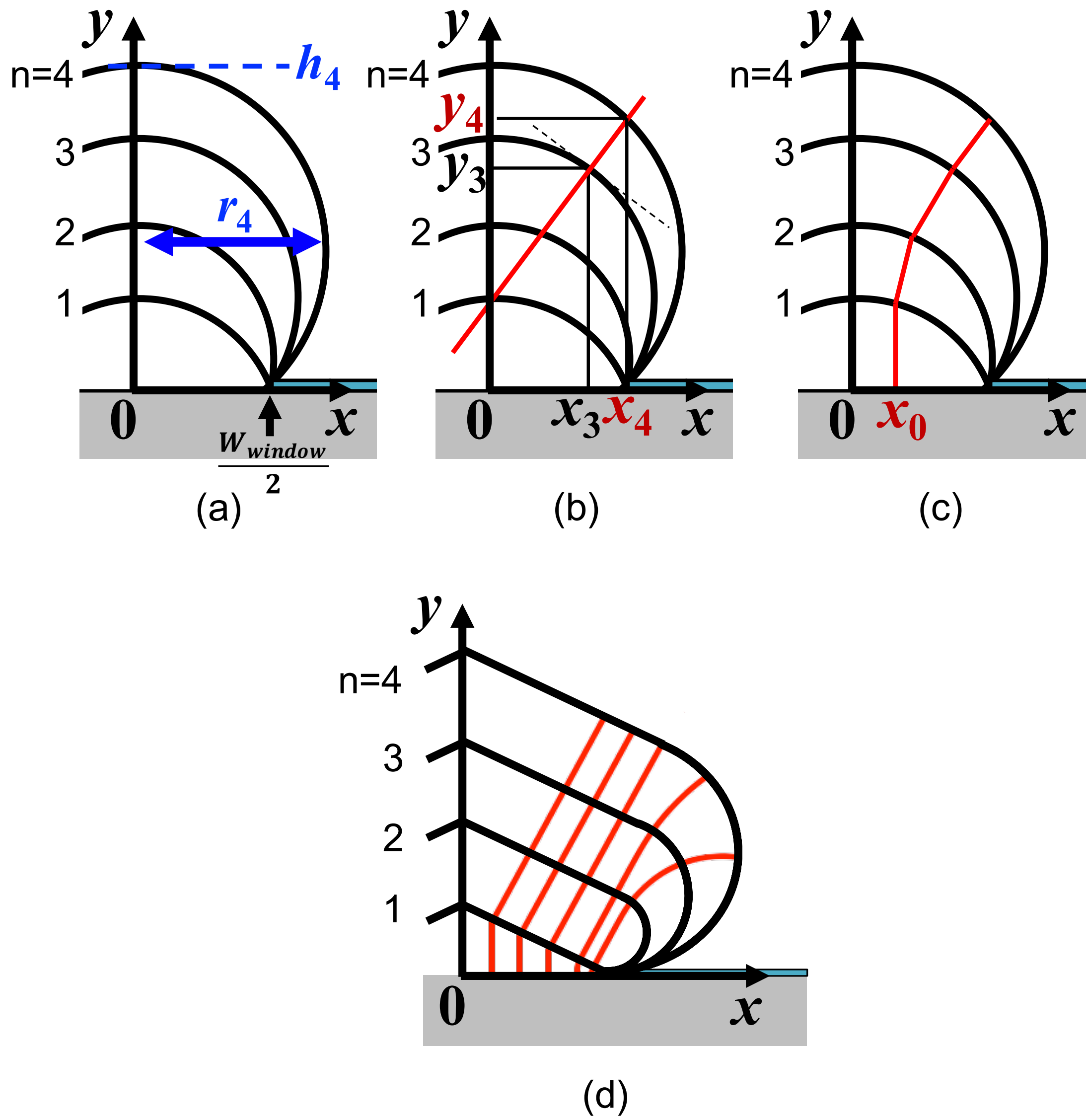

Figure 3.3: (a)–(c): Numerical calculation process to calculate a trajectory of a TD in a round-shaped SEG Ge. (d): Trajectories of TDs in a {113}-facetted SEG Ge

3.2.2 Reduction of TDD Induced by TD Bending and Coalescence

Figure 3.4 shows trajectories of TDs in round-shaped SEG Ge where $x_0 = 0, 0.2, 0.4, 0.6,$ and $0.8 \times \frac{W_{window}}{2}$. Here, assuming that the SEG Ge coalesce with the adjacent one, the TDs generated at $x_0 = 0$ and $0.2 \times \frac{W_{window}}{2}$ penetrate to the top surface, while the TDs generated at $x_0 = 0.4, 0.6$ and $0.8 \times \frac{W_{window}}{2}$ penetrate to the bottom surface, i.e., terminated to the void remained as the result of the coalescence. The ratio of TDs penetrating to the bottom surface depends on the aperture ratio (APR) of the SEG masks. APR is defined as Eq. 3.4, in the case for line-and-space SEG.

$$\text{APR} = \frac{W_{window}}{W_{window} + W_{mask}}. \tag{3.4}$$

In Fig. 3.4, APR is set as 0.5, i.e., $W_{window} = W_{mask}$. 3 dislocations generated at $x_0 = 0.4$, 0.6, and $0.8 \times \frac{W_{window}}{2}$ penetrate to the bottom surface, and 2 dislocations generated at $x_0 = 0$ and $0.2 \times \frac{W_{window}}{2}$ penetrate to the top surface, in this case. Thus, 3 dislocations are reduced as the results of image-force-induced dislocation bending and coalescence of SEG Ge layers.

Since TDs in Ge on Si are originated from the lattice mismatch between Ge and Si, it is assumed that TD generation occurs only at interfaces between Ge and Si. In other words, regardless of cross-section of SEG Ge, TDD should be reduced as APR decreases, i.e., TDD in coalesced Ge is in proportion to APR. Here, introduce a factor f in order to express the reduction of TDs induced by image force and coalescence of SEG Ge, as in Eq. 3.5.

$$\rho_{coalesced} = \rho_{blanket} \times \text{APR} \times f \tag{3.5}$$

where, $\rho_{coalesced}$ is TDD in the coalesced Ge epitaxial layer, $\rho_{blanket}$ is TDD in the planar blanket Ge of the same thickness with coalesced Ge, and APR is as defined in Eq. 3.4. In the case when APR = 0.5, shown in Fig. 3.4, there is a boundary at $x_0 = 0.2687 \times \frac{W_{window}}{2}$, i.e., dislocations generated at $x_0 > 0.2687 \times \frac{W_{window}}{2}$ penetrate to the bottom surface, and at $x_0 < 0.2687 \times \frac{W_{window}}{2}$ penetrate to the top surface. Thus, the TDD reduction factor f is 0.2687.

The factor f is calculated in round-shaped SEG Ge and {113}-facetted SEG Ge as a function of APR, as shown in Fig. 3.5. It is understandable that the ratio of TDs penetrating to the bottom surface increase as APR decrease. It is also reasonable that the factor f for {113}-facetted SEG Ge is larger than that for round-shaped SEG Ge when APR > 0.11, taking into account that {113} facets face top surface rather than bottom surface, as shown in Fig. 3.3 (d). However, it is not self-evident that there is a "crossing" between the factor f for round-shaped SEG Ge and {113}-facetted SEG Ge when APR is 0.11.

In order to understand the origin of the "crossing" at APR = 0.11 in Fig. 3.5, trajectories of 6 TDs ($x_0 = 0.04, 0.1, 0.2, 0.4, 0.6,$ and $0.8 \times \frac{W_{window}}{2}$) are calculated when APR = 0.1 and

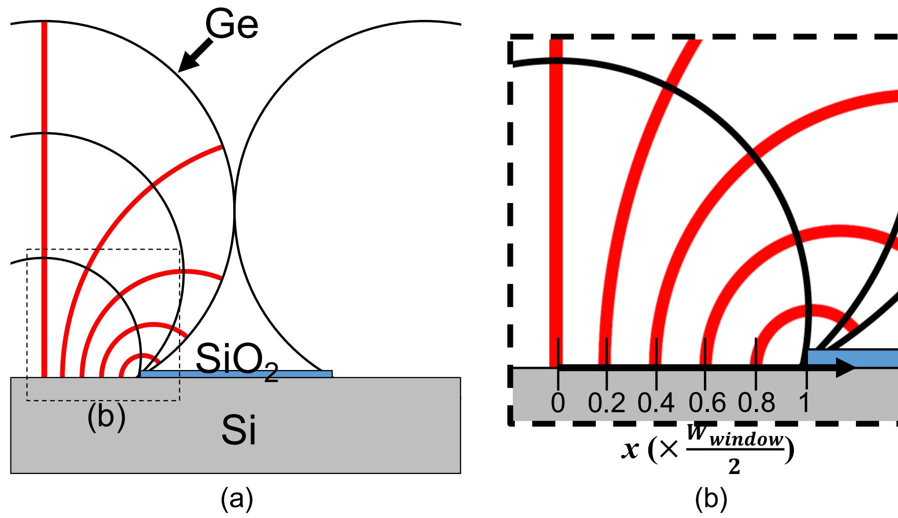

Figure 3.4: TD reduction as the results of bending and coalescence

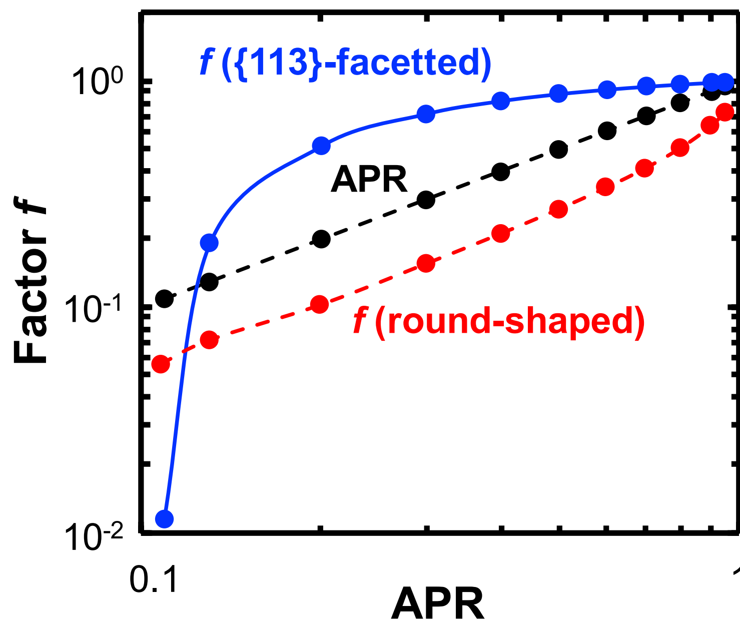

Figure 3.5: Calculated TDD reduction factor f as a function of APR. Dots indicate calculated values.

0.8, as shown in Fig. 3.6. Here, it is shown that

(a) round-shaped SEG origin, APR = 0.1: 5/6 TDs are trapped, $f = 0.0503$.

(b) round-shaped SEG origin, APR = 0.8: 2/6 TDs are trapped, $f = 0.5009$.

(c) {113}-facetted SEG origin, APR =0.1: 6/6 TDs are trapped, $f = 0.0324$.

(d) {113}-facetted SEG origin, APR = 0.8: 0/6 TDs are trapped, $f = 0.9697$.

It is clearly shown that round-shaped SEG and then coalesced Ge is more effective to reduce TDD when APR is 0.8, than {113}-facetted case. On the other hand, when APR is 0.1, {113}-facetted and then coalesced Ge is more effective than round-shaped case. These calculation results indicate the "crossing" phenomenon, which is shown in Fig. 3.5.

Figure 3.6 shows the origin of "crossing" as well. From Figs. 3.6 (a) and (c), it is found that the TD generated at $x_0 = 0.04$ in round-shaped SEG Ge penetrate to the top surface, while the one in {113}-facetted SEG Ge penetrate to the bottom surface. Such a difference is ascribed to the presence of {113} facets near the SEG top: {113} facets are more deviated from [001] direction than round-shaped surfaces. The presence of {113} facets near the SEG top promote the bending of TDs generated near the center of SEG Ge ($x_0 \ll 1$), and the positive effect of {113} facets on the reduction of TDD become larger as APR become smaller. This is the reason of the "crossing" at $x_0 = 0.11$.

In the calculation shown in Fig. 3.6, it is assumed that Ge does not grow on SiO_2 masks. Under certain growth conditions such as relatively high GeH_4 source gas pressure and/or relatively low growth temperature, however, Ge shows wetting growth on SiO_2 masks even Ge nucleation does not happen on SiO_2. Such a "wetting" growth of Ge on SiO_2 has been widely reported in Ge coalescence to perform ART [78, 80, 90, 94–97]. In fact, the previous works on ART have been worked so as not to form voids on SiO_2 masks [98]. However, such a wetting growth has a negative effect on the TDD reduction in our model, as shown in Fig. 3.7. Figure 3.7 shows coalesced Ge with APR of 0.1, assuming that Ge wetting growth happens on the SiO_2 mask. Here,

(a) round-shaped SEG origin, APR = 0.1, Ge grows on SiO_2 masks: 0/6 TDs are trapped.

(b) 113-facetted SEG origin, APR = 0.1, Ge grows on SiO_2 masks: 0/6 TDs are trapped.

As obviously shown in Fig. 3.7, if wetting growth occurs, no semicylindrical void is formed when SEG Ge layers coalesce. Thus, all TDs penetrate to the top surface, showing no reduction of TDD, i.e., $f = 1$.

From Eq. 3.5, reduction of TDD is expressed as $\mathrm{APR} \times f = \frac{\rho_{coalesced}}{\rho_{blanket}}$. Here, note that $\frac{\rho_{coalesced}}{\rho_{blanket}}$ indicates a TDD in coalesced Ge normalized by TDD in blanket Ge of the same thickness. Figure 3.8 shows numerical calculation results of $\mathrm{APR} \times f = \frac{\rho_{coalesced}}{\rho_{blanket}}$ as a function of APR, summarizing the effect of TDD reduction induced by image force and coalescence of SEG Ge.

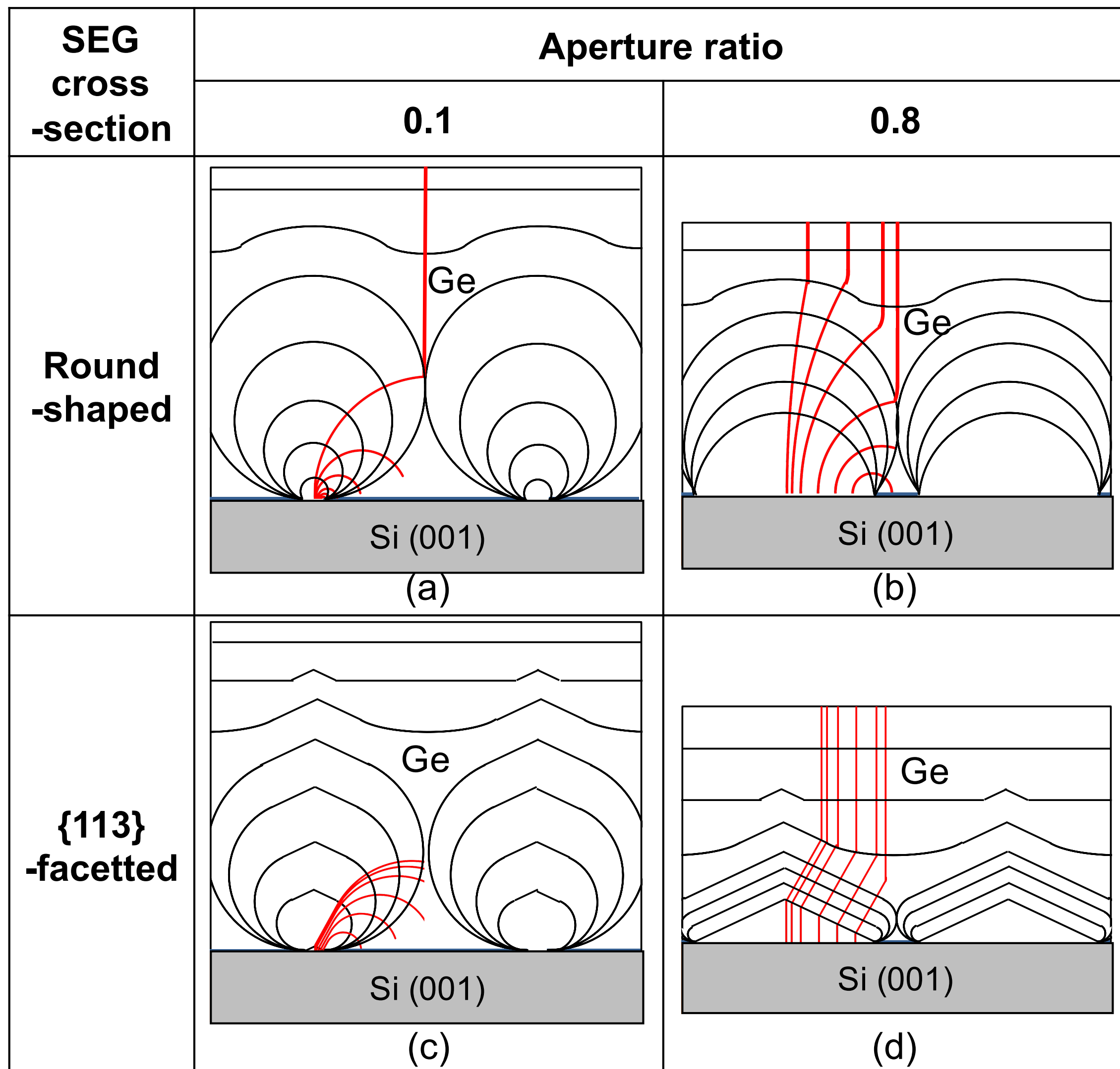

Figure 3.6: Trajectories of TDs in coalesced Ge when Ge does not grows on SiO_2 masks.

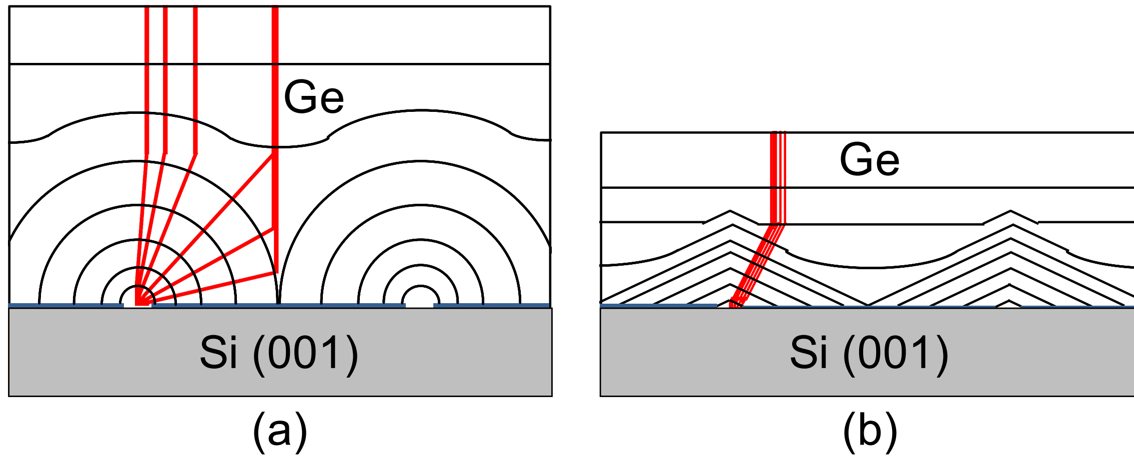

Figure 3.7: Trajectories of TDs in coalesced Ge originated from (a) round-shaped SEG Ge and (b) {113}-facetted SEG Ge, in the case for Ge grows on SiO_2 masks.

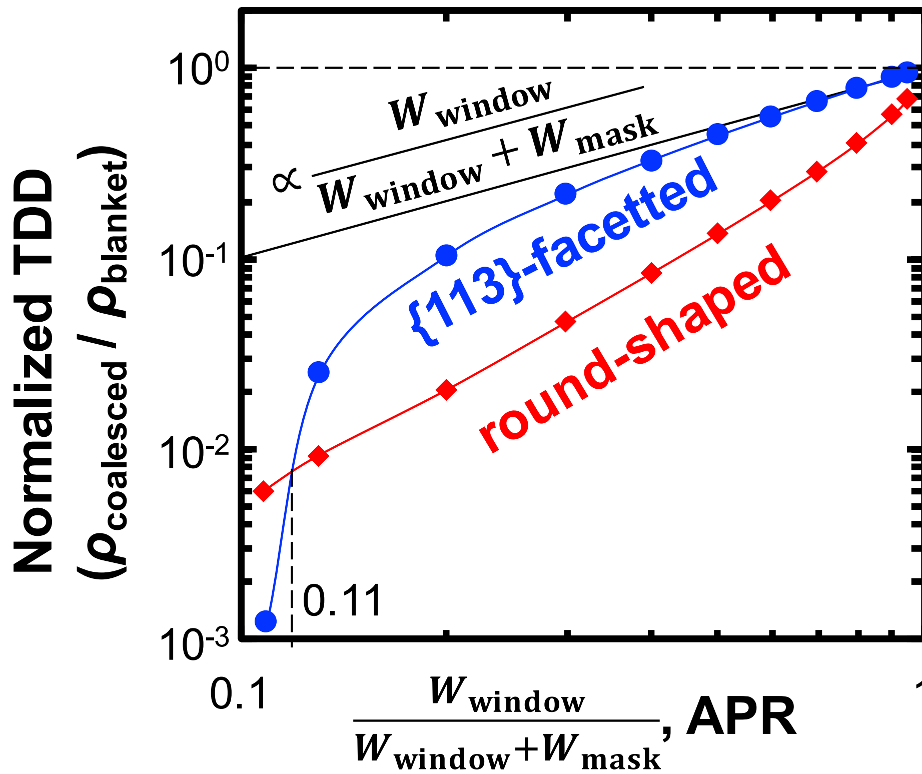

Figure 3.8: Calculated TDD in coalesced Ge as a function of aperture ratio

In Fig. 3.8, the red squares and line are calculated TDDs and their eye-guide line in coalesced Ge originated from round-shaped SEG Ge, and the blue dots and line are calculated TDDs and their eye-guide line in coalesced Ge originated from {113}-facetted SEG Ge. The "crossing" shown in Fig. 3.5 is also shown in Fig. 3.8 when APR = 0.11. When APR is larger than 0.11, the round-shaped SEG Ge is more effective than {113}-facetted one, corresponding to the situation shown in Figs. 3.6 (b) and (d). When APR is smaller than 0.11, on the other hand, {113}-facetted SEG Ge become more effective than round-shaped one, corresponding to Figs. 3.6 (a) and (c). As in Fig. 3.6, such a "crossing" of TDD reduction effect is ascribed to the presence of {113} facets near the SEG top (x_0 is almost 0). Theoretically, TDD become 0 ($f = 0$) when APR = 0.09739 in the case for {113}-facetted SEG Ge.

It is notable that TDDs can be reduced for 10^{-2} times compared to blanket Ge regardless of cross-sectional structure of SEG Ge. For example, when TDD in blanket Ge is 10^9 cm^{-2}, TDD in coalesced Ge (APR = 0.1) should be smaller than 10^7 cm^{-2}. Note that the situation in Fig. 3.7 correspond to the black line in Fig. 3.8, showing the TDD reduction owing to the reduction of APR, but not to the coalescence ($f = 1$). Thus, Ge wetting growth on SiO_2 masks has a negative effect in terms of the TDD reduction.

3.2.3 Extensibility to other hetero-epitaxy

In this chapter, image-force-induced TD bending and TDD reduction are described in the case for Ge epitaxial layers on Si. However, since image force is applied in all materials where near free surfaces, the image-force-induced TD bending and TDD reduction should be applicable to all hetero-epitaxy as long as SEG is possible. For instance, GaAs form {111} facets when line-shaped GaAs SEG is performed in [110] direction on a Si(001) substrate [99]. Then, the calculation performed to {113}-facetted Ge on Si can be applied to {111}-facetted GaAs on Si only by changing the angle between (001) plane and appearing facets; incase for {113} facets: 25.2°, and for {111} facets: 54.7°. Such simple modification is applicable because image force is not related to crystal orientation. It is also notable that the magnitude of TDD reduction increase as the angre between (001) plane and appearing facets become larger because TDs are deviated from [001] direction more easily. Although the rest part of this dissertation employs Ge epitaxial layers on Si for experimental verification, note that the image-force-induced TDD reduction would be applicable to all material system as long as SEG is possible.

4 Lateral Growth and Coalescence of SEG Ge Layers

Ge grows on Si, while does not grow on SiO_2 [100]. Thanks to the useful nature, selective epitaxial growth (SEG) of Ge on Si has been achieved and widely employed in Si photonics research [54, 89]. In order to achieve experimental verification of the theoretical model described in chapter 3, SEG Ge and their coalescence should be achieved as a major premise. However, there has been no report on Ge growth overhanging SiO_2 masks since previously reported attempts on Ge growth over SiO_2 in lateral direction were all "wetting growth" except for several unintentional formation of voids on SiO_2 masks. [101, 102] Therefore, the kinetics of Ge overhang growth and the conditions for coalescence should be investigated before the examination of the TDD reduction model, and will be described in this section.

4.1 Experimental Procedure: Ge SEG on Si

4.1.1 Preparation of SEG Masks

Boron-doped *p*-Si wafers (resistivity range: 1–100 Ω cm) were oxidized in a tube furnace to form thermal SiO_2 layers used as SEG mask layers. In order to remove ART effect from the observation of TDDs, the Si wafers were oxidized at 900 °C for 2 hours. According to an optical interference type film thickness measurement system *nanospec*, the thickness of thermal SiO_2 layers were 39 ± 1 nm as oxidized.

The thermal SiO_2 layers were patterned into stripe shape employing electron beam (EB) lithography followed by wet chemical etching. EB lithography was carried out using a surfactant "OAP" and a positive EB resist "ZEP 520A." The operation conditions were summarized in Table 4.1. Please note that the operation conditions were optimized from the standard conditions in order to use ZEP 520A for wet chemical etching: ZEP 520A coated by the standard conditions cannot survive the following wet chemical etching.

Table 4.1: Process conditions for photoresist coating, EB lithography, and development.

Process	Temperature	Time	Note
Surface cleaning	Room temp.	10 sec	Use DI water
Pre-OAP bake	110 °C	300 sec	
OAP coating	Room temp.	30 sec	Spin 3000 rpm
Pre-ZEP bake	110 °C	60 sec	
ZEP coating	Room temp.	60 sec	Spin 1000 rpm
Pre-exposure bake	180 °C	300 sec	
Cool down	180 → 50 °C	30 ~ 40 min	On hotplate
EB exposure	Room temp.	depends on pattern	Dose: 120 μC/cm^2
Development	Room temp.	60 sec	Developer: ZED
Post-exposure bake	140 °C	3 min	

The length direction of the SEG masks were set to be parallel to [110] orientation as schematically shown in Fig. 4.1. W_{window} and W_{mask} were set to be 0.5–10 μm in design. The minimum widths of W_{window} and W_{mask} were limited by the resolution of EB writer, and the maximum widths were set to be wide enough to prevent coalescence of SEG Ge layers. The actual W_{window} and W_{mask} were deviated from the designed ones because of fabrication error in lithography and isotropic wet chemical etching. The actual W_{window} was experimentally obtained by AFM and SEM, and will be shown in later part (section 4.2.1).

Wet chemical etching was carried out using a buffered-HF "BHF-63SE," which etches thermal SiO_2 at a rate of 80 nm/min. The Si wafers after EB lithography were dipped into the BHF for 1 min in order to completely remove the thermal SiO_2 layers. ZEP 520A resist coated by the standard conditions cannot survive the wet chemical etching process, and thus the EB conditions were optimized as summarized in Table 4.1. The important process is the "ZEP coating," "Cool down," and "Post-exposure bake." The standard ZEP coating recipe is "2500 rpm for 60 sec" or so, resulting in ZEP thickness of 400 nm. The optimized recipe give s ZEP thicker than the standard recipe, 700-nm-thick. Cool down process is added as the result of process optimization, resulting in a good adhesion between resist and substrate. The cool down process should be operated on a hotplate without any intentional cooling down operation. Post-exposure bake is also added as the result of process optimization, making ZEP 520A stronger in terms of wet chemical etching. The baking temperature was set to be

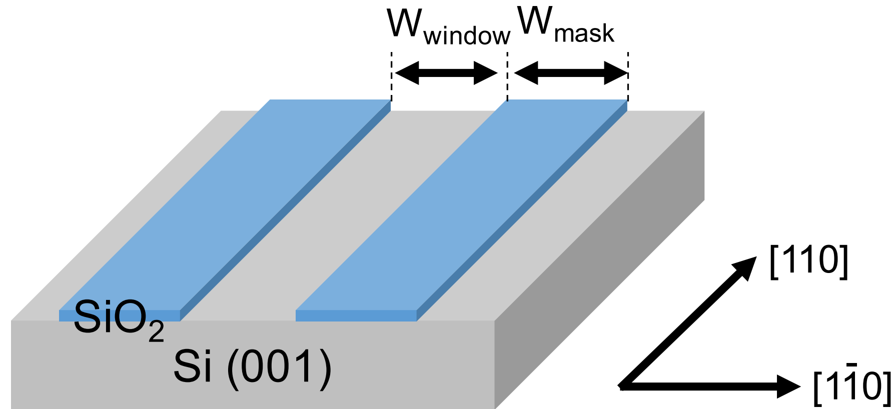

Figure 4.1: Schematic illustrations of SEG mask, W_{window}, and W_{mask}

above the glass transition temperature; 105 °C for ZEP 520A.

After wet chemical etching by BHF, ZEP 520A was removed using Hakuri 104 (photoresist remover) at room temperature for 30 min with ultrasonic vibration. The Si wafers were cleaned using Piranha solution (H_2O_2 20 ml + H_2SO_4 80ml) and 0.5 % diluted HF for three times in order to remove organic/metal impurities on the wafer surfaces. Prior to loading into Ge growth machine, the Si wafers were dipped into 0.5 % diluted HF for 4 min in order to remove native oxide on Ge growth window areas. As the results of the cleaning processes above, ~20-nm-thick SiO_2 layers were remained on the Si wafers as the SEG mask layers according to thickness measurements using *nanospec*.

4.1.2 Ge Epitaxial Growth on Si

Ge epitaxial layers were grown on the Si wafers with patterned SiO_2 SEG mask layers using an UHV-CVD method. In the UHV-CVD chamber, base pressure was kept mid-10^{-7} Pa, leading extremely small amount of impurities such as carbon, oxygen, etc. in epitaxial layers. A loaded wafer is heated up by thermocouple, and the chamber wall is cooled down by running water. Thus, source gases are decomposed by thermal assist at the surface of the loaded wafer.

A two-step Ge growth method [54] was employed in order to grow epitaxial Ge layers on Si (see section 2.1). A pure Ge buffer layer was deposited at relatively low temperature (below 400 °C) followed by a main Ge layer deposited at an elevated temperature (typically 500–700 °C). In this thesis, "growth temperature" means the temperature during the main layer deposition. The thickness of Ge buffer layer was several tens of nano meter. A GeH_4 gas diluted at 9 % in Ar was used as the source gas for Ge layers, and its partial pressure was kept 0.5–0.8 Pa during the buffer/main Ge growth. The thickness of Ge layer was controlled by changing the duration of main growth. Under the conditions, growth rate of Ge on (001) plane is 8–12 nm/min, depending on temperature and partial pressure. After the growth of

main Ge layer, a Si capping layer was successively deposited in the same UHV-CVD chamber at 600 °C in order to protect chemically unstable Ge layers. The thickness of the Si capping layer is sensitive to growth temperature and difficult to control precisely. According to single wavelength ellipsometry (λ = 0.633 μm), the thickness of Si capping layer was 22 ± 5 nm at blanket area for the samples used in this thesis.

4.2 Ge Lateral Growth Over SiO_2 Masks

4.2.1 Experimental Observations of W_{window}

In order to obtain the widths of Ge overgrowth in lateral direction, W_{window} were measured by atomic force microscope (AFM) and SEM as shown in Fig. 4.2. The AFM observations were carried out on a Si wafer without Ge growth, which experienced all processes including 4 min cleaning by 0.5 % HF under the same conditions on the same day. Thus, the SEG masks should be identical with a Si wafer loaded into UHV-CVD chamber. The sidewall angles of the SiO_2 layer were obtained as 8–23° according to the AFM observations. These sidewall angles are within the detection angle determined by the angle of the probe edge, and thus the observed W_{window} is trustable.

Figure 4.2 (b) shows the relation between designed W_{window} and experimentally obtained W_{window}. In Fig. 4.2 (b), the black dashed line shows where W_{window} by AFM = Designed W_{window}, and the red dashed line shows where W_{window} by AFM = Designed W_{window} + 100 nm. It is found that the experimentally obtained W_{window} is wider than designed ones for 100 nm. The expansion of W_{window} is reasonable because the wet chemical etching is an isotropic etching process, i.e., the SiO_2 layer should be etched in lateral direction as well as depth direction. Since the Si wafer was dipped into BHF for 1 min, the SiO_2 layer should be etched for 80 nm in both depth and lateral direction. Taking into account that W_{window} start to be expanded as Si substrate is exposed, expansion of W_{window} for 100 nm is reasonable.

In addition to the AFM observations, cross-sectional SEM observations were carried out after Ge growth as will be shown in Fig. 4.4. W_{window} obtained from the cross-sectional SEM images are also plotted on the graph in Fig. 4.2 (b), and the W_{window} obtained by SEM observations (blue outlined squares) well correspond to the W_{window} obtained by AFM observations. The correspondence of W_{window} obtained by AFM and SEM ensure that the obtained W_{window} is trustable. From now, the word "W_{window}" means W_{window} obtained by SEM taken for each SEG Ge layer unless otherwise stated.

4.2.2 Ge Growth in Lateral Direction at 700 °C

Ge SEG at 700 °C was carried out on the Si wafer with SEG masks for 150 min (duration of main growth). Observations for cross-sectional structure of blanket/SEG Ge layers were carried out by scanning electron microscopy (SEM). Figure 4.3 shows a cross-sectional SEM

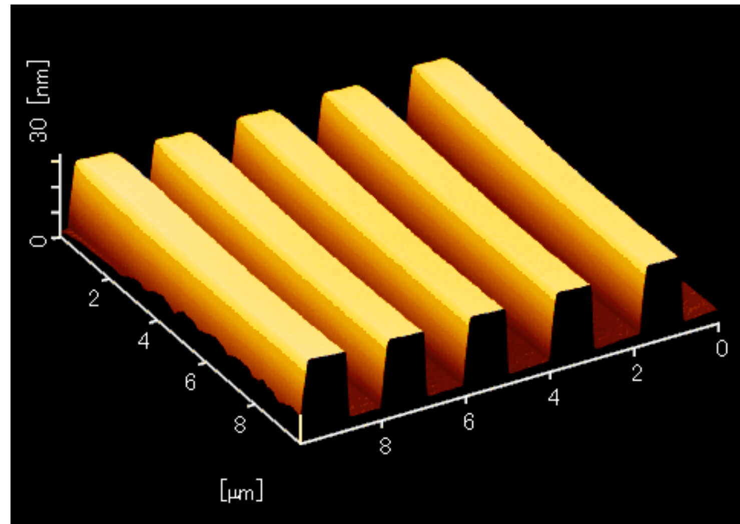

(a)

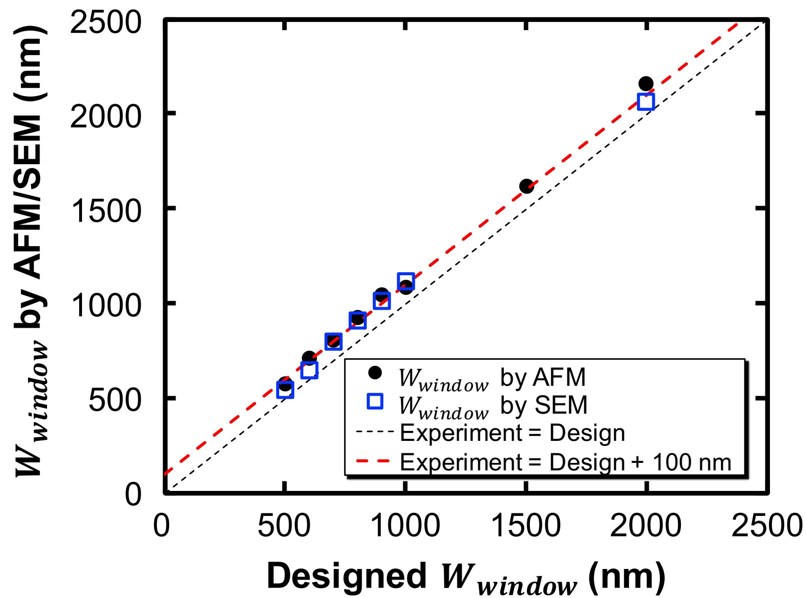

(b)

Figure 4.2: (a) A bird's eye view AFM image of SEG mask before Ge growth and (b) the relation between designed W_{window} and experimentally obtained W_{window}

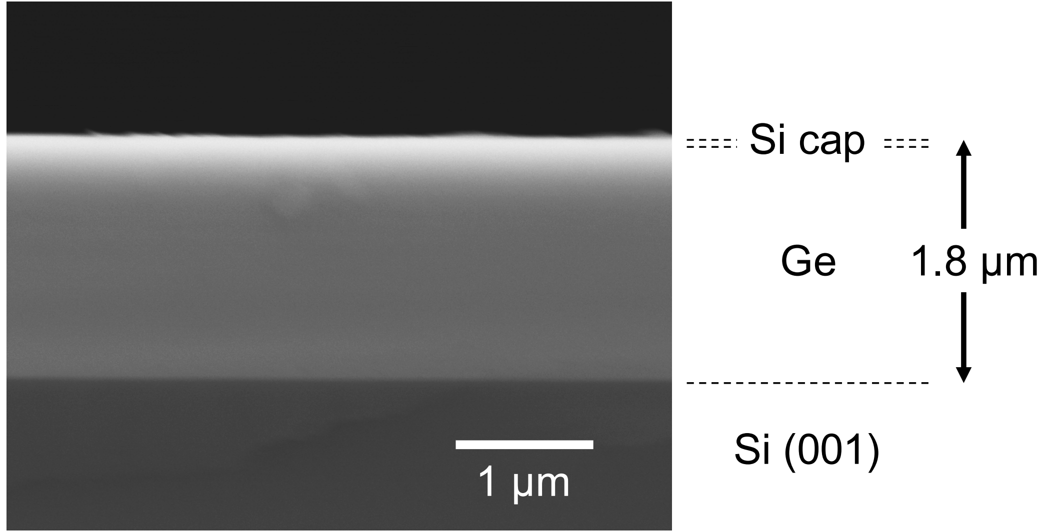

Figure 4.3: A cross-sectional SEM image of Ge grown in blanket area at 700 °C

image of Ge grown in blanket area at 700 °C. The thickness of Ge in blanket area is 1.8 μm from the SEM image.

Figure 4.4 (a) shows a typical cross-sectional SEM image of a SEG Ge layer grown at 700 °C (designed W_{window} = 0.8 μm). The observed cross section of SEG Ge layers are exposed by cleaving followed by polishing using focused ion beam (FIB). Thus, there is a Pt layer deposited to protect Ge layers during the FIB polishing. The SEG Ge layer grown at 700 °C shows round-shaped cross-section, which is assumed in the calculation shown in Figs. 3.3 (a)–(c) and the red lines in Figs. 3.5 and 3.8. The growth rate of SEG Ge in [001] direction is obtained as 5.6 nm/min. The growth rate is related to the growth rate on {113} facets, as will be described in Fig. 4.5. From the SEM image, the width of SEG Ge (W_{Ge}) was obtained for 1.42 μm. Since the actual W_{window} is obtained for 0.906 μm from the SEM image, the width of Ge overhanging the SiO_2 mask $W_{overhang}$ is obtained as $\frac{1.42-0.906}{2}$ = 0.257 μm. The relation among W_{window}, W_{Ge}, and $W_{overhang}$ is expressed by Eq. 4.1, and schematically illustrated in Fig. 4.4 (b).

$$\frac{W_{Ge} - W_{window}}{2} = W_{overhang}. \tag{4.1}$$

As shown in the SEM image and schematically illustrated, Ge wetting growth on SiO_2 is not completely suppressed. From the SEM image, Ge grows on SiO_2 for ~50 nm.

Thicknesses of Si capping layers grown on facet sidewalls are thinner than those of Si grown on (001) top surfaces, as reported in Ref. [103]. Since the thickness of Si capping layer grown on (001) top surfaces was ~20 nm according to a single wavelength ellipsometry, the Si capping layer on facet sidewalls should be only several nano meter. Thus, the Si capping

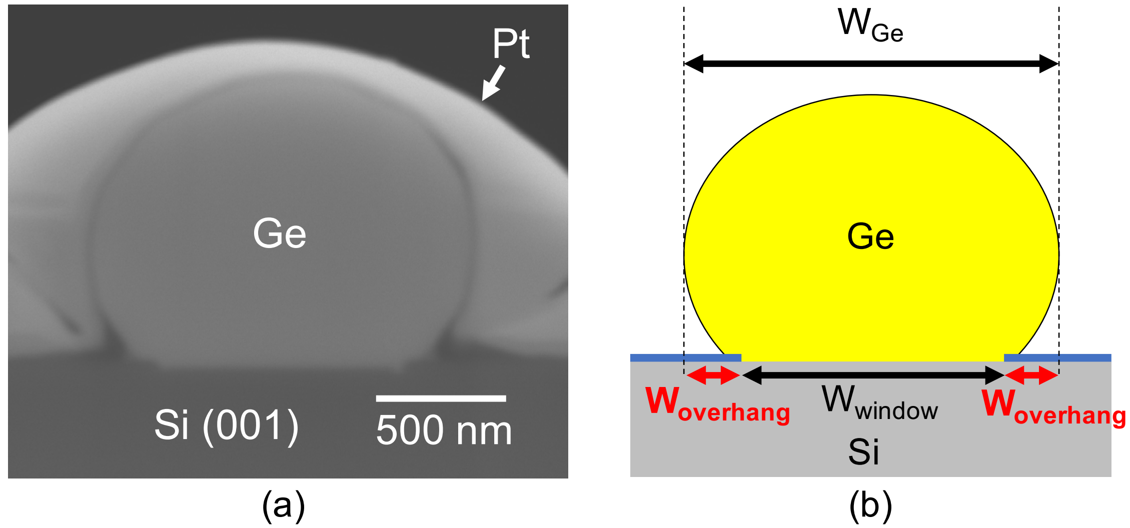

Figure 4.4: (a) A typical cross-sectional SEM image of a SEG Ge layer grown at 700 °C (W_{window} = 0.8 μm in design) and (b) schematic illustration showing the relation among W_{window}, W_{Ge}, and $W_{overhang}$

layers are difficult to be found in SEM images and ignored in the observations for W_{Ge}.

$W_{overhang}$ for other SEG Ge layers were obtained from cross-sectional SEM images for each SEG Ge layers in the same way, and the obtained results are summarized in Fig. 4.5. Black dots indicate experimentally obtained $W_{overhang}$ by cross-sectional SEM observations. It is clearly shown that $W_{overhang}$ become wider as W_{window} become narrower. In particular, there is an "inflection point" around 2 μm, i.e., the correlation between $W_{overhang}$ and W_{window} changes around 2 μm. Such $W_{overhang}$ dependence on W_{window} is explainable by the round-shaped cross-sectional growth model, which is schematically shown in Fig. 3.3 (a). The growth model assumes that cross-sectional structure of SEG Ge is a circle passing (0, h), ($\frac{W_{window}}{2}$, 0), and ($-\frac{W_{window}}{2}$, 0), where h is the height of the SEG Ge. In Fig. 4.5 (a), the red dashed line indicates $W_{overhang}$ derived from the round-shaped growth model. The growth rate of SEG Ge in [001] direction and the width of Ge grown on SiO_2 masks are estimated by fitting using least-squares method as 5.5 nm/sec and 42 nm, respectively. It is notable that the growth rate obtained by fitting well correspond to the one obtained from the SEM observation shown in Fig. 4.4 (5.6 nm/min). $W_{overhang}$ calculated by the fitted growth rate (5.5 nm/min) and wetting growth width (42 nm) well reproduces the experimental results. However, the derived growth rate of SEG Ge in [001] direction, 5.5 nm/sec, is significantly smaller than the growth rate of Ge on (001) planes, and close to the growth rate of Ge on {113} facets as shown by the yellow star in Fig. 4.5 (b) [104]. Therefore, it is found that the round-shaped SEG Ge growth is limited by {113} facet growth, which shows the slowest growth rate in Ge

crystal [105].

4.2.3 Ge Growth in Lateral Direction at 650 °C

Ge SEG at 650 °C was carried out on the Si wafer with SEG masks for 270 min (duration of main growth). Such a long duration of main growth was chosen in order to obtain coalesced Ge layers even with smaller growth rate on {113} facets (Fig. 4.5 (b)). Figure 4.6 shows a cross-sectional SEM image of Ge grown in blanket area at 650 °C. From the SEM image, the thickness of Ge in blanket area is obtained as 3.5 μm.

Different from Ge growth at 700 °C, SEG Ge layers grown at 650 °C shows {113}-facetted cross-section instead of round-shaped one, as shown in Fig. 4.7 (a). The thickness of the SEG Ge layer is 1.3 μm from the SEM image, corresponding to the growth rate of 4.4 nm/min. The growth rate of the SEG Ge correspond to that of Ge on {113} facets as shown by the blue star in Fig. 4.5 (b). The sidewalls of the SEG Ge layer is round-shaped so as not to grow on SiO_2 masks. Therefore, in terms of cross-sectional shape, the SEG Ge grown at 650 °C corresponds to the assumption in calculation shown as Figs. 3.3 (d) and as the blue lines in Figs. 3.5 and 3.8. However, as schematically shown in Fig. 4.7 (b), Ge wetting growth on SiO_2 is shown for ~900 nm wide on one side. The enhancement of Ge wetting growth on SiO_2 is ascribed to the reduction of growth temperature (700 °C → 650 °C) promoting nucleation of Ge on SiO_2, as reported in Ref. [98]. Assuming that the Ge start to grow on SiO_2 when the SEG Ge layer is surrounded by {113} facets (indicated by the green line in Fig. 4.7 (c)), the growth rate in lateral direction is estimated to be 3.5 nm/min.

The SEM image was taken without FIB polishing since SEG Ge layers grown at 650 °C changed its shape by the FIB polishing. This would be ascribed to physical unstability of the SEG Ge layers grown at 650 °C. As reported in [106], Ge/SiO_2 interfaces remain grown-in tensile strain in Ge, i.e., Ge/SiO_2 interfaces are not flexible. Thus, there would be non-uniform strain in SEG Ge, leading physical unstability of the SEG Ge layers.

4.2.4 Ge Wetting Growth on SiO_2

Comparing Fig. 4.4 (a) and Fig. 4.7 (a), it is clearly shown that Ge does not grow on SiO_2 at 700 °C, while Ge grows on SiO_2 at 650 °C. The difference in wetting growth on SiO_2 can be understood as follows. Assuming that the contact angle between Ge and SiO_2 (θ) is determined by Young's equation:

$$\gamma_{SiO2} = \gamma_{Ge} \cos\theta + \gamma_{int} \tag{4.2}$$

Here, γ_{SiO2}, γ_{Ge}, and γ_{int} are SiO_2 surface free energy, Ge surface free energy, and Ge/SiO_2 interfacial free energy, respectively. The angle of SEG Ge sidewall becomes larger as Ge growth proceeds. When the angle of SEG Ge sidewall reaches the contact angle θ, SEG Ge needs to grow in vertical ([001]) or lateral ([1$\bar{1}$0]) direction. In the case for 650 °C growth,

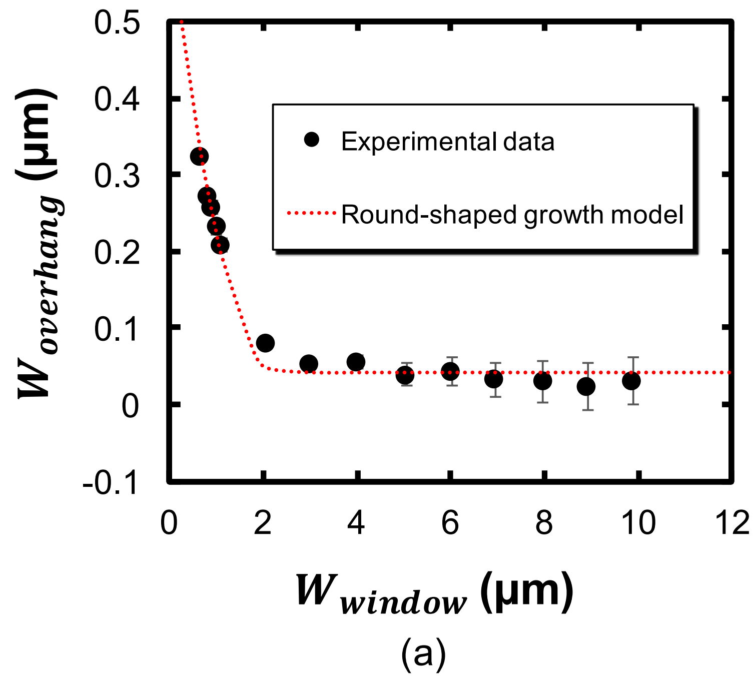

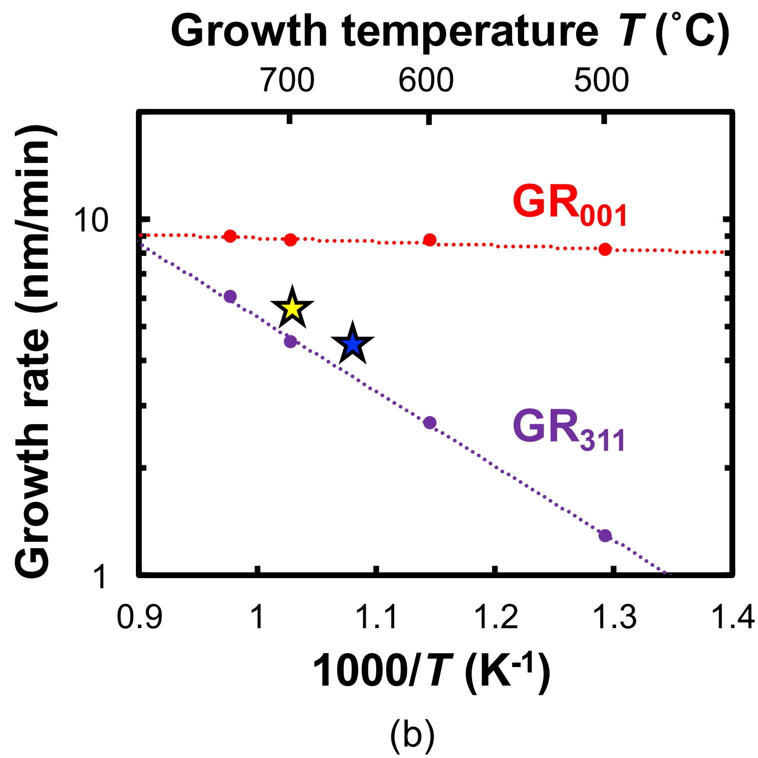

Figure 4.5: (a) $W_{overhang}$ as a function of W_{window} and (b) growth rates of Ge on (001) planes (GR_{001}) and {113} facets (GR_{113}). Growth rates are obtained from *Y. Mizuno, Master's thesis, The University of Tokyo, 2010*.

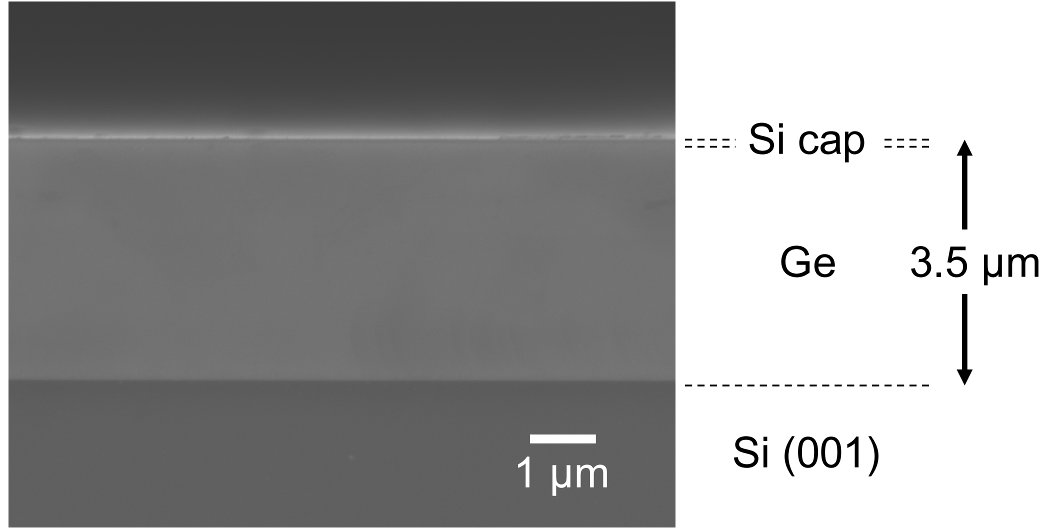

Figure 4.6: A cross-sectional SEM image of Ge grown in blanket area at 650 °C

the vertical growth is severely limited by {113} facets, and thus SEG Ge prefers to grow in lateral direction, i.e., wetting growth. Even though the wetting could generate dislocations at the Ge and SiO_2 interface, it is finally to be terminated at the semicylindrical void surface. In the case for 700 °C growth, Ge can grow in vertical direction, and the contact angle is larger than that for 650 °C because of larger γ_{int}. These would be the reason why 650 °C-grown Ge shows wetting over SiO_2 while 700 °C grown-Ge does not.

4.3 Coalescence of SEG Ge Layers Over SiO_2 Masks

Simply thinking, SEG Ge layers would coalesce with adjacent ones when meet together, i.e., $W_{overgrowth} > \frac{W_{window}}{2}$. The calculated area where $W_{overgrowth} > \frac{W_{window}}{2}$ or $W_{overgrowth} < \frac{W_{window}}{2}$ is shown in Figs. 4.8 (a) and (b). Blue area shows the parameter sets satisfying $W_{overgrowth} > \frac{W_{window}}{2}$, where SEG Ge layers should be coalesced. On the other hand, red area shows the parameter sets satisfying $W_{overgrowth} < \frac{W_{window}}{2}$, where SEG Ge layers should not be coalesced. Experimentally obtained structure is also in Figs. 4.8 (a) and (b). Blue dots indicate the parameter sets where SEG Ge layers are coalesced and formed a flat-top film. A cross-sectional SEM image and a plan-view optical microscope (OM) image of coalesced Ge with flat-top surface are shown in Figs. 4.8 (c) and (d). The OM image shows no structure because of the flat-top surface of the coalesced Ge. Green triangles indicate the parameter sets where SEG Ge layers are coalesced, but the top surface is not flat but mountain-shaped. A cross-sectional SEM image and a plan-view OM image of coalesced Ge with non-flat-top surface is shown in Figs. 4.8 (e) and (f). The OM image slightly shows stripe structure parallel to [110] direction, which is the length direction of SiO_2 masks underneath. Red

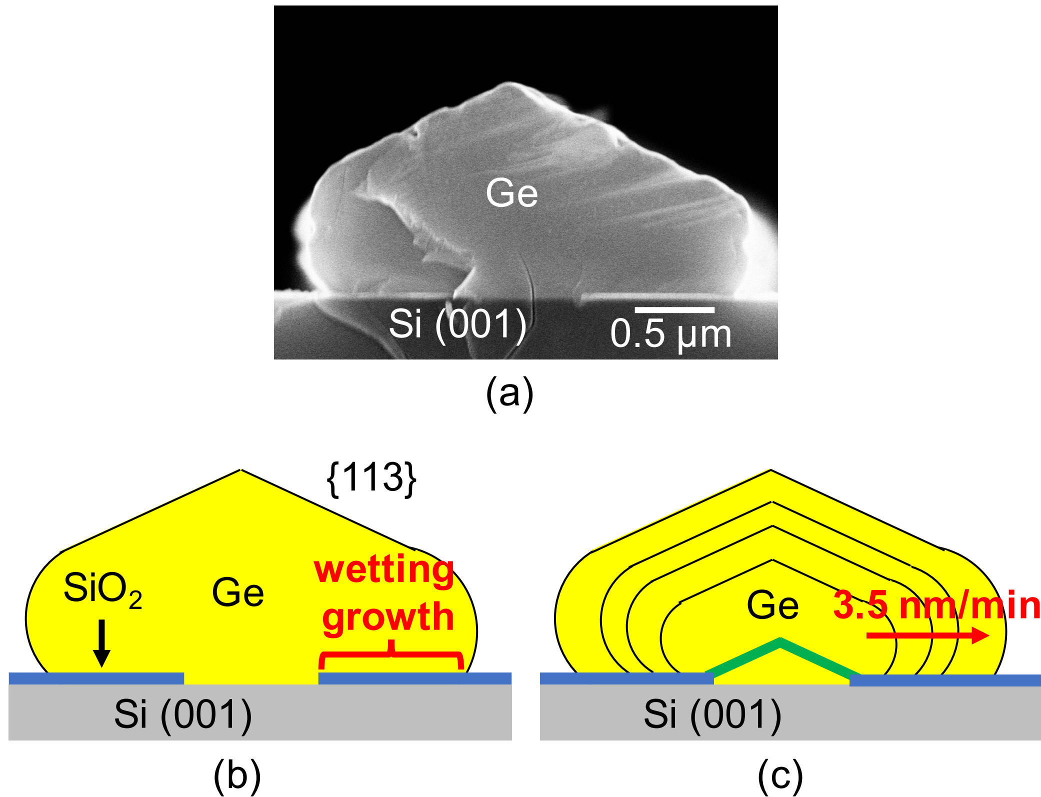

Figure 4.7: (a) A cross-sectional SEM image of SEG Ge grown at 650 °C, (b) a schematic illustration of the SEM image, and (c) a schematic illustration of Ge wetting growth on SiO_2 masks.

crosses indicate the parameter sets where SEG Ge layers are not coalesced, i.e., completely separated SEG Ge layers are observed. Figures 4.4 (a) and 4.7 (a) show typical SEM images of SEG Ge layers without coalescence. It is obvious that the calculation results well correspond with the experimental results.

In Fig. 4.8 (c), tunnel-shaped voids were periodically observed on the SiO_2 masks. This indicates that the flat-top coalesced Ge layer was formed due to the coalescence between the Ge SEG layers. The thicknesses of the flat-top coalesced Ge layers were 20%–40% smaller than that for the blanket Ge layer. This difference in thickness is ascribed to the difference of growth rate in [001] direction between planar Ge growth and SEG Ge, as shown in Fig. 4.5 (b). In the SEM images of coalesced Ge layers (Figs. 4.8 (c) and (e)), there are white lines connecting top surfaces and voids. Note that the white lines are not defects but geometrical steps because the images are taken by SEM, which cannot detect crystal defects. As will be described in later part, there is strain concentration at the top of the voids, and thus such steps are formed when the sample chips were cleaved.

Flatness of a coalesced Ge layer (W_{window} = 0.5 μm, W_{mask} = 0.6 μm in design) was

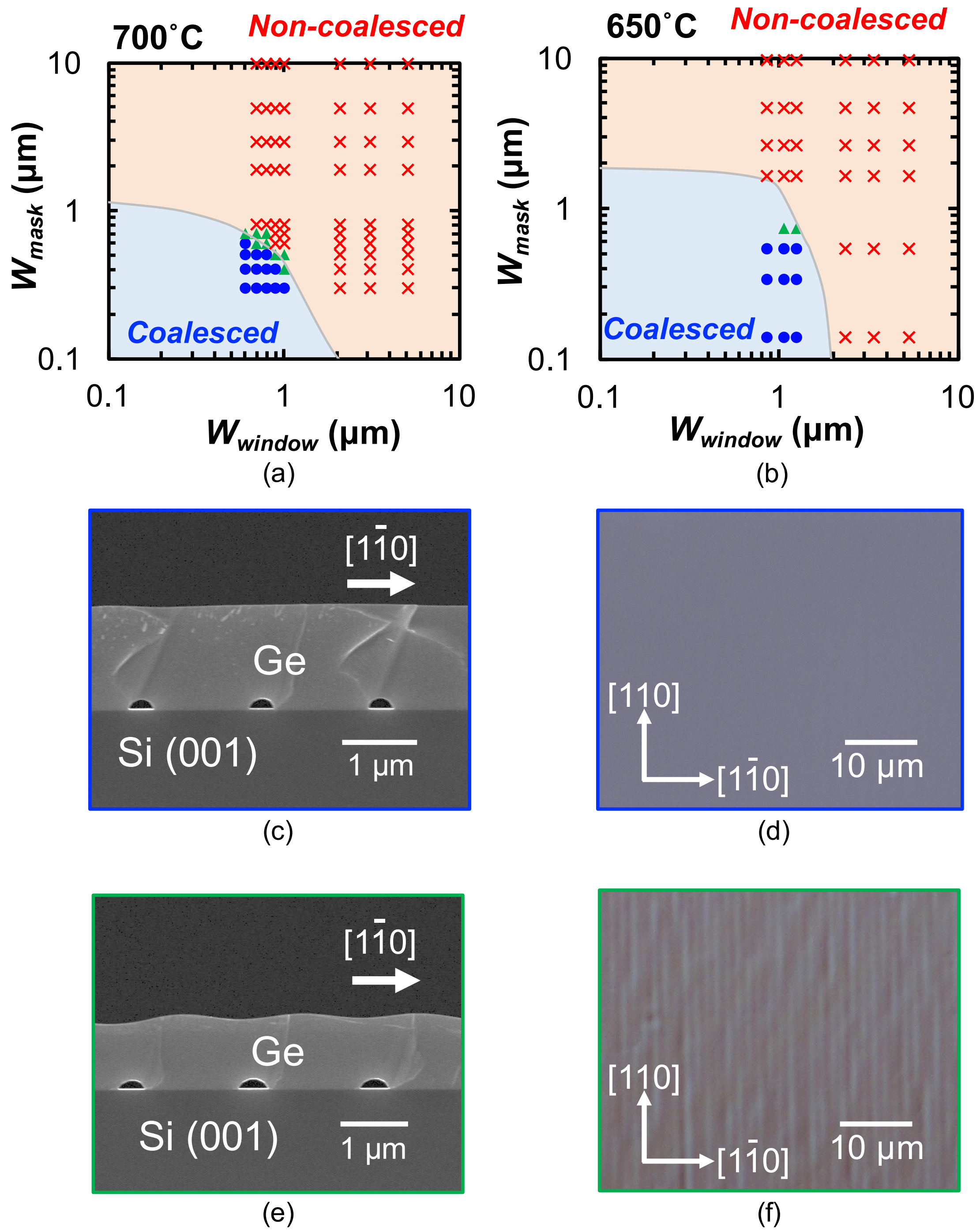

Figure 4.8: A distribution maps of coalesced/non-coalesced Ge grown at (a) 700 °C and (b) 650 °C, (c) a cross-sectional SEM image and (d) plan-view OM image of coalesced Ge with flat-top surface, and (e) a cross-sectional SEM image and (f) plan-view OM image of coalesced Ge with non-flat-top surface.

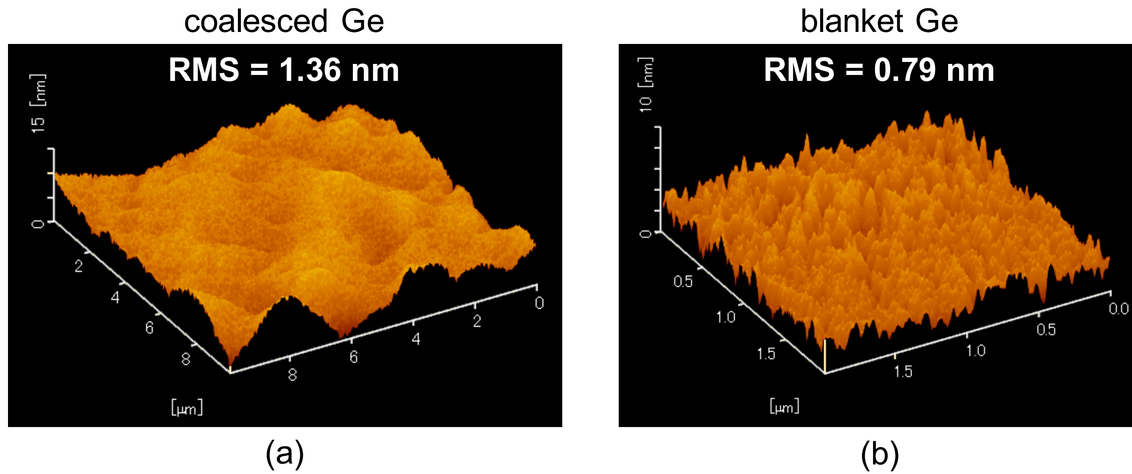

Figure 4.9: Bird's eye view AFM images of (a) coalesced Ge (W_{window} = 0.5 μm, W_{mask} = 0.6 μm in design) and (b) blanket Ge grown on the same Si wafer

observed by AFM in 10×10 μm^2 large area as shown in Fig. 4.9 (a). The surface root means square (RMS) is obtained for 1.36 nm at the area. Although the RMS value is slightly larger than that for blanket Ge (0.79 nm) shown in Fig. 4.9 (b), the RMS of 1.36 nm is small enough for the application of photonic devices because light scattering on the surface of RMS = 1.36 is negligible for near-infrared light used in optical communication (1.3–1.6 μm).

In order to understand the coalescence process of SEG Ge layers more deeply, a SEG Ge growth was carried out inserting 10-nm-thick $Si_{0.3}Ge_{0.7}$ layers every 15 min during the growth of main Ge layer. The $Si_{0.3}Ge_{0.7}$ layers were inserted to visualize growth surfaces, which is the method employed in ART research [102, 107]. The coalesced Ge with $Si_{0.3}Ge_{0.7}$ layers were observed by high-angle annular dark field (HAADF) scanning transmission electron microscope (STEM). A STEM specimen was picked up from a target area by a micro sampling method using focused Ga ion beam, and the thickness (in direction perpendicular to a paper/display surface) of the STEM specimen was 200 nm according to SEM observation. Acceleration voltage of 200 kV was employed for the STEM observation. Figure 4.10 (a) shows a cross-sectional HAADF STEM image of a coalesced Ge with $Si_{0.3}Ge_{0.7}$ demarcation layers grown at 700 °C. A schematic illustration of the STEM image is shown in Fig. 4.10 (b). The growth surfaces of the SEG Ge layers are clearly visualized by the $Si_{0.3}Ge_{0.7}$ layers, which are shown as black-ish lines in Fig. 4.10 (a). At the initial stage of Ge growth, SEG Ge layers start to grow from growth windows and their cross-section are round-shaped. Then, SEG Ge layers overhang the SiO_2 masks and coalesce with adjacent SEG Ge layers. Coalesced Ge forms non-flat-top surface just after the coalescence, and finally form flat-top surface by filling the "valley" area above the voids.

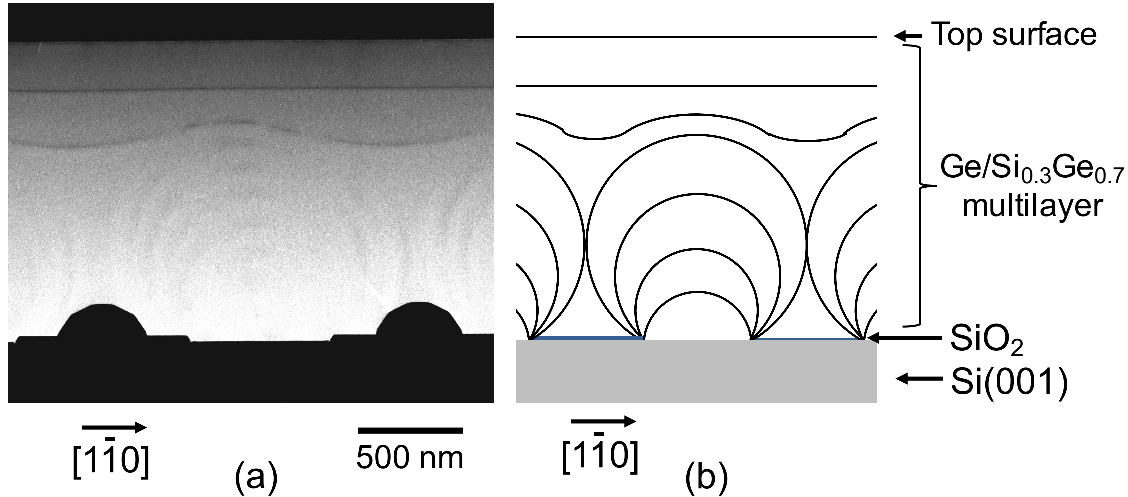

Figure 4.10: (a) A cross-sectional HAADF STEM image of SEG Ge grown at 700 °C with $Si_{0.3}Ge_{0.7}$ layers and (b) a schematic illustration of the STEM image

The STEM image shows Ge wetting growth on SiO_2 masks at 700 °C, unlike other SEG/coalesced Ge layer growth at 700 °C. The enhancement of Ge wetting growth on SiO_2 would be ascribed to the insertion of $Si_{0.3}Ge_{0.7}$ layers. $Si_{0.3}Ge_{0.7}$ layers would be easier to grow on SiO_2 than Ge because nucleation of Si on SiO_2 is more difficult to suppress than that of Ge on SiO_2 [108]. Thus, the nucleation of $Si_{0.3}Ge_{0.7}$ would occur on SiO_2 more frequently, leading Ge growth on the $Si_{0.3}Ge_{0.7}$ on SiO_2, resulting in the enhancement of Ge wetting growth on SiO_2.

4.4 Orientation Dependence for Lateral Growth and Coalescence of Ge

So far, the length direction of SEG masks has been aligned to be parallel to [110] direction. However, the lateral growth rate may depends on orientation since lateral growth rate is related to the growth rate of {113} facets, which is the slowest growth facets in Ge crystal. In order to investigate the orientation dependence of lateral growth rate, Ge growth was carried out at 600 °C over SEG masks deviated from [110] direction. SEG Ge layers aligned to [110] direction and the ones deviated from [110] direction for 30° were observed by plan-view SEM observations, showing clear difference. Figure 4.11 shows plan-view SEM images of 0.7-μm-wide (in design) SEG Ge layers grown at 600 °C. Although the SEG Ge layers aligned to [110] direction (Fig. 4.11 (a)) have smooth sidewalls, the SEG Ge layers deviated from [110] direction for 30° (Fig. 4.11 (b)) have rough sidewalls. Taking a closer look, the rough sidewalls of SEG Ge layers deviated from 30° are surrounded by facets as shown in Fig. 4.11

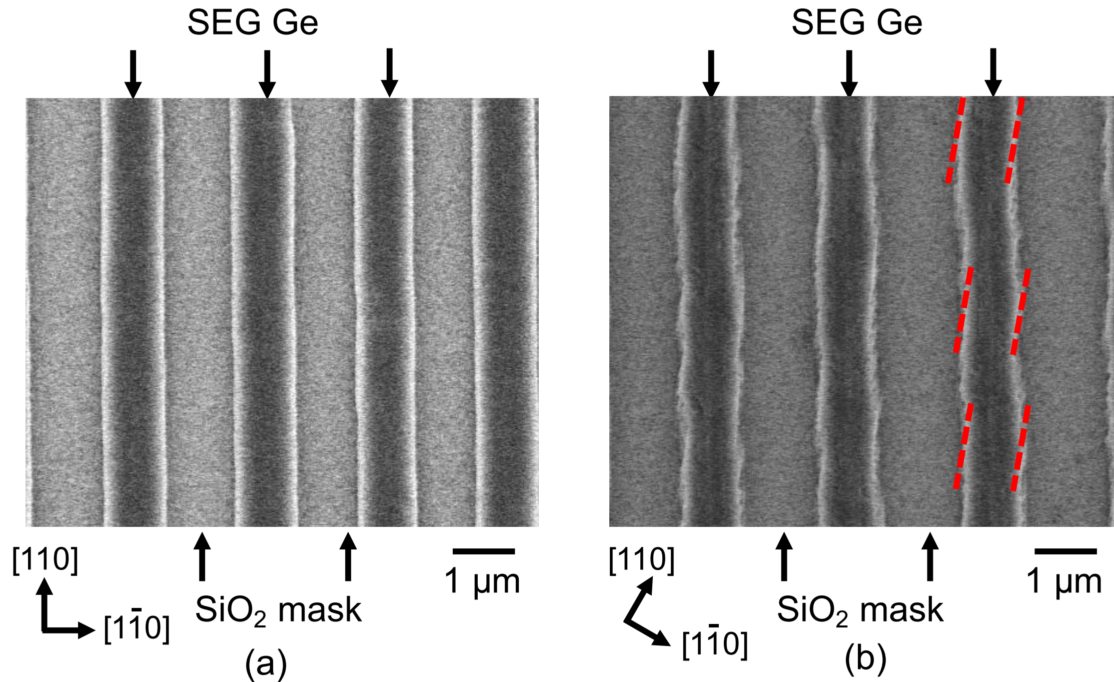

Figure 4.11: Plan-view SEM images of 0.7-μm-wide (in design) SEG Ge layers aligned to (a) 0°and (b) 30° deviated from [110] direction

(b) by red dashed lines. The facets would be {113} or {111} facets, which are stable facets in Ge crystal. Such rough sidewalls of SEG Ge layers are, however, not suitable for experimental verification of TDD reduction model because it is difficult to determine the cross-section of SEG Ge, resulting in difficulty in theoretical calculation of TDDs in coalesced Ge. Therefore, in this work, SEG Ge layers aligned to be parallel to [110] direction and their coalesced layers were examined in order to verify theoretical model by experiments.

In terms of practical application, however, the investigation of SEG Ge layers deviated from [110] direction is important. In particular, since Ge is an active device material, micro disk or micro ring structures have been widely interested [109–111]. Thus, it should be important challenge to fabricate micro disk/ring via SEG and coalescence of Ge.

In order to fabricate micro disk/ring via SEG and coalescence, circle-shaped SEG was carried out as shown in Fig. 4.12. Figure 4.12 (a) shows an OM image of a circle-shaped SEG mask (W_{window} = 0.9 μm, W_{mask} = 0.5 μm in design), and Fig. 4.12 (b) shows OM image of Ge grown on the SEG mask. Although the SEG mask is completely circle-shaped according to the OM observation, there are 8 convex parts radially spreading on the top surface of the grown Ge. The convex parts are more obviously shown by bird's eye view AFM observation as shown in Fig. 4.12 (c), and it is found that the convex parts are ~150 nm thicker than other

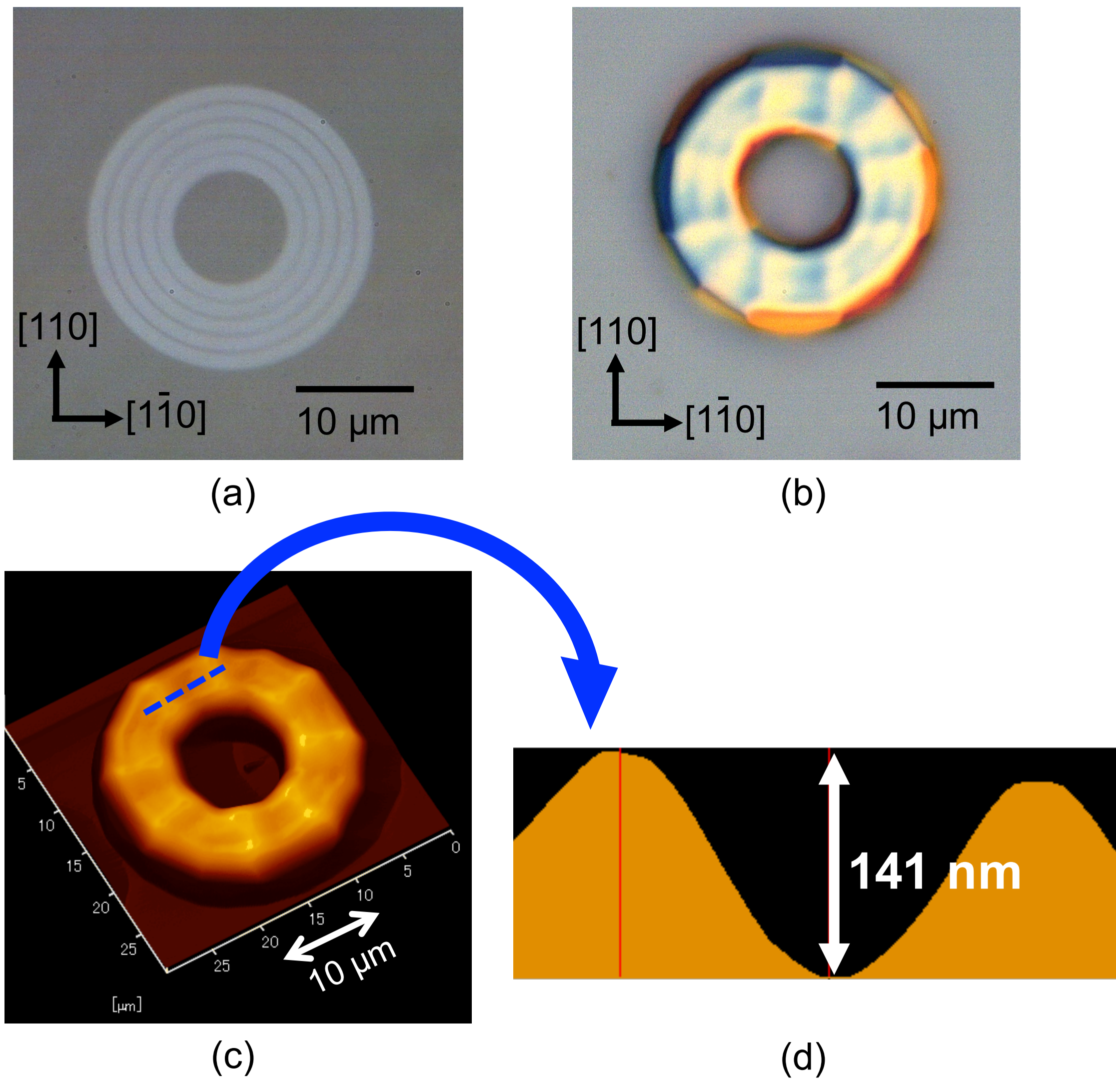

Figure 4.12: OM images of (a) circle-shaped SEG mask (W_{window} = 0.9 μm, W_{mask} = 0.5 μm in design) and (b) coalesced Ge ring grown on the SEG mask, (c) a bird's eye view AFM image of the coalesced Ge ring, and (d) cross-sectional profile of convex part indicated by blue dashed line in (c).

parts, as in Fig. 4.12 (d) showing cross-sectional profile of convex part indicated by blue dashed line in (c).

The formation of convex parts would be ascribed to crystal orientation since the convex parts are symmetric in four directions; [110], [$\bar{1}\bar{1}0$], [$1\bar{1}0$], and [$\bar{1}10$]. The results suggest that there are specific orientation enhancing growth in lateral direction, resulting in earlier coalescence of SEG Ge layers and formation of the convex parts. From the OM and AFM observations, it is found that the convex parts are formed where 21° deviated from <110> directions. This result suggests that growth in lateral direction would be enhanced when SEG masks are alined to be 21° deviated from <110> directions. However, in this work, such specific angled SEG masks are not employed because of the reason described above. It is also notable that longer Ge growth is required to obtain flat-top coalesced Ge rings because of the presence of the convex parts.

5 Experimental Verification of Theoretical Model by Measurements of TDDs

Experimental verification of theoretical model described in section 3 has been carried out in terms of TDD reduction and distribution of TDs in coalesced Ge layers. In this section, an etch pit density (EPD) method is employed in order to characterize large area of Ge epitaxial layers grown on Si. Since the SEG Ge layers and their coalesced layers are thinner than blanket Ge, thickness dependence of TDD in Ge on Si is also observed by EPD method.

5.1 Experimental Procedure: Measurements of TDDs by EPD Method

Prior to EPD measurements, Si capping layers grown on Ge epitaxial layers were removed because the Si capping layers are chemically stable, and thus prevent to visualize TDs in Ge by the solution used in EPD method. In order to remove Si capping layers without inducing any chemical/physical damage in Ge epitaxial layers, wet chemical etching by 2.38 % Tetramethylammonium hydroxide (TMAH, $[(CH_3)_4]^+[OH]^-$) was carried out at 80 °C. According to Ref. [112], using 2 % TMAH at 80 °C, etching rate of Si is 39 μm/h = 650 nm/min. It has been reported that etching rate of $Si_{1-x}Ge_x$ by TMAH decreases as the composition of Ge x increases [113]. In the present work, the etching rate of Si by 2.38 % TMAH (production name: NMD-3) at 80 °C was obtained for ~830 nm/min as shown in Fig. 5.1. Samples for EPD measurement were dipped into buffered-HF in order to remove native oxide on Si capping layers because SiO_2 is not etched by TMAH. Then, the samples were etched by 2.38 % TMAH for 5 min at 80 °C. During the removal process of Si capping layer, reduction of Ge thickness was not observed. Note that the etching rate of Si by TMAH decreases as TMAH become thicker, which easily happens during heating up. In the present work, densification of TMAH was avoided by putting teflon plate on a beaker used for the etching.

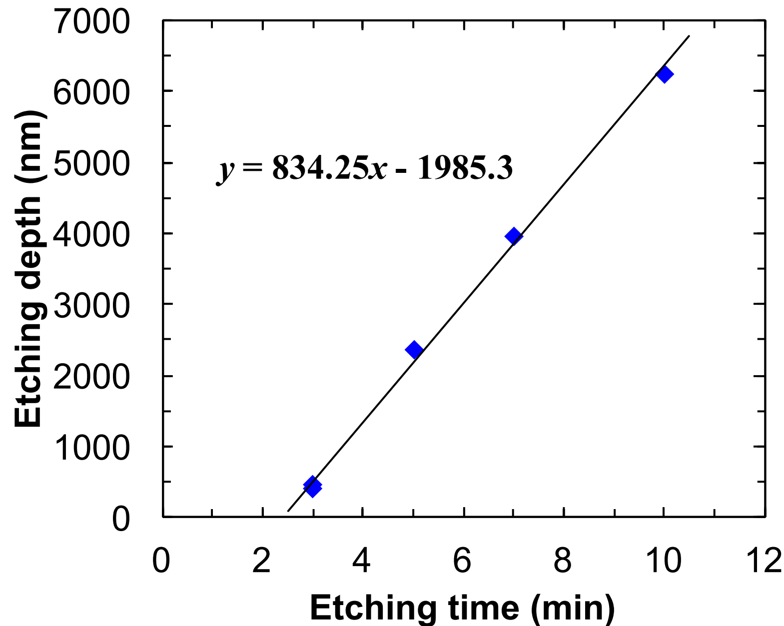

Figure 5.1: Si etching rate by 2.38 % TMAH (NMD-3) at 80 °C

After the removal of Si capping layers, TDDs in blanket/coalesced Ge layers were measured by EPD method. EPD method visualizes TDs appearing on top surfaces as small pits by preferential etching of Ge around the TDs, as schematically shown in Fig. 5.2. TDs in Ge layers were visualized by a wet chemical etching at room temperature using a mixture of CH_3COOH (67 ml), HNO_3 (20 ml), HF (10 ml), and I_2 (32 mg). The etching time was intended to be 5–7 sec. This mixture has been employed in EPD method and TDDs in Ge have successfully measured by the method [54, 89, 114]. Ge top surface away from TDs were etched by 200 nm on average in the etching process. Ge top surface around TDs were etched 100–150 nm deeper than Ge away from TDs. Note that the $CH_3COOH/HNO_3/HF/I_2$ solution gradually lose its oxidizability, and thus the solution should be renewed ideally for each sample.

The etched pits were observed by AFM since the diameter of pits are several hundreds nano meter, which is hard to observe by OM. The AFM observations were carried out in five different areas of 10 μm × 10 μm. As shown in Fig. 5.3, the obtained EPDs are equal to TDDs determined by plan-view transmission electron microscopy (TEM) observations, when the etching conditions above and AFM are employed [115]. Therefore, in this work, EPD is considered to be equal to TDD, i.e., EPD = TDD.

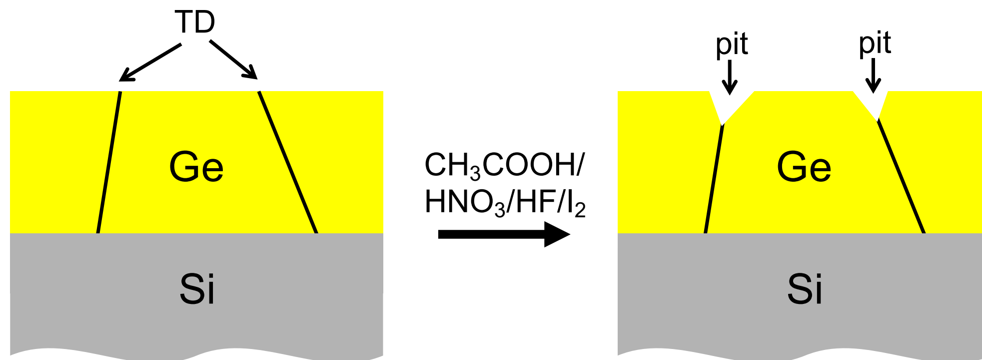

Figure 5.2: Schematic illustration of TDs visualization by $CH_3COOH/HNO_3/HF/I_2$ solution

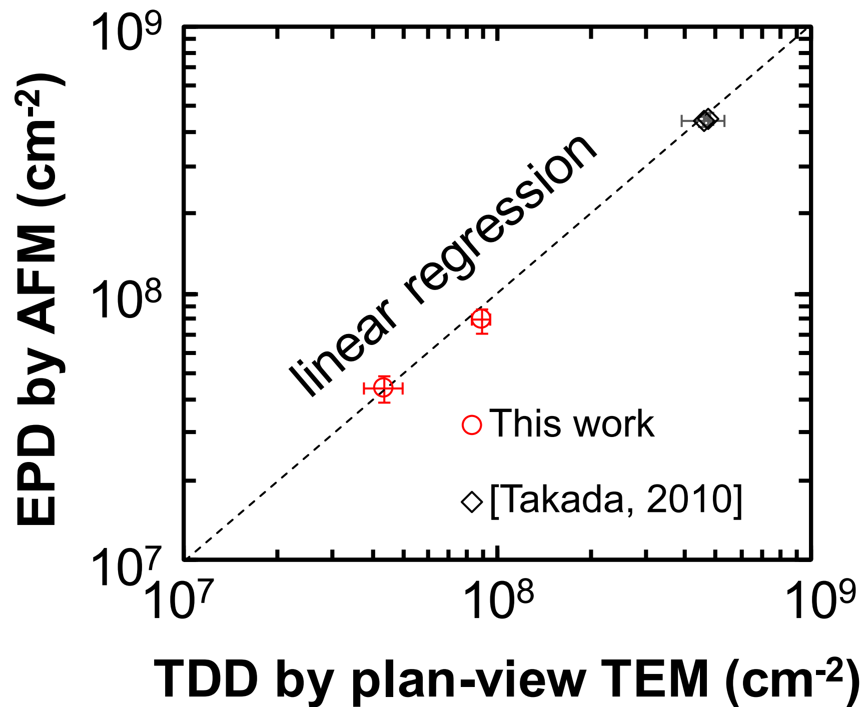

Figure 5.3: Correlation between EPD measured by AFM and TDD obtained by plan-view TDD. The data indicated as black opened diamonds are obtained from *Y. Takada, Master's thesis, The University of Tokyko, 2010*.

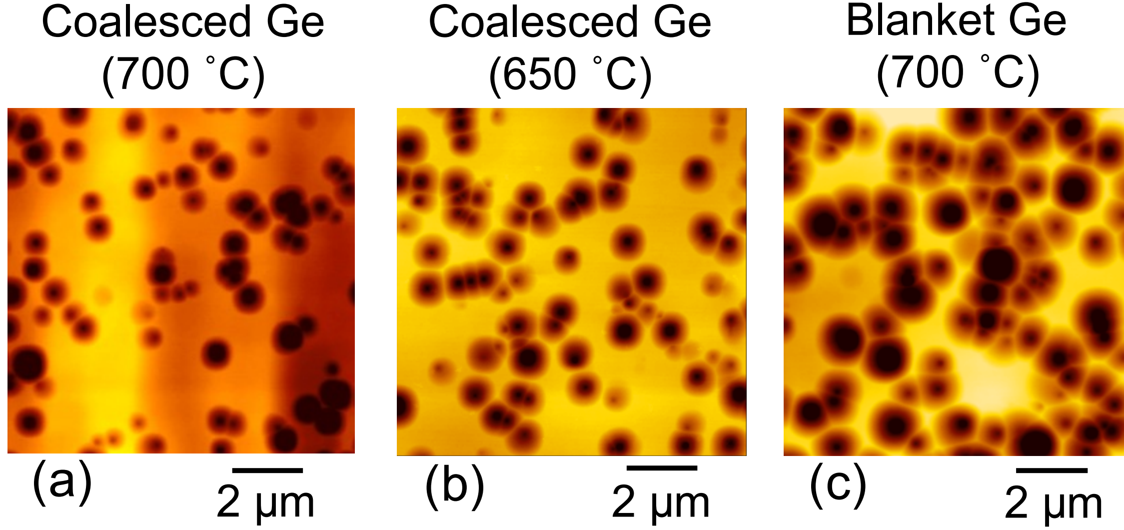

Figure 5.4: Typical AFM images of (a) coalesced Ge grown at 700 °C, (b) coalesced Ge grown at 650 °C, and (c) blanket Ge grown at 700 °C after wet etching for TDs visualization

Table 5.1: Cross-sectional structures and EPDs of Ge layers shown in Fig. 5.4

AFM image	W_{window} (μm)	W_{mask} (μm)	Ge thickness (μm)	Growth temp. (°C)	TDD (cm^2)
Fig. 5.4 (a)	0.66	0.44	1.15	700	6.5×10^7
Fig. 5.4 (b)	0.86	0.34	2.67	650	6.9×10^7
Fig. 5.4 (c)	blanket		1.89	700	8.1×10^7

5.2 Comparison of TDDs Between Experimental Results and Theoretical Calculation

5.2.1 TDDs in Coalesced SEG Ge Layers

Figure 5.4 shows typical AFM images of (a) coalesced Ge grown at 700 °C, (b) coalesced Ge grown at 650 °C, and (c) blanket Ge grown at 700 °C after the wet etching for TD visualization. Cross-sectional structures of the Ge layers, the thicknesses of Ge layers, growth temperature, and obtained TDDs are summarized in Table 5.1. Here, a notable results are obtained for the growth at 700 °C. The EPD results obtained for Ge grown at 700 °C indicate that the TDD in the coalesced Ge layer is smaller than that for the blanket Ge, although the coalesced Ge layer (1.15-μm-thick) is thinner than the blanket Ge layer (1.89-μm-thick).

According to the previous reports, [116, 117] TDD in a lattice-mismatched heteroepitaxial layer decreases as the thickness of the layers increases. Therefore, taking into account the thickness of Ge layers, the coalesced Ge (Fig. 5.4 (a)) shows significantly lower TDD than the

blanket Ge (Fig. 5.4 (c)). For a quantitative comparison between coalesced Ge and blanket Ge, the relation between TDD and Ge thickness should be clarified in order to compensate the difference of Ge thickness between blanket Ge and coalesced Ge.

5.2.2 Correlation Between TDDs and Layer Thickness for Blanket Ge Layers

As mentioned above, the relation between TDD and Ge thickness should be investigated in order to compare blanket Ge and coalesced Ge on a quantitative basis. Figure 5.5 shows TDDs in blanket Ge layers as a function of the layer thickness. It is obvious that the TDD decrease as the thickness increase, and the relation is empirically and approximately obtained depending on growth temperature as:

$$\rho_{blanket} = 2.52 \times 10^{13} \times (d\ [\mathrm{nm}])^{-1.57} \quad (\text{at } 530-650\ ^{\circ}\mathrm{C}) \tag{5.1a}$$

$$\rho_{blanket} = 2.67 \times 10^{12} \times (d\ [\mathrm{nm}])^{-1.37} \quad (\text{at } 700\ ^{\circ}\mathrm{C}) \tag{5.1b}$$

where $\rho_{blanket}$ is the TDD in blanket Ge, and d is the thickness of the Ge layer. The exponent indices of -1.57 and -1.37 agree with previous reports [116, 117] showing the exponent indices between -1 and -2. It is interestingly found that the relation between TDD and layer thickness is described by Eq. (5.1a) when the Ge layers are grown at 530–650 °C, while it is described by Eq. (5.1b) when the Ge layers are grown at 700 °C.

A possible reason for the difference of thickness-TDD relation between 650 °C and 700 °C is the movement of TDs in Ge epitaxial layers. As discussed in Ref. [11], the rearrangement of dislocations occurs when growth/annealing temperature is above 750 °C. Since the starting temperature for the rearrangement of dislocations has not been precisely investigated, it would be possible that the rearrangement of dislocations start to occur at 700 °C, resulting in reduction of TDDs. If the rearrangement of dislocations cause the difference of thickness-TDD relation, TDD should be reduced as the growth temperature increase in the range above 700 °C. However, it has not been investigated in this work because Ge growth above 700 °C is not allowed in our UHV-CVD machine.

5.2.3 Normalized TDDs vs. Theoretical Model

After taking into account the relation between layer thickness and TDD, the theoretical model and experimental results are able to be compared on a quantitative basis. The relation between normalized TDD and APR is shown in Fig. 5.6. The vertical axis is set to be normalized TDD defined as $\frac{\rho_{coalesced}}{\rho_{blanket}}$ in order to include the effect of layer thickness. The black solid line indicates the line regression, i.e., normalized TDD = APR. The blue solid line and the red solid line indicate calculated relation between TDD and APR in coalesced Ge originated from {113}-facetted SEG Ge and round-shaped SEG Ge, respectively. Experimental results are shown as blue triangles for Ge grown at 650 °C, and red diamonds for Ge grown at 700 °C. It is clearly shown that the experimentally obtained TDDs in Ge grown at 650 °C and 700

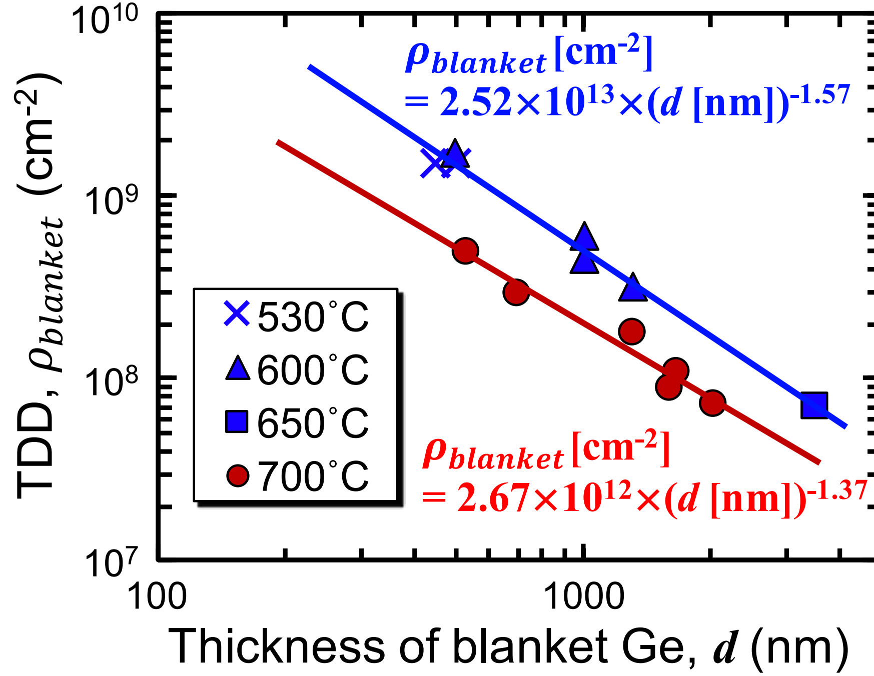

Figure 5.5: TDDs in blanket Ge layers as a function of the layer thickness

°C well correspond with calculated TDDs in coalesced Ge originated from {113}-facetted SEG Ge and round-shaped SEG Ge, respectively.

As shown in Fig. 4.7 (a) and Fig. 4.4 (a), SEG Ge layers grown at 650 °C have {113}-facetted cross-sectional structure, and SEG Ge layers grown at 700 °C have round-shaped cross-sectional structure. Therefore, the comparison between theoretical model and experimental results shown in Fig. 5.6 indicate that the experimentally obtained TDDs well reproduce the calculated effect of image force and coalescence, in terms of cross-sectional structure. Note that the SEG Ge grown at 650 °C shows wetting growth on SiO_2 masks, as shown in Fig. 4.7. Since coalesced Ge with complete wetting growth should show TDD reduced only by APR as shown in Fig. 3.7, TDDs in coalesced Ge grown at 650 °C should be between {113}-facetted case (blue solid line) and linear regression case (black solid line). The experimentally obtained TDDs in coalesced Ge grown at 650 °C is actually between the blue solid line and the black solid line. The difference between linear regression and {113}-facetted case become larger as APR become smaller. Thus, further reduction of APR will show the difference clearer. This will be an interesting future work. Table 5.2 shows a summary of the experimentally obtained TDDs, APR, Ge thickness, TDDs in blanket Ge of the same thickness $\rho_{blanket}$, and normalized TDDs ($\frac{\rho_{coalesced}}{\rho_{blanket}}$).

Table 5.2: Cross-sectional structures and TDDs in Ge layers shown in Fig. 5.6

Growth temp. (°C)	W_{window} (nm)	W_{mask} (nm)	d (nm)	$\rho_{coalesced}$ ($\times 10^7$cm^2)	$\rho_{blanket}$ ($\times 10^7$cm^2)	Normalized TDD
650	820	160	2840	8.1 ± 1.1	9.9	0.82 ± 0.11
	860	340	2670	7.2 ± 1.3	11.2	0.64 ± 0.12
	810	590	2360	6.6 ± 1.3	13.2	0.50 ± 0.10
	1070	110	2720	9.8 ± 1.9	10.5	0.93 ± 0.18
	1080	300	2450	9.3 ± 1.2	12.4	0.75 ± 0.10
	1050	530	2200	8.7 ± 1.2	14.7	0.59 ± 0.08
	1330	80	2600	9.7 ± 1.3	11.3	0.86 ± 0.11
	1250	340	2270	9.6 ± 1.5	14.0	0.68 ± 0.11
	blanket		3490	7.0 ± 0.8	7.1	0.98 ± 0.12
700	660	440	1150	4.4 ± 0.5	17.1	0.26 ± 0.03
	830	110	1250	6.2 ± 0.7	15.3	0.41 ± 0.04
	830	450	1150	4.6 ± 0.5	17.1	0.27 ± 0.03
	1050	110	1160	7.3 ± 0.6	16.9	0.43 ± 0.03
	1090	400	1120	5.5 ± 0.3	17.7	0.31 ± 0.02
	1100	110	1300	7.3 ± 0.3	14.5	0.51 ± 0.02
	110	440	1070	5.3 ± 0.4	18.9	0.28 ± 0.02
	blanket		1890	7.9 ± 0.8	8.7	0.91 ± 0.09

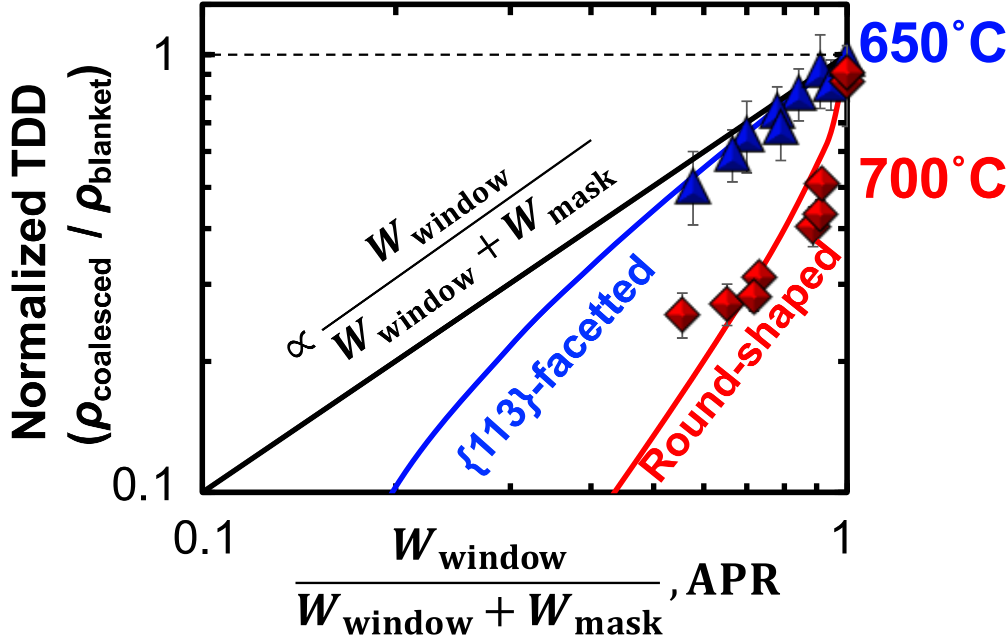

Figure 5.6: TDDs in coalesced Ge layers as a function of the layer thickness

5.3 Distribution of TDs in Coalesced Ge

In addition to the reduction of TDDs, characteristic distribution of TDs in coalesced Ge is predicted by the theoretical model as well. More specifically, TDs in SEG Ge would be bent to be away from the center of Si seed area, where $W_{window} = 0$, as schematically shown in Fig. 3.3, and thus TDs in coalesced Ge would tend to be located above SiO_2 masks, as schematically shown in Fig. 3.6.

On the coalesced Ge layers with flat-top surfaces, however, it is difficult to recognize where the SEG masks lay underneath, as shown by plan-view OM image in Fig. 4.8 (d). In order to observe the correlation between distribution of TDs and the location of SEG masks, TD observation was carried out in coalesced Ge with non-flat-top surface grown at 700 °C (indicated as green triangles in Fig. 4.8 (a)) by EPD method. Figure 5.7 shows a 10 μm × 10 μm bird's eye view AFM image on non-flat-top coalesced Ge. W_{window} and W_{mask} are designed to be 1.0 μm and 0.7 μm, respectively. It is shown that TDs concentrate on the "valley" area, where above SEG masks. From the AFM image, TD densities are obtained as 7.5×10^7 cm^{-2} for the Ge top surface above Si seeds, and 1.3×10^8 cm^{-2} for the Ge top surface above SEG masks. Such distribution of TDs, TD accumulation above the SiO_2 masks, corresponds to the prediction given by the theoretical model. Thus, the observation result of TD dislocation is also a supporting material for the theoretical model.

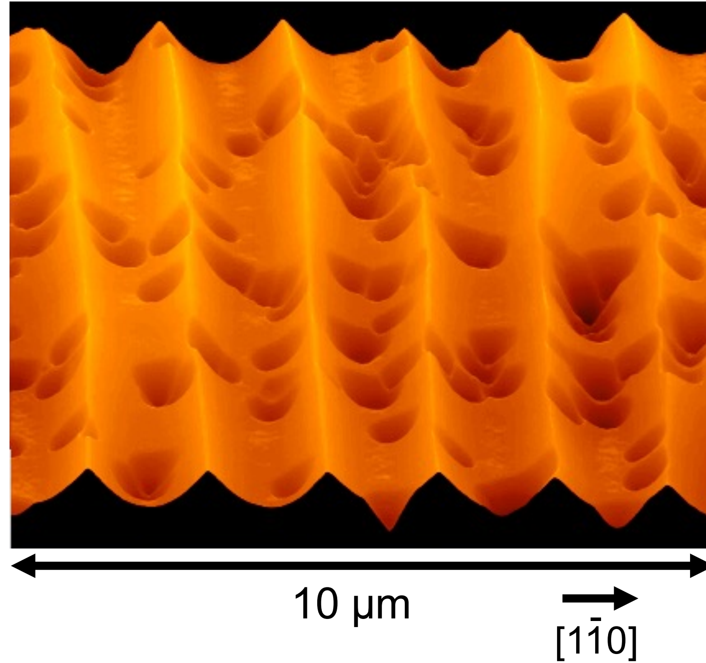

Figure 5.7: A 10 μm × 10 μm bird's eye view AFM image on non-flat-top coalesced Ge (W_{window} = 1.0 μm and W_{mask} = 0.7 μm in design) after wet chemical etching for TD visualization

5.4 Discussions

5.4.1 Absence of "TDD Re-Increase" in Coalesced Ge

In previous reports on ART, generation of TDs when SEG Ge layers coalesce has been reported when SEG Ge layers coalesce [78, 97, 118], and "TDD re-increase" has been observed as the result of the generation of TDs [80]. In this work, on the other hand, such "TDD re-increase" was not observed. The comparison between ART work and this work is shown in Fig. 5.8 in terms of TDD re-increase. The blue triangles and red diamonds are normalized TDDs obtained in this work (same data as Fig. 5.6), and the black dots are normalized TDDs in an ART work (data obtained from [80]). The solid lines are calculated TDD for the data obtained in this work (red and blue lines), and eye-guide line for ART work (black line). The coalesced Ge in ART shows normalized TDD larger by a factor of more than 10. The increase of normalized TDD in the ART work indicates the "TDD re-increase" as described above. In this work, on the other hand, no TDD re-increase is shown for both 650 °C and 700 °C.

In ART works, it has been considered that atomic-scale crystalline misorientations would be generated between the adjacent Ge SEG layers grown from the bottom of trench regions as deep as 100 nm or larger, leading to an increase of TDDs in the coalescence process [118, 119]. Absence of TDD re-increase in this work would be related to the presence of voids formed on the SEG masks. The coalescence of SEG Ge layers takes place above the voids. The

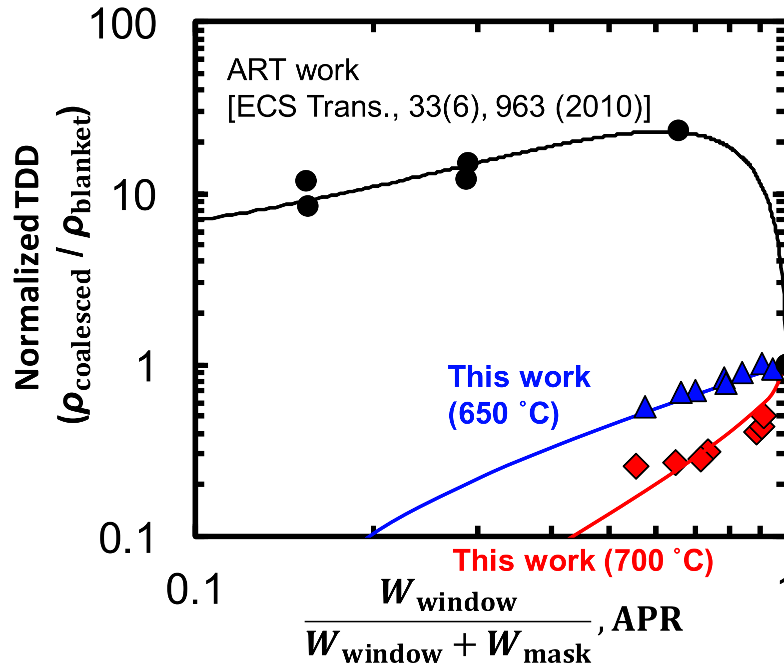

Figure 5.8: Comparison between ART work (J. G. Fiorenza, *et al.*, 2010) and this work in terms of TDD re-increase

misorientation between the adjacent Ge SEG layers could be compensated if atomic re-arrangements occur to prevent the generation of coalescence defects. If this is the case, TDDs could be reduced even in the case of ART when voids are formed on the mask surfaces. In fact, it has been briefly reported that coalescence of SEG Ge layers takes place without generation of TD when there are voids on SEG masks [101], supporting the hypothesis. However, the previous report [101] just showed the absence of generation of TD, but not discussion had been made.

The other possible reason is the use of thin SiO_2 layers as SEG masks from the fabrication point of view. The SEG mask patterns were fabricated through a wet chemical etching process, where the sidewall roughness should be smaller than that for the deep trench formation in ART employing a dry etching process. Growth of Ge with touching rough SiO_2 sidewalls could induce atomic-scale crystal misorientation in SEG Ge layers, leading generation of TDs when the SEG Ge layers with misorientation coalesce each other.

This point will be discussed in the later part being accompanied by TEM observation results.

5.4.2 Comparison with Other TDD Reduction Methods

As described in section 2.4, conventional methods for TDD reduction have drawbacks in terms of light-emitting device applications. However, the TDD reduction induced by image

force and coalescence of SEG Ge layers is free from the drawbacks.

- (a) Since no post-growth annealing process is employed, Ge epitaxial layers are free from intermixing of Si and Ge, or out-diffusion of dopants.
- (b) As shown in Fig. 4.8 (c), there are ∼150-nm-high voids near the bottom Ge/Si interfaces. Thanks to the voids, as will be shown in Fig. 7.9 (a), light is well confined in the Ge active layer.
- (c) On the other hand, since the voids are only ∼150-nm-high, light coupling from Ge to bass Si waveguides should be easier than ART and Ge on Si pillar cases, which induce ∼ μm-thick optical isolation.
- (d) In addition to that, Fig. 5.8 reveals that there is one more advantage over ART method; absence of TDD re-increase.

In these respects, the proposed and verified TDD reduction method is preferable to light-emitting device applications.

5.4.3 Toward Further Reduction of TDD

In the present study, the coalescence-induced TDD reduction can be verified experimentally in the case of APR > 0.5. Further reduction of APR, corresponding to $W_{window} \ll W_{mask}$, should leads further reduction of TDD according to the theoretical model. The acceptable maximum of W_{mask} is determined by the duration of Ge growth in view of conduct of experiment. Increase of GeH_4 partial pressure is not preferable because it will promote Ge wetting growth on SiO_2 masks [98]. Although smaller W_{window} was not performed here (the minimum W_{window} of 0.5 μm in design), further shrinkage of W_{window} as small as 0.1 μm will be possible when the condition of EB lithography is well optimized. According to Fig. 3.8, TDDs theoretically become smaller than $\rho_{blanket} \times 10^{-2}$, on the order of 10^6 cm^2 assuming $\rho_{blanket}$ of 1×10^9 cm^2, in the case of APR < 0.11. It is notable that the TDD reduction on the order of 10^6 cm^2 will be achieved in coalesced Ge originated from both {113}-facetted SEG Ge and round-shaped SEG Ge. This suggests that the cross-sectional structure is not very important when APR is as small as 0.1, but APR itself and suppression of Ge growth on SiO_2 will be dominant factor to reduce TDDs.

There are two ways to reduce APR: reduction of W_{window} and enlargement of W_{mask}. The minimum limit of W_{window} is determined by resolution of lithography, and the maximum limit of W_{mask} is determined by acceptable growth time. Figure 5.9 shows the thickness of blanket Ge when SEG Ge layers coalesce as a function of W_{window} and W_{mask} at 700 °C. In the case for present study, 2 μm is the upper limit for the thickness of blanket Ge grown at 700 °C.

W_{window} (nm)

W_{mask} (nm)	100	200	300	400	500	600	700	800	900	1000
500	455	531	606	697	796	899	994	1092	1204	1322
1000	834	910	986	1090	1213	1343	1458	1577	1726	1886
1500	1213	1289	1365	1484	1631	1787	1922	2062	2247	2450
2000	1593	1669	1745	1878	2048	2230	2385	2547	2769	3014
2500	1972	2048	2124	2271	2465	2674	2849	3033	3290	3578
3000	2352	2427	2503	2665	2883	3118	3313	3518	3812	4142
3500	2731	2807	2883	3059	3300	3562	3776	4003	4334	4706
4000	3110	3186	3262	3452	3717	4006	4240	4488	4855	5270
4500	3490	3566	3641	3846	4135	4450	4704	4974	5377	5833
5000	3869	3945	4021	4240	4552	4894	5167	5459	5899	6397

Figure 5.9: The thickness of blanket Ge when SEG Ge layers coalesce as a function of W_{window} and W_{mask} at 700 °C

The black solid line in Fig. 5.9 indicates where the thickness of blanket Ge = 2 μm. Thus, W_{window} narrower than 200 nm is required to fabricate SiO_2 masks with APR ≤ 0.1.

In order to fabricate SiO_2 masks with APR ≤ 0.1, an i-line stepper (photolithography with reduction projection lens) was attempted as well as EB lithography. Figure 5.10 shows schematic illustration of (a) EB lithography system and (b) i-line stepper. An i-line stepper with 5x reduction optical system and a reticle with 1-μm-wide line-shaped windows were employed to fabricate SiO_2 masks with W_{window} of 200 nm wide. Exposure time was varied from 200 msec to 520 msec in order to find a suitable exposure time for 200-nm-wide line. Shorter exposure time brings narrower W_{window}, and longer exposure time brings wider W_{window}. Process conditions are summarized in Table 5.3.

Figure 5.11 shows top-view SEM images of SiO_2 masks with (a) continuous lines and (b) intermittent lines. Whitish areas are where Si substrate is covered by SiO_2, and blackish areas are where Si substrate is exposed. It is shown that continuous lines were successfully fabricated when exposure was such strong that W_{window} becomes 500 nm, as shown in Fig. 5.11 (a). However, the SiO_2 mask becomes intermittent lines where the exposure was such weak that W_{window} becomes 400 nm, as shown in Fig. 5.11 (b). Since i-line (λ = 365 nm) was used for exposure, the W_{window} as narrow as 400 nm would be strongly affected by interference.

In addition, it is notable that the in-plane uniformity is more critical than exposure time:

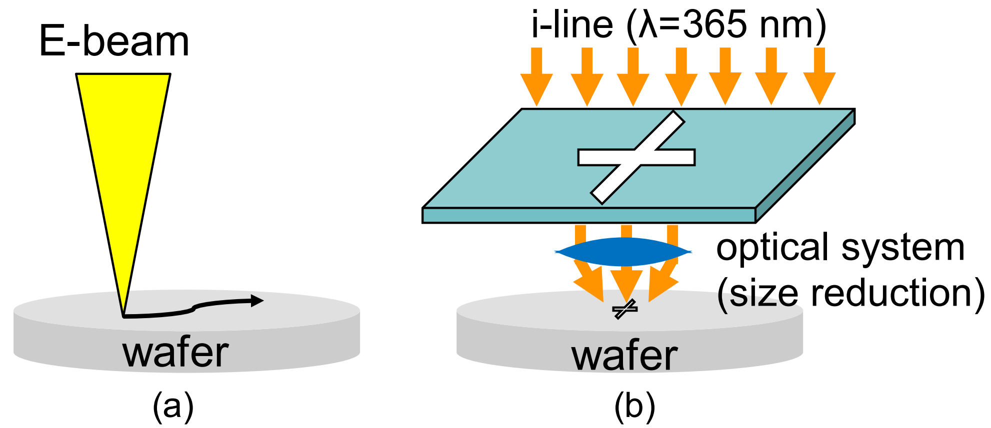

Figure 5.10: Schematic illustrations of (a) EB lithography system and (b) i-line stepper (photolithography with reduction projection lens)

Table 5.3: Process conditions for photoresist coating, lithography, and development.

Process	Temperature	Time	Note
Surface cleaning	Room temp.	–	Dip into piranha solution and blow by N_2 gas
OAP coating	Room temp.	5 → 50 sec	Spin 50 → 3000 rpm
ip-3100 coating	Room temp.	8 → 5 → 25 sec	Spin 200 → 500 → 5000 rpm
Exposure	Room temp.	400–520 msec	Dose: 100 mJ/cm^2 at 200 msec
Post-exposure bake	110 °C	90 sec	
Development	Room temp.	–	Fully automated
Post-development bake	110 °C	5 min	
Ashing	Room temp.	90 sec	To make sharp edges

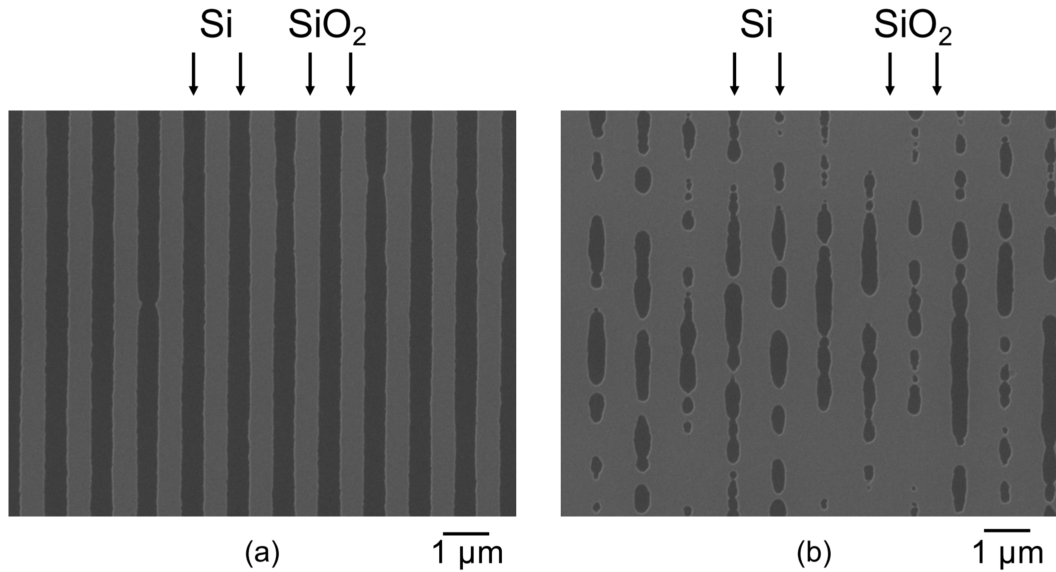

Figure 5.11: Top-view SEM images of SiO_2 masks with (a) continuous lines and (b) intermittent lines. Exposure time was 470 msec for both of (a) and (b).

exposure time was 470 msec for both Figs. 5.11(a) and (b). Such in-plane un-uniformity would be ascribed to the un-uniformity of the thickness of photoresist.

Since it is difficult to reduce APR simply optimizing the conditions of lithography, here I would like to propose processes to make SEG masks with small APR by converting W_{window} and W_{mask}. Figure 5.12 shows schematic illustrations showing two processes to convert W_{window} and W_{mask}.

Figures 5.12 (a)–(c) show conversion of W_{window} and W_{mask} employing lift-off process. First make line-and-space shaped photoresist employing EB lithography or photolithography (Fig. 5.12 (a)), and then deposit SiO_2 over the photoresist (Fig. 5.12 (b)). By removing the photoresist together with SiO_2 deposited on the photoresist (lift-off), Si substrate is exposed only where the photoresist located (Fig. 5.12 (c)). The finally determined W_{window} depends on the width of the photoresist, which can be easily reduced by over dose during the lithography using positive photoresist. Note that photoresist should be stand, i.e., aspect ratio should be small enough not to collapse. Considering lift-off process, physical vapor deposition (PVD) such as sputtering is preferable to deposit SiO_2 compared to CVD because SiO_2 is deposited on sidewalls when CVD is employed.

Figures 5.12 (d)–(f) show conversion of W_{window} and W_{mask} employing local oxidation of Si (LOCOS) process. First line-and-space shaped SiN_x masks employing EB lithography and dry/wet etching process (Fig. 5.12 (d)). Formation of thin pad SiO_2 layer is preferable to

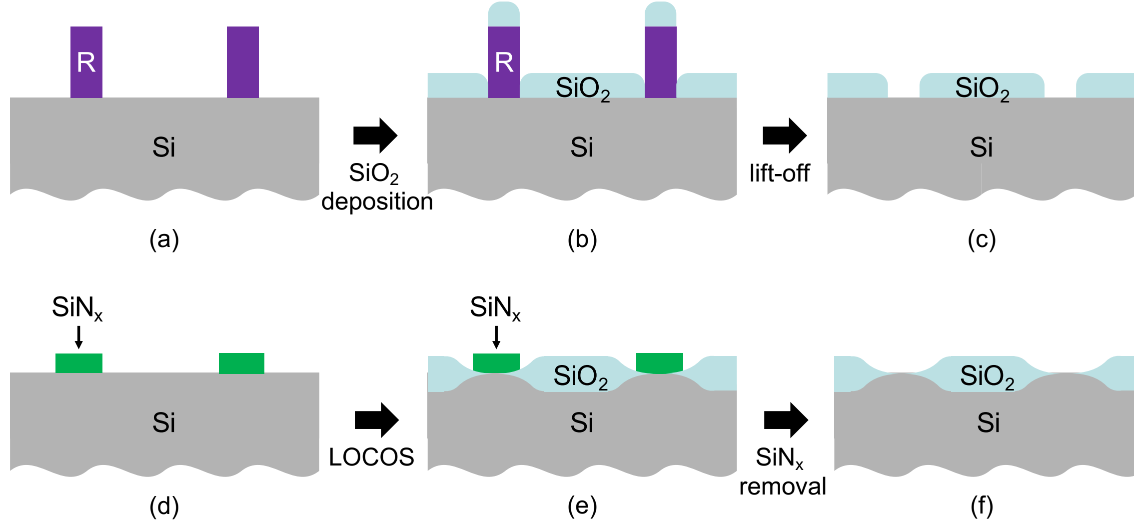

Figure 5.12: Schematic illustration showing conversion of W_{window} and W_{mask} employing (a)–(c) lift-off process and (d)–(f) LOCOS process

avoid strain accumulation at the Si under the SiN_x masks. When Si substrate with SiN_x masks are thermally oxidized, thermal oxidation occurs only where Si substrate is exposed, but not where SiN_x masks located (Fig. 5.12 (e)). By removing the SiN_x masks using phosphoric acid at high temperature, Si growth seed appears where SiN_x masks located (Fig. 5.12 (f)). The finally determined W_{window} depends on the width of the SiN_x masks, and thus it can be reduced by over dose during EB lithography using positive photoresist.

In addition to the reduction of APR as described above, note that combinations with post-growth annealing at high temperatures [54] and/or narrowing of SEG windows on the order of 10 nm [120] would be also effective to reduce TDDs. I.e., the image-force-induced TDD reduction method is compatible with other conventional TDD reduction method.

6 TEM Observations of TDs in Coalesced Ge

According to the theoretical model, it is predicted that the reduction of TDDs shown in previous section would be ascribed to bending of TDs in SEG/coalesced Ge layers resulting in termination of TDs at voids. In this chapter, cross-sectional/plan-view TEM observation results of SEG Ge, coalesced Ge, and blanket Ge layers are described in order to verify the theoretical model in terms of trajectories of TDs. In addition to that, unique behaviors of TDs are observed in coalesced Ge, and the mechanism of the unique behaviors are discussed in later part of this chapter.

6.1 Experimental Procedure: TEM Observations

TEM specimens from SEG Ge layers were fabricated employing Ar ion milling. Ar ion was injected from top surface to bottom surface of the SEG Ge layers. The thickness of the TEM specimens are not exactly obtained, but should be on the order of 100 nm because dislocations in Ge epitaxial layers could be observed under the acceleration voltage of 200 kV. Thermosetting resin layers were formed on the top surfaces of SEG Ge layers in order to protect the SEG Ge layers.

TEM specimens from coalesced/blanket Ge layers were picked up from target areas using focused Ga ion beam (FIB micro sampling method), and then polished in an ion milling system using Ar ion. TEM specimens with the thicknesses of 150–500 nm were prepared for observations on (110) cross-section, which is the cross-section perpendicular to both SEG masks and growth surfaces (schematically shown in Fig. 6.1 (a)). For plan-view observation, TEM specimens of 200 nm thick were prepared (schematically shown in Fig. 6.1 (b)). The thicknesses of the TEM specimens were given by SEM observations during FIB micro sampling. In particular, top 200 nm of the Ge layers were observed by plan-view TEM: top surfaces of the Ge layers were protected by amorphous layers, and then thinned down from the bottom (substrate) side of the Ge layers.

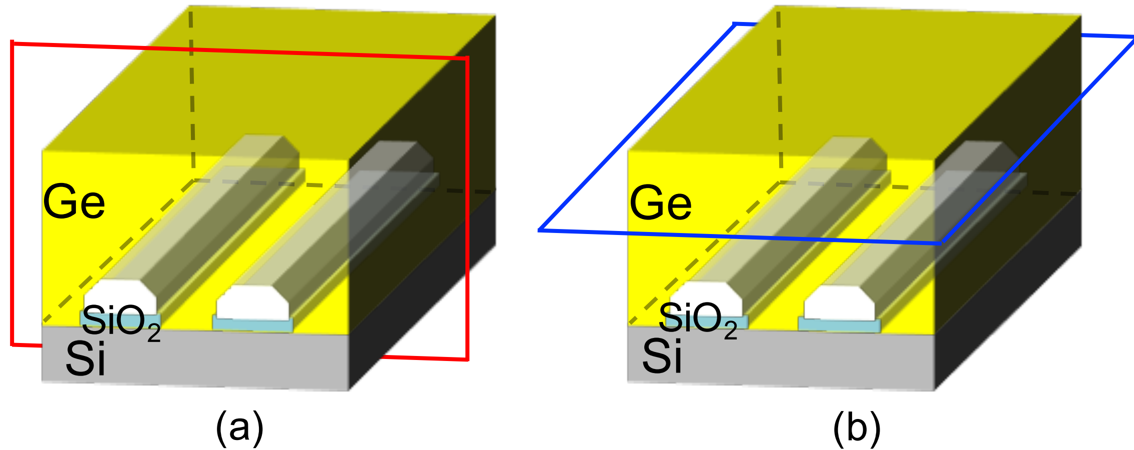

Figure 6.1: Schematic illustrations of TEM specimens for (a) cross-sectional and (b) plan-view TEM observations.

Cross-sectional and plan-view TEM observations were carried out using a JEM-2010HC (JEOL, Japan). Cross-sectional bright-field STEM observations were carried out to observe the thick (500 nm) TEM specimens. Acceleration voltage of 200 kV was employed for all TEM and STEM observations.

6.2 Cross-Sectional TEM Observations

6.2.1 TDs in SEG Ge; before coalescence

Figures 6.2 (a)–(c) show bright-field (110) cross-sectional TEM images of blanket/SEG Ge layers grown at 600 °C. Figure 6.2 (a) shows a TEM image taken for a blanket Ge (planar growth) of 1.4-μm-thick. A dislocation in [001] direction, i.e., vertical to the (001) growth surface, is observed. Figures 6.2 (b) and (c) show the side edges of SEG Ge layers. The SEG Ge layers are surrounded by {113} and {111} facets because of relatively low (600 °C) growth temperature.

In the SEG Ge layers, TDs normal to the non-planer surfaces ({113} and {111} facets) are observed, which are not observed in the planer Ge growth (Fig. 6.2 (a)). Traces of the TEM images are shown in Figs. 6.2 (d)–(f), showing the TDs as red lines. Figures 6.2 (d), (e) and (f) correspond to traces for Figs. 6.2 (a), (b) and (c), respectively. It is clearly shown that the TDs are bent to be normal to the growth surfaces, (001) in Figs. 6.2 (a) and (d), (113) in Figs. 6.2 (b) and (e), and (111) in Figs. 6.2 (c) and (f). This behavior of TDs agree with the prediction given in chapter 3 considering image-force-induced TD bending, and thus the obtained TEM results support the theoretical model.

At the edges of the SEG Ge layers, i.e., in Figs. 6.2 (b) and (c), it is shown that Ge (blackish

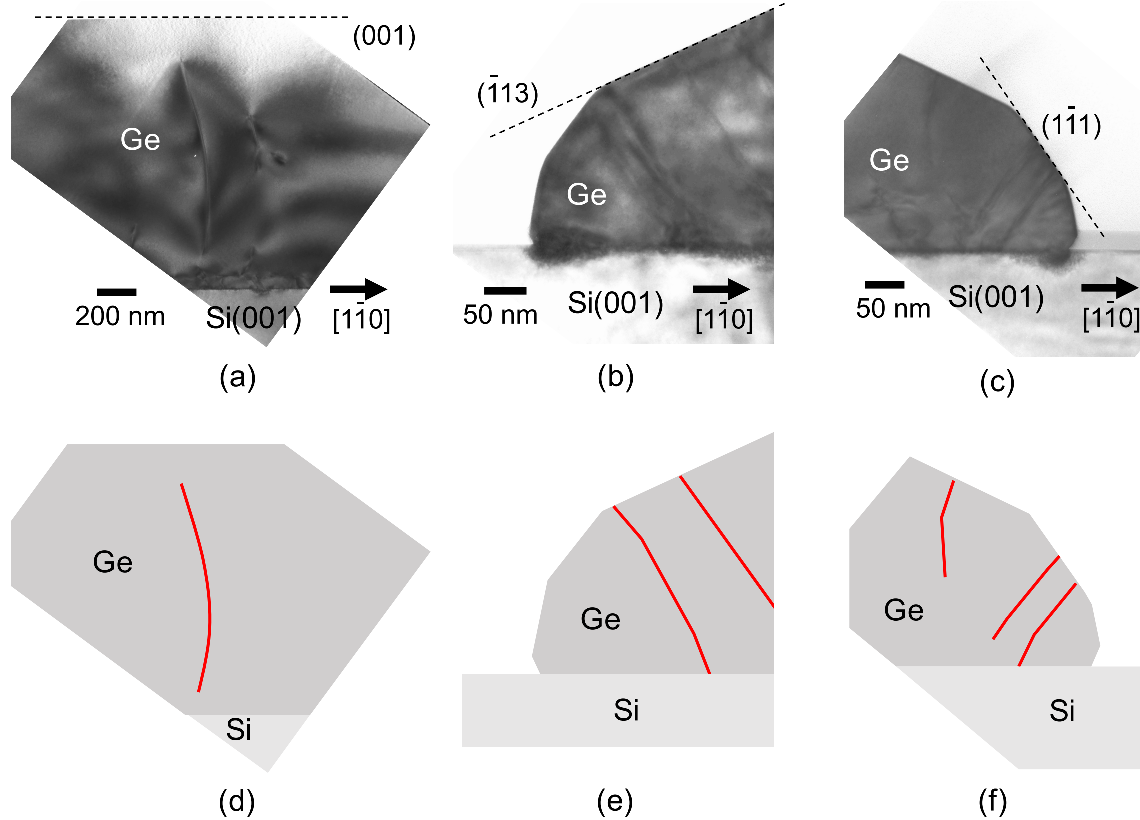

Figure 6.2: (a)–(c) Bright-field (110) cross-sectional TEM images of Ge selective epitaxial layers and (d)–(f) their schematic traces: (d), (e), and (f) correspond to (a), (b), and (c), respectively.

area) diffuse into Si substrate. This would be ascribed to accumulation of strain at the SEG edges.

6.2.2 TDs in coalesced SEG Ge

Figure 6.3 (a) shows a bright-field (110) cross-sectional TEM image of a coalesced Ge layer grown at 700 °C, where W_{window} = 0.66 μm and W_{mask} = 0.44 μm. A 1.3-μm-thick coalesced Ge layer was observed showing voids located over the SiO_2 masks. It should be marked here that there is no TD, which is usually propagating through the Ge layer in the vertical direction, i.e., from the Ge/Si interfaces at the bottom to the top surface. Considering the thickness of the TEM specimen (150 nm) and the width of the observed area (7 μm), the absence of TD in Fig. 6.3 (a) correspond to the TDD lower than 1 / (150 nm × 7 μm) = 1×10^8 cm^{-2}. In addition to that, there are two defects above the voids as pointed by white arrows in Fig. 6.3 (a). These defects are seen as black dots, which indicate that the defects are perpendicular to the paper/display direction, i.e., the [110] direction here. The defects in the [110] direction are observed in plan-view TEM images as well, as will be shown in later section.

A defect, which is bent and terminated on a surface of a semicylindrical void, was observed

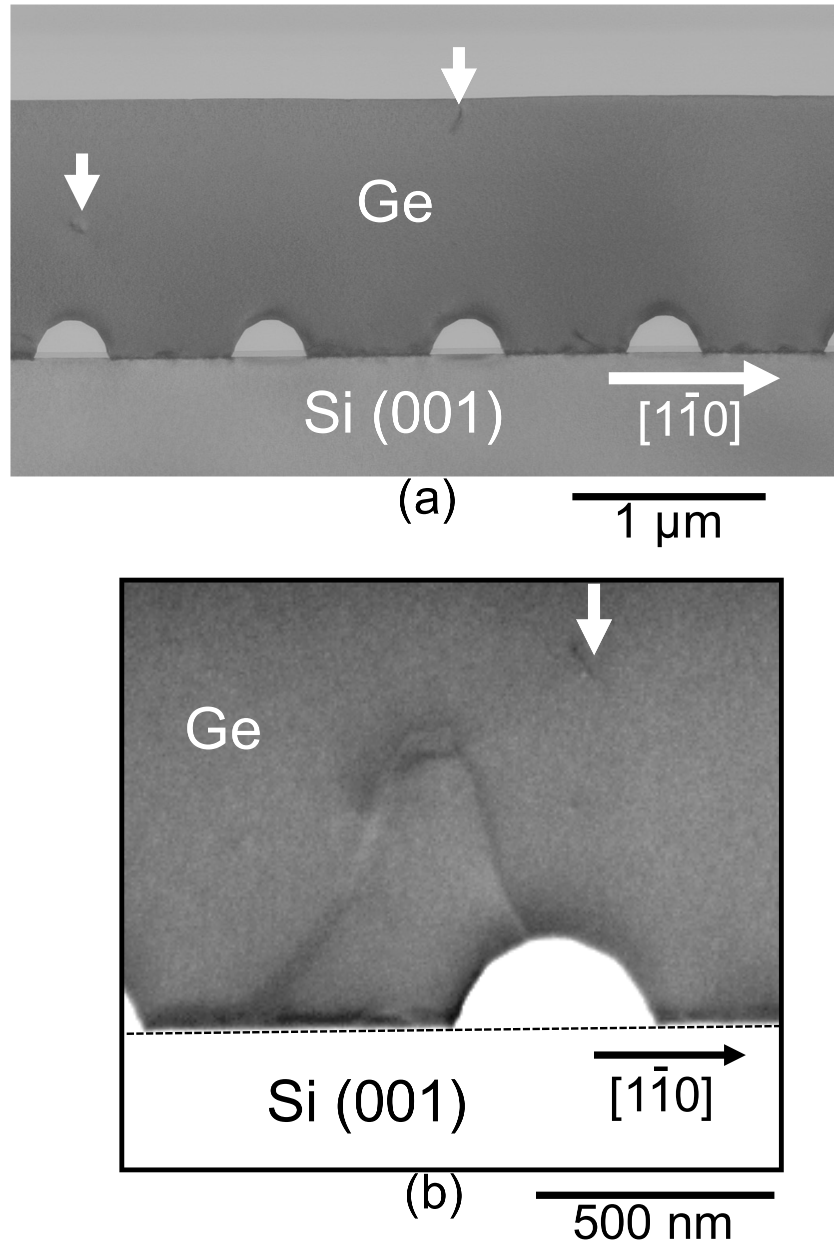

Figure 6.3: (a) A cross-sectional bright-field TEM image of coalesced Ge and (b) a cross-sectional bright-field STEM image of a TD terminated by a void.

in a 500-nm-thick specimen using bright-field cross-sectional STEM (Fig. 6.3 (b)). Such a thick specimen was prepared because of low density of dislocations in the coalesced Ge layers as shown in Fig. 6.3 (a). The dislocation is a very example of a TD that we predicted in the theoretical model on a qualitative basis. The observed trajectory of TD is, however, not exactly same as the calculated TD behavior shown in Fig. 3.4. The difference between the calculated trajectory and experimentally observed one would be related to the TD transformation to other type of dislocation to minimize the energy after the growth, such as cooling process from growth temperature to room temperature. Tensile strain is accumulated in the Ge layer on Si due to the mismatch of thermal expansion coefficient between Ge and Si [45], and there should be relaxation of tensile strain at the sub-surface layer of the voids, which would motivate TDs to glide. The strain and its accumulation in coalesced Ge layers will be described in later section. There is also a dislocation in the [110] direction above a void, as pointed by the white arrow in Fig. 6.3 (b).

A different type of defect was observed in the bright-field cross-sectional STEM, as shown in Fig. 6.4 (a). This defect seems not the one predicted in Fig. 3.4 but the one generated when the SEG Ge layers coalesce. In previous reports, it has been reported that two-dimensional (2D) defects such as stacking faults and twins are generated when SEG Ge layers coalesce. [80, 94–97, 118] However, the defect shown in Fig. 6.4 (a) is a dislocation but not a 2D defect because of its curved trajectory. One more type of dislocation was observed near the void as shown in the bright-field cross-sectional TEM image of Fig. 6.4 (b). The defect would be generated at the voids, although the generation point would be removed during the preparation of the TEM specimen. Thus, the defect would be generated at the surface of the void and propagates to the top surface. The defect in Fig. 6.4 (b) is close to be straight, but not on the {111} plane. In order to verify the defect in Fig. 6.4 (b) is whether a dislocation or a 2D defect, an electron diffraction pattern was obtained near the defect in Fig. 6.4 (b) as shown in Fig. 6.4 (c). In Fig. 6.4 (c), no streak pattern is present, which indicates that there should be no 2D structure and that the defect is a dislocation. This is against the previous reports showing 2D defects at the coalescence part. [80, 94–97, 118] The absence of 2D defects in the cross-sectional TEM supports our prediction that the free surfaces of the voids contribute to the strain release otherwise ending with the misorientations between SEG Ge layers. This is consistent with a previous report suggesting no 2D defects for the SEG Ge with voids on the SiO_2 masks. [101]

6.3 Plan-View TEM Observations

Figures 6.5 (a) and (b) show bright-field plan-view TEM images of a coalesced Ge layer (W_{window} = 0.82 μm, W_{mask} = 0.68 μm) and a blanket Ge layer, respectively, grown on the

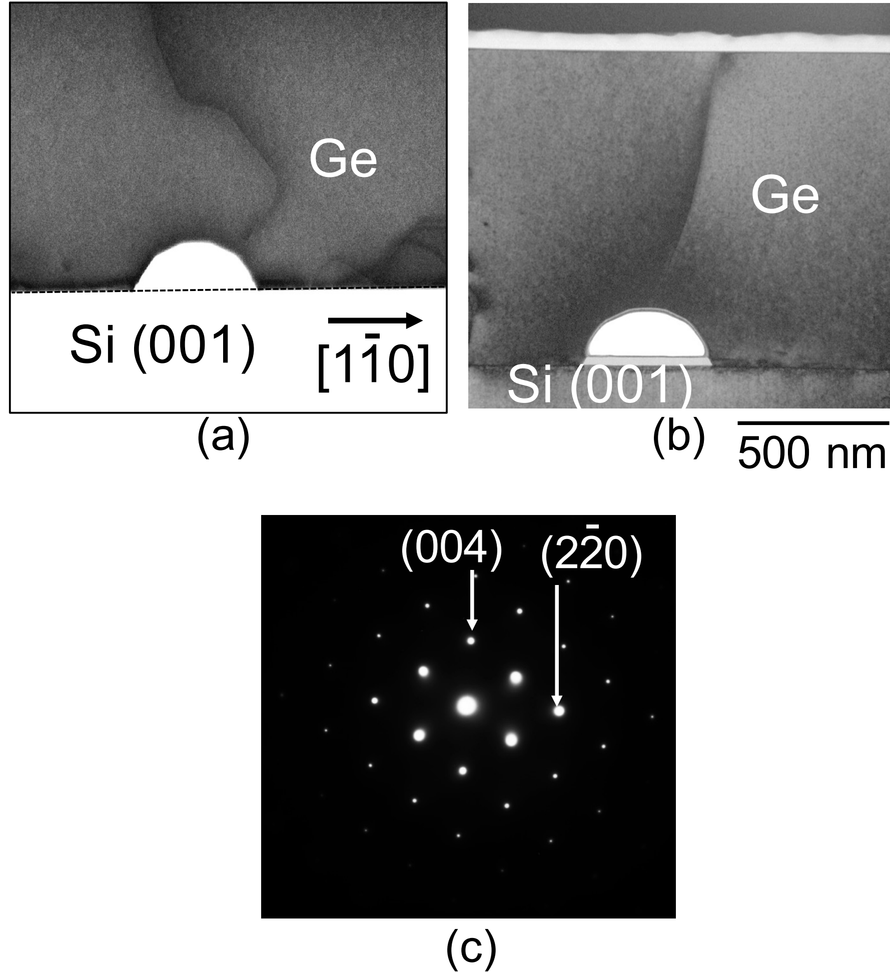

Figure 6.4: Examples of bright-field (110) cross-sectional (a) STEM and (b) TEM images showing TDs around semicylindrical voids with incident electron beam slightly tilted from the [110] zone axis, and (c) an electron diffraction pattern obtained around TD seen at the center of (b).

same wafer at 700 °C. Both TEM images were taken for the top 200 nm regions of Ge layers as indicated by black dashed squares in the schematic cross-sectional illustration at the top of Fig. 6.5. The coalesced Ge in Fig. 6.5 (a) was grown over the SiO_2 mask stripes aligned to the [110] direction. The plan-view TEM image in Fig. 6.5 (a) was taken for a 5 μm × 5 μm area. Since one pair of a SiO_2 mask and a Ge growth window is 1.5 μm, Although it is difficult to recognize SEG masks laying underneath, there should be more than three SiO_2 masks and three Si window areas in the TEM image. Despite of the possible non-uniformity in the window width for the growth, the Ge epitaxial layer is quite uniform near the top surface after the coalescence. In other words, the Ge epitaxial layers over the SiO_2 masks and Si windows are difficult to distinguish in the TEM image. It is found that TDDs obtained from Figs. 6.5

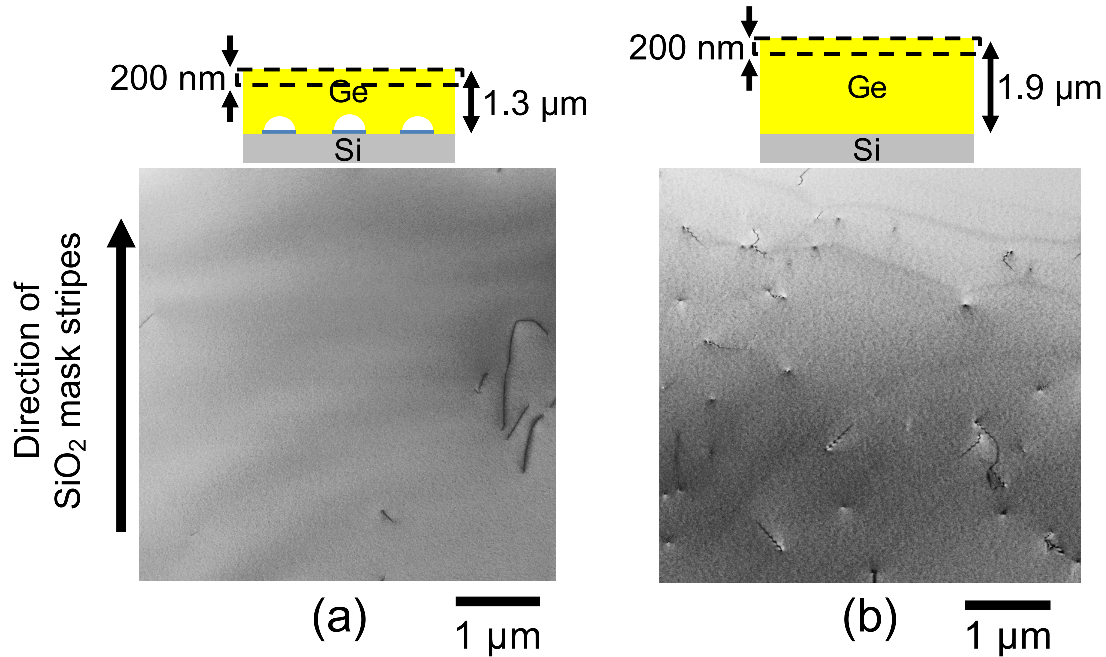

Figure 6.5: Examples of bright-field (001) plan-view TEM images taken for (a) coalesced Ge layer and (b) blanket Ge layer. Top 200 nm of the Ge layers are observed as schematically shown by black dashed squares. The electron beam is slightly tilted from the [001] zone axis.

(a) and (b) are 3.2×10^7 cm^{-2} and 1.1×10^8 cm^{-2}, respectively. As described in previous section, EPD measurements reveal that TDD in the coalesced Ge layer ($W_{window} = 0.82$ μm, $W_{mask} = 0.68$ μm) is 4×10^7 cm^{-2}. Thus, TDD in Fig. 6.5 (a) shows a good agreement with the EPD result. It is also notable that neither EPD measurements nor TEM observations show TDD re-increase reported in the ART work [80]. This suggests that the existence of voids on SEG masks is effective to suppress TDD re-increase. It should be remarked that a large (4 μm $\times$ 4 μm) TD-free area is realized, as shown in Fig. 6.5 (a). Compared to the blanket Ge shown in Fig. 6.5 (b), which shows TDs with a relatively uniform distribution, the coalesced Ge has high and low TDD areas. This ununiformity of TDD in coalesced Ge suggests that there would be further room of improvements in the coalesced Ge, which would be influenced by uncontrolled parameters.

Comparing Fig. 6.5 (a) with Fig. 6.5 (b), it is obvious that the lengths of the defect lines in Fig. 6.5 (a) are longer than those in Fig. 6.5 (b). The defect lines in Fig. 6.5 (a) are typically 1 μm long in the [110] direction, i.e., parallel to the SiO_2 masks. There are two possible explanation for defects showing the long lines; (i) 2D defects and (ii) dislocations inclined in the [110] direction. However, (i) 2D defects should be denied in this case because the widths of the observed defects are too narrow as the 2D defects on {111} planes according to

previous reports [80, 94–97, 118]. Considering the thickness of the TEM specimen (200 nm) and the angle between the {111} and (001) planes (54.74°), the defect lines should be 140 nm wide if the defects are 2D defects. In Fig. 6.5 (a), the widths of the defect lines are obtained to be 10–20 nm. Thus, (ii) dislocations inclined in the [110] direction should be responsible. A simple geometrical calculation gives the angle between the dislocation and (001) planes: $\tan^{-1}(200\text{ nm} / 1\ \mu\text{m}) = 11.3°$. Note that TDs in the blanket Ge without the post-growth annealing tend to be directed to be almost vertical to the substrate [54, 89], resulting in small black dots in the TEM image, as shown in Fig. 6.5 (b).

For more detailed analysis of the inclined TDs in plan-view TEM, a small area showing relatively high dislocation density ($\sim 1 \times 10^8$ cm^{-2}) was intentionally observed, as in Fig. 6.6. Similar to Fig. 6.5 (a), the top 200 nm of coalesced Ge layer was observed. Figures 6.6 (a) and (b) show dark-field (**g** = [220] and [$2\bar{2}0$]) plan-view TEM images taken at the same area. Four inclined dislocations were observed in the high dislocation density area as shown in Fig. 6.6 (a). Figure 6.6 (b) reveals that the red-circled inclined dislocation disappears when **g** = [$2\bar{2}0$], indicating that the dislocation is a screw dislocation. The other three of the inclined dislocations (white circled ones) are ascribed to the mixed dislocations because they did not disappear whatever diffraction vector **g** was chosen. Although the exact locations of the voids/SEG masks laying underneath cannot be determined, the dislocations inclined in the [110] direction would tend to be above the voids/SEG masks, taking into account the dislocations observed as black dots in Fig. 6.3.

6.4 Discussions: Coalescence Induced Generation/Bending of TDs

There are two possible mechanisms for the inclined TDs: (A) TDs generated at Ge/Si interfaces are inclined in the [110] direction and (B) the inclined TDs are generated when the SEG Ge layers coalesce.

For the mechanism (A), Fig. 6.7 (a) shows a plan-view SEM image showing the coalescence of SEG Ge layers partially occurs. Reflecting the edge undulation of line-and-space patterns formed by the EB lithography, the coalescence starts at some points, and then proceeds in the [110] and [$\bar{1}10$] directions above the SiO_2 masks. Figure 6.7 (b) shows a schematic illustration of ($1\bar{1}0$) cross-section along the line A–A' in Fig. 6.7 (a). White lines in Fig. 6.7 (b) indicate the evolution of Ge growth. The yellow-colored area shows Ge layers already grown in Fig. 6.7 (a), and the light green area shows Ge layers to be grown after Fig. 6.7 (a). The red solid line in Fig. 6.7 (b) shows a TD. TD generated at a growth window appears over the void, penetrating laterally to the sidewall of coalesced Ge due to the image force. This leads to TDs inclined in the [110] direction. Both edge and screw TDs should be generated

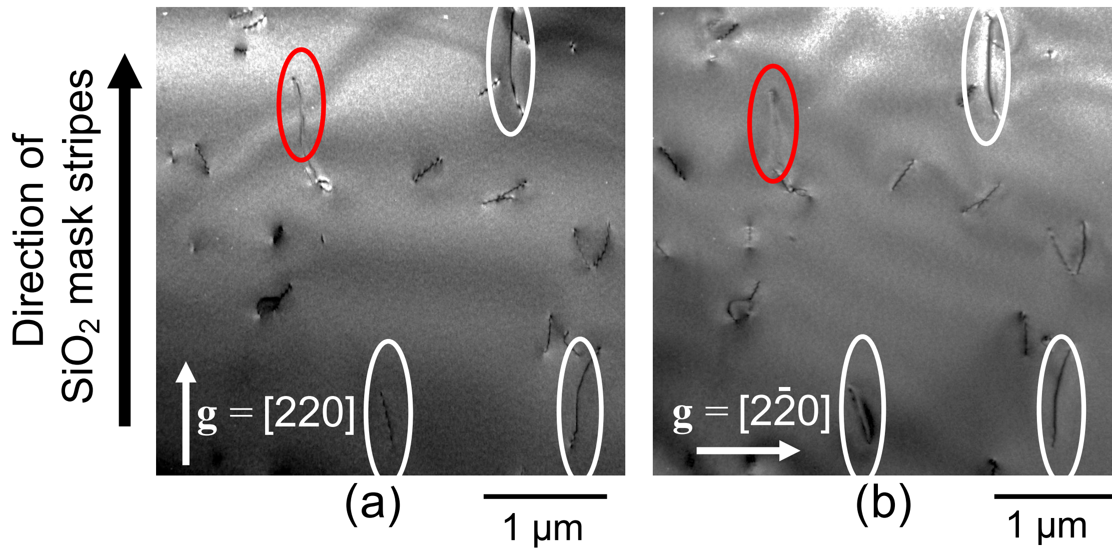

Figure 6.6: (001) dark-field plan-view TEM images of a coalesced Ge layer. A red-circled dislocation shown in (a) (**g** = [220]) is not shown in (b) (**g** = [2$\bar{2}$0]) indicating that the red-circled dislocation is a screw dislocation. On the other hand, white-circled dislocations do not disappear with any g vectors indicating that the green-circled dislocations are mixed dislocations.

considering the Burgers vectors of TDs generated at the Ge/Si interfaces. As in a previous report [121], edge misfit dislocations (MDs) are aligned in the [110] or [1$\bar{1}$0] direction. The Burgers vectors are a/2[1$\bar{1}$0] or *a*/2[$\bar{1}\bar{1}$0] (*a*: the lattice constant) for the threading segments of MDs in the [110] direction (MD_{110}), whereas the vectors are *a*/2[110] or *a*/2[$\bar{1}$10] for MDs in the [1$\bar{1}$0] direction ($MD_{1\bar{1}0}$). Edge TDs are formed when the TDs from MD110 inclined to the [110] direction, and screw TDs are formed when the TDs from $MD_{1\bar{1}0}$ inclined to the [110] direction.

For the mechanism (B), Fig. 6.8 shows schematics of defect generation when the SEG Ge layers coalesce. As reported previously [97], the misorientation between adjacent SEG Ge layers should generate defects at the coalescence interface. Misorientation between two SEG Ge layers in the [110] direction can be categorized into three types of rotations; the rotation on the [110] direction (Fig. 6.8 (a)), the one on the [001] direction (Fig. 6.8 (b)), and the one on the [1$\bar{1}$0] direction (Fig. 6.8 (c)). In Fig. 6.8, the coalescence of a SEG Ge layer with the adjacent SEG Ge layer with misorientation (m-Ge) is assumed. The rotation on the [110] direction in Fig. 6.8 (a) results in the generation of edge dislocations in the [110] direction at the twin boundary of {111} plane [97]. Similarly, as in Fig. 6.8 (b), the rotation on the [001] direction result in the edge dislocations in the [001] direction. On the other hand, rotation on the [1$\bar{1}$0] axis in Fig. 6.8 (c) results in generation of screw dislocations, being

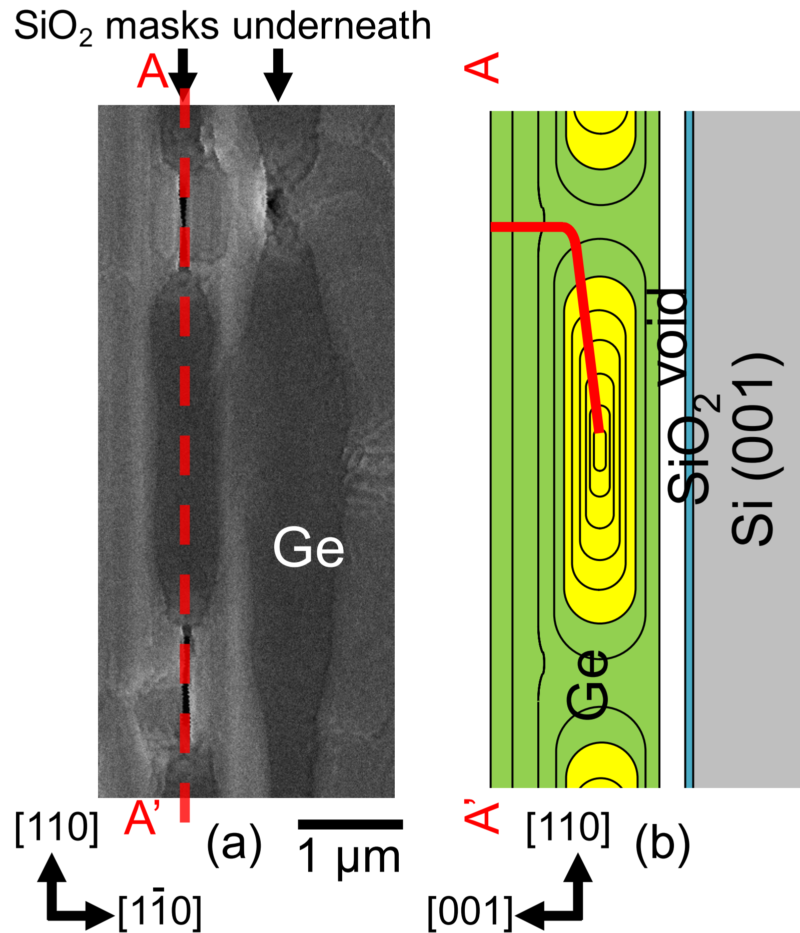

Figure 6.7: (a) A plan-view SEM image showing the beginning of coalescence of SEG Ge layers and (b) a schematic illustration of (1$\bar{1}$0) cross-section along the line A–A' in (a) showing the evolution of Ge coalescence. In (b), a TD inclined to [110] direction is also shown (red solid line), and the yellow area shows Ge layers already grown in Fig. 6.7 (a) whereas the light green area shows Ge layers to be grown.

similar to the direct bonding of Si (001) surfaces [122]. The screw TDs in Fig. 6.6 (a) could be ascribed to the rotation on the [1$\bar{1}$0] direction. The mixed TDs in Fig. 6.6 (a) could be ascribed to the combination of these rotations. Assuming that the misorientation generates dislocations at a density of $1{\times}10^7$ cm^{-2}, the average angle of the misorientation is estimated to be 0.034° [123]. In addition, it have already been reported that micro-beam X-ray diffraction reveals fluctuations of orientation in a line-shaped SEG Ge layer for 100 arcsec (= 0.028°) in line direction [124]. The reported fluctuations of orientations in SEG Ge layer agree well with the estimated angle of misalignment, supporting the mechanism (B).

The inclined TDs should be located above semicylindrical voids if the TDs were generated by the above two mechanisms. In fact, the cross-sectional TEM images in Figs. 6.3 (a)

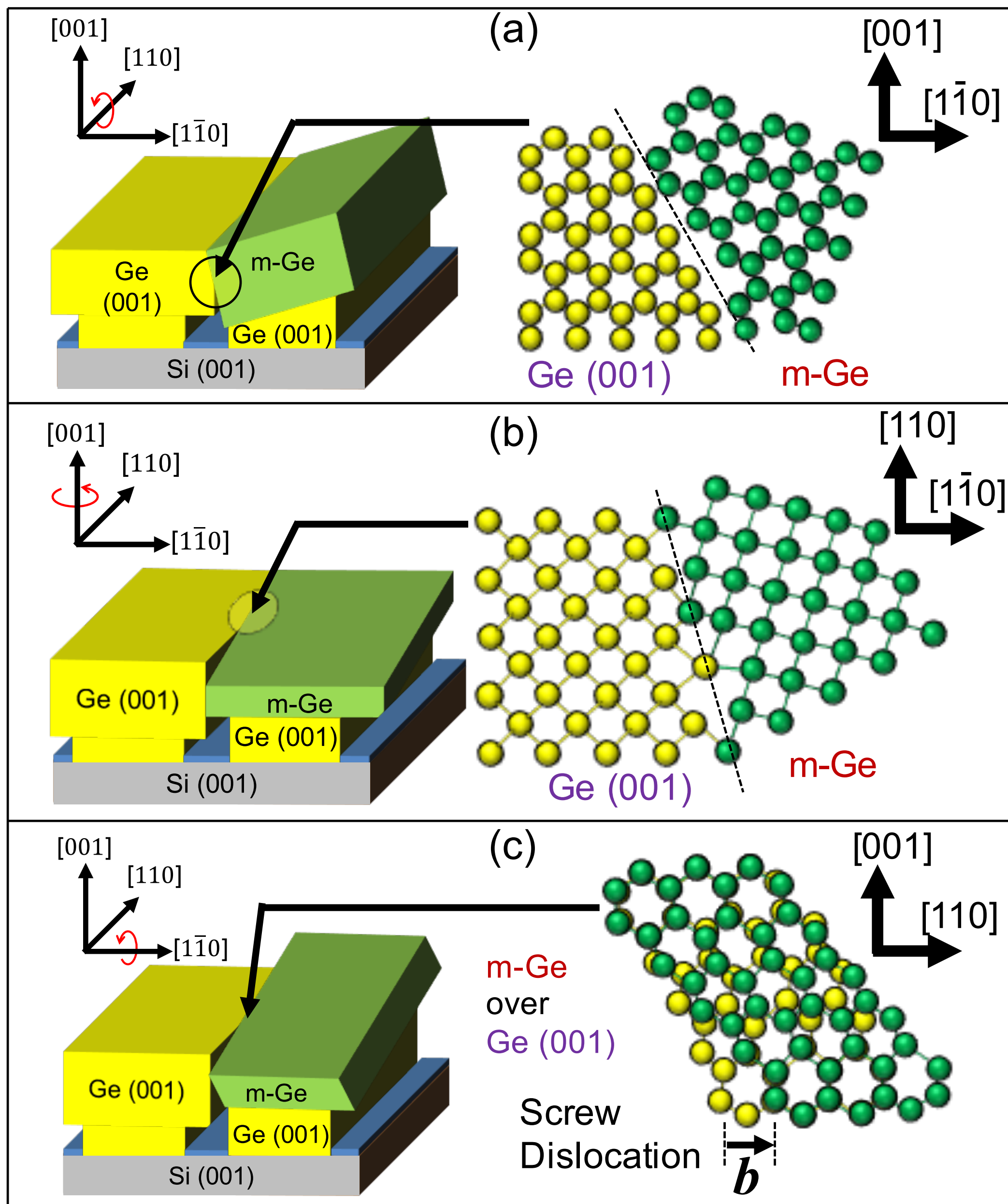

Figure 6.8: Schematic illustrations showing defect generation at the coalesced interface of SEG Ge layers. (a) Rotation on the [110] direction, (b) rotation on the [001] direction, and (c) rotation on the [1$\bar{1}$0] direction.

and 6.3 (b) showed that these inclined dislocations are located above the voids, although the mechanisms (A) and (B) cannot be discriminated. Further analyses on the $(1\bar{1}0)$ cross-sectional TEM observations ((110) cross-section in this study) would be effective; in the case of the mechanism (A), the inclined TDs would disappear near the voids, reflecting the TDs are originated from the Ge/Si interfaces, whereas in the case of the mechanism (B), the inclined TDs should penetrate the Ge layer from the semicylindrical void to the top surface.

7 Material Propaties of Coalesced Ge for Light-Emitting Device Applications

In order to employ coalesced Ge layers as a light-emitting device material, tensile strain and n-type doping is required as described in section 1.3. In this section, characterization of tensile strain in coalesced Ge and description about n-type doping employing thermal diffusion of phosphorous (P) will be shown. It will be also described in this section that coalesced Ge has an advantage over blanket Ge in terms of optical loss during light propagation in active Ge layers. A reduction of optical loss will bring a reduction of laser threshold.

7.1 Tensile Strain in Coalesced Ge

Introduction of tensile strain in Ge bring a shrinkage of energy gap between Γ valley (direct gap) and L valley (indirect gap), leading Ge to be more "direct-like" material as described in section 1.3.2. Application of tensile strain in Ge bring a shrinkage of Γ–Γ energy gap as well, and thus tensile strain of ~0.2 % is preferable to the on-chip laser working in optical communication wavelength (~1.6 μm). It is already reported that 0.1–0.2 % built-in tensile strain is induced in blanket Ge, resulting in Γ–Γ energy gap of 1.6 μm [11]. The built-in tensile strain is ascribed to the mismatch of thermal expansion coefficient between Ge and Si [11], i.e., the tensile strain is induced in Ge during cooling down from growth temperature (500–700 °C) to room temperature. In coalesced Ge layers, however, the built-in tensile strain can be smaller than blanket Ge because the contact area of Ge and Si is reduced compared to blanket Ge. In addition to that, there can be strain dispersion in coalesced Ge because of the presence of voids on SiO_2 masks.

7.1.1 Strain Simulation by Finite Element Method

Simulation for tensile strain induced in blanket/coalesced Ge layers were carried out employing finite element method (FEM). Figure 7.1 (a) shows a FEM simulation result showing distribution of strain in $[1\bar{1}0]$ direction induced in a coalesced Ge, where W_{window} = 0.5 μm,

$W_{mask} = 0.5$ μm, and 1-μm-thick grown at 700 °C. It is obviously shown that the tensile strain is accumulated at the top of the void, indicated by red color, and almost relaxed at the bottom of the void, indicated by blue color. At the top surface, on the other hand, almost uniform tensile strain of 0.21 % is applied as indicated by green color. Such accumulation of tensile strain has widely been observed in Ge microbridges [46,125]. Since the cross-sectional shape of the coalesced Ge is similar to a one dimensional microbridge, the accumulation of tensile strain at the top of the voids is reasonable.

In the viewpoint of application for light emitter, light is confined in relatively high effective refractive index (n_{eff}) area, where Ge on Si seeds. In Ge on Si seeds, 0.1–0.2 % tensile strain is almost uniformly induced in Ge, which is preferable to application for light emitter, as described in section 1.3.

The magnitude of strain in Ge on Si seeds depends on APR, as shown in Fig. 7.1 (b). As APR decrease, the influence of low-strain area at the bottom of the voids become larger, resulting in the decrease of strain in Ge on Si seeds. Although the strain is reduced as APR decrease, 0.1–0.2 % tensile strain is induced in Ge on Si seeds in the range $0.5 \leq \text{APR} \leq 1$, which is fabricated in this work.

7.1.2 Experimental Measurements of Strain in Coalesced Ge Layers

In general, Raman spectroscopy and XRD are used to measure strain in semiconductor crystal including Ge epitaxial layers on Si. However, since X-ray (Cu Kα line) deeply penetrate into Ge and Si for tens of μm, the full-width half-maximum (FWHM) is expanded owing to the strain distribution shown in Fig. 7.1. Thus, Raman spectroscopy was employed using excitation laser of 457 nm, penetration depth in Ge is 10–20 nm, to measure the strain in coalesced Ge.

Since Raman peak positions and Raman peak shift due to strain depend on machine calibration, exact peak position for Raman scattering from Ge-Ge bond and coefficient of peak shift due to strain are required to be determined. In order to determine the exact peak position and coefficient of peak shift, tensile strain in a blanket Ge layer was determined by (004) and (224) XRD measurements. As the result, tensile strain in blanket Ge was determined to be 0.1948 %. Then, Raman spectroscopy measurements were carried out on a Ge wafer (strain = 0 %) and a blanket Ge, as shown in Fig. 7.2. The Raman measurement results reveal that the Raman scattering from strained Ge-Ge bond ω_{GG} is expressed as Eq. (7.1), in our equipment at that time.

$$\omega_{GG} = 299.11 - 516.7\varepsilon \tag{7.1}$$

where ε is the strain (%) in Ge. Note that the obtained correlation is similar to the one previously reported in Ref. [126], $\omega_{GG} = 298.5 - 384\varepsilon$, in the range of Raman measurements carried out to observe Ge-Ge peak, 290–310 cm^{-1}.

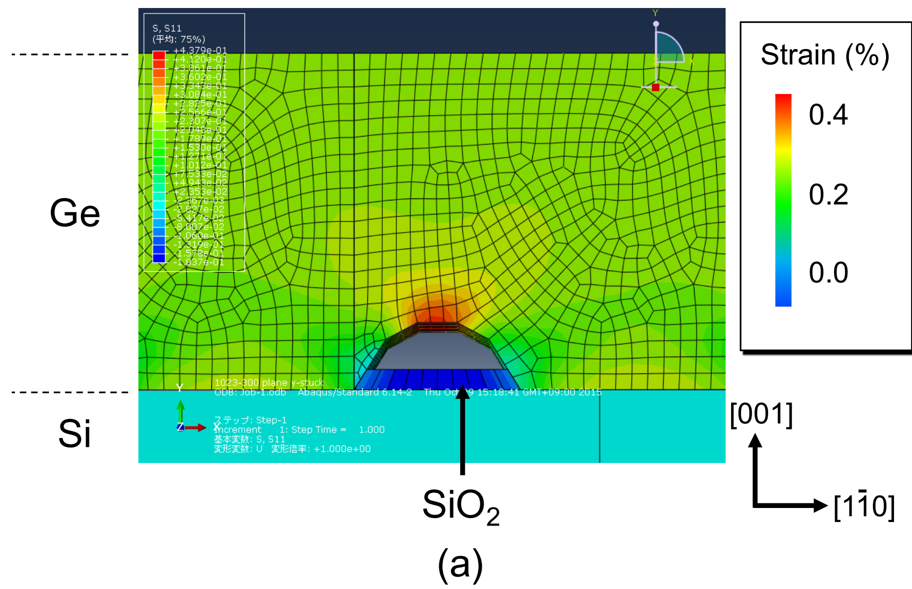

(a)

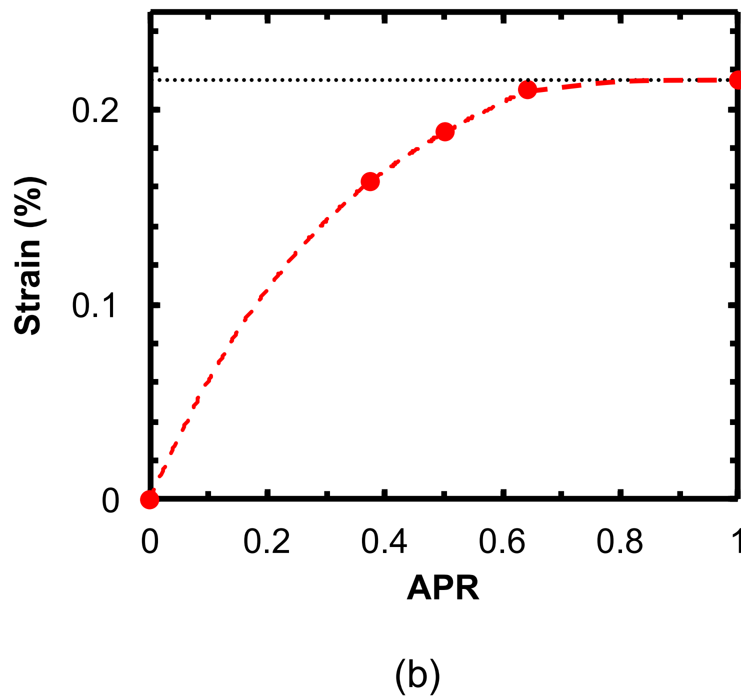

(b)

Figure 7.1: (a) A FEM simulation result showing strain profile in coalesced Ge, and (b) strain in coalesced Ge as a function of APR

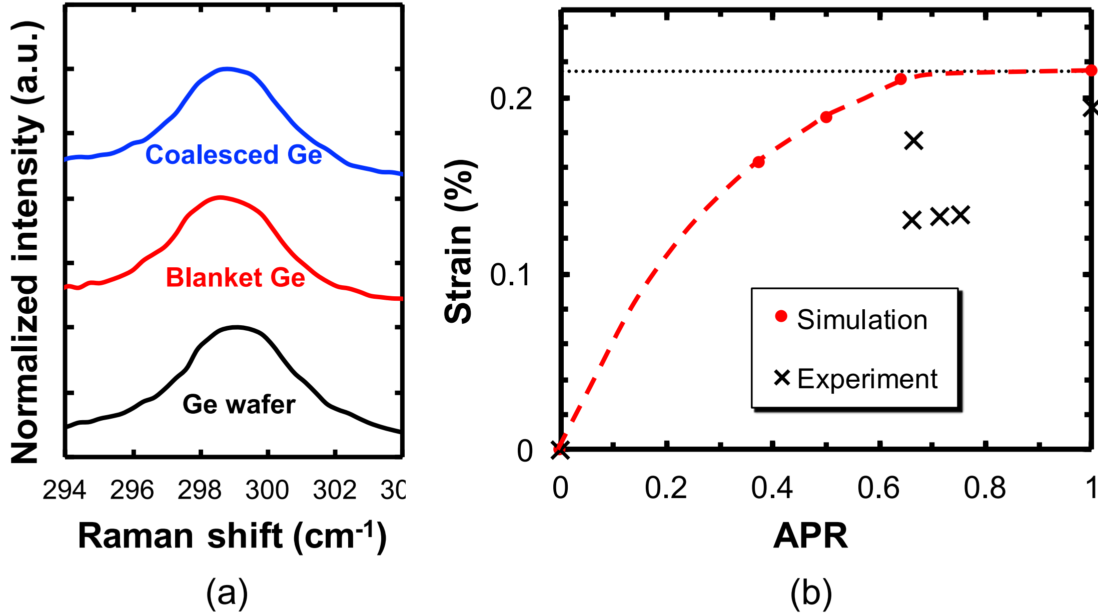

Figure 7.2: (a) Raman spectra for a Ge wafer (black), blanket Ge (red), and coalesced Ge (blue), and (b) comparison between experimental results and simulation

Using the relation in Eq. (7.1), strain in coalesced Ge layers were measured. Typical Raman spectrum for coalesced Ge (W_{window} = 0.66 μm, W_{mask} = 0.34 μm in design) is shown as blue line in Fig. 7.2 (a). The obtained strain in coalesced layers are compared with simulation results, as shown in Fig. 7.2 (b). Strain in coalesced Ge is 20–40 % smaller than the simulated strain, and 10–30 % smaller than the strain in blanket Ge. Although the strain in coalesced Ge is smaller than blanket Ge, tensile strain larger than 0.1 % is induced in coalesced Ge where APR ≥ 0.6.

In addition to strain, crystal quality can be quantitatively evaluated from the full-width half-maximum (FWHM) of the Raman spectra. I.e., FWHM decreases as TDD decreases, as reported in Si [127]. In the case for Si [127], TDD larger than 10^8 cm^{-2} can be evaluated by FWHM of Raman spectra. From the Raman results shown in Fig. 7.2 (a), FWHM for the Ge wafer, blanket Ge, and coalesced Ge are obtained for 3.78 cm^{-1}, 3.95 cm^{-1}, and 3.71 cm^{-1}, respectively. The coalesced Ge shows FWHM smaller than blanket Ge, and even smaller than Ge wafer, probably owing to the low TDD in coalesced Ge.

7.1.3 Characterization of Coalesced Ge Layers by Macro-XRD

2θ-ω XRD measurements were carried out in order to characterize the crystallinity of coalesced Ge layers. X-ray was injected through slit of 2 mm wide, and thus the XRD results are obtained from mm-sized square and averaged. Figure 7.3 shows the 2θ-ω curve obtained from

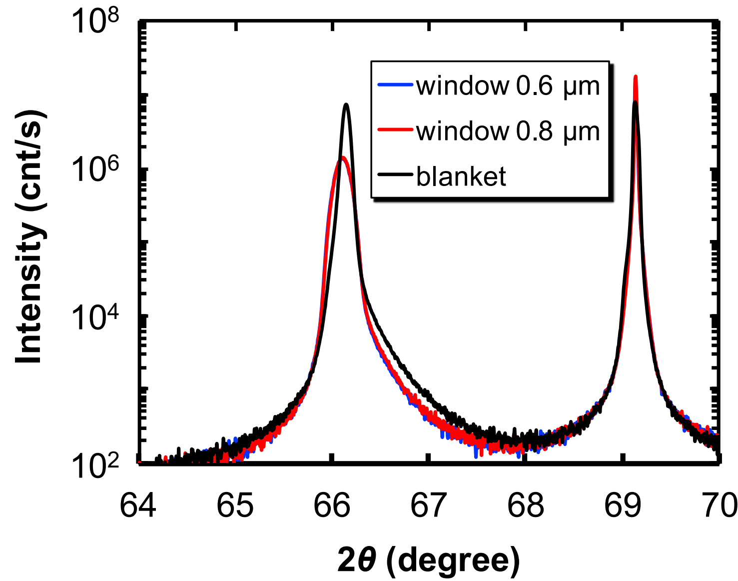

Figure 7.3: 2θ-ω XRD results obtained from blanket Ge (black) and coalesced Ge of W_{mask} = 0.6 μm in design (blue; W_{window} = 0.6 μm in design, red; W_{window} = 0.8 μm in design).

blanket Ge (black) and coalesced Ge of W_{mask} = 0.6 μm in design (blue; W_{window} = 0.6 μm in design, red; W_{window} = 0.8 μm in design). The peaks around 66° show XRD from Ge layers, and the peaks around 69° show XRD from Si substrates. It is found that coalesced Ge layers show steep rising-up/dropping-down with larger peak width. The steep rising-up/dropping-down of the peak around 66° implies good crystallinity. The larger peak width suggests that there is strain dispersion in coalesced Ge.

7.1.4 Characterization of Local Strain in Coalesced Ge Layers by μ-XRD

In order to characterize the local strain in coalesced Ge layers, XRD with micron-sized X-ray was carried out at SPring-8, Hyogo, Japan. The spot size of X-ray was as small as 0.44 μm × 2.4 μm when the measurements were carried out. Figure 7.4 shows a schematic illustration of scan direction Z during the μ-XRD measurements. The gray narrow rectangles indicates SiO_2 masks underneath. Thus, the focused X-ray crossed the SiO_2 masks, expecting the difference between Ge on Si seeds and Ge on voids.

ω scan was performed scanning in Z direction, and the ω-Z map is shown in Fig. 7.5. Although the spot size of X-ray in Z direction was narrower than the W_{window} and W_{mask}, no periodicity is shown in the ω-Z map. This would be because the strain field by a dislocation is wider than W_{window} or W_{mask}. Strain spreading wider than W_{window} or W_{mask} would affect ω scan, making the periodicity obscure. In addition to that, comparing the coalesced Ge with blanket Ge, coalesced Ge layers obviously show wider FWHM than blanket Ge. This would be ascribed to the strain distribution in coalesced Ge, as shown in Fig. 7.1.

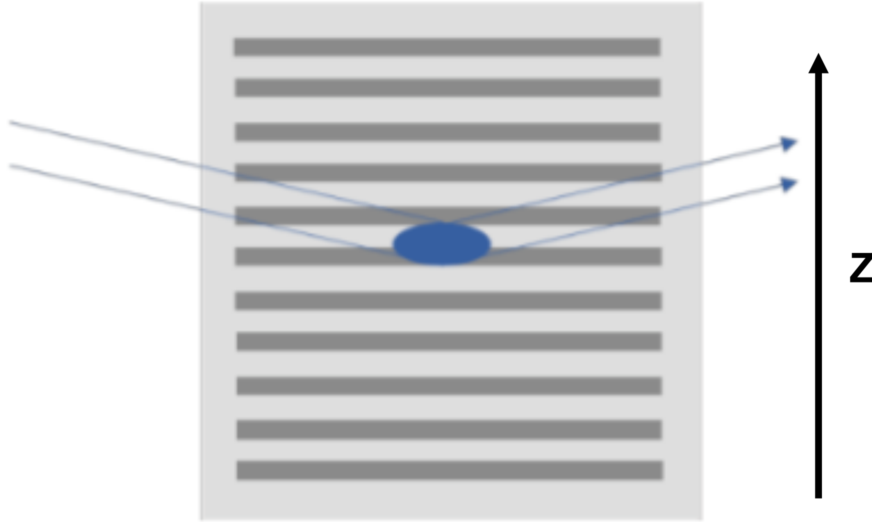

Figure 7.4: A schematic illustration of scan direction Z during the μ-XRD measurements

7.2 N-Type Doping by Thermal Diffusion

N-type doping as high as 1×10^{19} cm^{-3} is required to use Ge as an optical gain material, as described in section 1.3. Phosphorous (P) has widely been used as an n-type dopant in Ge because of its high solid solubility in Ge, as high as 10^{20} cm^{-3} [128]. *In-situ* doping method has been employed to fabricate heavily n-type doped Ge [129]. However, *in-situ* doping method has a trade-off between doping level and crystal quality. It has been reported that n-type dopants (P) diffuse out of Ge as growth/anneal temperature exceeds 650 °C [130, 131]. In terms of TDD in Ge, growth temperature higher than 700 °C is effective to reduce TDD. Thus, the doping level and crystal quality is in trade-off relation, as will be shown in Fig. 7.8.

Besides *in-situ* doping, there are methods to dope in Ge; ion implantation and thermal diffusion. Ion implantation method is, however, not suitable for light emitter because the impact of ion implantation destructs crystal structure, resulting in severe decrease of light emission intensity [131].

Thus, a thermal diffusion method was employed to dope P into coalesced Ge in this study. Since a Si capping layer works as a barrier for P diffusion [132], Si capping layers were removed using 2.38 % TMAH before the P diffusion processing. Phosphosilicate glass (PSG) was employed as a dopant diffusion source. PSG layers were deposited on Ge epitaxial layers on Si by a sub-atmospheric chemical vapor deposition (SACVD). Tetraethyl orthosilicate (TEOS) and triethylphosphate (TEPO) were employed as source gases, and the deposition was carried out at 480 °C. Deposited PSG layer was 450-nm-thick, and P concentration in the PSG layer was $\sim 4 \times 10^{21}$ cm^{-3} according to secondary ion mass spectroscopy (SIMS)

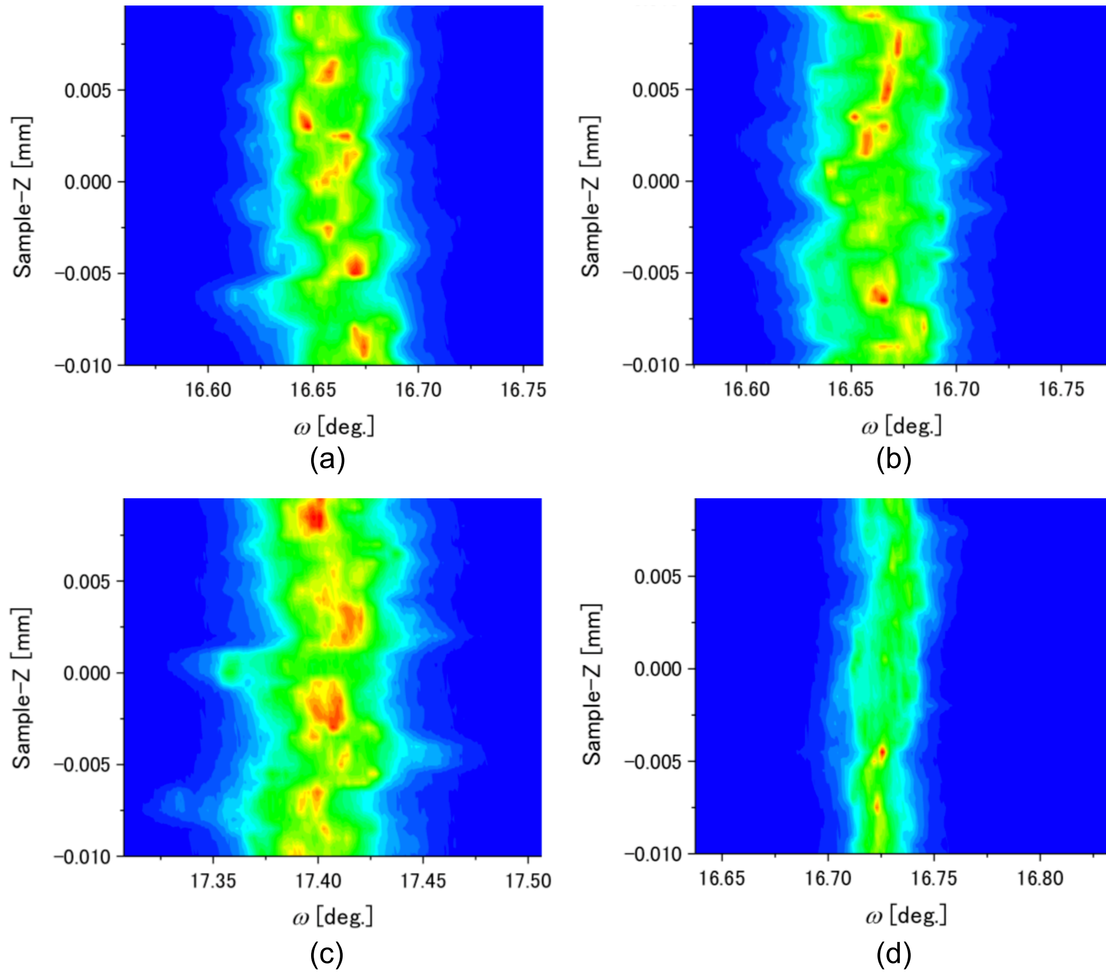

Figure 7.5: ω-Z map obtained from (a) coalesced Ge (W_{window} = 0.6 μm, W_{mask} = 0.5 μm in design), (b) coalesced Ge (W_{window} = 0.8 μm, W_{mask} = 0.6 μm in design), (c) coalesced Ge (W_{window} = 0.6 μm, W_{mask} = 0.5 μm in design), and (d) blanket Ge.

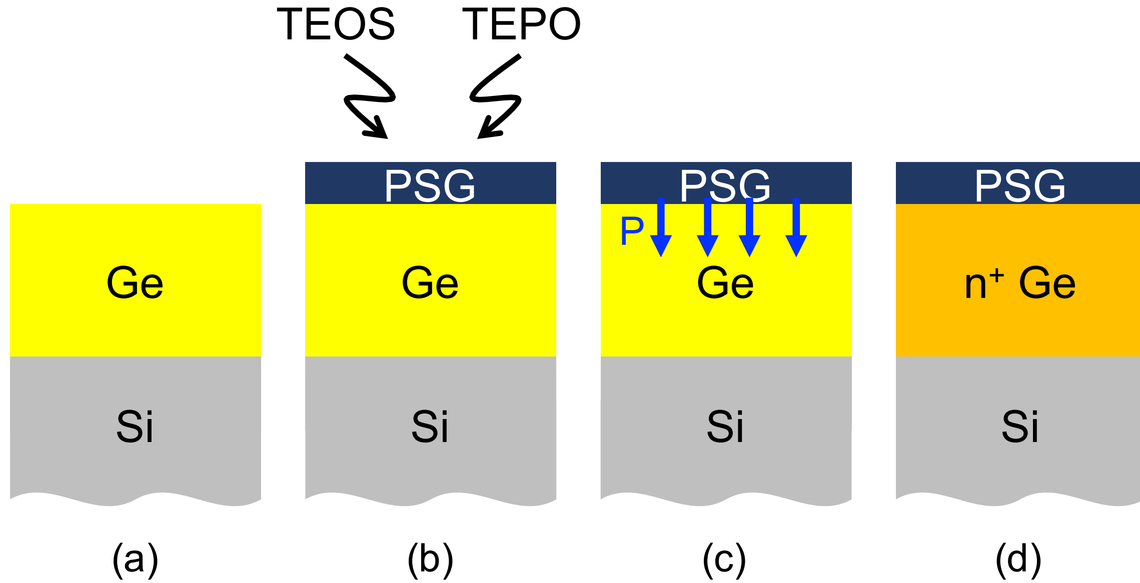

Figure 7.6: Schematic illustrations of P diffusion process; (a) Ge epitaxial layer on Si, (b) PSG deposition, (c) P thermal diffusion into Ge, and (d) n-type Ge as the result of diffusion.

measurements. Thermal diffusion was carried out at 850 °C for 5 min, in order to obtain uniform and dense P profile in Ge. Schematic illustration of PSG deposition/diffusion process is shown in Fig. 7.6. The PSG layer was removed by buffered-HF as the P diffusion process finished.

As the result of thermal diffusion at 850 °C for 5 min, uniform P concentration of $\sim 1\times10^{19}$ cm^{-3} was observed in a ~900-nm-thick Ge, as shown in Fig. 7.7. Such a uniform and dense doping is necessary to achieve Ge lasers. In addition to the P diffusion from PSG, Si diffuse into Ge from substrate as the result of thermal diffusion annealing, and $Si_{0.01}Ge_{0.99}$ was formed where 100 nm from the bottom. The formation of Si_xGe_{1-x} has a good effect on light emission from Ge because the formation of Si_xGe_{1-x} would be effective to passivate defect-rich Ge/Si interfaces as reported in Ref. [64].

Figure 7.8 shows the correlation between growth/annealing temperature and doping concentration. Previously reported doping concentration in *in-situ* doped Ge (black opened circles) decreases as the growth temperature increases, which is ascribed to P out-diffusion. The thermal diffusion method, shown as the yellow star in Fig. 7.8, could overcome the trade-off relation between process temperature and doping concentration. The high temperature (850 °C) annealing bring two positive effects on light emission from Ge: improvement of crystal quality and enhancement of tensile strain. In addition to that, in the case for coalesced Ge, high temperature annealing bring a great PL enhancement probably due to out-diffusion

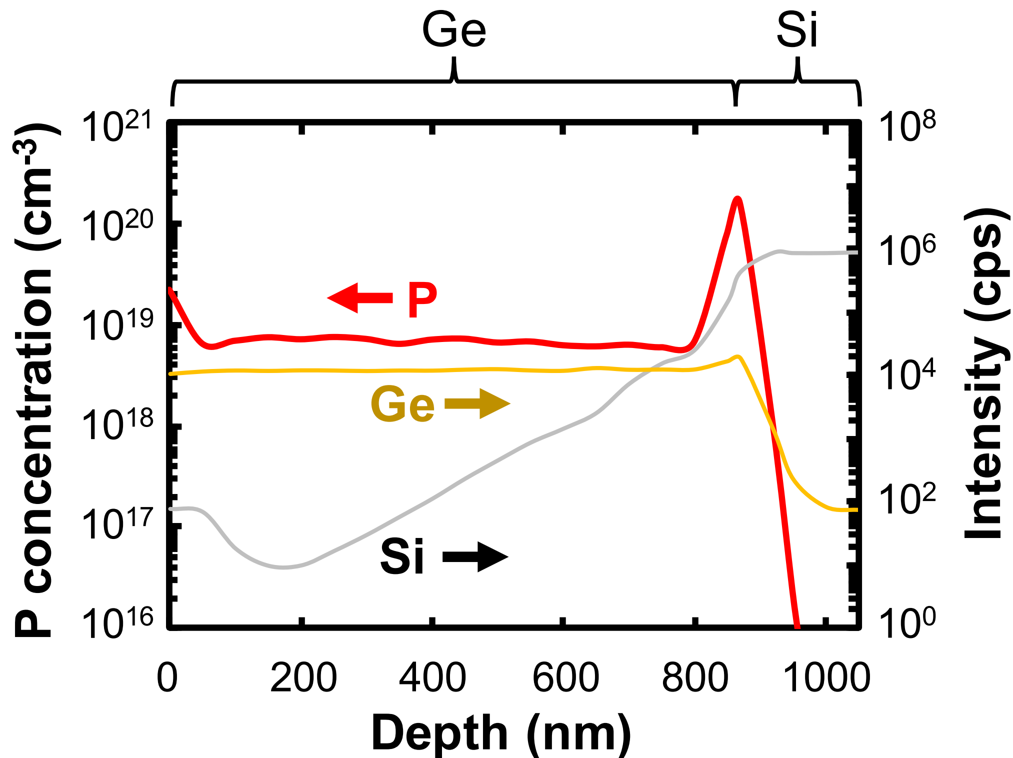

Figure 7.7: SIMS profiles of Si, Ge, and P in P-diffused Ge

of point defects. The enhancement of PL induced by the high temperature annealing will be described in section 8.

7.3 Optical Propagation Mode Push-Up in Coalesced Ge

The confinement of light in the coalesced Ge should be much different from the structures in the previous studies using Ge channel waveguides on Si [41–43] in terms of the presence of air voids with the low refractive index at the bottom Ge/Si interfaces. Figure 7.9 shows the simulated profiles of electric field strength in the transverse-electric (TE) mode with the wavelength of 1.55 μm for the Ge reverse-rib structure in this study (Fig. 7.9 (a)) as well as those for the previous studies (Figs. 7.9 (b) and 7.9 (c)) [41, 42]. For the Ge coalesced Ge shown in Fig. 7.9 (a), the air voids are found to be responsible for the confinement of light in the lateral direction, operating as an inverted-rib cross-sectional optical waveguide. It is also found that, compared with the results for the previous structures, the light is confined slightly apart from the Ge/Si interfaces. This would be effective to reduce the effect of NRR at the defect-rich Ge/Si interfaces due to the lattice mismatch between Ge and Si as large as 4 %.

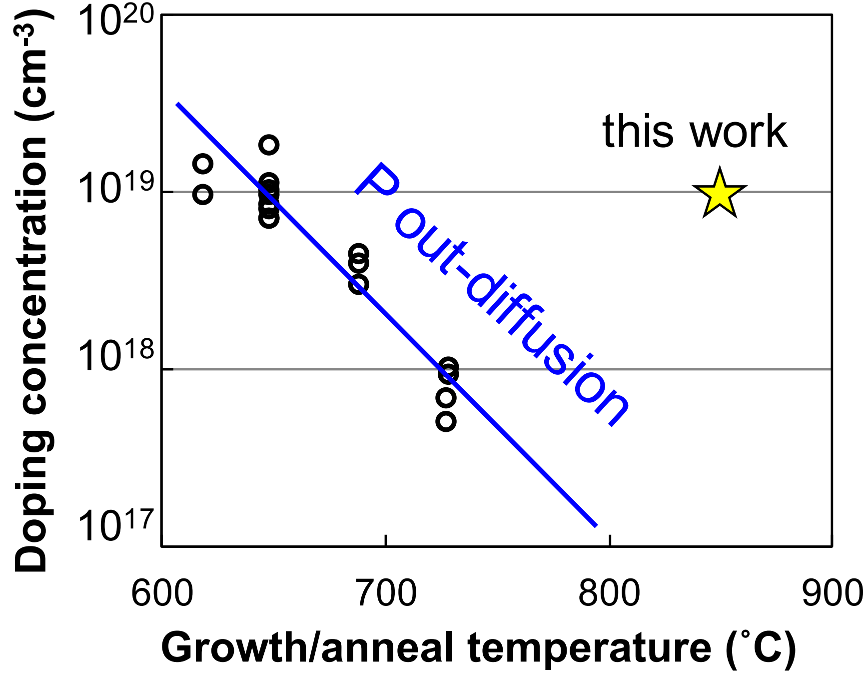

Figure 7.8: Correlation between growth/anneal temperature and active doping concentration. Black opened circles are from J. Liu, *et al.*, *Thin Solid Films*, 520(8), 3354 (2012), showing decrease of doping concentration owing to out-diffusion. The yellow star indicates P concentration achieved by thermal diffusion in this work.

The confinement factor in Ge, Γ_{Ge} calculated as Eq. (7.2), is 99.91 % for the coalesced in Fig. 7.9 (a).

$$\Gamma_{\text{Ge}} = \frac{\iint_{\text{Ge}} \varepsilon_{\text{Ge}} E^2 dxdy}{\iint_{\infty} \varepsilon_i E^2 dxdy} \tag{7.2}$$

This value is significantly larger than the previously reported channel waveguide structures employed in Ge lasers, which are shown in Figs. 7.9 (b) and 7.9 (c) (96.83 % and 89.54 %, respectively). Furthermore, the coalesced Ge has an advantage in terms of the reduction of sidewall roughness. Since the sidewalls of Ge/air interfaces are formed during crystal growth, the sidewalls are formed by automatically-flat facet planes. Such automatically-flat sidewalls should be useful for the reduction of propagation loss due to the light scattering, as reported in waveguide researches [133–135]. These characteristics (spacial location of optical mode, large Γ_{Ge}, and flat sidewalls) should have a positive effect to reduce optical losses, i.e., increase of optical net gain.

Figure 7.10 shows the effect of air voids in terms of optical mode push-up in Ge layers on Si. Since the voids on SEG masks ($n = 1$) reduce effective refractive index near Ge/Si interfaces, the optical mode profile is pushed up toward the top surface and separated from the

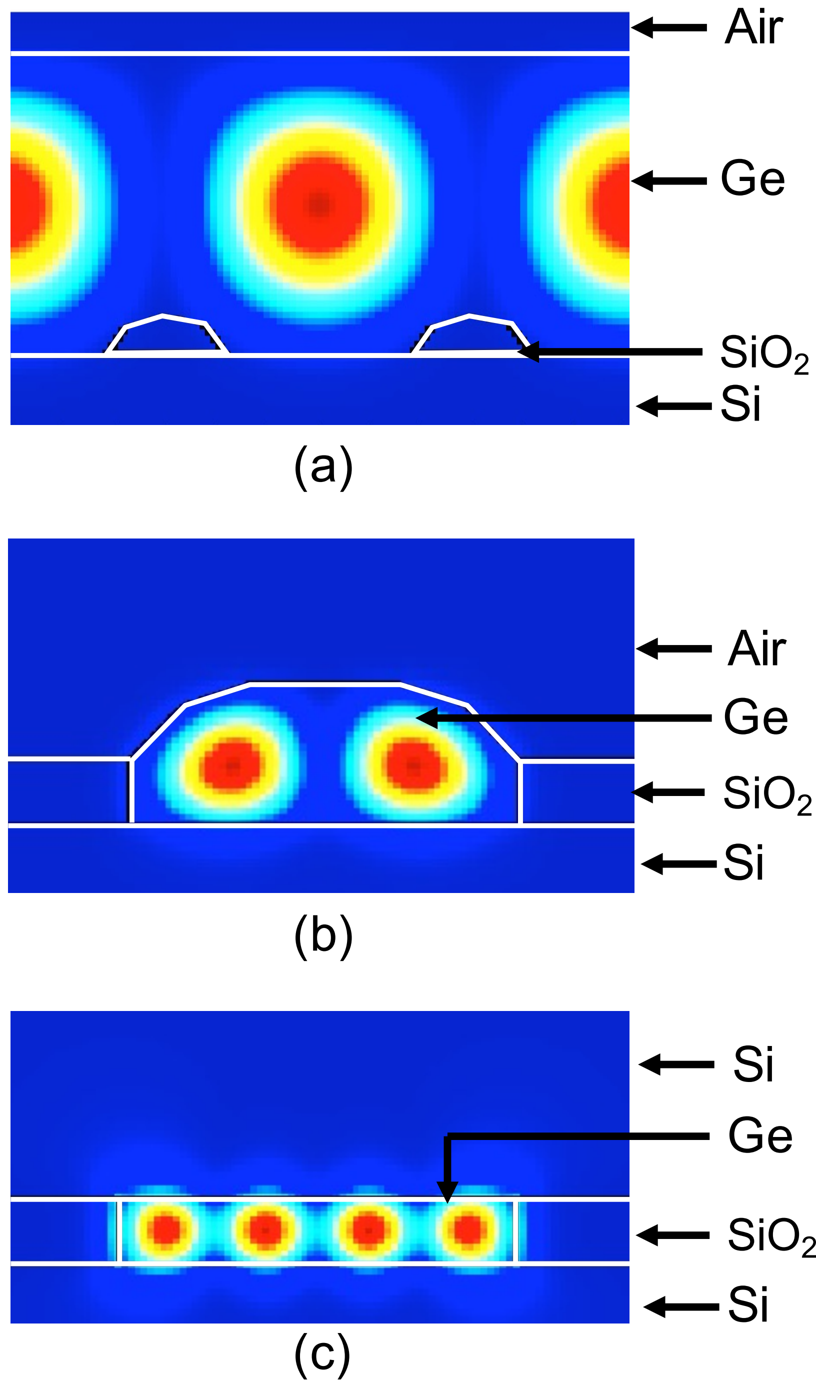

Figure 7.9: Optical propagation modes in (a) coalesced Ge, (b) optically pumped Ge laser reported by J. Liu, *et al.*, *Opt. Lett.*, 35(5), 679 (2010), and (c) electrically pumped Ge laser reported by R. E. Camacho-Aguilera *et al.*, *Opt. Exp.*, 20(10), 11316 (2012).

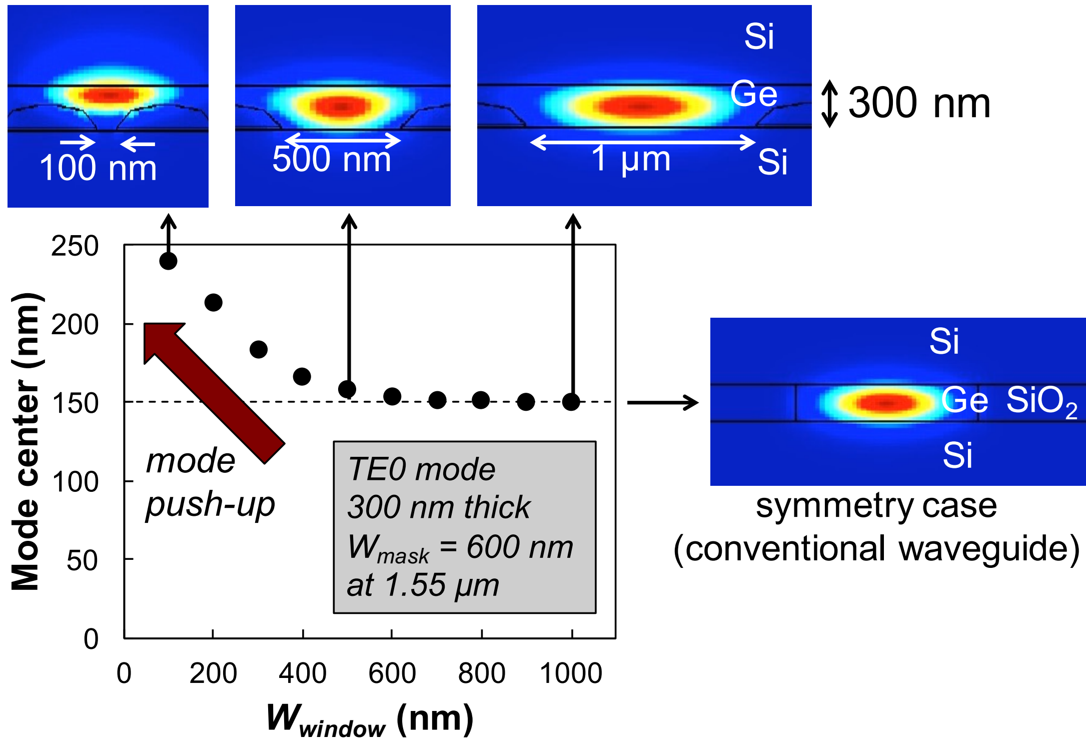

Figure 7.10: Optical propagation modes push-up in coalesced Ge layers

Ge/Si interfaces, resulting in optical passivation of Ge/Si defect-rich interfaces. The effect of optical mode push-up is shown in Fig. 7.10, showing fundamental TE mode profiles in coalesced Ge layers of W_{mask} = 600 nm, where the thickness of the Ge layers were 300 nm, same as the structure employed in [42]. According to the mode simulation, it is obviously shown that the optical propagation mode in coalesced Ge is pushed up as the W_{window} become narrower than 600 nm, i.e., APR become smaller than 0.5. Since the Ge/Si interfaces have negative effects on light emission from Ge as reported in Ref. [66] and will be shown in Appendix I, the mode push-up should have a positive effect on light emission from Ge on Si.

In terms of the reduction of J_{th}, the thinner Ge layers are the better. The coalesced Ge layers used in the present study is ~1 μm thick, which is 3–4 times thicker than the previously reported Ge LDs [42, 43]. Thinning process was not employed in order not to induce damage in active Ge layers. Thus, thinning of the active Ge layers is an important further work.

8 Light Emission From Coalesced Ge Layers

The improvement of crystal quality in coalesced Ge layers was described in section 3–6, and the tensile strain and n-type doping in coalesced Ge layers were described in section 7. In this section, characterizations of light emission from coalesced Ge are described using micro-photoluminescence (μ-PL) systems (vertical excitation and vertical detection) and optical pumping systems (vertical excitation and lateral detection, as a feasibility study for light-emitting device applications.

8.1 PL from Coalesced Ge Layers at Room Temperature

μ-PL measurements were carried out at room temperature in order to characterize the coalesced Ge layers as a light emission material. Since TDs works as NRR centers, PL intensity is conceivable to increase as TDD is reduced.

8.1.1 Measurement Setup

μ-PL measurements were carried out at room temperature using a 785-nm laser. Figure 8.1 shows a schematic illustration of μ-PL measurement system used at room temperature. The sample surface was illuminated from the top. The diameter of $1/e^2$ intensity for the excitation laser was approximately 2 μm using a 50× objective lens. Note that the diameter of $1/e^2$ intensity was wider than $W_{window} + W_{mask}$, indicating that PL from Ge on Si seeds and from Ge above SiO_2 masks are not separable. PL emitted from the top surface was collected by the objective lens and detected through a grating with an extended InGaAs array detectors. The InGaAs detectors were cooled down by liquid nitrogen, and can detect 800–2200 nm wavelength range. A short pass filter was put before the excitation laser reaches beam splitter in order to remove the noise at wavelength of 785 nm × 2 = 1570 nm (adjacent order of diffraction). The excitation laser passing to the detector side was removed by long pass filters located before grating (red dashed line in Fig. 8.1). The power of the excitation laser was 4.1 mW, corresponding to the power density of 130 kW/cm^2.

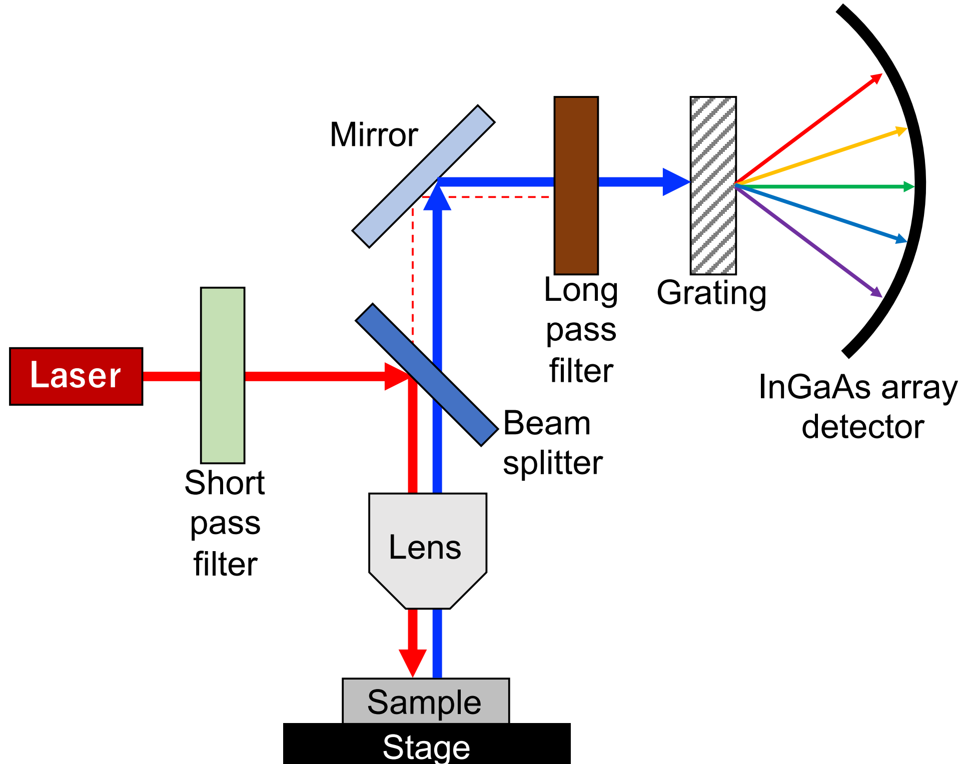

Figure 8.1: A schematic illustration of μ-PL measurement system used at room temperature. Red arrow indicates 785-nm excitation laser, and blue arrow indicates PL from Ge.

8.1.2 Results and Discussions

Since the TDDs in coalesced Ge decrease as APR decrease (Fig. 5.6), and TDs work as NRR centers in Ge, the PL from coalesced Ge was predicted to increase as APR decreases. Figure 8.2 (a) shows typical PL spectra from a Ge wafer (black), blanket Ge (blue), and coalesced Ge of APR = 0.6 (red). It is clearly shown that the PL from coalesced Ge is lower than PL from blanket Ge (APR = 1). For quantitative analysis, the integrated PL intensity in the direct-gap wavelength range (1500–1700 nm) is shown in Fig. 8.2 (b) as a function of APR. PL from coalesced Ge layers are obviously lower than PL from blanket Ge layers. These results suggest that there are NRR centers in as-grown coalesced Ge, which are not related to TDs.

PL from coalesced Ge layers after thermal diffusion of P was observed as well, using the same μ-PL system. As shown in Fig. 8.3, the obtained PL from P diffused Ge was obviously different from the one from as-grown Ge. The PL intensity increases as the result of P diffusion, for both blanket Ge and coalesced Ge. The P diffusion results in PL enhancement in blanket Ge by a factor of 4, which is ascribed to the reduction of TDD and n-type doping, as indicated by white arrow in Fig. 8.3 (a). In coalesced Ge, however, the P diffusion results

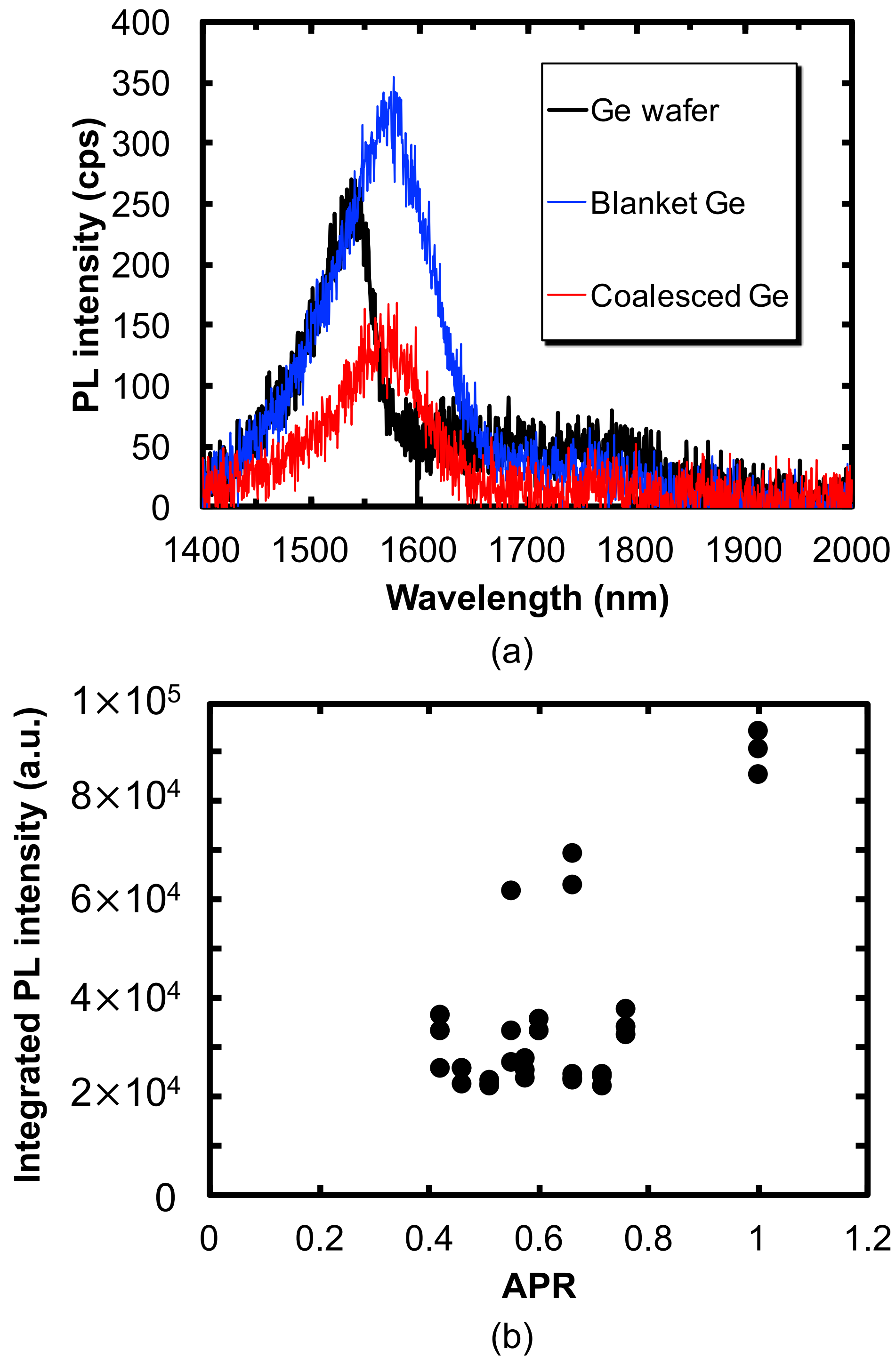

Figure 8.2: (a) Typical PL spectra from Ge wafer and as-grown blanket/coalesced Ge. (b) Integrated PL intensity (1500–1700 nm) as a function of APR.

in PL enhancement by a factor of 10–50, and it is clearly shown that PL intensity increases as APR decreases, as shown in Fig. 8.3 (b). This behavior, PL increase as APR decrease, is the one expected from the TDD observation results. Such a drastic change in PL intensity from coalesced Ge would be ascribed to the presence of NRR centers in as-grown coalesced Ge, which are not related to TDs. I.e., the NRR centers in as-grown coalesced Ge would be removed during the thermal diffusion of P into Ge.

Point defects are a feasible reason for the NRR centers in as-grown coalesced Ge, which are not related to TDs. It has been already known that point defects in semiconductors work as NRR centers and shorten the carrier lifetime [136]. Since point defects are defects in atomic-scale and one-dimensional, they are not able to be observed by EPD method nor TEM observations. In addition to that, the measurement results in Fig. 8.3, showing that the NRR centers in coalesced Ge are removed as the result of P diffusion, can be explained if the NRR centers are ascribed to point defects. I.e., out-diffusion of point defects would be the reason why the NRR centers disappeared as the result of high temperature annealing for P diffusion. Since the diffusion coefficient for Ge self-diffusion in Ge, which is equal to the diffusion of point defects in Ge, is 1/20 of that for P diffusion in Ge [137], P diffusion for 900 nm (as in Fig. 7.7) correspond to the point defects diffusion for 200 nm. Such a long diffusion would result in out-diffusion of the point defects in coalesced Ge, leading the enhancement of PL intensity.

A remaining question is the source of the point defects. A possible reason for the introduction of point defects is the rapid growth of Ge when SEG Ge layers coalesce. As shown in Fig. 8.4, the growth rate of Ge was rapidly enhanced as the SEG Ge layers coalesce, as fast as ~30 nm/min. The growth rate on the top of SEG Ge layers was ~7 nm/min as indicated by green arrow in Fig. 8.4, and the growth rate in [001] direction was ~14 nm/min as indicated by blue arrow in Fig. 8.4. Therefore, the growth rate is enhanced for 2–4 times when SEG Ge layers coalesce. Such a rapid growth would be ascribed to enhanced Ge supply at the coalescence point: SEG Ge sidewalls are surrounded by stable facets and the Ge atoms landing on SEG Ge accumulate to the coalescence point. In Ge epitaxial growth with relatively small growth rate, Ge atoms migrate around the Ge growth surface to minimize free energy. In the case for rapid growth, however, Ge atoms would be supplied before former Ge atoms find energy minima. Thus, rapidly-grown Ge would have more point defects than Ge grown at slower growth rate.

Although it is difficult to measure the concentration of point defects in Ge directly, the carrier lifetime measurements will show the concentration of point defects as long as TDD is the same. Thus, comparison of the carrier lifetimes in blanket Ge and coalesced Ge (both are as-grown, same TDD) will be information in terms of the presence of point defects. This will

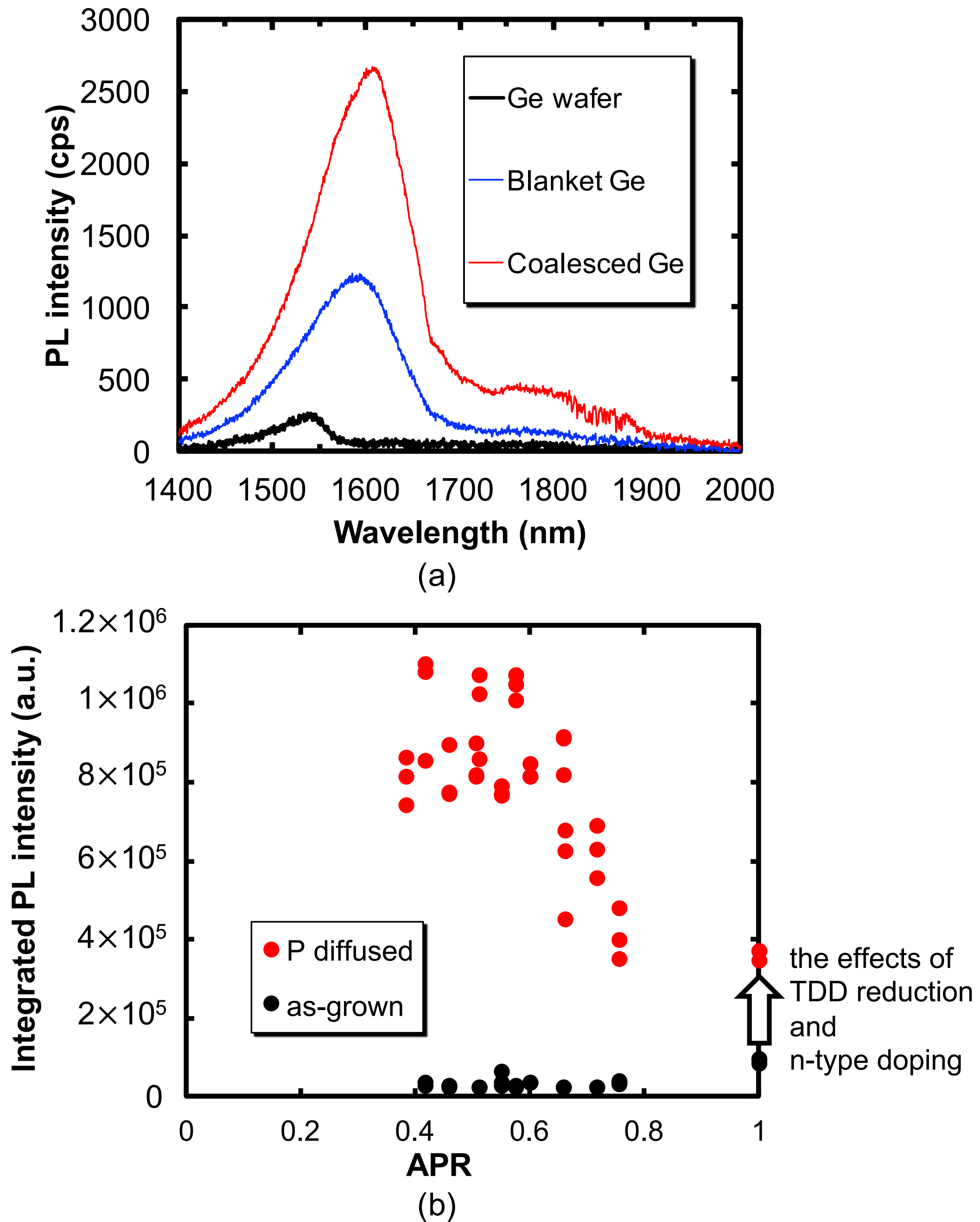

Figure 8.3: (a) Typical PL spectra from Ge wafer and P diffused blanket/coalesced Ge. (b) Integrated PL intensity (1500–1700 nm) as a function of APR.

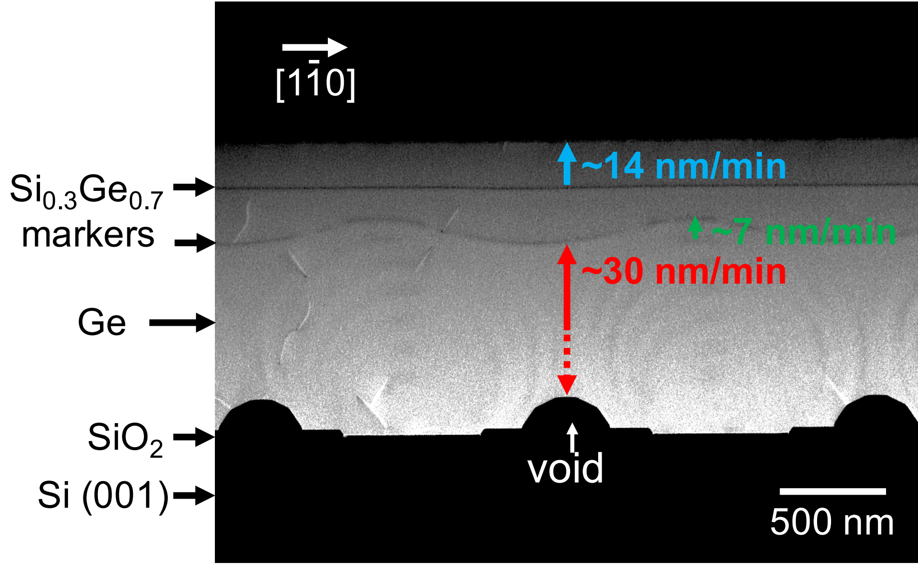

Figure 8.4: A (110) cross-sectional STEM image of a coalesced Ge layer with $Si_{0.3}Ge_{0.7}$ demarcation layers showing difference of growth rates.

be an interesting future work.

8.2 Temperature Dependence of PL from Coalesced Ge Layers

8.2.1 Theoretical Background

Temperature dependence of PL reveals energy gap between Γ-valley and L-valley in conduction band. As reported in GeSn, temperature dependence of PL changes from positive relation to negative relation as band structure changes from indirect to direct [138]. Figure 8.5 shows schematic illustrations of (a) indirect (bulk Ge) and (b) pseudo-direct (n-type doped) band structure for Ge. In indirect bandgap (bulk) Ge, as schematically indicated in Fig. 8.5 (a), some carriers in L-valley are thermally excited to Γ-valley. Thus, PL from bulk Ge increases as temperature increases. In n-type (pseudo-direct) Ge, as schematically indicated in Fig. 8.5 (b), excited carriers are already at Γ-valley, and thus the PL from n-type Ge should be independent of temperature, or might decrease as temperature increase due to phonon scattering. In the case for 0.25 % tensile strained Ge, pseudo-direct bandgap is achieved with n-type concentration of 3.5×10^{19} cm^{-3} [139].

8.2.2 Measurement setup

Temperature dependence of PL from coalesced Ge layers were observed in the temperature range of 4–200 K using a 532-nm laser. Figure 8.6 shows a schematic illustration of μ-PL measurement system used at low temperature (4–200 K). The sample surface was illuminated from the top, and the diameter of $1/e^2$ intensity for the excitation laser was approximately 20 μm. The diameter of $1/e^2$ intensity was again wider than $W_{window} + W_{mask}$, indicating that

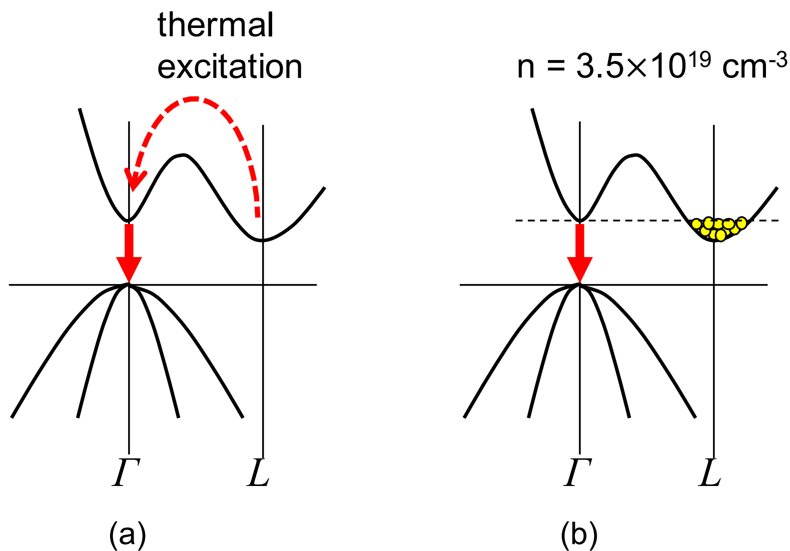

Figure 8.5: Schematic illustrations of (a) indirect (bulk Ge) and (b) pseudo-direct (n-type doped) band structure for Ge.

PL from Ge on Si seeds and from Ge above SiO_2 masks are not separable. PL emission was collected from the top and detected through a monochrometer with an InGaAs detector. The InGaAs detector can detect 800–1700 nm wavelength range. The power of the excitation laser was 490 mW, corresponding to the power density of 156 kW/cm^2. Measured samples were put in a chamber, and the chamber was vacuumed to be 0.6 Pa. The chamber was cooled down to 4 K first, and then PL measurements were carried out by increasing the temperature up to 200 K.

8.2.3 Results and Discussions

Figure 8.7 shows PL spectra obtained at 4–200 K from (a) P diffused coalesced Ge and (b) bulk Ge, and (c) integrated PL intensity (1200–1700 nm) as a function of temperature. Both P diffused coalesced Ge and bulk Ge shows PL peak around 1.4–1.5 μm. The observed PL peaks are shifted to shorter wavelength compared to PL peaks at room temperature (as in Fig. 8.3 (a)). Such blue shift of PL peaks are ascribed to temperature dependence of bandgap of Ge. Correlation between temperature (T [K]) and Ge direct bandgap (E_g [eV]) is expressed as Eq. (8.1) [140].

$$E_g = 0.89 - \frac{5.82}{10^4 \times T^2 \times (T + 296)}. \tag{8.1}$$

As for the PL intensity, it is clearly shown that the P diffused coalesced Ge has smaller dependence of integrated PL intensity on temperature compared to bulk Ge. However, the PL intensity from P diffused coalesced Ge still has a positive correlation to temperature, i.e.,

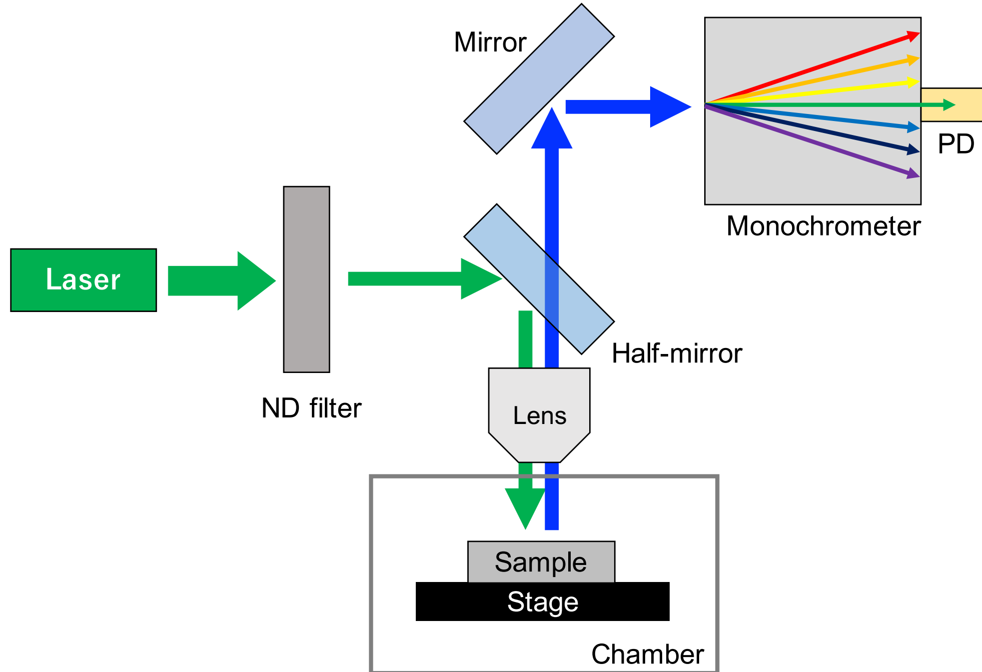

Figure 8.6: A schematic illustration of μ-PL measurement system used at low temperature (4–200 K). Green arrow indicates 532-nm excitation laser, and blue arrow indicates PL from Ge.

PL intensity increases as temperature increases. As mentioned in theoretical background (section 8.2.1), PL intensity from indirect (bulk) Ge should increase as temperature increases. On the other hand, if Ge is tensile-strained and n-type doped to be pseudo-direct bandgap (tensile-strain of 0.25 % and n-type concentration of 3.5×10^{19} cm^{-3} [139]), PL intensity should be independent of temperature. Thus, if Ge is n-type doped but the n-type dopant concentration is not enough to be pseudo-direct bandgap, the temperature dependence of PL intensity should be smaller than bulk Ge case (Fig. 8.5 (a)), but PL from n-type Ge still increases as temperature increases. Taking into account the SIMS profile in Fig. 7.7 showing n-type dopant (P) concentration of $\sim 1 \times 10^{19}$ cm^{-3}, the PL intensity from P diffused Ge is predicted to have smaller dependence on temperature than bulk Ge.

8.3 Optical Pumping Measurements

In vertical PL measurements, a small area (2 μm in diameter) of coalesced Ge is excited, and thus radiative optical mode is excited. In semiconductor lasers, however, active layers (in this case, tensile-strained n-type Ge) should be uniformly excited so as the active layers to be resonators. Many types of resonators have been reported toward Ge laser such as fabry-pérot (FP) [41, 42], microdisk [110, 111], and microring [109]. In this work, FP resonator structure

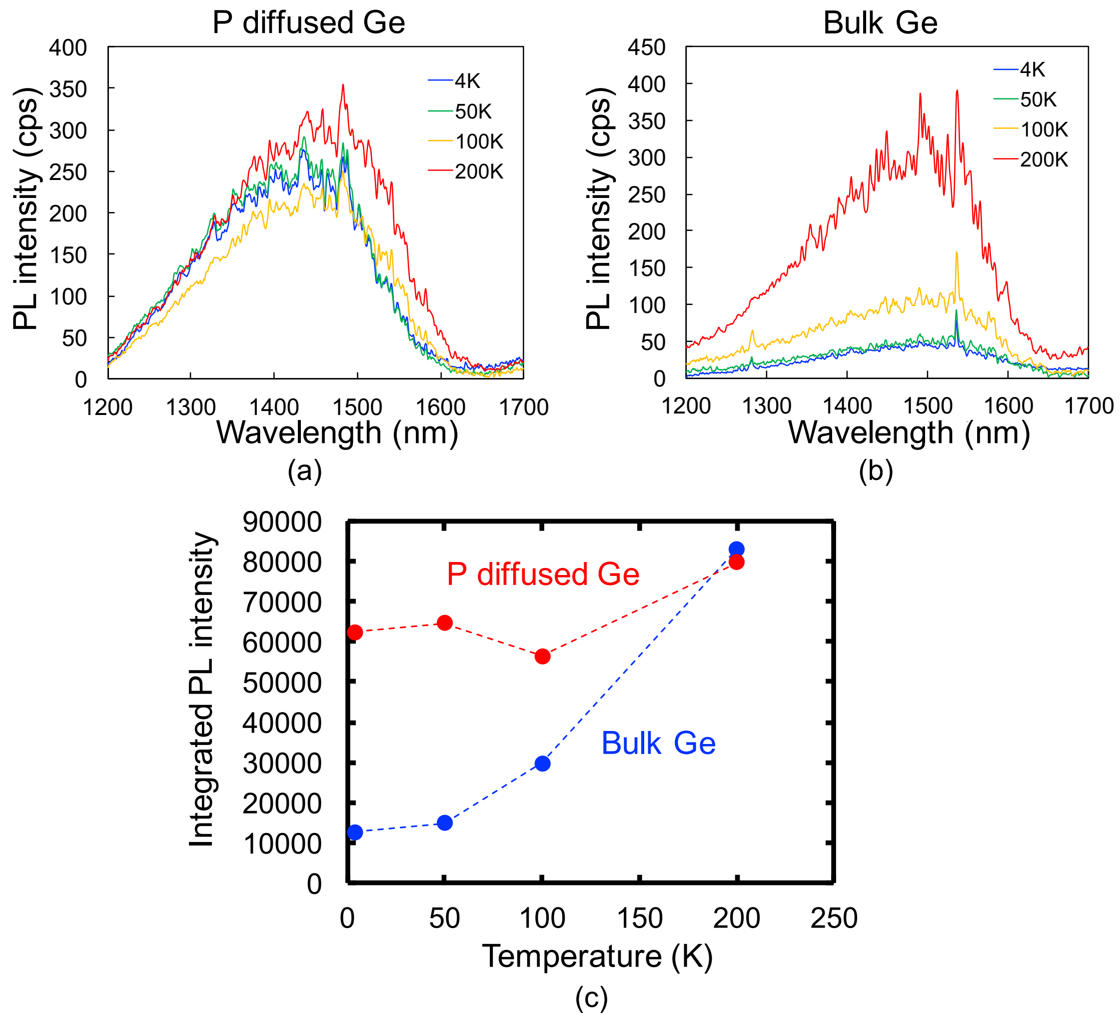

Figure 8.7: PL spectra obtained at 4–200 K from (a) P diffused coalesced Ge and (b) bulk Ge, and (c) integrated PL intensity (1200–1700 nm) as a function of temperature.

is employed since circle-shaped structure is difficult to fabricate as described in section 4.4.

8.3.1 Fabrication of Fabry-Pérot Resonators

Figure 8.8 shows the fabrication process of FP resonators employing coalesced Ge. The fabrication process is as follows:

1. SEG Ge layers were grown on a Si substrate at 700 °C, and they coalesced with adjacent ones forming flat-top films.

2. PSG with P concentration of $\sim 4 \times 10^{21}$ cm^{-3} was deposited on the coalesced Ge layers by SACVD at 480 °C.

3. P was diffused into the coalesced Ge layers by thermal annealing at 850 °C for 5 min.

4. The PSG layers were removed by buffered-HF (BHF). The SiO_2 layers for SEG masks were simultaneously removed by the BHF etching.

5. Surfaces of the coalesced Ge layers were oxidized in order to reduce surface NRR velocity, as will be described in Appendix I. The oxidation was carried out at 500 °C for 30 min, forming ~20-nm-thick GeO_2 on the coalesced Ge layers.

6. A ~200-nm-thick SiO_2 layer was deposited in order to protect GeO_2 layers, which is so chemically unstable as usually removed by DI water [73].

7. The coalesced Ge layers, 4 mm long in [110] direction, were cut to form mirror edges at Ge/air interfaces at the edges of the coalesced Ge layers.

Finally, 3 mm long FP resonators were fabricated.

The samples were cleaved using diamond pens at the first trial, but as the result of process optimization, the samples were cut using laser dicer and the edges were polished by focused ion beam (FIB) in order to form smooth mirror edges. Longer L_{FP} is more preferable than shorter one for FP laser because longer L_{FP} effectively reduce the negative effect at the cleaving/cutting edges, i.e., light scattering when light reflect at the edges [41]. L_{FP} was defined by the cutting process to be 3 mm, which is shorter than the length of excitation laser used in the measurement system; 4 mm,

The width of the FP resonators W_{FP} was defined by SEG masks, and set as 300 μm expecting "gain guide" operation at first, but finally set as ≤10 μm, which is narrower than the width of excitation laser (20 μm). The the excitation laser wider than the FP resonator enables uniform excitation, which is preferable to laser operation.

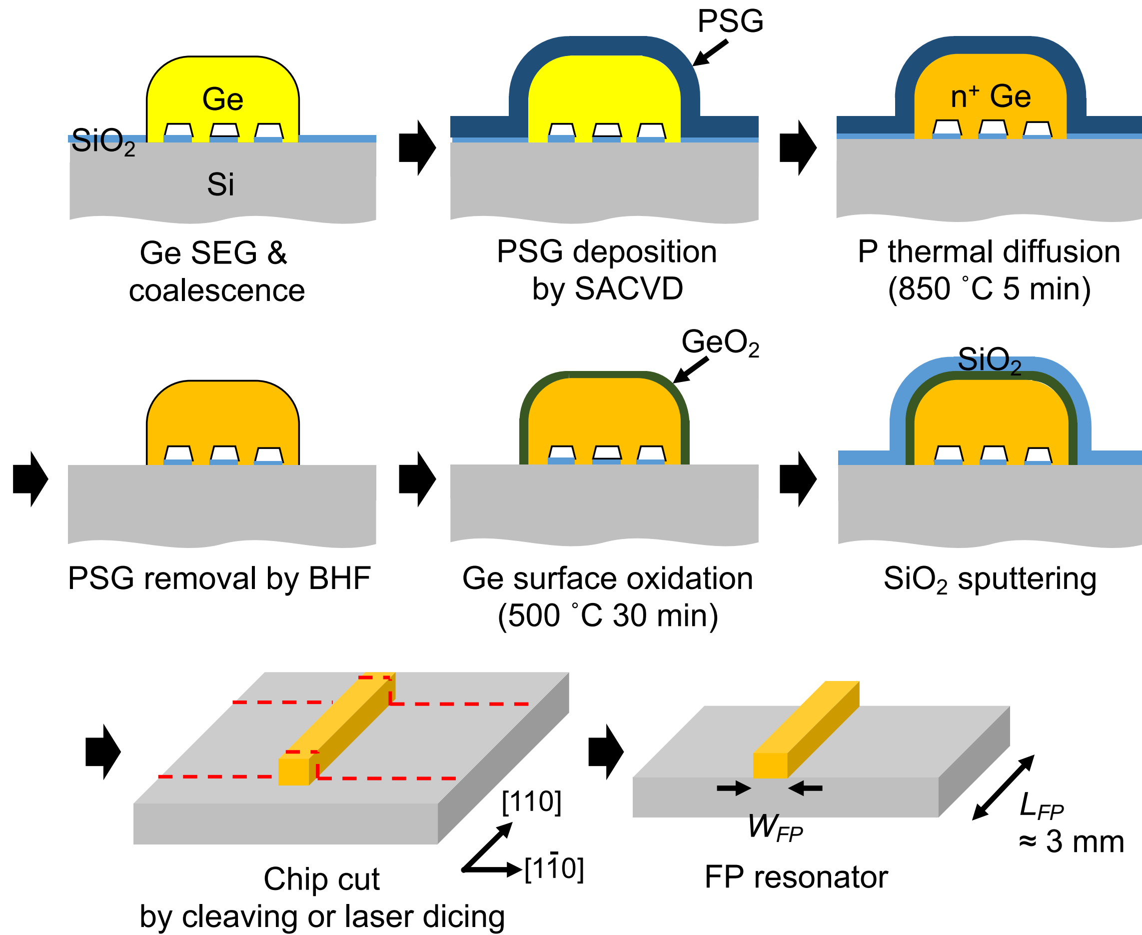

Figure 8.8: Schematic illustrations of fabrication process flow for a FP resonator

8.3.2 Measurement Setup

Different from the PL measurements, the excitation laser illuminated samples from top and light was emitted from coalesced Ge layers in lateral direction, as schematically shown in Fig. 8.9. A 1.07-μm fiber laser was used for continuous-wave (CW) and micro-sec pulsed excitation, and a Q-swiched 1.06-μm fiber laser was used for nano-sec pulsed excitation. The penetration depth in Ge at 1.06–1.07 μm is $\sim$1 μm.

For CW and micro-sec pulsed excitation, the 1.07-μm fiber laser was expanded by a beam shaper to be a rectangle shape, which is 4 mm long and 20 μm wide. The FP resonators fabricated through the process shown in Fig. 8.8 were located on a 3D movable sample stage, and excited from the top surface. Light from the FP resonator was emitted in lateral direction as shown by blue arrow in Fig. 8.9, and collected by a Ge or InGaAs photodetector (PD) through a monochrometer. A trans-impedance amplifier (TIA) is integrated with the Ge PD,

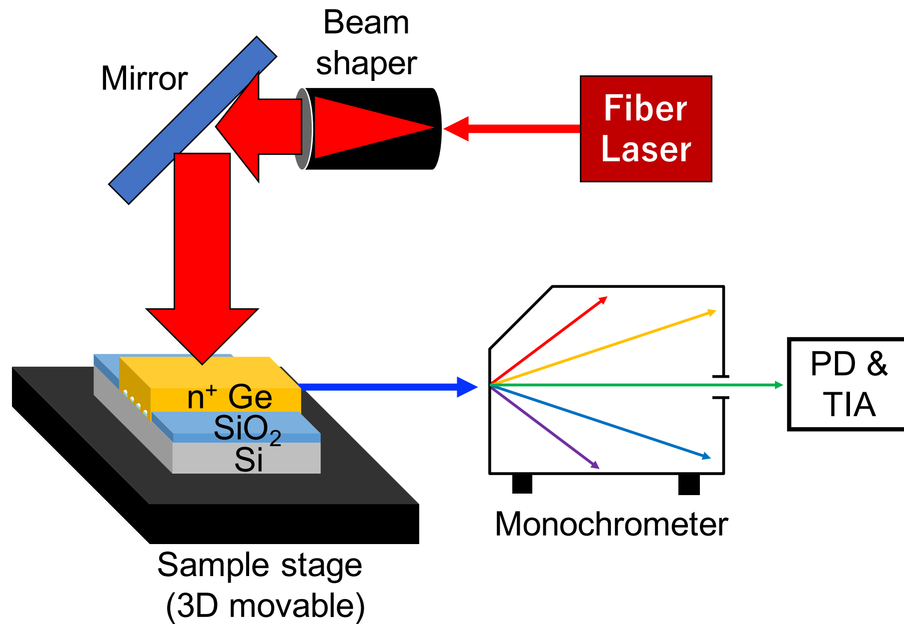

Figure 8.9: Schematic illustrations of optical pumping measurement system for CW and micro-sec pulsed excitation

and the signal gain was set as 1×10^8 V/A. The position of excited area was controlled by a galvano mirror system. The alignment between the excitation laser and the FP resonators was roughly carried out using a guiding laser (wavelength = 633 nm), and precisely done using a near-infrared (NIR) camera. Finally, the optical pumping measurements were carried out where the light emission from the FP resonators became maximum.

Figure 8.10 shows schematic illustrations of the optical pumping measurement system for nano-sec laser excitation. The 1.06-μm fiber laser of 7 mm Φ large spot was used through a short pass filter (SPF), cutting edge of 1.2 μm, to remove any unintentional emission within the measured wavelength range. The FP resonators were tilted for 90°, and the top surface of FP resonators were illuminated by nano-sec laser. The light emission from a FP resonator is gathered through a 50× objective lens and detected by an InGaAs array detector (detection range; 800–2200 nm) through a long pass filter (LPF; cutting edge of 1100 nm) and a grating. In Fig. 8.10, light from input laser is indicated as a red arrow, and light from a FP resonator is indicated as blue arrows. Since the laser diameter (7 mm Φ) is much lager than a FP resonator (3 mm long × 10 μm wide), the alignment between the excitation laser and the FP resonator was carried out using a guiding laser (wavelength = 633 nm). The alignment between the FP resonator and the objective lens was carried out by using a CCD camera through the objective lens.

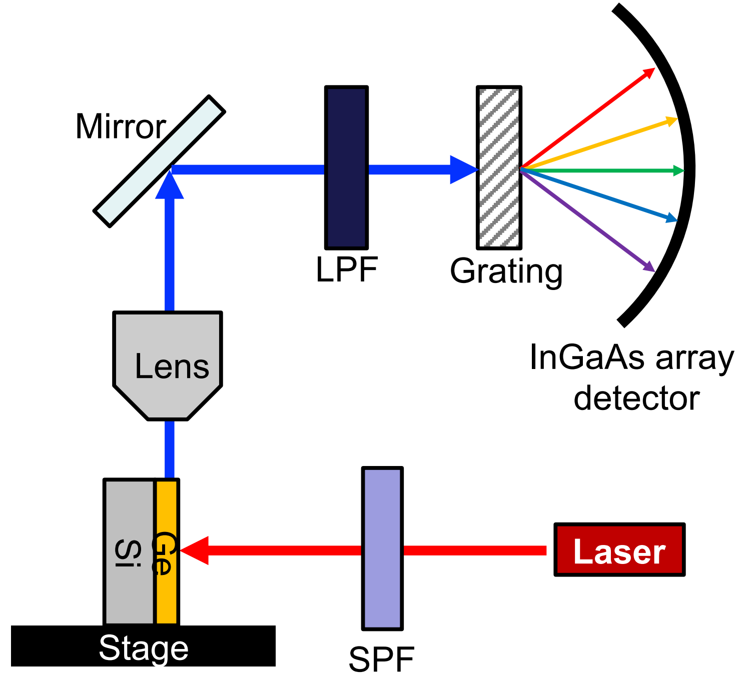

Figure 8.10: Schematic illustrations of optical pumping measurement system for nano-sec pulsed excitation

8.3.3 Light Emission Under Excitation by a CW Laser

For the first trial, a CW laser was used to illuminate the 300-μm-wide FP Ge resonators. Figure 8.11 shows (a) light emission spectra from the coalesced Ge and (b) light emission intensity as a function of input power density. Note that the spectra shown in Fig. 8.11 (a) reflects the wavelength dependency of the PD responsivity. In this case, the sample with W_{window} = 0.7 μm and W_{mask} = 0.6 μm was used. As in Fig. 8.11, a clear threshold behavior was observed with the threshold power density of 18 kW/cm^2. The observed threshold power density is smaller than the one reported in Ref. [41], which was 30 kW/cm^2 corresponding to the threshold current density of 35 kA/cm^2.

As shown in Fig. 8.11 (a), however, sharp resonance peak was not observed, which should be observed if the threshold behavior is originated from lasing. Therefore, the threshold behavior shown in Fig. 8.11 (b) should be not lasing but an amplified spontaneous emission (ASE).

The sample after the optical pumping measurements were observed by an NIR microscope and shown in Fig. 8.12. The white area is Ge, and the black area is Si substrate. It is clearly shown that the center of the Ge area changes its color to be black. The black area in Ge would be melt Ge owing to the high-power illumination by the CW laser. Thus, in the next step, a micro-sec pulsed laser will be used to excite the Ge FP resonators, which should induce less

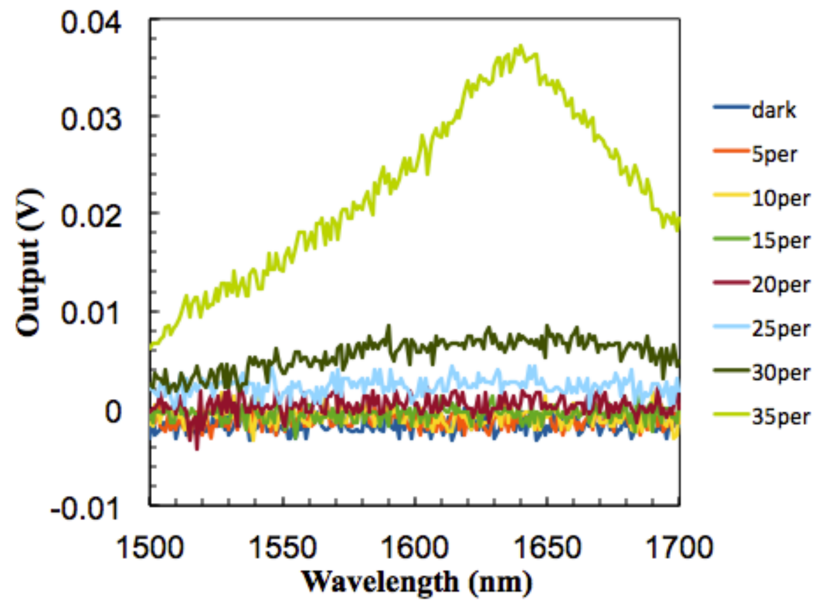

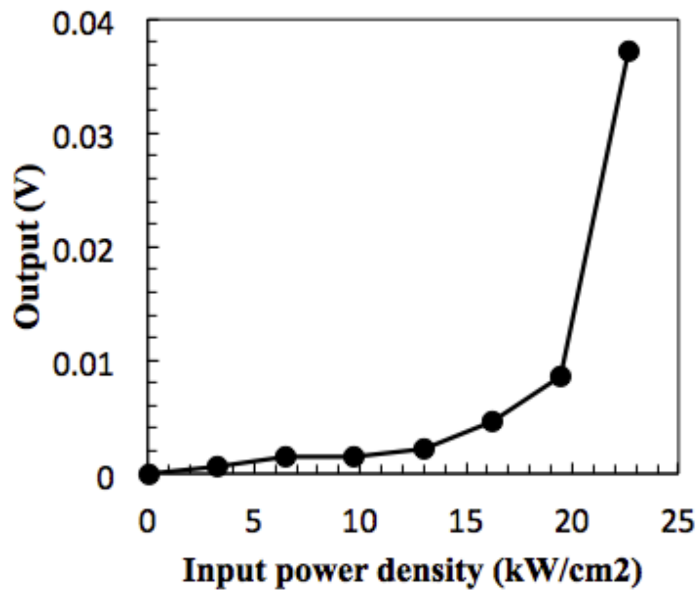

Figure 8.11: (a) Light emission spectra from the coalesced Ge and (b) light emission intensity as a function of input power density

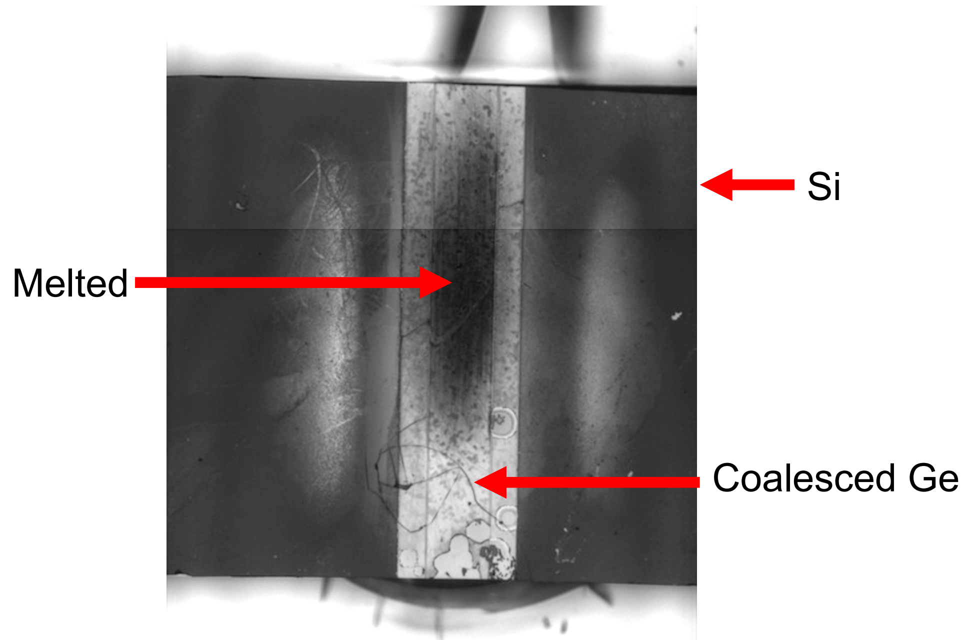

Figure 8.12: A plan-view NIR microscope image of a coalesced Ge after optical pumping measurements by CW excitation

heat than a CW laser.

8.3.4 Light Emission Under Excitation by a Micro-sec Pulsed Laser

In order to avoid heating up of Ge FP resonators during optical pumping measurements, a micro-sec pulsed laser was used for excitation. The pulse length of the laser was 50 μs, and the repetition speed was 10 kHz. In addition to the change of excitation laser from CW to micro-sec pulse, the width of Ge FP resonators become narrow (300 μm $\rightarrow$ $\leq$10 μm). The narrower structure of Ge FP resonators enables uniform excitation of the resonators using the laser (width = 20 μm), which is preferable to achieve a lasing operation.

Figure 8.13 shows (a) Light emission spectra and (b) integrated emission intensity as a function of input power density. Similar to the results shown in Fig. 8.11, excitation with a CW laser, a clear threshold behavior was observed with the threshold power density of 18 kW/cm^2, but any resonance-origin sharp peak was not observed. Thus, the threshold behavior should be ascribed to an ASE again.

In order to achieve a lasing operation instead of ASE, the optical net gain from the Ge FP resonators should be increased. Since the tensile strain and n-type doping level is same level as the reported Ge laser [41], I tried to find the cause of optical loss in our Ge FP resonators. Then, I found that the rough cleaving edges in our structure should cause light scattering, i.e., optical loss. Figure 8.14 shows a bird's eye view SEM image of an as-cleaved edge of coalesced Ge. Rough cleaved edge is shown, which is also observed in cross-sectional

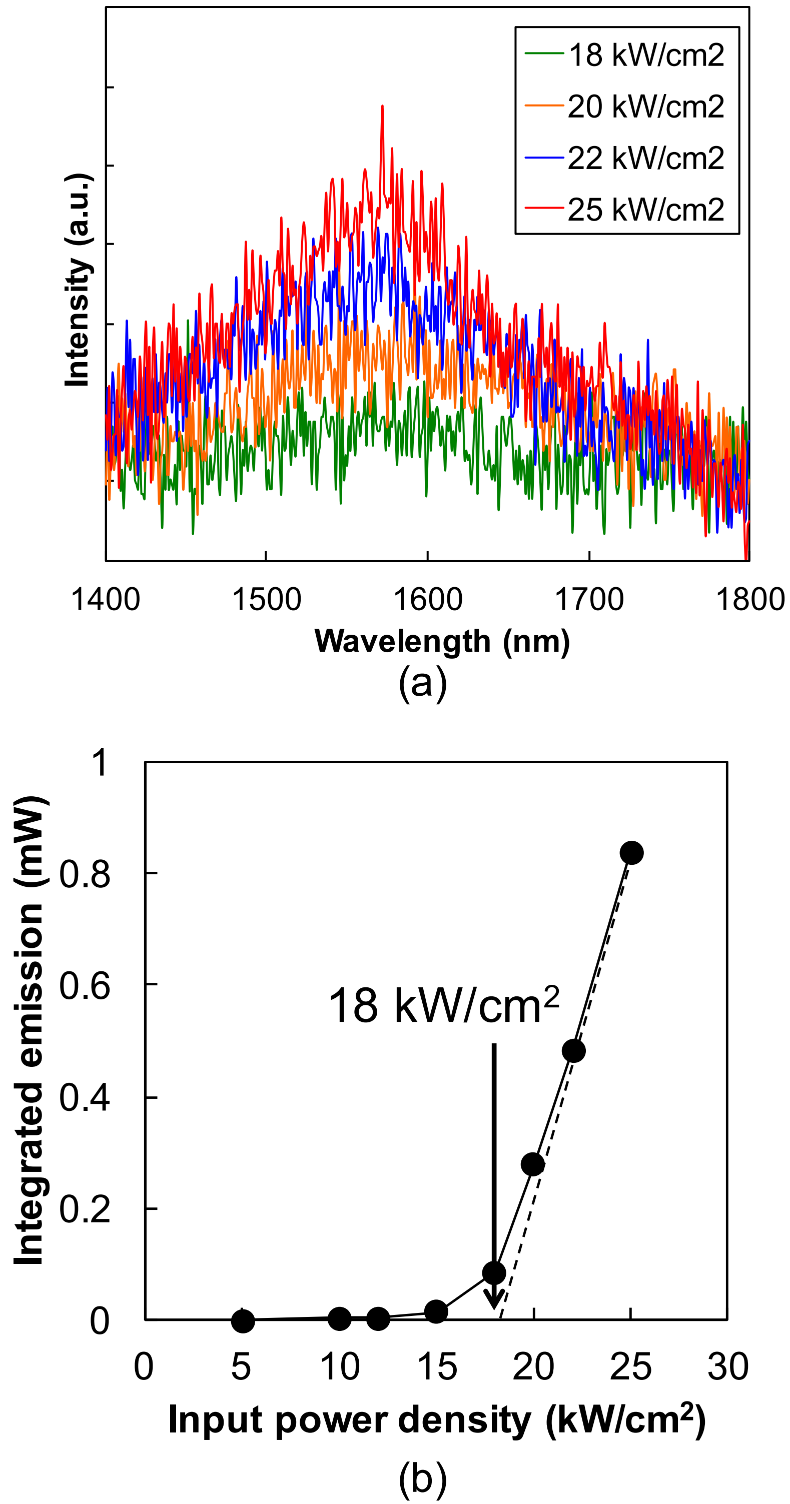

Figure 8.13: (a) Light emission spectra and (b) integrated emission intensity as a function of input power density

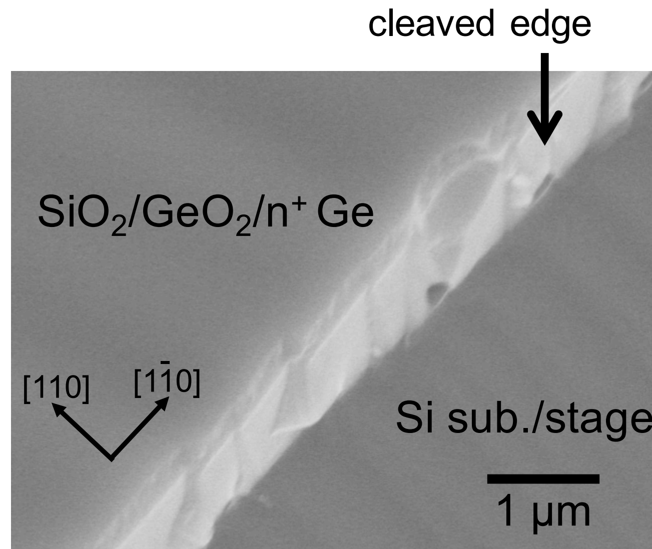

Figure 8.14: A bird's eye view SEM image of an as-cleaved edge of coalesced Ge

SEM observations (Figs. 4.8(c) and 4.8(e)). The edges are clearly rougher than the reported Ge laser [41]. The rough cleaving edges would be originated from strain distribution in cross-sectional dimension, as shown in Fig. 7.1 (a).

Thus, in order to reduce the light scattering at the cleaving edges, I tried to cut the substrate using a laser dicer instead of simple cleaving using a diamond pen. Laser dicer can cut substrates by inducing defects, which assist substrate cleaving. However, as shown in Fig. 8.15 (a), the Ge FP resonators melted for ~25 μm from the edges as the result of the laser dicing. Regardless of the cleaving method, the cleaving edges are need to be polished in order to reduce light scattering. Thus, the edges of the Ge FP resonators were polished using Ga focused ion beam (FIB) as shown in Fig. 8.15 (b).

As the result of FIB polishing, the edges of Ge FP resonators became smooth as shown in Fig. 8.16. The smoother cleaving edge should bring less scattering loss at the edges.

Figure 8.17 (a) shows integrated intensities of light emission from a Ge FP resonator as a function of input power density, and (b) shows a typical spectra of light emission from the Ge FP resonators. It is clearly shown that the FIB polished edges brought increase of light emission from the Ge FP resonators, indicating the reduction of optical loss. In Fig. 8.17 (b), there is a sharp peak on the "after FIB" spectrum around 1750 nm.

In order to see the reproducibility of the peak around 1750 nm, shown in Fig. 8.17 (b), light emission spectra were observed for 10 times and the average of the 10 measurements is shown in Fig. 8.18, considering the responsivility of PD. The peak at 1750 nm was reproduced as indicated by a black arrow in Fig. 8.18. Thus, the peak at 1750 nm could be a resonance

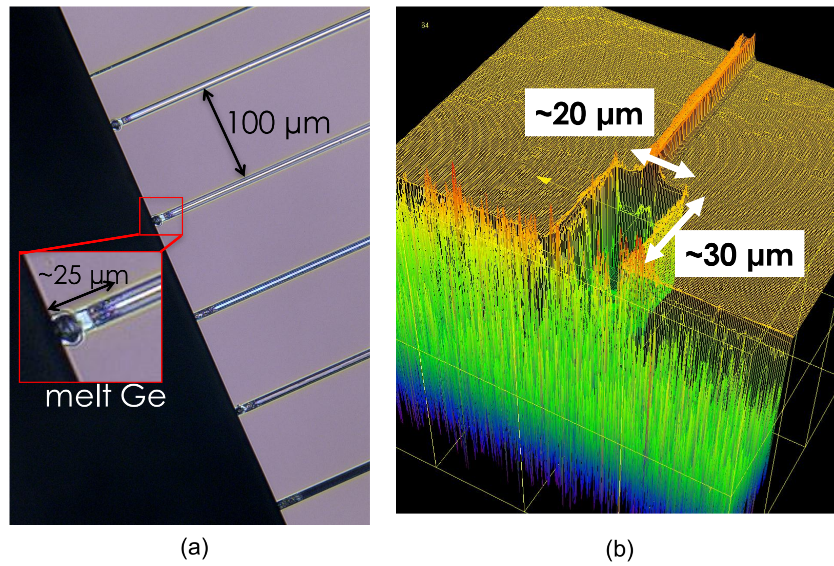

Figure 8.15: (a) An optical microscope image of melted Ge FP resonators after laser dicing and (b) a 3D laser microscope image of FIB polished edge of a Ge FP resonator

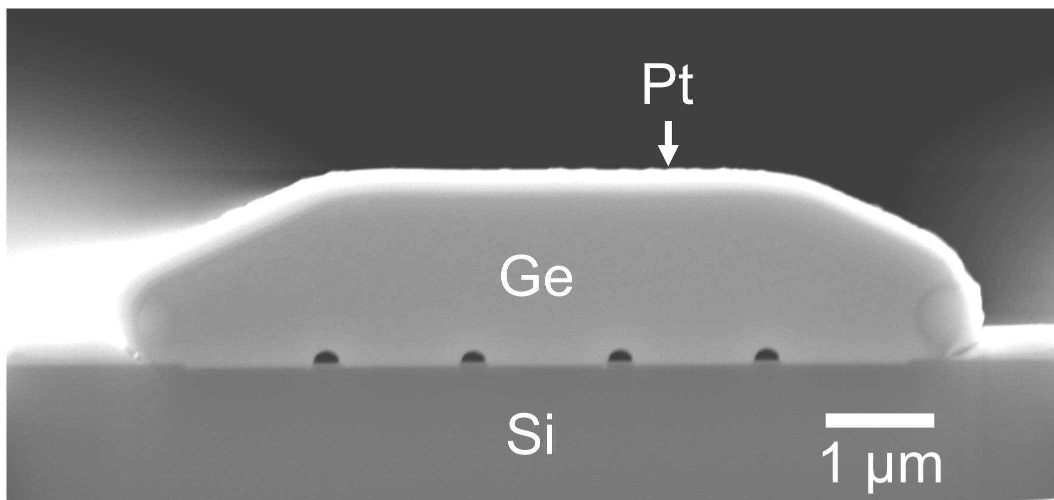

Figure 8.16: A cross-sectional SEM image of an FIB polished edge of Ge FP resonator

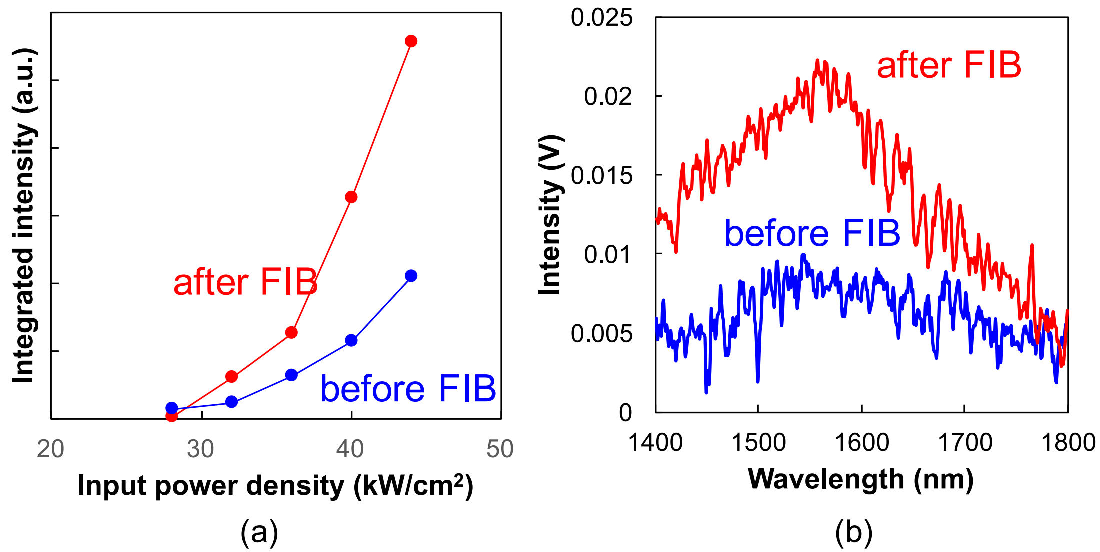

Figure 8.17: (a) Integrated intensities of light emission from a Ge FP resonator as a function of input power density, and (b) a typical spectra of light emission from the Ge FP resonators

peak, but the low signal-to-noise (S/N) ratio makes it difficult to analyze the peak and to find other smaller peaks. Because of the low S/N ratio, free spectra range (FSR) is difficult to be determined, leading it difficult to determine if it is resonance peak or not. Higher input power density is required for higher S/N ratio, which is limited by the laser.

In addition to the peak at 1750 nm, there is a broad peak around 1700 nm. The broad peak would be ASE, which is similar to the ones in Figs. 8.11 (a) and 8.13 (a). The red shift of the ASE peak from the bulk Ge (1.55 μm) would be ascribed to heating up. According to the correlation between temperature and direct bandgap of Ge (Eq. (8.1)), temperature of the Ge FP resonators is estimated as ~200 °C during the laser illumination. Such a temperature is low enough to avoid Ge melt, but in terms of operation at optical communication wavelength (1.53–1.625 μm), the red-shifted light emission is not preferable. Thus, further reduction of laser duration or cooling system is required to achieve lasing operation at optical communication wavelength.

Finally, the Ge FP resonators with inverted-rib structure (coalesced Ge) and slab structure (blanket Ge) are compared in terms of light emission intensity as a function of input power density. As shown in Fig. 8.19, both inverted-rib FP resonators and slab FP resonators show threshold-like behavior, and the observed threshold power densities were clearly, inverted-rib structure < slab structure. Ge FP resonators with inverted-rib structure show threshold power densities of 15–30 kW/cm^2, while Ge FP resonators with slab structure show those of 30–35 kW/cm^2. I.e., the inverted-rib structure formed through the coalescence of SEG Ge layers

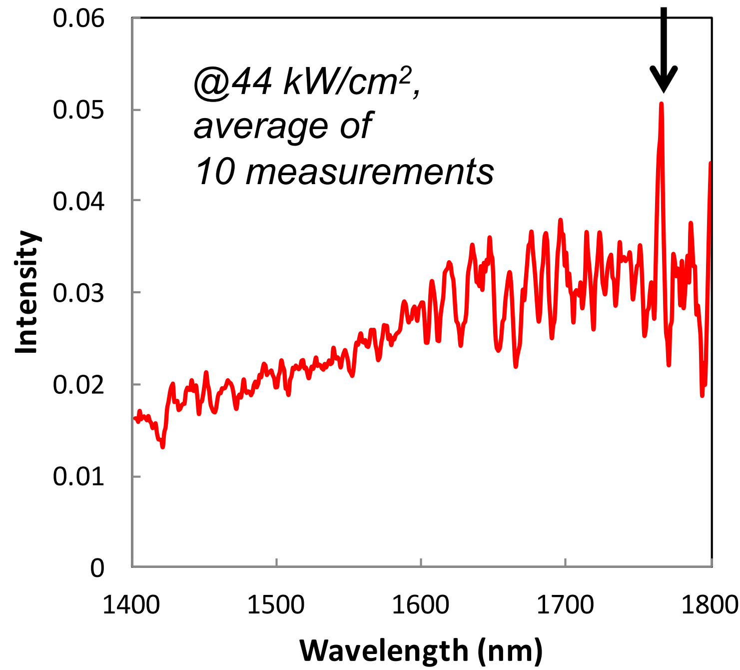

Figure 8.18: Light emission spectrum obtained through measurements for 10 times. The peak indicated by black arrow reproduced during the 10 measurements.

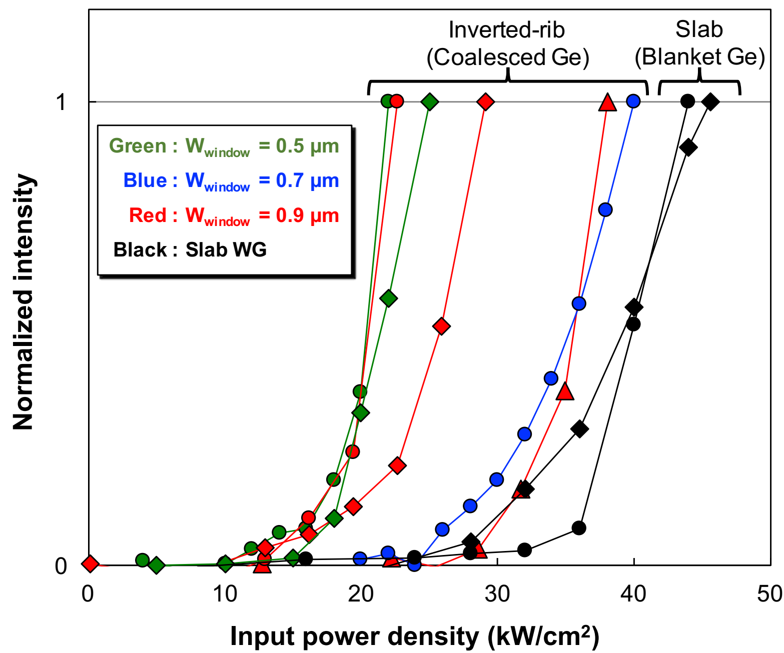

Figure 8.19: Integrated emission intensities from Ge FP resonators

results in reduction of the threshold power densities for 15–60 %. Note that the observed threshold power densities from slab FP resonators are almost equal to the reported threshold of optically pumped Ge laser [41]. Considering the injected carrier concentration, threshold power densities of 15 kW/cm^2 correspond to the J_{th} of 17 kA/cm^2.

The observed threshold power densities show tendency that the narrower W_{window}, i.e., smaller APR, brings smaller threshold power densities in Ge FP resonators with the inverted-rib structure. This tendency is consistent with the relation of APR and TDD shown in Fig. 5.6. I.e., smaller APR leads smaller TDD, indicating that reduced chances of defect-assisted NRR in Ge. However, it is difficult to conclude the relation between APR and the threshold power densities because of small amount of data and low reliability.

8.3.5 Light Emission Under Excitation by Nano-sec Pulsed Laser

As described in section 8.3.2, a Q-switched fiber laser was employed to excite inverted-rib Ge layers with nano-sec pulsed laser. The pulse length of the excitation laser was set as 5 ns, and the repetition frequency was set as 50 kHz. Input power was measured using a power meter, and power density was calculated assuming rectangular pulses taking into account the pulse length and the frequency. Measured samples were the ones measured by the micro-sec excitation laser, i.e., 3 mm long and 10 μm wide, and FIB polished as shown in Fig. 8.15 (b) and Fig. 8.16.

Figure 8.20 shows spectra of light1600–1700 nm as input power density becomes 190–300 kW/cm^2. The peak position is pointed by black arrows, indicating that the peak shifts to longer wavelength as the input power density increases. The peak shift would be ascribed to the heating up of the sample as discussed in micro-sec pulsed excitation part. The heating up issue happens even with nano-sec pulsed excitation, when the input power intensity reaches 200–300 kW/cm^2. According to the relation between temperature and direct bandgap of Ge (Eq. (8.1)), temperature of Ge FP resonator is estimated to be 120 °C when it is illuminated by the nano-sec laser at the power density of 300 kW/cm^2.

Since the light emission from direct bandgap of Ge is obtained at 1600–1700 nm, the integrated emission intensities were obtained in the range of 1550–1800 nm. Figure 8.21 shows the integrated emission intensity as a function of the input power density. From 0 kW/cm^2 to 150 kW/cm^2, the light emission from the Ge FP resonator was not observed. The integrated emission intensity increases where input power density is 150 kW/cm^2, and the intensity again increases where input power density is 250 kW/cm^2.

As shown in Fig. 8.20, no resonance peak was observed from the Ge FP resonator. Thus, the light emission is again considered to be ASE. In the nano-sec excitation measurement, disalignment between the Ge FP resonator and the objective lens would prevent observation of resonance peak, as schematically illustrated in Fig. 8.22. Resonated light in a FP resonator

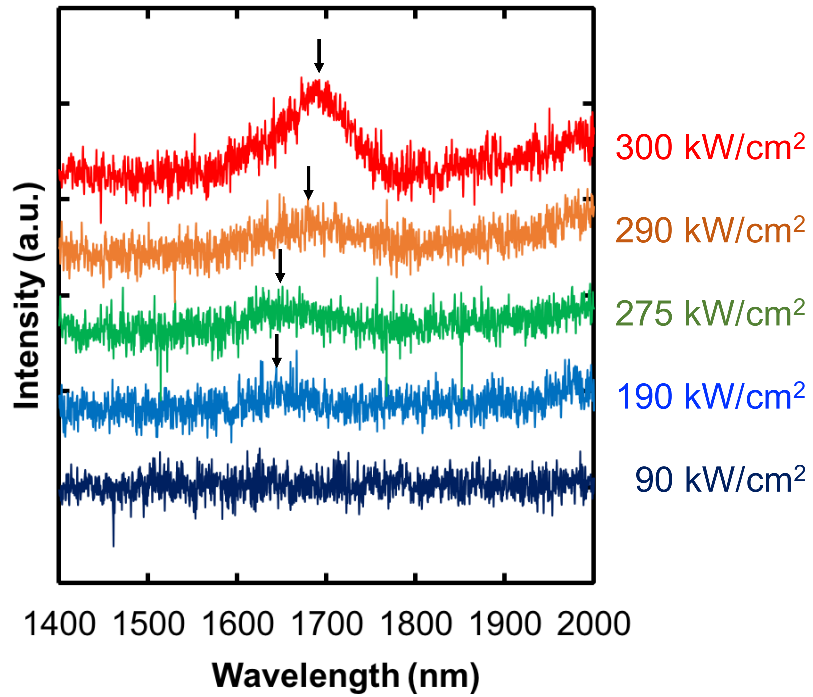

Figure 8.20: Spectra of light emission from FP resonators excited by a nano-sec pulsed laser

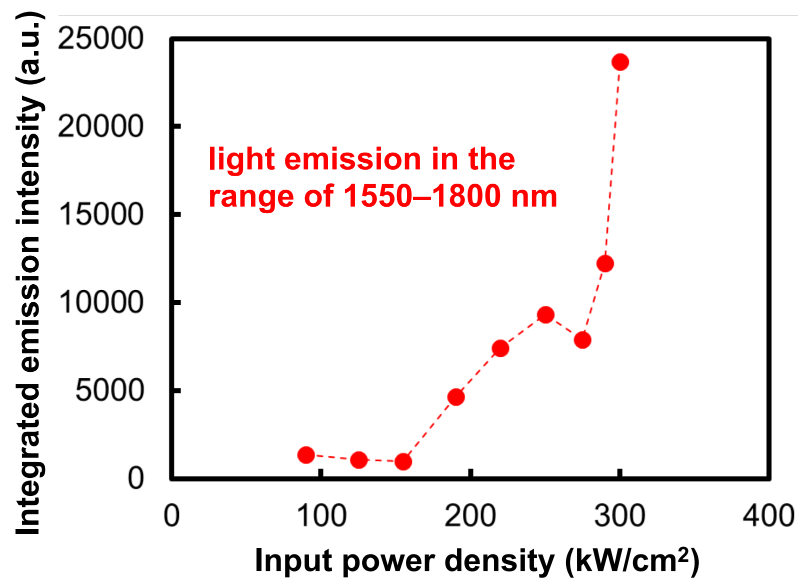

Figure 8.21: Integrated emission intensity (in the range of 1550–1800 nm) as a function of input power density

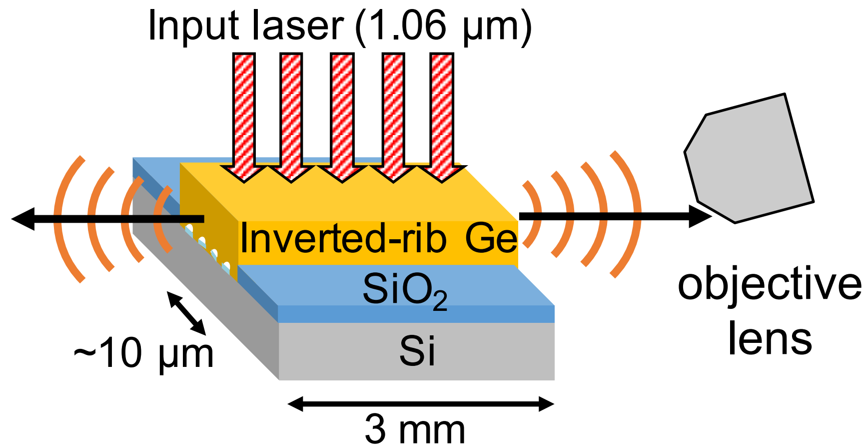

Figure 8.22: A schematic illustration showing disalignment between an inverted-rib Ge FP resonator and the objective lens

is directed to be parallel to the length direction of the FP resonator. In the case for inverted-rib Ge FP resonator, resonated light is emitted as the blue arrow in Fig. 8.22, and ASE is emitted as the orange circular arcs in Fig. 8.22. If the objective lens is tilted against the Ge FP resonator, resonated light is not collected but only ASE is observed.

The observed threshold-like point for the nano-sec laser excitation (150 and 250 kW/cm^2) is 5–10 times higher than that for micro-sec laser excitation (15–35 kW/cm^2). This increase of threshold-like point is reasonable considering the ratio of pulse length and interval length. For micro-sec laser excitation, pulse length was 50 μs and frequency was 10 kHz, corresponding to interval length of 100 μs. Then, the ratio of pulse length and interval length is $\frac{50\mu s}{100\mu s} = 0.5$. For nano-sec laser excitation, on the other hand, pulse length was 5 ns and frequency was 50 kHz, corresponding to interval length of 20 μs. The ratio of pulse length and interval length is $\frac{5ns}{20\mu s} = 0.00025$. Thus, effective duration for excitation by micro-sec laser is 2000 times longer than that by nano-sec laser. The effectively shorter duration for excitation by nano-sec laser would bring weaker ASE, leading higher threshold-like point.

8.4 Discussions: Toward Low J_{th} Ge LDs

8.4.1 Optimization of the Measurement System

In terms of measurement system, following optimization will be effective:

(i) to inject more carriers using micro-sec laser, i.e., stronger excitation, and

(ii) to avoid disalignment between a FP resonator and the objective lens.

(i) To inject more carriers, i.e., stronger excitation, will simply bring stronger light emission from Ge. 44 kW/cm^2, shown in Fig. 8.18, is the strongest power in the current system.

However, the illumination at 44 kW/cm^2 with 1.07 μm laser corresponds to current injection at 51 kA/cm^2 in terms of carrier concentration, which is 6–10 times lower than the reported J_{th} in reported Ge LDs. Thus, the stronger excitation will be effective to see laser operation. For example, if the width of laser spot (currently 20 μm) is reduced to 10 μm without any optical loss, input power density is doubled. Such optimizations in illumination system will help.

(ii) To avoid disalignment between a FP resonator and an objective lens, a simple solution is to use an objective lens with smaller magnification. In the present work, an objective lens with 50× magnification was used. Since there was an aperture 500 μm in diameter behind the objective lens, 10 μ in diameter was actually observed. Thus, if the objective lens is replaced to the one with 10× magnification, 50 μ in diameter will be observed. However, the use of smaller magnification lens will bring worse resolution of wavelength. Finer alignment is required in any case to obtain sharp peak from FP resonators.

8.4.2 Optimization of the Active Ge Layers

In addition to the measurement system, optimization of the active Ge layers should be effective to reduce J_{th}, i.e.,

(iii) to remove Pt layer on top deposited for FIB polishing,

(iv) further reduction of TDD by reducing APR,

(v) to increase P concentration,

(vi) to use micro cavity structure expecting the Purcell effect,

and, (vii) Optimization of the thickness of active Ge layer.

(iii) To remove Pt layer on top deposited for FIB polishing will reduce light scattering and/or absorption at the FIB polished edges of the Ge FP resonators. Pt protection layers were deposited at several μm from the polished edges in order to protect Ge from FIB damage. Pt removal, or FIB polishing without Pt will be needed to reduce losses by Pt at the edges.

(iv) Further reduction of TDD by reducing APR, as predicted by the calculation shown in Fig. 3.8, will enable further reduction of defect-assisted carrier recombination in Ge LDs. According to the calculation, TDD as low as 10^6 cm^{-2} will be achieved if APR is as low as 0.1, which will enable TD-free Ge LDs.

(v) To increase P concentration will bring reduction of J_{th}, as shown in Ref. [141]. Optimization of the thermal diffusion conditions should be performed in order to increase P concentration in Ge. Since the solid solubility of P in Ge is higher than mid-10^{19} [142], it will be possible to increase P concentration in Ge by process optimization.

(vi) To use micro cavity structure will bring the reduction of J_{th} thanks to the Purcell effect [109, 143, 144]. Micro disks [111, 145], micro rings [109], and micro FP resonators with distributed Bragg reflector [44, 146] are widely used as micro resonators. These micro

resonators can be fabricated using coalesced Ge, once flat-top surface is formed.

(vii) Optimization of the thickness of active Ge layer will reduce J_{th} by reducing the layer thickness. Since thicker active layer cause smaller concentration of carrier when applied current density is constant, J_{th} is in reverse proportion to the thickness of the active layer. Thus, J_{th} will be reduced as the layer thickness is reduced. In the present study, the thickness of the active layer was ~1 μm. A simple way to reduce the thickness of the active layer is to polish the coalesced Ge. Chemical mechanical polishing with diluted H_2O_2 can reduce thickness of Ge keeping top surface flat [147]. Thermal oxidation followed by wet etching using HF may reduce thickness of Ge keeping top surface flat without any mechanical damage, while oxidation and etching should be repeated in order to reduce the thickness of Ge layers for hundreds of nano meters.

Assuming the active layer of 300-nm-thick, with optimized measurement conditions, APR = 0.1, and P concentration of 4.5×10^{19} cm^{-3}, J_{th} of 1.8 kA/cm^2 is theoretically calculated following the calculation in Ref. [48].

9 Summary and Future Outlook

The goal of this thesis was to propose a new method of TDD reduction toward Ge lasers based on theoretical calculation, to verify the method by experimental measurements and observations, and to design and show prototype for light emitting devices employing the TDD reduction method.
This chapter gives a brief summary of this dissertation and future outlook; further application of image-force-induced dislocation bending, ideal cross-sectional structure for Ge LDs, and possible applications of inverted-rib structure.

9.1 Summary

As briefly described in **Chapter 1**, the development of on-chip light-emitting devices has been one of the most challenging issues for practical application of Si photonics technique. Tensile-strained n-type Ge has been investigated as a on-chip laser material, and Ge LD has successfully been reported. However, reported threshold current density J_{th} was two orders of magnitude higher than theoretical prediction.

Toward low J_{th} Ge LD, the cause of the huge J_{th} should be revealed. Then, at first, the importance of the reduction of non-radiative recombination NRR toward Ge lasers were described in **Chapter 2**. It was shown that reduction of TDs in Ge and NRR at Ge surfaces are important factors to achieve Ge lasers with J_{th} as small as 10 kA/cm^2. It was also shown that the NRR at Ge surfaces can be reduced by surface oxidation, from mid-10^5 cm/s to the order of 10^3 cm/s.

For the reduction of TDs toward low J_{th} Ge LD, conventional TD reduction methods are not preferable because they have drawbacks in terms of applications for light-emitting devices. Thus, a novel method is proposed and verified for light-emitting device applications, as described in Chapters 3–6.

The proposal of a new method of TDD reduction toward Ge lasers were described in **Chapter 3** with theoretical model and numerical calculation. Image force was investigated on

a quantitative basis as a driving force of TD bending in SEG Ge. Image-force-induced TDD reduction was numerically calculated showing TDD reduction on the order of 10^{-2} when aperture ratio (APR) is as small as 0.1.

In **Chapter 4**, Ge growth in lateral direction (in [110] orientation) over SiO_2 masks was investigated. It was found that the Ge growth rate in lateral direction is related to the growth rate on {113} facets. It was shown that Ge epitaxial layers with voids are formed as the result of SEG Ge coalescence. Under the conditions employed in this work, SEG Ge layers coalesced when both W_{window} and W_{mask} are small enough. The coalesced Ge layers finally formed flat-top surfaces, as flat as RMS $\approx$ 1 nm, which is the same level as a blanket epitaxial Ge layer.

In **Chapter 5**, the verification of the theoretical model shown in chapter 3 was shown via measurements of TDDs using etch pit density (EPD) counting method. Observed TDDs well reproduced the calculated ones, supporting the model proposed in this work. In addition to the reduction of TDD, the distribution of TDs in coalesced Ge was consistent with the theoretical model, i.e., TDs in coalesced Ge layers accumulate above SiO_2 masks. It was also found that TDD re-increase, which has been observed in previous aspect ratio trapping researches employing SEG Ge coalescence, was not observed the coalesced Ge layers in this work on a TDD basis.

In **Chapter 6**, observations of TDs via transmission electron microscope (TEM) were shown. Cross-sectional TEM observations showed that the TDs in SEG Ge layers are bent to be normal to growth surfaces, which was predicted in the theoretical model. It was also found that a TD in a coalesced Ge layer is terminated to a void, which are also predicted by the theoretical model. In addition to those, cross-sectional TEM observations showed TD generation when SEG Ge layers coalesce. Plan-view TEM observations showed a unique behavior of TDs in coalesced Ge; TDs inclined to be parallel to substrate.

Chapters 7 and 8 describe the material design and measurements of light emission toward Ge lasers.

In **Chapter 7**, characterization and design of coalesced Ge will be described in view of a light emission material. Simulation of strain distribution and characterization of tensile strain in coalesced Ge layers were carried out via FEM simulation and Raman spectroscopy, respectively. It was found that 0.1–0.2 % tensile strain is uniformly induced in coalesced Ge layers. N-type doping of the coalesced Ge layers was described in this chapter employing thermal diffusion method. N-type Ge with a dopant (P) concentration of $\sim 1 \times 10^{19}$ cm^{-3} was formed by the thermal diffusion method. It was also described that inverted-rib cross-sectional structure, formed as the result of coalescence of SEG Ge, has advantage over conventional slab structure in terms of the reduction of NRR.

In **Chapter 8**, light emission characteristics were described via micro-photoluminescence (μ-PL) at room temperature, μ-PL at lower temperature (4–200K), and optical pumping measurements, as a feasibility study for light-emitting device applications. μ-PL measurements revealed that there are NRR centers in coalesced Ge, which is removed as the result of thermal diffusion of n-type dopant. Coalesced Ge after thermal diffusion shows a tendency that PL intensity increases as APR decreases. Such a tendency is consistent with the reduction of TDD, which is described in Chapter 5. μ-PL measurements at lower temperature (4–200K) revealed that the P diffused Ge has smaller temperature dependence of PL intensity, indicating that the L-valley is filled by n-type doping. Optical pumping measurements were carried out on Fabry-Pérot resonators. In optical pumping measurements, CW, micro-sec pulsed lasers, and nano-sec pulsed lasers were used as excitation lasers. Clear threshold-like behaviors were observed as the result of optical pumping measurements. However, obtained data would be ascribed to amplified spontaneous emission (ASE), but not lasing.

9.2 Future Outlook

9.2.1 Controlling trajectories of TDs

In the present work, TDs in Ge on Si were successfully reduced by image force. Extending the basic mechanism, i.e., TDs are bent to be normal to growth surfaces, trajectories of TDs would be controlled by designing some specific SEG masks.

Figure 9.1 shows schematic illustrations showing an idea to control trajectories of TDs. Grey area shows Si growth seed, blue area shows SiO_2 masks, and yellow area shows where Ge grows. Preparing SiO_2 SEG masks as Fig. 9.1 (a), Ge grows on Si area as shown in Fig. 9.1 (b). Key point is to make SEG Ge layers coalesce from the center to the edges; in Fig. 9.1, from the center to the top/bottom, as indicated by the black arrows in Fig. 9.1 (b). As predicted in Chapter 3 and verified in Chapter 6, TDs are bent to be normal to growth surface owing to image force. Thus, in the case for Fig. 9.1, TDs would be bent toward the edge of the coalesced Ge, and thus the center of the coalesced Ge (blue circled area in Fig. 9.1 (c)) would have lower TDD than other area. Based on this idea, TD-free area should be locally achievable.

9.2.2 Promising cross-sectional structure for Ge LDs

As described in Chapter 2, Ge/GeO_2 interfaces show NRR recombination rate as low as 10^3–10^4 cm/s, which would be low enough for Ge LDs with J_{th} of 10 kA/cm^2. Based on this, I propose desirable cross-sectional structures for Ge LDs as schematically shown in Fig. 9.2.

An ideal cross-sectional structure would be n-type Ge completely surrounded by GeO_2, as shown in Fig. 9.2 (a). However, the structure shown in Fig. 9.2 (a) has difficulty in electrical pumping since GeO_2 is a dielectric material. Figure 9.2 (b) shows an n-type Ge surrounded

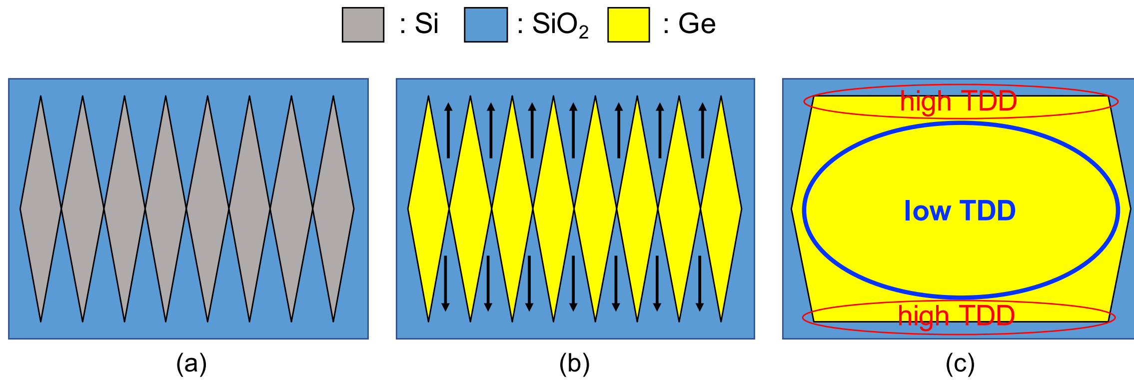

Figure 9.1: Schematic illustrations showing an idea to control trajectories of TDs: (a) SiO_2 SEG masks, (b) SEG Ge before coalescence, and (c) Ge after coalescence. The red circles in (c) indicate where TDs accumulate (high TDD), and the blue circle in (c) indicates where low TDD area.

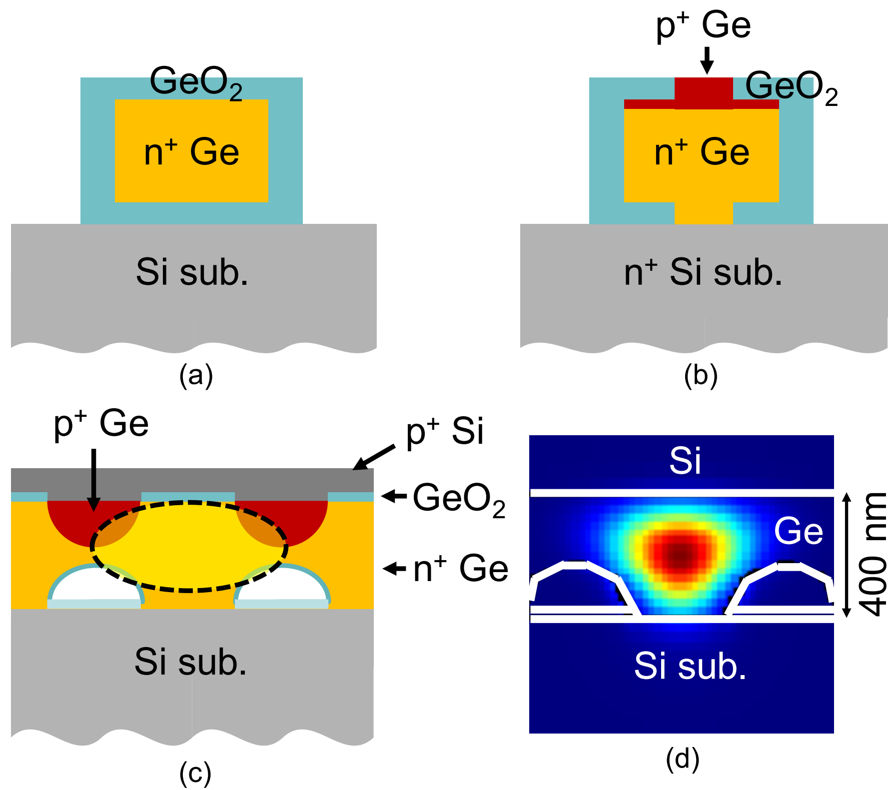

Figure 9.2: Schematic illustrations showing (a) n-type Ge completely surrounded by GeO_2, (b) n-type Ge surrounded by GeO_2 with small contact window, (c) an inverted-rib Ge structure with pn junction, and (d) simulated optical mode in inverted-rib Ge shown in (c).

by GeO_2 with small contact window. The surfaces of n-type Ge layer is for the most part surrounded by GeO_2 to reduce NRR velocity, except for contact windows to inject carriers. Although the structure shown in Fig. 9.2 (b) would be effective to reduce NRR, the structure would be difficult to fabricate. Employing inverted-rib structure, optical confinement similar to Fig. 9.2 (b) can be fabricated during epitaxial growth, as illustrated in Fig. 9.2 (c). The inverted-rib structure shown in Fig. 9.2 (c) would be available employing SEG of Ge and their coalescence as described in Chapter 4, or combination with chemical mechanical polishing (CMP) of Ge on Si [147]. Optical mode in the inverted-rib structure is simulated as Fig. 9.2 (d), showing that optical mode is located above the Si growth seeds due to existence of voids (refractive index = 0). In addition to that, optical mode in the inverted-rib structure is pushed-up to be away from the Ge/Si interface, same as Fig. 7.10. The mode push-up would have positive effect in terms of light emission since Ge/Si interfaces have large NRR velocity, as described in Chapter 2.

Appendix

Appendix I. Enhancement of PL Induced by a Wet Chemical Treatment

As mentioned in section 2.3, Ge/Si interfaces have large NRR velocity: $S_{Ge/Si}$ is as large as mid-10^5 cm/s. Since such a large NRR velocity at Ge/Si interfaces should have a negative effects on light emission from Ge, I considered to remove the Ge/Si interfaces at the bottom, i.e., between Ge epitaxial layers and Si substrate.
In this appendix, a wet chemical treatment is proposed for preferential removal of Ge/Si interfaces, and the effect of the wet chemical treatment in terms of light emission from Ge is described.

Preferential Wet Etching

In order to remove Ge near the bottom Ge/Si interface, I attempted a preferential etching of the defect-rich Ge near the Ge/Si hetero-interface at the bottom, as schematically shown in Figs. 10.1 (a) and 10.1 (b), employing a wet chemical treatment in a $CH_3COOH/HNO_3/HF/I_2$ solution. This wet chemical treatment has been used to visualize the dislocations penetrating to Ge surfaces as etch pits, as schematically illustrated in Fig. 10.1 (c) [54, 114, 148]. Note that the visualization of dislocations as etch pits is performed as the results of preferentially removal of Ge around the dislocations.

Experimental Procedure

Prior to Ge epitaxial growth, SEG masks of SiO_2 were formed on a Si wafer as follows. A B-doped p-Si(001) wafer (1–100 Ωcm) was oxidized in a tube furnace at 900 °C for 2 hours in a dry O_2 ambient. The SiO_2 layer formed on the Si wafer was patterned into stripes with the width of Si window as small as 1 μm for the SEG of Ge, employing electron beam lithography and a wet etching in buffered HF. The stripes were aligned in the [110] direction. Large window areas (1 cm × 1 cm) were also prepared as un-patterned (blanket) region for comparison. The SiO_2 thickness before the growth was 30 nm. A 1.3-μm-thick (in blanket

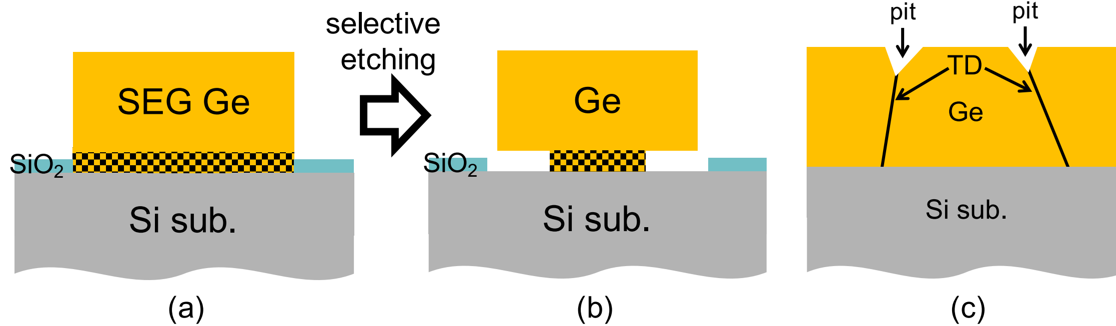

Figure 10.1: Cross-sectional SEM images of an SEG Ge layer (a) before and (b) after the wet chemical treatment. The traces of the SEM images are shown and overlapped in (c).

area) Ge epitaxial layer and a ~20-nm-thick Si capping layer were grown by UHV-CVD. Then, the wafer was divided into small chips. After the removal of Si capping layer in a 2.38 % TMAH solution, some of the chips were dipped into a $CH_3COOH/HNO_3/HF/I_2$ solution for 5 s for the preferential removal of Ge near the bottom Ge/Si interface. The PL measurements were carried out with an excitation wavelength of λ_{ex} = 785 nm. The $1/e^2$ laser diameter and the excitation power were 2 μm and 4.1 mW, respectively.

Cross-Sectional Observations

Figures 10.2 (a) and 10.2 (b) show typical cross-sectional SEM images for an SEG Ge layer before and after the treatment in $CH_3COOH/HNO_3/HF/I_2$, respectively. It is clearly shown that Ge near the bottom Ge/Si hetero-interfaces are preferentially removed as a result of the wet chemical treatment. In addition to that, the sidewall of the SEG Ge layers become almost vertical to the Si substrate owing to the wet chemical treatment. Figure 10.2 (c) shows traces of the SEG Ge layers before (blue line) and after (red line) the wet chemical treatment. The black hatched area indicates Ge removed by the wet chemical treatment. From the SEM observations, the lateral etching rate of Ge near the bottom Ge/Si hetero-interfaces is as large as 80 nm/s, which is 2–4 times faster than those at other areas (20–40 nm/s), reflecting the presence of high density of defects near the interface.

PL Enhancement Induced by the Wet Chemical Treatment

Figure 10.3 shows a typical PL spectrum in the logarithmic scale for the SEG Ge after the wet chemical treatment in $CH_3COOH/HNO_3/HF/I_2$ together with the one before the treatment as well as the ones for the blanket and bulk Ge. The Si capping layers were removed before the PL measurements for all the samples. Compared to the blanket Ge without the $CH_3COOH/HNO_3/HF/I_2$ treatment, the SEG Ge after the treatment showed an 83 times larger

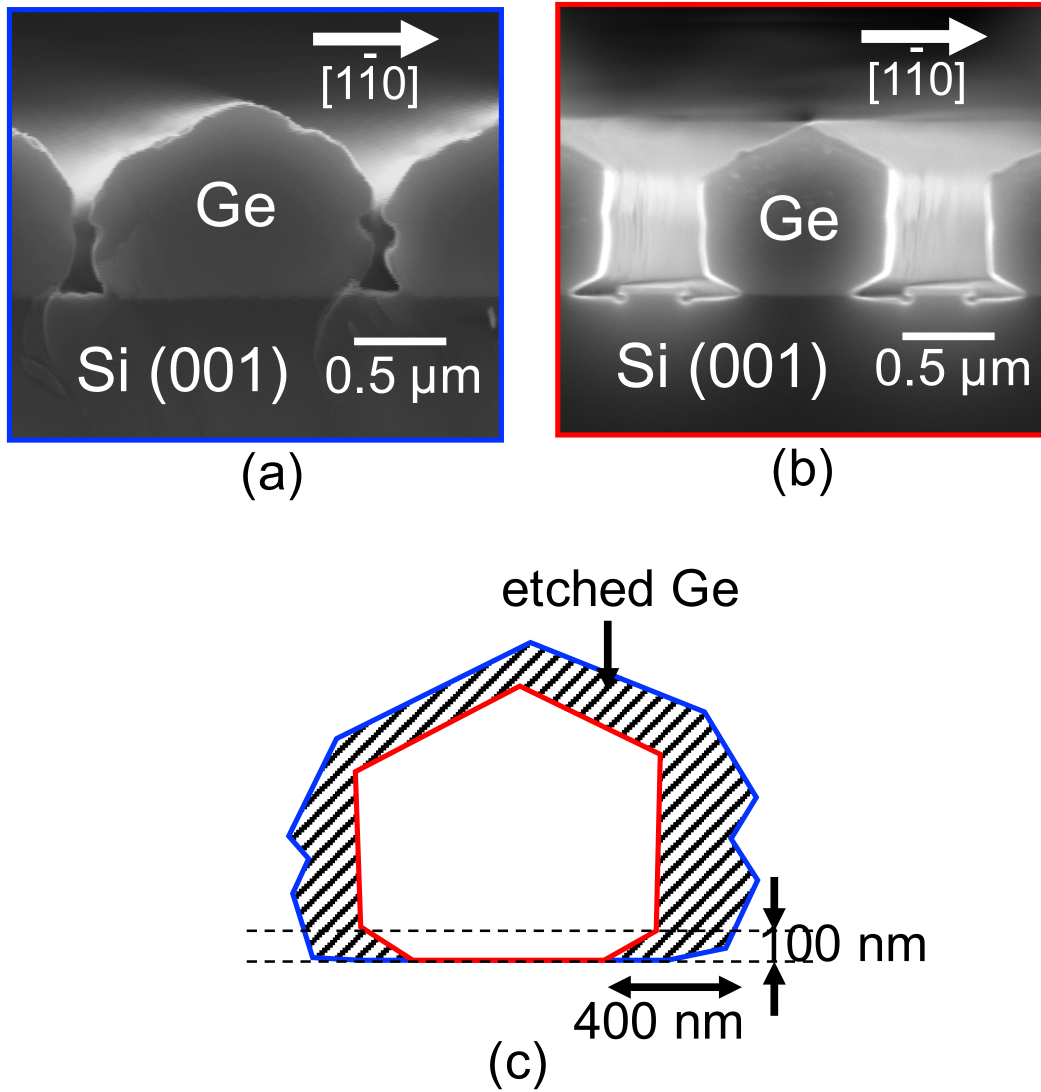

Figure 10.2: Cross-sectional SEM images of an SEG Ge layer (a) before and (b) after the wet chemical treatment. The traces of the SEM images are shown and overlapped in (c).

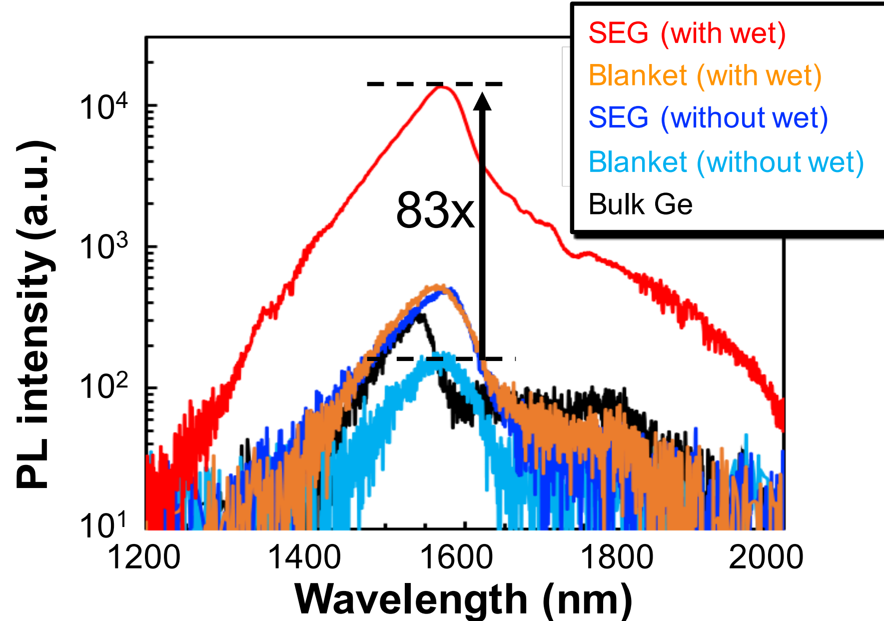

Figure 10.3: PL spectra from SEG/blanket Ge layers before/after the wet chemical treatment

PL peak intensity.

A suppression of NRR near the bottom of SEG Ge layer could contribute to this enhancement. However, as shown in Figs. 2.3 (a) and 2.3 (b) in section 2.3, the excess carrier concentrations at the bottom would not be large enough to show the PL emission. There should be several possible mechanisms to explain the observed 83 times enhancement for the SEG Ge after the treatment in $CH_3COOH/HNO_3/HF/I_2$:

(I) generation of excess carriers even near the bottom of SEG Ge due to the structural change induced by the treatment,

(II) increase in the excess carrier concentrations in the narrow SEG Ge due to the spatial carrier confinement,

(III) termination of dangling bonds at the Ge surfaces including the top and sidewall surfaces to reduce NRR at the surfaces, or to increase the excess carrier concentrations,

(IV) increase in the extraction efficiency of PL emission due to the structural change, and

(V) reduction in the light scattering at the sidewalls to confine the light in SEG Ge, resulting in the increased light intensity in the SEG Ge. The first three mechanisms (I), (II), and (III) are related to the increase in the excess carrier concentrations, and the latter two mechanisms (IV) and (V) are related to the confinement/extraction of light.

In order to examine the mechanism (I), two-dimensional finite-difference time-domain (FDTD) simulations were performed for the light illumination to the SEG Ge. Figure 10.4

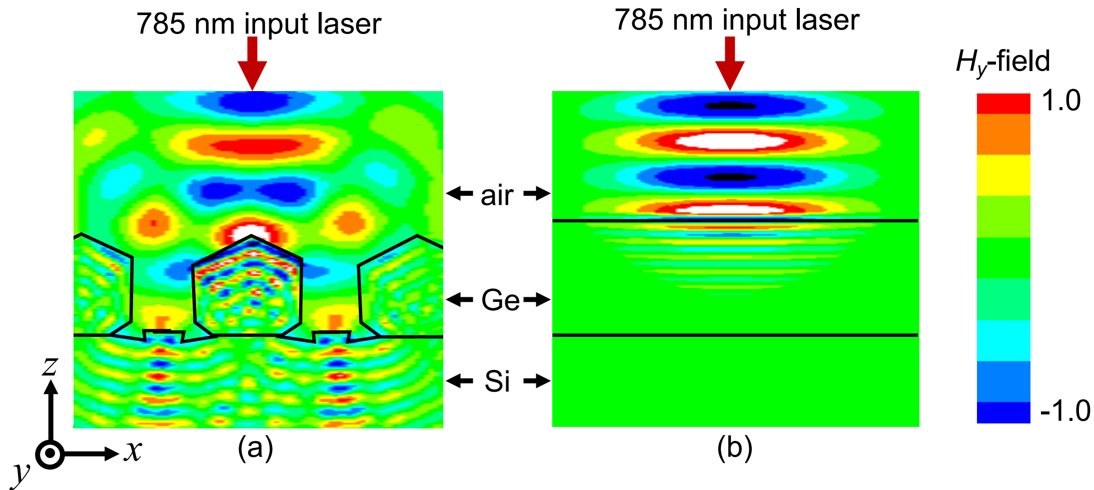

Figure 10.4: 2D FDTD simulation results of magnetic field in (a) SEG Ge and (b) blanket Ge layers illuminated by x-polarized gaussian beam in 2-μm-diameter.

shows a typical snapshot of magnetic field H_y distribution in the x-z cross-section. An x-polarized 785-nm continuous laser light with a Gaussian beam of 2 μm in diameter was directed from the top. As in Fig. 10.4, the light penetrates into the SEG Ge more efficiently in comparison with the blanket Ge layer, probably due to the enhanced transmission through the inclined top surfaces of {113} planes as well as the coupling of evanescent light from the sidewalls. The enhanced penetration of light induces an increase in the excess carrier concentrations in Ge even near the bottom. Thus, the mechanism (I) of generation of excess carriers near the bottom of SEG Ge should occur, and the removal of the defective Ge near the Si wafer should partly contribute to the observed PL enhancement.

On the other hand, the effect of mechanism (II), related to the spatial carrier confinement in a narrow SEG Ge layer, might be negligible, since the carrier diffusion length is as small as 100 nm in the present study, which is smaller than the width/thickness of SEG Ge layer.

As to the mechanism (III) of termination of dangling bonds at the Ge surfaces would be partly effective, since an enhancement approximately by 3 times was seen for the blanket Ge layer after the treatment. It has been reported that a wet chemical treatment in HF decreases the surface recombination velocities for Si and Ge surfaces [149] as the result of termination of dangling bonds [150], and a similar effect might take place in a $CH_3COOH/HNO_3/HF/I_2$ mixture containing HF.

The contributions of other two mechanisms (IV) and (V), related to the confinement/extraction of light, would have roughly an enhancement factor of 3, since the PL intensity was enhanced by 3 times for the SEG Ge before the treatment in comparison with the blanket Ge. Detailed

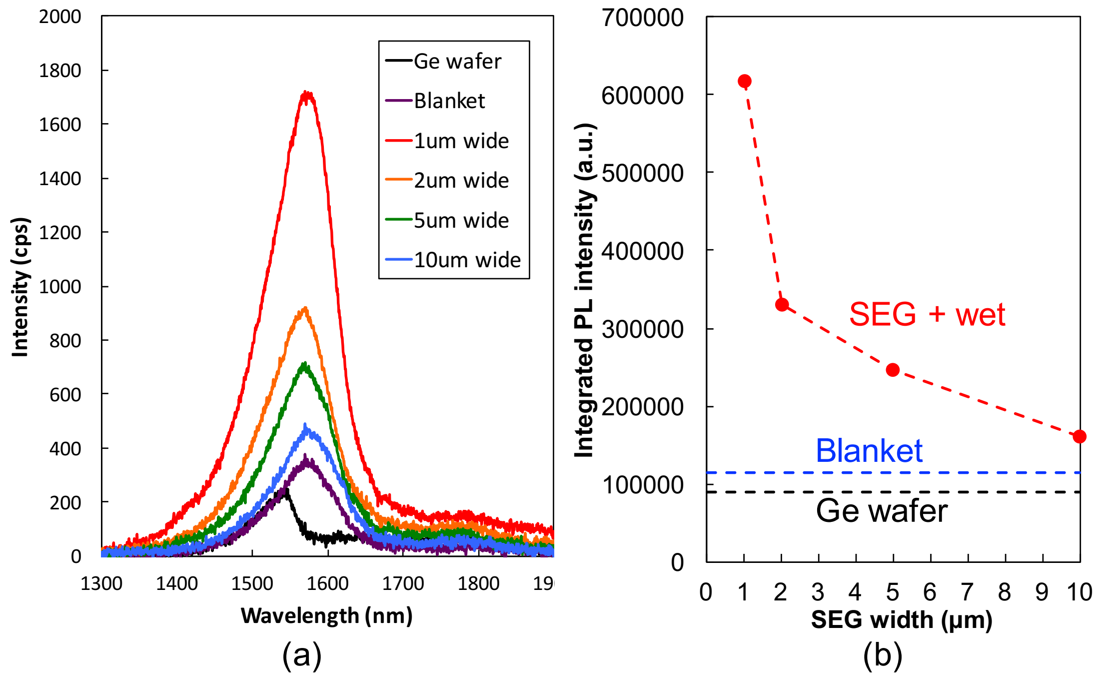

Figure 10.5: (a) PL spectra after the wet chemical treatment, and (b) integrated PL intensity (1300–1900 nm) as a function of SEG width.

FDTD analyses should be necessary how the light is confined in the SEG Ge surrounded with smooth sidewalls and how such light is radiated to the top [151]. Tanking into account the enhancement factors of 3 by the mechanism (III) and 3 by the mechanisms (IV) and (V), the PL enhancement by the mechanism (I) of excess carriers excited near the bottom of SEG Ge would have roughly the enhancement factor of 10. In the actual Ge/Si DH laser structures, propagation mode of light in the in-plane direction is more important than the radiation mode observed in the PL measurements. In terms of the reduction of scattering loss, the smoothing of SEG Ge sidewalls induced by the wet chemical treatment would be also effective. Further enhancement could be obtained if a thermal oxidation is combined, since the Ge layers are mostly surrounded by Ge/GeO_2 with a small NRR velocity.

SEG Width Dependence of PL Intensity After the Wet Chemical Treatment

Figure 10.5 shows (a) PL spectra after the wet chemical treatment, and (b) integrated PL intensity (1300–1900 nm) as a function of SEG width. It is clearly shown that the PL intensity increases as the width of SEG Ge decreases. Such a SEG width dependence on PL intensity is reasonable because the volume ratio of preferentially-etched defect-rich Ge layer increase as the SEG width decreases.

In Fig. 10.5 (a), it is also found that the PL peak slightly shifts to shorter wavelength as SEG width is reduced. The peak shift suggests that the built-in tensile strain is slightly released owing to the wet chemical treatment, while the strain release does not show negative effect on PL from Ge.

Appendix II. Thickness Dependence of PL from Ge Epitaxial Layers on Si

Although it has been widely known that TDs in Ge work as NRR centers, there has been no report showing TDD dependence of PL from Ge epitaxial layers on Si. In Appendix II., correlation between TDD and PL intensity is shown, changing TDDs employing Ge epitaxial layers with various thickness.

Experimental Procedure

Experimental procedure for the epitaxial growth of Ge on Si is conducted as described in Chapters 2 and 4. The main growth duration was varied in order to grow Ge epitaxial layers with various thickness. The thicknesses of Ge epitaxial layers were set as 70, 200, 700, 1300, and 2000 nm. 70-nm-thick Ge was grown at 370 °C as 70-nm-thick low-temperature buffer layer. Followed by the low-temperature buffer growth, Ge epitaxial layers were grown at 700 °C to be 200–2000 nm thick.

PL measurements were carried out using 457-nm excitation laser, similar to the experiments described in Chapter 8. Such a short wavelength laser was used in order to measure PL from Ge near the surface, i.e., to localize the PL measurement in depth direction. The top surfaces of Ge epitaxial layers were exposed to the air, and thus the NRR velocity at Ge top surface should be $\sim 1 \times 10^5$ cm/s, as described in Chapter 2.

Results and Discussions

Figure 10.6 (a) shows PL spectra observed on Ge epitaxial layers with various thicknesses. PL peaks around 1600 nm are shown for the Ge epitaxial layers of 200–2000 nm thick, although 70-nm-thick Ge shows a broad and weak peak.

Since TDD in Ge epitaxial layers on Si depends on their thicknesses as shown in Fig. 5.5, the thickness dependence of PL indicates TDD dependence of PL. Figure 10.6 (b) shows integrated PL intensity (1200–2000 nm) as a function of thickness. TDD is estimated from the TDD-thickness relation for blanket Ge grown at 700 °C, which is shown in Fig. 5.5. It is found that the PL intensity is independent with thickness where the thickness is more than 200 nm. Thickness of 200 nm corresponds to TDD of 1.9×10^9 cm^{-2}, according to the relation shown in Fig. 5.5. Thus, it is revealed that PL from Ge is independent with TDD in the range TDD $\leq 1.9 \times 10^9$ cm^{-2}, in the case for surface NRR velocity of $\sim 1 \times 10^5$ cm/s.

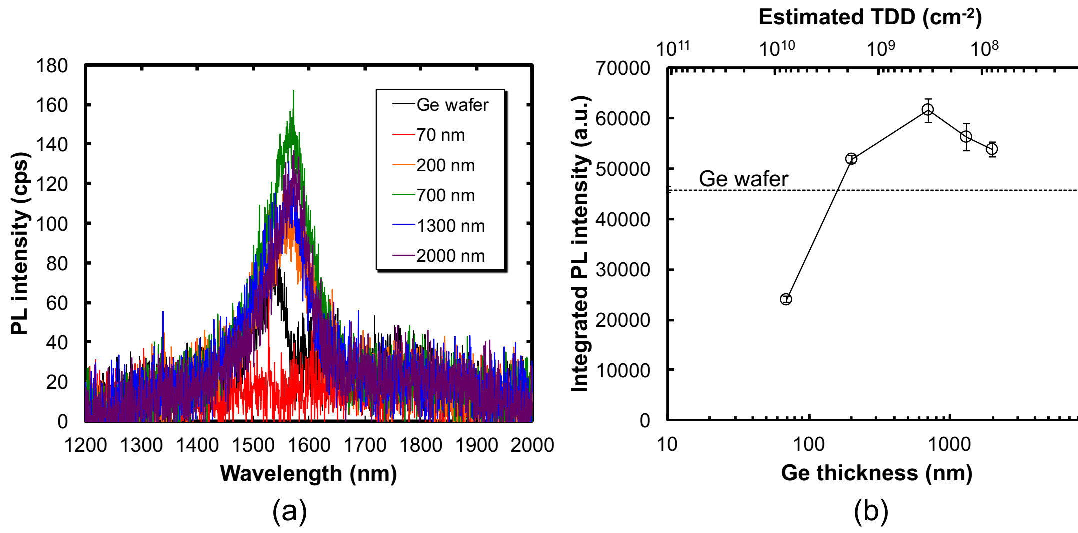

Figure 10.6: (a) PL spectra observed on Ge epitaxial layers with various thicknesses, and (b) integrated PL intensity (1200–2000 nm) as a function of thickness. TDD is estimated from the TDD-thickness relation shown in Fig. 5.5.

Note that the broad and weak PL from the 70-nm-thick Ge epitaxial layer is ascribed to several reasons such as high TDD, low growth temperature (bring higher TDD), excitation at Ge/Si hetero-interface, Ge epitaxial layer working as anti-reflection, and so on.

Bibliography

[1] LightCounting. Silicon photonics' effect more evolutionary than revolutionary: LightCounting, Jan 2017.

[2] Yole Développement. Silicon photonics has reached its tipping point! Silicon Photonics 2018 report, Jan 2018.

[3] BIS RESEARCH. Global Silicon Photonics Market, Analysis & Forecast, 2017–2022, 2017.

[4] Igor L. Markov. Limits on fundamental limits to computation. *Nature*, 512:147–154, 08 2014.

[5] L. C. Kimerling, D. Ahn, A. B. Apsel, M. Beals, D. Carothers, Y.-K. Chen, T. Conway, D. M. Gill, M. Grove, C.-Y. Hong, M. Lipson, J. Liu, J. Michel, D. Pan, S. S. Patel, A. T. Pomerene, M. Rasras, D. K. Sparacin, K.-Y. Tu, A. E. White, and C. W. Wong. Electronic-photonic integrated circuits on the CMOS platform, 2006.

[6] Ling Liao, Dean Samara-Rubio, Michael Morse, Ansheng Liu, Dexter Hodge, Doron Rubin, Ulrich D. Keil, and Thorkild Franck. High speed silicon Mach-Zehnder modulator. *Opt. Express*, 13(8):3129–3135, Apr 2005.

[7] L. Colace, G. Masini, G. Assanto, Hsin-Chiao Luan, K. Wada, and L. C. Kimerling. Efficient high-speed near-infrared Ge photodetectors integrated on Si substrates. *Applied Physics Letters*, 76(10):1231–1233, 2000.

[8] H.-C. Luan, K. Wada, L.C. Kimerling, G. Masini, L. Colace, and G. Assanto. High efficiency photodetectors based on high quality epitaxial germanium grown on silicon substrates. *Optical Materials*, 17(1):71 – 73, 2001. Optoelectronics I: Materials and Technologies for Optoelectronic Devices.

[9] Laura M. Giovane, Hsin-Chiao Luan, Anuradha M. Agarwal, and Lionel C. Kimerling. Correlation between leakage current density and threading dislocation density in SiGe p-i-n diodes grown on relaxed graded buffer layers. *Applied Physics Letters*, 78(4):541–543, 2001.

[10] G. Masini, L. Calace, G. Assanto, Hsin-Chiao Luan, and L. C. Kimerling. High-performance p-i-n Ge on Si photodetectors for the near infrared: from model to demonstration. *IEEE Transactions on Electron Devices*, 48(6):1092–1096, June 2001.

[11] Yasuhiko Ishikawa, Kazumi Wada, Jifeng Liu, Douglas D. Cannon, Hsin-Chiao Luan, Jurgen Michel, and Lionel C. Kimerling. Strain-induced enhancement of near-infrared absorption in Ge epitaxial layers grown on Si substrate. *Journal of Applied Physics*, 98(1):013501, 2005.

[12] M. Jutzi, M. Berroth, G. Wohl, M. Oehme, and E. Kasper. Ge-on-Si vertical incidence photodiodes with 39-GHz bandwidth. *IEEE Photonics Technology Letters*, 17(7):1510–1512, 2005.

[13] M. Morse, O. Dosunmu, G. Sarid, and Y. Chetrit. Performance of Ge-on-Si p-i-n Photodetectors for Standard Receiver Modules. *IEEE Photonics Technology Letters*, 18(23):2442–2444, 2006.

[14] Donghwan Ahn, Ching yin Hong, Jifeng Liu, Wojciech Giziewicz, Mark Beals, Lionel C. Kimerling, Jurgen Michel, Jian Chen, and Franz X. Kärtner. High performance, waveguide integrated Ge photodetectors. *Opt. Express*, 15(7):3916–3921, Apr 2007.

[15] S. Klinger, M. Berroth, M. Kaschel, M. Oehme, and E. Kasper. Ge-on-Si p-i-n Photodiodes With a 3-dB Bandwidth of 49 GHz. *IEEE Photonics Technology Letters*, 21(13):920–922, July 2009.

[16] Laurent Vivien, Johann Osmond, Jean-Marc Fédéli, Delphine Marris-Morini, Paul Crozat, Jean-François Damlencourt, Eric Cassan, Y. Lecunff, and Suzanne Laval. 42 GHz p.i.n Germanium photodetector integrated in a silicon-on-insulator waveguide. *Opt. Express*, 17(8):6252–6257, Apr 2009.

[17] J. Osmond, G. Isella, D. Chrastina, R. Kaufmann, M. Acciarri, and H. von Känel. Ultralow dark current Ge/Si(100) photodiodes with low thermal budget. *Applied Physics Letters*, 94(20):201106, 2009.

[18] Jurgen Michel, Jifeng Liu, and Lionel C. Kimerling. High-performance Ge-on-Si photodetectors. *Nature Photonics*, 4:527 EP –, 07 2010.

[19] Shirong Liao, Ning-Ning Feng, Dazeng Feng, Po Dong, Roshanak Shafiiha, Cheng-Chih Kung, Hong Liang, Wei Qian, Yong Liu, Joan Fong, John E. Cunningham, Ying Luo, and Mehdi Asghari. 36 GHz submicron silicon waveguide germanium photodetector. *Opt. Express*, 19(11):10967–10972, May 2011.

[20] Mitsuru Takenaka, Kiyohito Morii, Masakazu Sugiyama, Yoshiaki Nakano, and Shinichi Takagi. Dark current reduction of Ge photodetector by GeO2 surface passivation and gas-phase doping. *Opt. Express*, 20(8):8718–8725, Apr 2012.

[21] Laurent Vivien, Andreas Polzer, Delphine Marris-Morini, Johann Osmond, Jean Michel Hartmann, Paul Crozat, Eric Cassan, Christophe Kopp, Horst Zimmermann, and Jean Marc Fédéli. Zero-bias 40Gbit/s germanium waveguide photodetector on silicon. *Opt. Express*, 20(2):1096–1101, Jan 2012.

[22] Léopold Virot, Paul Crozat, Jean-Marc Fédéli, Jean-Michel Hartmann, Delphine Marris-Morini, Eric Cassan, Frédéric Boeuf, and Laurent Vivien. Germanium avalanche receiver for low power interconnects. *Nature Communications*, 5:4957 EP –, 09 2014.

[23] Xiankai Sun, Ke Xu, and Hong X. Tang. Monolithically integrated, ultrahigh-frequency cavity nano-optoelectromechanical system with on-chip germanium waveguide photodetector. *Opt. Lett.*, 39(8):2514–2517, Apr 2014.

[24] H. Chen, P. Verheyen, P. De Heyn, G. Lepage, J. De Coster, S. Balakrishnan, P. Absil, W. Yao, L. Shen, G. Roelkens, and J. Van Campenhout. -1 V bias 67 GHz bandwidth Si-contacted germanium waveguide p-i-n photodetector for optical links at 56 Gbps and beyond. *Opt. Express*, 24(5):4622–4631, Mar 2016.

[25] H. Chen, P. Verheyen, P. De Heyn, G. Lepage, J. De Coster, S. Balakrishnan, P. Absil, G. Roelkens, and J. Van Campenhout. Dark current analysis in high-speed germanium p-i-n waveguide photodetectors. *Journal of Applied Physics*, 119(21):213105, 2016.

[26] Nobuyoshi Koshida and Hideki Koyama. Visible electroluminescence from porous silicon. *Applied Physics Letters*, 60(3):347–349, 1992.

[27] L. Pavesi, L. Dal Negro, C. Mazzoleni, G. Franzò, and F. Priolo. Optical gain in silicon nanocrystals. *Nature*, 408:440–444, 11 2000.

[28] P Bettotti, M Cazzanelli, L Dal Negro, B Danese, Z Gaburro, C J Oton, G Vijaya Prakash, and L Pavesi. Silicon nanostructures for photonics. *Journal of Physics: Condensed Matter*, 14(35):8253, 2002.

[29] D. J. Eaglesham, J. Michel, E. A. Fitzgerald, D. C. Jacobson, J. M. Poate, J. L. Benton, A. Polman, Y.- H. Xie, and L. C. Kimerling. Microstructure of erbium- implanted Si. *Applied Physics Letters*, 58(24):2797–2799, 1991.

[30] B. Zheng, J. Michel, F. Y. G. Ren, L. C. Kimerling, D. C. Jacobson, and J. M. Poate. Room-temperature sharp line electroluminescence at λ =1.54 μ m from an erbium- doped, silicon light-emitting diode. *Applied Physics Letters*, 64(21):2842–2844, 1994.

[31] Hak-Seung Han, Se-Young Seo, and Jung H. Shin. Optical gain at 1.54 μm in erbium-doped silicon nanocluster sensitized waveguide. *Applied Physics Letters*, 79(27):4568–4570, 2001.

[32] E. Desurvire, J. R. Simpson, and P. C. Becker. High-gain erbium-doped traveling-wave fiber amplifier. *Opt. Lett.*, 12(11):888–890, Nov 1987.

[33] R. J. Mears, L. Reekie, I. M. Jauncey, and D. N. Payne. Low-noise erbium-doped fibre amplifier operating at 1.54 μm. *Electronics Letters*, 23(19):1026–1028, 1987.

[34] Herbert Venghaus and Norbert Grote, editors. *Fibre Optic Communication*. Number p. 746. Springer, 2017.

[35] G. Sun, R. A. Soref, and H. H. Cheng. Design of an electrically pumped SiGeSn/GeSn/SiGeSn double-heterostructure midinfrared laser. *Journal of Applied Physics*, 108(3):033107, 2010.

[36] S. Wirths, R. Geiger, N. von den Driesch, G. Mussler, T. Stoica, S. Mantl, Z. Ikonic, M. Luysberg, S. Chiussi, J. M. Hartmann, H. Sigg, J. Faist, D. Buca, and D. Grützmacher. Lasing in direct-bandgap GeSn alloy grown on Si. *Nature Photonics*, 9:88–92, 01 2015.

[37] Daniela Stange, Stephan Wirths, Richard Geiger, Christian Schulte-Braucks, Bahareh Marzban, Nils von den Driesch, Gregor Mussler, Thomas Zabel, Toma Stoica, Jean-Michel Hartmann, Siegfried Mantl, Zoran Ikonic, Detlev Grützmacher, Hans Sigg, Jeremy Witzens, and Dan Buca. Optically Pumped GeSn Microdisk Lasers on Si. *ACS Photonics*, 3(7):1279–1285, 07 2016.

[38] Qiang Li, Yating Wan, Alan Y. Liu, Arthur C. Gossard, John E. Bowers, Evelyn L. Hu, and Kei May Lau. 1.3-μm InAs quantum-dot micro-disk lasers on V-groove patterned and unpatterned (001) silicon. *Opt. Express*, 24(18):21038–21045, Sep 2016.

[39] Justin Norman, M. J. Kennedy, Jennifer Selvidge, Qiang Li, Yating Wan, Alan Y. Liu, Patrick G. Callahan, McLean P. Echlin, Tresa M. Pollock, Kei May Lau, Arthur C. Gossard, and John E. Bowers. Electrically pumped continuous wave quantum dot lasers epitaxially grown on patterned, on-axis (001) Si. *Opt. Express*, 25(4):3927–3934, Feb 2017.

[40] Jifeng Liu, Xiaochen Sun, Dong Pan, Xiaoxin Wang, Lionel C. Kimerling, Thomas L. Koch, and Jurgen Michel. Tensile-strained, n-type Ge as a gain medium for monolithic laser integration on Si. *Optics Express*, 15(18):11272–11277, Sep 2007.

[41] Jifeng Liu, Xiaochen Sun, Rodolfo Camacho-Aguilera, Lionel C. Kimerling, and Jurgen Michel. Ge-on-Si laser operating at room temperature. *Opt. Lett.*, 35(5):679–681, Mar 2010.

[42] Rodolfo E. Camacho-Aguilera, Yan Cai, Neil Patel, Jonathan T. Bessette, Marco Romagnoli, Lionel C. Kimerling, and Jurgen Michel. An electrically pumped germanium laser. *Opt. Express*, 20(10):11316–11320, May 2012.

[43] Roman Koerner, Michael Oehme, Martin Gollhofer, Marc Schmid, Konrad Kostecki, Stefan Bechler, Daniel Widmann, Erich Kasper, and Joerg Schulze. Electrically pumped lasing from Ge Fabry-Perot resonators on Si. *Opt. Express*, 23(11):14815–14822, Jun 2015.

[44] Shuyu Bao, Daeik Kim, Chibuzo Onwukaeme, Shashank Gupta, Krishna Saraswat, Kwang Hong Lee, Yeji Kim, Dabin Min, Yongduck Jung, Haodong Qiu, Hong Wang, Eugene A. Fitzgerald, Chuan Seng Tan, and Donguk Nam. Low-threshold optically pumped lasing in highly strained germanium nanowires. *Nature Communications*, 8(1):1845, 2017.

[45] Yasuhiko Ishikawa, Kazumi Wada, Douglas D. Cannon, Jifeng Liu, Hsin-Chiao Luan, and Lionel C. Kimerling. Strain-induced band gap shrinkage in Ge grown on Si substrate. *Applied Physics Letters*, 82(13):2044–2046, 2003.

[46] M. J. Süess, R. Geiger, R. A. Minamisawa, G. Schiefler, J. Frigerio, D. Chrastina, G. Isella, R. Spolenak, J. Faist, and H. Sigg. Analysis of enhanced light emission from highly strained germanium microbridges. *Nature Photonics*, 7:466–472, 04 2013.

[47] Rodolfo Camacho-Aguilera, Zhaohong Han, Yan Cai, Lionel C. Kimerling, and Jurgen Michel. Direct band gap narrowing in highly doped Ge. *Applied Physics Letters*, 102(15):152106, 2013.

[48] Y. Cai, Z. Han, X. Wang, R. E. Camacho-Aguilera, L. C. Kimerling, J. Michel, and J. Liu. Analysis of Threshold Current Behavior for Bulk and Quantum-Well Germanium Laser Structures. *IEEE Journal of Selected Topics in Quantum Electronics*, 19(4):1901009–1901009, 2013.

[49] Jane G. Zhu and C. Barry Carter. 60° dislocations in (001) GaAs/Si interfaces. *Philosophical Magazine A*, 62(3):319–328, 09 1990.

[50] A. Vilà, A. Cornet, J. R. Morante, P. Ruterana, M. Loubradou, and R. Bonnet. Structure of 60° dislocations at the GaAs/Si interface. *Journal of Applied Physics*, 79(2):676–681, 1996.

[51] L. Sfaxi, L. Bouzaiene, H. Sghaier, and H. Maaref. Effect of growth temperature on InAs wetting layer grown on (113)A GaAs by molecular beam epitaxy. *Journal of Crystal Growth*, 293(2):330 – 334, 2006.

[52] M. T. Currie, S. B. Samavedam, T. A. Langdo, C. W. Leitz, and E. A. Fitzgerald. Controlling threading dislocation densities in Ge on Si using graded SiGe layers and chemical-mechanical polishing. *Applied Physics Letters*, 72(14):1718–1720, 1998.

[53] D. J. Eaglesham and M. Cerullo. Dislocation-free Stranski-Krastanow growth of Ge on Si(100). *Phys. Rev. Lett.*, 64(16):1943–1946, Apr 1990.

[54] Hsin-Chiao Luan, Desmond R. Lim, Kevin K. Lee, Kevin M. Chen, Jessica G. Sandland, Kazumi Wada, and Lionel C. Kimerling. High-quality Ge epilayers on Si with low threading-dislocation densities. *Applied Physics Letters*, 75(19):2909–2911, 1999.

[55] Peter T. Landsberg. *Recombination in Semiconductors*. Cambridge University Press, 1992.

[56] Shun Lien Chuang. *Physics of Photonic Devices*. Wiley, Hoboken, New Jersey, 2nd edition, January 2009.

[57] Josephine J. Sheng, Darin Leonhardt, Sang M. Han, Steven W. Johnston, Jeffrey G. Cederberg, and Malcolm S. Carroll. Empirical correlation for minority carrier lifetime to defect density profile in germanium on silicon grown by nanoscale interfacial engineering. *Journal of Vacuum Science & Technology B*, 31(5):051201, 2013.

[58] R. Geiger, J. Frigerio, M. J. Süess, D. Chrastina, G. Isella, R. Spolenak, J. Faist, and H. Sigg. Excess carrier lifetimes in Ge layers on Si. *Applied Physics Letters*, 104(6):062106, 2014.

[59] Shinichi Saito, Frederic Yannick Gardes, Abdelrahman Zaher Al-Attili, Kazuki Tani, Katsuya Oda, Yuji Suwa, Tatemi Ido, Yasuhiko Ishikawa, Satoshi Kako, Satoshi Iwamoto, and Yasuhiko Arakawa. Group IV Light Sources to Enable the Convergence of Photonics and Electronics. *Frontiers in Materials*, 1:15, 2014.

[60] S. A. Srinivasan, C. Porret, M. Pantouvaki, Y. Shimura, P. Geiregat, R. Loo, J. Van Campenhout, and D. Van Thourhout. Carrier scattering induced linewidth broadening in in situ P-doped Ge layers on Si. *Applied Physics Letters*, 113(16):161101, 2018.

[61] L. Huldt. Auger recombination in germanium. *Physica Status Solidi (a)*, 24(1):221–229, 1974.

[62] E. Gaubas and J. Vanhellemont. Comparative Study of Carrier Lifetime Dependence on Dopant Concentration in Silicon and Germanium. *Journal of The Electrochemical Society*, 154(3):H231–H238, 2007.

[63] Xiaoxin Wang, Haofeng Li, Rodolfo Camacho-Aguilera, Yan Cai, Lionel C. Kimerling, Jurgen Michel, and Jifeng Liu. Infrared absorption of n-type tensile-strained Ge-on-Si. *Opt. Lett.*, 38(5):652–654, Mar 2013.

[64] Naoki Higashitarumizu and Yasuhiko Ishikawa. Enhanced direct-gap light emission from Si-capped n^+-Ge epitaxial layers on Si after post-growth rapid cyclic annealing: impact of non-radiative interface recombination toward Ge/Si double heterostructure lasers. *Opt. Express*, 25(18):21286–21300, Sep 2017.

[65] D. Baek, S. Rouvimov, B. Kim, T.-C. Jo, and D. K. Schroder. Surface recombination velocity of silicon wafers by photoluminescence. *Applied Physics Letters*, 86(11):112110, 2005.

[66] H. Pan, R. Takahashi, K. Takinai, and K. Wada. Photoluminescence quenching effect by Si cap in n+ Ge on Si. In Graham T. Reed and Michael R. Watts, editors, *SPIE 9367, Silicon Photonics X, 93671E*, 2015.

[67] Hiroshi Matsubara, Takashi Sasada, Mitsuru Takenaka, and Shinichi Takagi. Evidence of low interface trap density in GeO_2/Ge metal-oxide-semiconductor structures fabricated by thermal oxidation. *Applied Physics Letters*, 93(3):032104, 2008.

[68] Akira Toriumi, Toshiyuki Tabata, Choong Hyun Lee, Tomonori Nishimura, Koji Kita, and Kosuke Nagashio. Opportunities and challenges for Ge CMOS – Control of interfacing field on Ge is a key. *Microelectronic Engineering*, 86(7):1571 – 1576, 2009. INFOS 2009.

[69] C. H. Lee, T. Nishimura, K. Nagashio, K. Kita, and A. Toriumi. High-Electron-Mobility Ge/GeO_2 n-MOSFETs With Two-Step Oxidation. *IEEE Transactions on Electron Devices*, 58(5):1295–1301, 2011.

[70] Xuejun Xu, Hideaki Hashimoto, Kentarou Sawano, Hiroshi Nohira, and Takuya Maruizumi. Enhanced light emission from germanium microdisks on silicon by surface passivation through thermal oxidation. *Applied Physics Express*, 9(5):052101, 2016.

[71] Fatemeh Sadat Minaye Hashemi, Shruti Thombare, Anna Fontcuberta i Morral, Mark L. Brongersma, and Paul C. McIntyre. Effects of surface oxide formation on germanium nanowire band-edge photoluminescence. *Applied Physics Letters*, 102(25):251122, 2013.

[72] S M. Sze. *Physics of semiconductor devices 2nd edition*. Number p. 29. Wiley-Interscience, New York, USA, 01 1981.

[73] Bart Onsia, Thierry Conard, Stefan De Gendt, Marc M. Heyns, I. Hoflijk, Paul W. Mertens, Marc Meuris, G. Raskin, Sonja Sioncke, I. Teerlinck, Antoon Theuwis, Jan Van Steenbergen, and Chris Vinckier. A Study of the Influence of Typical Wet Chemical Treatments on the Germanium Wafer Surface. In *Ultra Clean Processing of Silicon Surfaces VII*, volume 103 of *Solid State Phenomena*, pages 27–30. Trans Tech Publications, 3 2005.

[74] Ammar Nayfeh, Chi On Chui, Krishna C. Saraswat, and Takao Yonehara. Effects of hydrogen annealing on heteroepitaxial-Ge layers on Si: Surface roughness and electrical quality. *Applied Physics Letters*, 85(14):2815–2817, 2004.

[75] Donghun Choi, Yangsi Ge, James S. Harris, Joel Cagnon, and Susanne Stemmer. Low surface roughness and threading dislocation density Ge growth on Si (001). *Journal of Crystal Growth*, 310(18):4273–4279, 2008.

[76] J. L. Liu, S. Tong, Y. H. Luo, J. Wan, and K. L. Wang. High-quality Ge films on Si substrates using Sb surfactant-mediated graded SiGe buffers. *Applied Physics Letters*, 79(21):3431–3433, 2001.

[77] Tae-Sik Yoon, Jian Liu, Atif M. Noori, Mark S. Goorsky, and Ya-Hong Xie. Surface roughness and dislocation distribution in compositionally graded relaxed SiGe buffer layer with inserted-strained Si layers. *Applied Physics Letters*, 87(1):012104, 2005.

[78] T. A. Langdo, C. W. Leitz, M. T. Currie, E. A. Fitzgerald, A. Lochtefeld, and D. A. Antoniadis. High quality Ge on Si by epitaxial necking. *Applied Physics Letters*, 76(25):3700–3702, 2000.

[79] J.-S. Park, J. Bai, M. Curtin, B. Adekore, M. Carroll, and A. Lochtefeld. Defect reduction of selective Ge epitaxy in trenches on Si(001) substrates using aspect ratio trapping. *Applied Physics Letters*, 90(5):052113, 2007.

[80] James G. Fiorenza, Ji-Soo Park, Jennifer Hydrick, Jason Li, Jizhong Li, Mike Curtin, Mark Carroll, and Anthony Lochtefeld. Aspect Ratio Trapping: A Unique Technology for Integrating Ge and III-Vs with Silicon CMOS. *ECS Transactions*, 33(6):963–976, 2010.

[81] R. Bergamaschini, F. Isa, C.V. Falub, P. Niedermann, E. Müller, G. Isella, H. von Känel, and L. Miglio. Self-aligned Ge and SiGe three-dimensional epitaxy on dense Si pillar arrays. *Surface Science Reports*, 68(3):390–417, 2013.

[82] Marco Salvalaglio, Roberto Bergamaschini, Fabio Isa, Andrea Scaccabarozzi, Giovanni Isella, Rainer Backofen, Axel Voigt, Francesco Montalenti, Giovanni Capellini, Thomas Schroeder, Hans von Känel, and Leo Miglio. Engineered Coalescence by Annealing 3D Ge Microstructures into High-Quality Suspended Layers on Si. *ACS Applied Materials & Interfaces*, 7(34):19219–19225, 2015. PMID: 26252761.

[83] Fabio Isa, Marco Salvalaglio, Yadira Arroyo Rojas Dasilva, Mojmír Meduňa, Michael Barget, Arik Jung, Thomas Kreiliger, Giovanni Isella, Rolf Erni, Fabio Pezzoli, Emiliano Bonera, Philippe Niedermann, Pierangelo Gröning, Francesco Montalenti, and Hans von Känel. Highly Mismatched, Dislocation-Free SiGe/Si Heterostructures. *Advanced Materials*, 28(5):884–888, 2015.

[84] S. Mader and A. E. Michel. Dislocation reactions in arsenic‐implanted and annealed silicon. *Physica Status Solidi (a)*, 33(2):793–805, 1976.

[85] S. Ha, P. Mieszkowski, M. Skowronski, and L. B. Rowland. Dislocation conversion in 4H silicon carbide epitaxy. *Journal of Crystal Growth*, 244(3):257–266, 2002.

[86] A.K. Head. The Interaction of Dislocations and Boundaries. *The London, Edinburgh, and Dublin Philosophical Magazine and Journal of Science*, 44(348):92–94, 1953.

[87] J. D. Eshelby. Screw Dislocations in Thin Rods. *Journal of Applied Physics*, 24(2):176–179, 1953.

[88] D M Barnett and J Lothe. An image force theorem for dislocations in anisotropic bicrystals. *Journal of Physics F: Metal Physics*, 4(10):1618–1635, oct 1974.

[89] Yasuhiko Ishikawa and Shinichi Saito. Ge-on-Si photonic devices for photonic-electronic integration on a Si platform. *IEICE Electronics Express*, 11(24):1–17, 2014.

[90] J. Bai, J.-S. Park, Z. Cheng, M. Curtin, B. Adekore, M. Carroll, A. Lochtefeld, and M. Dudley. Study of the defect elimination mechanisms in aspect ratio trapping Ge growth. *Applied Physics Letters*, 90(10):101902, 2007.

[91] Francesco Montalenti, Fabrizio Rovaris, Roberto Bergamaschini, Leo Miglio, Marco Salvalaglio, Giovanni Isella, Fabio Isa, and Hans von Känel. Dislocation-Free SiGe/Si Heterostructures. *Crystals*, 8(6), 2018.

[92] H. L. Zhang. Calculation of shuffle 60° dislocation width and Peierls barrier and stress for semiconductors silicon and germanium. *The European Physical Journal B*, 81(2):179–183, May 2011.

[93] M. N. Kabler. Dislocation Mobility in Germanium. *Physical Review*, 131:54–58, July 1963.

[94] J.-S. Park, M. Curtin, J. M. Hydrick, J. Bai, J.-T. Li, Z. Cheng, M. Carroll, J. G. Fiorenza, and A. Lochtefeld. Low-Defect-Density Ge Epitaxy on Si(001) Using Aspect Ratio Trapping and Epitaxial Lateral Overgrowth. *Electrochemical and Solid-State Letters*, 12(4):H142–H144, 2009.

[95] Qiming Li, Ying-Bing Jiang, Huifang Xu, Stephen Hersee, and Sang M. Han. Heteroepitaxy of high-quality Ge on Si by nanoscale Ge seeds grown through a thin layer of SiO_2. *Applied Physics Letters*, 85(11):1928–1930, 2004.

[96] M. Halbwax, C. Renard, D. Cammilleri, V. Yam, F. Fossard, D. Bouchier, Y. Zheng, and E. Rzepka. Epitaxial growth of Ge on a thin SiO_2 layer by ultrahigh vacuum chemical vapor deposition. *Journal of Crystal Growth*, 308(1):26–29, 2007.

[97] Darin Leonhardt, Swapnadip Ghosh, and Sang M. Han. Origin and removal of stacking faults in Ge islands nucleated on Si within nanoscale openings in SiO_2. *Journal of Applied Physics*, 110(7):073516, 2011.

[98] Ju Hyung Nam, Sabri Alkis, Donguk Nam, Farzaneh Afshinmanesh, Jaewoo Shim, Jin-Hong Park, Mark Brongersma, Ali Kemal Okyay, Theodore I. Kamins, and Krishna Saraswat. Lateral overgrowth of germanium for monolithic integration of germanium-on-insulator on silicon. *Journal of Crystal Growth*, 416:21–27, 2015.

[99] Hiroaki Kuriyama, Masahiro Ito, Keita Suzuki, and Yoshiji Horikoshi. Determination of the Facet Index in Area Selective Epitaxy of GaAs. *Japanese Journal of Applied Physics*, 39(Part 1, No. 4B):2457–2459, apr 2000.

[100] Scott K. Stanley, Shawn S. Coffee, and John G. Ekerdt. Interactions of germanium atoms with silica surfaces. *Applied Surface Science*, 252(4):878–882, 2005.

[101] Amir Sammak, Wiebe de Boer, and Lis K. Nanver. Ge-on-Si: Single-Crystal Selective Epitaxial Growth in a CVD Reactor. *ECS Transactions*, 50(9):507–512, 2013.

[102] Ji-Soo Park, Jie Bai, Michael Curtin, Mark Carroll, and Anthony Lochtefeld. Facet formation and lateral overgrowth of selective Ge epitaxy on SiO_2-patterned Si(001) substrates. *Journal of Vacuum Science & Technology B: Microelectronics and Nanometer Structures Processing, Measurement, and Phenomena*, 26(1):117–121, 2008.

[103] Michiharu Nishimura, Kazuki Kawashita, and Yasuhiko Ishikawa. Silicon-Germanium Stressors for Germanium Photonic Devices on Silicon. *ECS Transactions*, 86(7):3–10, 2018.

[104] Yasutaka Mizuno. Germanium selective epitaxial growth on submicron scaled trenches and strain tuning of optical devices by selective growth mask. Master's thesis, The University of Tokyo, 2014.

[105] L. G. Lavrent'eva, I. S. Zakharov, and Yu. M. Rumyantsev. Anisotropy of the growth rate and doping level of self-epitaxial germanium in the crystallographic range (111)-(100). *Soviet Physics Journal*, 13(4):517–522, Apr 1970.

[106] Katsuya Oda, Tadashi Okumura, Junichi Kasai, Satoshi Kako, Satoshi Iwamoto, and Yasuhiko Arakawa. Crystallinity improvements of Ge waveguides fabricated by epitaxial lateral overgrowth. *Japanese Journal of Applied Physics*, 55(4S):04EH06, 2016.

[107] Roberto Bergamaschini, Marco Salvalaglio, Andrea Scaccabarozzi, Fabio Isa, Claudiu V. Falub, Giovanni Isella, Hans von Känel, Francesco Montalenti, and Leo Miglio. Temperature-controlled coalescence during the growth of Ge crystals on deeply patterned Si substrates. *Journal of Crystal Growth*, 440:86–95, 2016.

[108] Hiroyuki Hirayama, Masayuki Hiroi, Kazuhisa Koyama, and Toru Tatsumi. Selective heteroepitaxial growth of Si1 − xGex using gas source molecular beam epitaxy. *Applied Physics Letters*, 56(12):1107–1109, 1990.

[109] Peng Huei Lim, Yosuke Kobayashi, Shinya Takita, Yasuhiko Ishikawa, and Kazumi Wada. Enhanced photoluminescence from germanium-based ring resonators. *Applied Physics Letters*, 93(4):041103, 2008.

[110] Szu-Lin Cheng, Gary Shambat, Jesse Lu, Hyun-Yong Yu, Krishna Saraswat, Theodore I. Kamins, Jelena Vuckovic, and Yoshio Nishi. Cavity-enhanced direct band electroluminescence near 1550 nm from germanium microdisk resonator diode on silicon. *Applied Physics Letters*, 98(21):211101, 2011.

[111] Abdelrahman Zaher Al-Attili, Satoshi Kako, Muhammad K. Husain, Frederic Y. Gardes, Naoki Higashitarumizu, Satoshi Iwamoto, Yasuhiko Arakawa, Yasuhiko Ishikawa, Hideo Arimoto, Katsuya Oda, Tatemi Ido, and Shinichi Saito. Whispering Gallery Mode Resonances from Ge Micro-Disks on Suspended Beams. *Frontiers in Materials*, 2:43, 2015.

[112] U. Schnakenberg, W. Benecke, and P. Lange. TMAHW etchants for silicon micromachining. In *TRANSDUCERS '91: 1991 International Conference on Solid-State Sensors and Actuators. Digest of Technical Papers*, pages 815–818, June 1991.

[113] Virginie Loup, Laurence Gabette, Marie-Christine Roure, Riadh Kachtouli, Marine Jourdan, Pascal Besson, and Sebastien Petitdidier. Si and SiGe Alloys Wet Etching Using TMAH Chemistry. *ECS Transactions*, 58(6):47–55, 2013.

[114] Yoichi Takada, Jiro Osaka, Yasuhiko Ishikawa, and Kazumi Wada. Effect of Mesa Shape on Threading Dislocation Density in Ge Epitaxial Layers on Si after Post-Growth Annealing. *Japanese Journal of Applied Physics*, 49(4S):04DG23, 2010.

[115] Yoichi Takada. Master's thesis. The University of Tokyo, 2010.

[116] J.E. Ayers, L.J. Schowalter, and S.K. Ghandhi. Post-growth thermal annealing of GaAs on Si(001) grown by organometallic vapor phase epitaxy. *Journal of Crystal Growth*, 125(1):329–335, 1992.

[117] G. Wang, R. Loo, E. Simoen, L. Souriau, M. Caymax, M. M. Heyns, and B. Blanpain. A model of threading dislocation density in strain-relaxed Ge and GaAs epitaxial films on Si (100). *Applied Physics Letters*, 94(10):102115, 2009.

[118] Darin Leonhardt, Swapnadip Ghosh, and Sang M. Han. Defects in Ge epitaxy in trench patterned SiO2 on Si and Ge substrates. *Journal of Crystal Growth*, 335(1):62–65, 2011.

[119] Yourui Huangfu, Wenbo Zhan, Xia Hong, Xu Fang, Guqiao Ding, and Hui Ye. Heteroepitaxy of Ge on Si(001) with pits and windows transferred from free-standing porous alumina mask. *Nanotechnology*, 24(18):185302, 2013.

[120] G. Vanamu, A.K. Datye, and Saleem H. Zaidi. Heteroepitaxial growth on microscale patterned silicon structures. *Journal of Crystal Growth*, 280(1):66–74, 2005.

[121] Yu. B. Bolkhovityanov, A. K. Gutakovskii, A. S. Deryabin, and L. V. Sokolov. Edge misfit dislocations in Ge_xSi_{1-x}/Si(001) ($x \sim 1$) heterostructures: role of buffer Ge_ySi_{1-y}($y < x$) interlayer in their formation. *Physics of the Solid State*, 53(9):1791, Sep 2011.

[122] A. Bourret. How to control the self-organization of nanoparticles by bonded thin layers. *Surface Science*, 432(1):37–53, 1999.

[123] J. P. Hirth and J. Lothe. *"Grain boundaries," in Theory of Dislocations*. Wiley, 2nd ed. ch. 19, pp. 697–750, New York, NY, USA, 1982.

[124] Y. Mizuno, M. Yako, N. M. Luan, and K. Wada. Strain tuning of germanium bandgap by selective epitaxial growth for electro-absorption modulators. In Graham T. Reed and Michael R. Watts, editors, *Proc. SPIE 9367, Silicon Photonics X, 93670E*, 2015.

[125] Jinendra Raja Jain, Aaron Hryciw, Thomas M. Baer, David A. B. Miller, Mark L. Brongersma, and Roger T. Howe. A micromachining-based technology for enhancing germanium light emission via tensile strain. *Nature Photonics*, 6:398–405, 05 2012.

[126] T. S. Perova, J. Wasyluk, K. Lyutovich, E. Kasper, M. Oehme, K. Rode, and A. Waldron. Composition and strain in thin $Si_{1-x}Ge_x$ virtual substrates measured by micro-Raman spectroscopy and x-ray diffraction. *Journal of Applied Physics*, 109(3):033502, 2011.

[127] J. Macia, E. Martin, A. Pérez-Rodoriguez, J. Jiménez, J. R. Morante, B. Aspar, and J. Margail. Raman microstructural analysis of silicon-on-insulator formed by high dose oxygen ion implantation: As-implanted structures. *Journal of Applied Physics*, 82(8):3730–3735, 1997.

[128] N. Kanani R. W. Olesinski and G. J. Abbaschian. The Ge − P (Germanium-Phosphorus) system. *Bulletin of Alloy Phase Diagrams*, 6(3):262–266, 1985.

[129] Yan Cai, Rodolfo Camacho-Aguilera, Jonathan T. Bessette, Lionel C. Kimerling, and Jurgen Michel. High phosphorous doped germanium: Dopant diffusion and modeling. *Journal of Applied Physics*, 112(3):034509, 2012.

[130] Rodolfo E. Camacho-Aguilera, Yan Cai, Jonathan T. Bessette, Lionel C. Kimerling, and Jurgen Michel. High active carrier concentration in n-type, thin film Ge using delta-doping. *Opt. Mater. Express*, 2(11):1462–1469, Nov 2012.

[131] Jifeng Liu, Rodolfo Camacho-Aguilera, Jonathan T. Bessette, Xiaochen Sun, Xiaoxin Wang, Yan Cai, Lionel C. Kimerling, and Jurgen Michel. Ge-on-Si optoelectronics. *Thin Solid Films*, 520(8):3354–3360, 2012. ICSI-7.

[132] Chan-Hyuck Park, Han Pan, Yasuhiko Ishikawa, Kazumi Wada, and Donghwan Ahn. N-type doping of germanium epilayer on silicon by ex-situ phosphorus diffusion based on POCl3 phosphosilicate glass. *Thin Solid Films*, 662:1–5, 2018.

[133] Kuan Pei Yap, André Delâge, Jean Lapointe, Boris Lamontagne, Jens H. Schmid, Philip Waldron, Barry A. Syrett, and Siegfried Janz. Correlation of Scattering Loss, Sidewall Roughness and Waveguide Width in Silicon-on-Insulator (SOI) Ridge Waveguides. *J. Lightwave Technol.*, 27(18):3999–4008, Sep 2009.

[134] Lionel C. Kimerling, Dim-Lee Kwong, and Kazumi Wada. Scaling computation with silicon photonics. *MRS Bulletin*, 39(8):687–695, 2014.

[135] Ziyi Zhang, Motoki Yako, Kan Ju, Naoyuki Kawai, Papichaya Chaisakul, Tai Tsuchizawa, Makoto Hikita, Koji Yamada, Yasuhiko Ishikawa, and Kazumi Wada. A new material platform of Si photonics for implementing architecture of dense wavelength division multiplexing on Si bulk wafer. *Science and technology of advanced materials*, 18(1):283–293, 04 2017.

[136] Henry Kressel. The Effect of Crystal Defects on Optoelectronic Devices. In R.K. Willardson and Albert C. Beer, editors, *Defects, (HgCd)Se, (HgCd)Te*, volume 16 of *Semiconductors and Semimetals*, chapter 1, pages 1–52. Elsevier, 1981.

[137] Hartmut Bracht and Sergej Brotzmann. Atomic transport in germanium and the mechanism of arsenic diffusion. *Materials Science in Semiconductor Processing*, 9(4):471 – 476, 2006. Proceedings of

Symposium T E-MRS 2006 Spring Meeting on Germanium based semiconductors from materials to devices.

[138] Richard Geiger, Thomas Zabel, and Hans Sigg. Group IV Direct Band Gap Photonics: Methods, Challenges, and Opportunities. *Frontiers in Materials*, 2:52, 2015.

[139] Rodolfo E. Camacho-Aguilera. Ge-on-Si LASER for Silicon Photonics. *Ph. D. dissertation, Massachusetts Institute of Technology*, June 2013.

[140] Y. P. Varshni. Temperature dependence of the energy gap in semiconductors. *Physica*, 34(1):149–154, 1967.

[141] B. Dutt, D. S. Sukhdeo, D. Nam, B. M. Vulovic, Z. Yuan, and K. C. Saraswat. Roadmap to an Efficient Germanium-on-Silicon Laser: Strain vs. n-Type Doping. *IEEE Photonics Journal*, 4(5):2002–2009, 2012.

[142] R. W. Olesinski, N. Kanani, and G. J. Abbaschian. The Ge–P (Germanium-Phosphorus) system. *Bulletin of Alloy Phase Diagrams*, 6(3):262–266, Jun 1985.

[143] E. M. Purcell, H. C. Torrey, and R. V. Pound. Resonance Absorption by Nuclear Magnetic Moments in a Solid. *Physical Review*, 69(1-2):37–38, 01 1946.

[144] T. Baba and D. Sano. Low-threshold lasing and Purcell effect in microdisk lasers at room temperature. *IEEE Journal of Selected Topics in Quantum Electronics*, 9(5):1340–1346, 2003.

[145] Gary Shambat, Szu-Lin Cheng, Jesse Lu, Yoshio Nishi, and Jelena Vuckovic. Direct band Ge photoluminescence near 1.6 μm coupled to Ge-on-Si microdisk resonators. *Applied Physics Letters*, 97(24):241102, 2010.

[146] Jan Petykiewicz, Donguk Nam, David S. Sukhdeo, Shashank Gupta, Sonia Buckley, Alexander Y. Piggott, Jelena Vučković, and Krishna C. Saraswat. Direct Bandgap Light Emission from Strained Germanium Nanowires Coupled with High-Q Nanophotonic Cavities. *Nano Letters*, 16(4):2168–2173, 04 2016.

[147] Yan Cai, Wei Yu, Lionel C. Kimerling, and Jurgen Michel. Chemical Mechanical Polishing of Selective Epitaxial Grown Germanium on Silicon. *ECS Journal of Solid State Science and Technology*, 3(2):P5–P9, 2014.

[148] Sho Nagatomo, Yasuhiko Ishikawa, and Satohiko Hoshino. Near-infrared laser annealing of Ge layers epitaxially grown on Si for high-performance photonic devices. *Journal of Vacuum Science & Technology B*, 35(5):051206, 2017.

[149] E. Yablonovitch, D. L. Allara, C. C. Chang, T. Gmitter, and T. B. Bright. Unusually Low Surface-Recombination Velocity on Silicon and Germanium Surfaces. *Phys. Rev. Lett.*, 57:249–252, Jul 1986.

[150] Jillian M. Buriak. Organometallic Chemistry on Silicon and Germanium Surfaces. *Chemical Reviews*, 102(5):1271–1308, 2002. PMID: 11996538.

[151] M. Fujita, Y. Tanaka, and S. Noda. Light Emission From Silicon in Photonic Crystal Nanocavity. *IEEE Journal of Selected Topics in Quantum Electronics*, 14(4):1090–1097, 2008.

Publication List

Journal Articles with Peer Review

1) **M. Yako**, Y. Ishikawa, and K. Wada, "Coalescence induced dislocation reduction in selectively grown lattice-mismatched heteroepitaxy: Theoretical prediction and experimental verification," *Journal of Applied Physics*, 128(18), 185304 (2018).

2) **M. Yako**, Y. Ishikawa, E. Abe, and K. Wada, "Defects and their reduction in Ge selective epitaxy and coalescence layer on Si with semicylindrical voids on SiO_2 masks," *IEEE Journal of Selected Topics in Quantum Electronics*, 24(6), 8201007 (2018).

3) **M. Yako**, N. Higashitarumizu, and Y. Ishikawa, "Impact of interface recombination on direct-gap photoluminescence from Ge epitaxial layers on Si," *Japanese Journal of Applied Physics*, Accepted.

Conference Proceedings with Peer Review

1) **M. Yako**, N. J. Kawai, Y. Mizuno, and K. Wada, "The kinetics of Ge lateral overgrowth on SiO_2," *MRS Advances*, 1(23), 1703-1708 (2016).

2) **M. Yako**, C. H. Park, D. Ahn, Y. Ishikawa, and K. Wada, "Low threshold light emission from reverse-rib n^+ Ge cavity made by P diffusion," *ECS Transactions*, 75(8), 193-198 (2016).

3) **M. Yako** and Y. Ishikawa, "Order-of-magnitude enhancement of direct-gap photoluminescence from patterned Ge epitaxial layers on Si induced by a wet chemical treatment," *International Conference on Solid State Devices and Materials*, H-1-03, 487–488, 2018.

4) **M. Yako**, Y. Ishikawa, E. Abe, and K. Wada, "Reduction of threading dislocations by image force in Ge selective epilayers on Si," *Proceedings of SPIE Photonics Asia Nanophotonics and Micro/Nano Optics IV*, 108230F (25 October 2018).

Technical Report Without Peer Review

1) 八子 基樹, 石川 靖彦, 和田 一実, "トンネル状空隙の導入による Si 上 Ge 層の貫通転位密度低減," 電子情報通信学会信学技報, SDM2018-15 (2018). (in Japanese)

International Conferences with Peer Review

1) **M. Yako**, N. J. Kawai, Y. Mizuno, and K. Wada, "The kinetics and quality of Ge lateral overgrowth on SiO_2," Materials Research Society Fall Meeting, MA, USA, Dec. 2015.

2) **M. Yako**, C. H. Park, D. Ahn, and K. Wada, "Design and Fabrication of Grown-in Reverse Ge Rib Structure for Efficient Lasing," Materials Research Society Spring Meeting, AZ, USA, Mar. 2016.

3) **M. Yako**, C. H. Park, D. Ahn, Y. Ishikawa, and K. Wada, "Low Threshold Light Emission from Reverse-Rib n^+ Ge Cavity Made By P Diffusion," ECS 230th meeting, HI, USA, Oct. 2016.

4) **M. Yako**, Y. Ishikawa, E. Abe, and K. Wada, "Threading dislocation trapping by air tunnels in Ge-on-Si," 29th International Conference on Defects in Semiconductors, Shimane, Japan, Aug. 2017.

5) **M. Yako** and Y. Ishikawa, "Order-of-magnitude enhancement of direct-gap photoluminescence from patterned Ge epitaxial layers on Si induced by a wet chemical treatment," International Conference on Solid State Devices and Materials, Tokyo, Japan, Sep. 2018.

6) **M. Yako**, Y. Ishikawa, E. Abe and K. Wada, "Reduction of threading dislocations by image force in Ge selective epilayers on Si," SPIE Photonics Asia, Asia, Beijing, China, Oct. 2018.

Domestic Conferences Without Peer Review

1) 八子 基樹, 水野 泰孝, 河合 直行, 和田 一実, "Ge 選択成長における SiO_2 マスク上への横方向成長促進," 第 76 回応用物理学会秋季学術講演会, 愛知県名古屋市, 2015 年 9 月

2) 八子 基樹, 和田 一実, "SiO_2 上横方向成長を用いた極低貫通転位密度 Ge 薄膜," 第 63 回応用物理学会春季学術講演会, 東京都目黒区, 2016 年 3 月

3) 八子 基樹, 石川 靖彦, 和田 一実, "Si 基板上逆リブ構造 Ge 選択成長層における貫通転位密度低減," 第 64 回応用物理学会春季学術講演会, 神奈川県横浜市, 2017 年 3 月

4) 八子 基樹, 石川 靖彦, 和田 一実, "Si 基板上 inverted-rib 構造 Ge 選択成長層における貫通転位密度低減," 第 65 回応用物理学会春季学術講演会, 東京都新宿区, 2018 年 3 月

5) 八子 基樹, 石川 靖彦, 和田 一実, "トンネル状空隙の導入による Si 上 Ge 層の貫通転位密度低減," 電子情報通信学会 シリコン・デバイス研究会, 愛知県豊橋市, 2018 年 5 月